MULTI-SCALE EVOLUTION OF A DERECHO-PRODUCING MCS

by Ligia Ribeiro Bernardet

William R. Cotton, P.I.

Colorado
State
University

DEPARTMENT OF
ATMOSPHERIC SCIENCE

PAPER NO. 636

MULTI–SCALE EVOLUTION OF A DERECHO–PRODUCING MCS

by

Lígia Ribeiro Bernardet

Department of Atmospheric Science

Colorado State University

Fort Collins, CO 80523

September 10, 1997

Atmospheric Science Paper No. 636

ABSTRACT

MULTI–SCALE EVOLUTION OF A DERECHO–PRODUCING MCS

In this dissertation we address one type of severe weather: strong straight-line winds. In particular, we focus on *derechos*, a type of wind storm caused by a convective system and characterized by its long duration and by the large area it covers.

One interesting characteristic of these storms is that they develop at night, on the cold side of a thermal boundary. This region is not characterized by large convective instability. In fact, surface parcels are generally stable with respect to vertical displacements.

To gain understanding of the physical processes involved in these storms, we focused on the case of a MCS that developed in eastern Colorado on 12–13 May, 1985. The system formed in the afternoon, was active until early morning, and caused strong winds during the night.

A multi–scale full physics simulation of this case was performed using a non-hydrostatic mesoscale model. Four telescopically nested grids covering from the synoptic scale down to cloud scale circulations were used. A Lagrangian model was used to follow trajectories of parcels that took part in the updraft and in the downdraft, and balance of forces were computed along the trajectories.

Our results show that the synoptic and mesoscale environment of the storm largely influences convective organization and cloud-scale circulations. During the day, when the boundary layer is well mixed, the source of air for the clouds is located within the boundary layer. At night, when the boundary layer becomes stable, the source of air shifts to the top of the boundary layer. It is composed of warm, moist air that is brought by the nocturnal low-level jet.

i

The downdraft structure also changes from day to night. During the day, parcels acquire negative buoyancy because of cooling due to evaporation and melting. As they sink, they remain colder than the environment, and end up at the surface constituting the cold pool.

During the night, downdrafts are stronger, generating the strong surface winds. The most important branch of the downdraft has an "up-down" trajectory. Parcels start close to the ground, are lifted up by a strong pressure gradient force, and become colder than their surroundings as they ascend in a stable environment. Then, as they go through the precipitation shaft, they sink due to negative buoyancy enhanced by condensate loading. The upward pressure gradient force is partially related to mid-level rotation in the storm, which has characteristics of a high-precipitation supercell.

Lígia Ribeiro Bernardet
Department of Atmospheric Science
Colorado State University
Fort Collins, Colorado 80523
Fall 1997

ACKNOWLEDGEMENTS

Several people contributed to the success of this project. In particular, I would like to thank my adviser, Bill Cotton and committee members Mike Montgomery and Dick Johnson for their help in understanding the complex world of convective systems and the dynamics of the atmosphere.

Special thanks to Jason Nachamkin, Cathy Finley and Louie Grasso, who were always available for enlightening discussions about the model and about convective systems. They were a big source of support. Also, Jason Nachamkin and Bjorn Stevens are acknowledged for an in depth reading of the original manuscript, and for the numerous suggestions that led to improvements in the final text. Bob Walko and Jim Edwards were very helpful in answering questions about RAMS.

A couple people helped with the data, Jerry Schmidt, the first one to work with this case, and Ray McAnelly, who provided the Limon radar data. Brenda Thompson helped with the editing and Judy Sorbie-Dunn drafted some of the figures.

Last, I want to thank Jim Edwards and the friends that gave me personal support during this long journey.

TABLE OF CONTENTS

LIST OF FIGURES

LIST OF TABLES

Chapter 1

INTRODUCTION

In this dissertation we focus on mesoscale convective systems that produce sustained straight-line winds at the surface. These systems, known as *derechos* are a form of severe weather that is quite common in the United States, with an average of 17 cases per warm season (Johns and Hirt 1987).

The climatology of derecho events shows that they usually occur in the warm season, on the cold side of a thermal boundary, such as the cold pool left by previous convection or, more usually, a weak stationary summertime front. Since, by definition, derechos are caused by convective systems, the climatology of deep convection can also be used to shed light on the derecho environment. In the Central United States there is a summertime nocturnal maximum of convection, and indeed, several derechos described in the literature occurred at night.

The nocturnal character of the convection, associated with its location on the cold side of a front, characterizes the derecho environment with strong low level stability, which leads to two questions. First, if the boundary layer is stable, what is the source of air for the cloud mass? And second, how can downdrafts penetrate to the surface and cause strong winds in a stable environment? The first question has been addressed by several studies in the literature, and its answer has been tied to the nocturnal low level jet (LLJ), a southerly current that flows on top of the nocturnal stable boundary layer and transports warm, moist air to the region of MCS development. In this study, we show that air from the stable layer can also contribute to the updraft, as long as a mechanism to extract it from the boundary layer is present. The scientific community has payed little attention to the second question, the role of the stable boundary layer, regarding it as having just the

passive role of providing a surface over which the LLJ could glide, or as a factor to retard the onset of convection.

Because derechos often form on top of a stable boundary layer, we hypothesize that this layer has fundamental importance in their development and maintenance, and we explore this connection here.

This research focused on the case of a MCS that crossed Kansas on 12–13 May, 1985. It had the characteristics discussed above: the strong winds occurred at night on the northern side of a stationary front. A multi-grid numerical model initialized from real physiographic and three-dimensional atmospheric data was used to simulate the case. Four grids with horizontal spacings of 80/40/10/2 km were used to simulate features from the synoptic scale down to the meso and cloud-scale. The model was initialized at 06 CST. The formation of the convective system in eastern Colorado on the afternoon of May 12, and its progression towards the northeast into Kansas were well simulated. Due to the long duration of this integration (24 hours), we were able to study the daytime phase of the MCS as it evolved on top of a well mixed boundary layer, and its night–time phase. At night, the model captured the development of the LLJ, as well as the development of the stable PBL. The modeled system produced surface winds in excess of 22ms^{-1} for seven and a half hours, beginning after sunset.

The outline of this manuscript is as follows. Chapter 2 reviews previous studies examining the characteristics of convection in the central United States and possible mechanisms for the generation of strong winds. Chapter 3 reviews the observations of the 12–13 May, 1985 case. A summary of the model configuration employed in this study is presented in Chapter 4. The simulated storm dynamics is presented in Chapter 5, with emphasis on both the mesoscale environment and the cloud scale aspects. Chapter 6 presents a detailed analysis of circulation branches in the convective system. For this analysis, winds produced by the Eulerian model were used to drive a parcel model that computed trajectories of parcels that composed the updraft and the downdraft. Along the trajectories several properties of the parcels were computed, such as temperature and moisture content. Also, a vertical balance of forces was computed, which permitted the differentiation of circulations driven by buoyancy from those forced by pressure gradients. This was necessary to identify locations

where the boundary layer stability caused negative buoyancy, and the parcel relied on other forces to be displaced either up or down. An interpretation of modeling results is presented in Chapter 7, and final conclusions and suggestions for future work are in Chapter 8.

Chapter 2

BACKGROUND

"I am not sure how clouds get formed, but clouds know how to do it and that is the
important thing!"
From a 6th grader

In this chapter we will review the forms of convective organization that are most important in the High Plains of the United States. We will focus on those associated with strong straight-line winds and review mechanisms that can cause the winds. We will also review the use of numerical models to study deep convection.

2.1   Introduction

Precipitating systems can assume a variety of forms. In stratiform systems, precipitation is spread out and horizontally homogeneous, though it can be quite heavy, as in the case of nimbostratus clouds. Precipitation can also be localized and have a high spatial variability, as in the case of ordinary thunderstorms. Further, thunderstorms can organize in mesoscale convective systems (MCSs), which themselves can encompass regions of convective and stratiform rain.

Convective organization is determined by the environment in which storms form. Atmospheric parameters that have proven useful in describing the storm environment include Convective Available Potential Energy (CAPE), vertical shear of the horizontal winds, vertical relative vorticity, jet streaks and inertial instability. Surface parameters include topography and soil moisture.

In the following two sections we describe the characteristics of the prominent forms of convective organization in the High-Plains of the United States. Section 2.4 discusses in

detail what controls convective organization. Storm propagation, downdraft development and a review of the interaction between convection and gravity waves are presented in the following three sections. Section 2.8 reviews previous studies of derechos. Finally, Section 2.9 discusses approaches to modeling convection.

2.2 Mesoscale Convective Systems

MCS is a term that does not have a precise definition. According to Cotton and Anthes (1989): " The term MCS describes a deep convective system that is considerably larger than an individual thunderstorm and that is often marked by an extensive middle to upper tropospheric stratiform-anvil cloud of several hundred kilometers in horizontal dimension".

One of the common configurations of MCSs in the High Plains of the United States is the squall line with a leading convective line and trailing stratiform region. The main characteristics of this system are described below. This system is not the only form of MCS organization in the Plains, but it is certainly an important one.

2.2.1 Squall Lines

Houze et al. (1990) documented two types of squall lines in the High Plains (Figure 2.1), which he called symmetric and asymmetric systems. Although the distribution of the rain regions vary, they both have convective cells in the leading edge, and a region of lighter stratiform rain behind. To a first approximation, the circulation in a squall line may be described in a two-dimensional sense, assuming that the line is uniform and infinite in the along-line direction. The main flow branches of the squall line are illustrated in Figure 2.2. They comprise the ascending front-to-rear jet (FTRJ), that enters the system from its front, ascends and exits the convective line on its back, and continues a slow ascent in the stratiform region, and the descending rear-inflow jet (RIJ), that enters the storm from its rear in mid levels and descends to the surface behind the convective line.

Johnson and Hamilton (1988) have documented the surface pressure patterns associated with squall lines with a trailing stratiform region (Figure 2.3). Under the leading convective line, a mesoscale region of high pressure (meso-high) is present. It is caused by
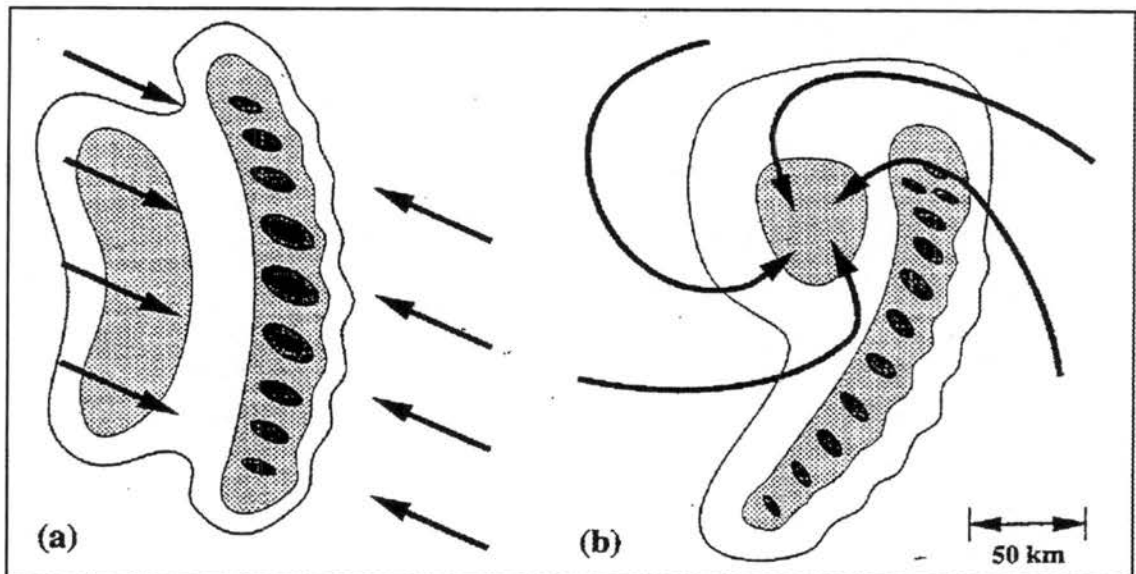
Figure 2.1: Midlevel cross-sections through conceptual models of a) a symmetric leading-line trailing stratiform MCS and b) an asymmetric MCS with a well-defined vortex. The storm relative flow is superposed on the low–level radar reflectivity with heavier stippling denoting heavier reflectivity. Adapted from Houze et al. (1989) and Houze et al. (1990) by Skamarock et al. (1994).
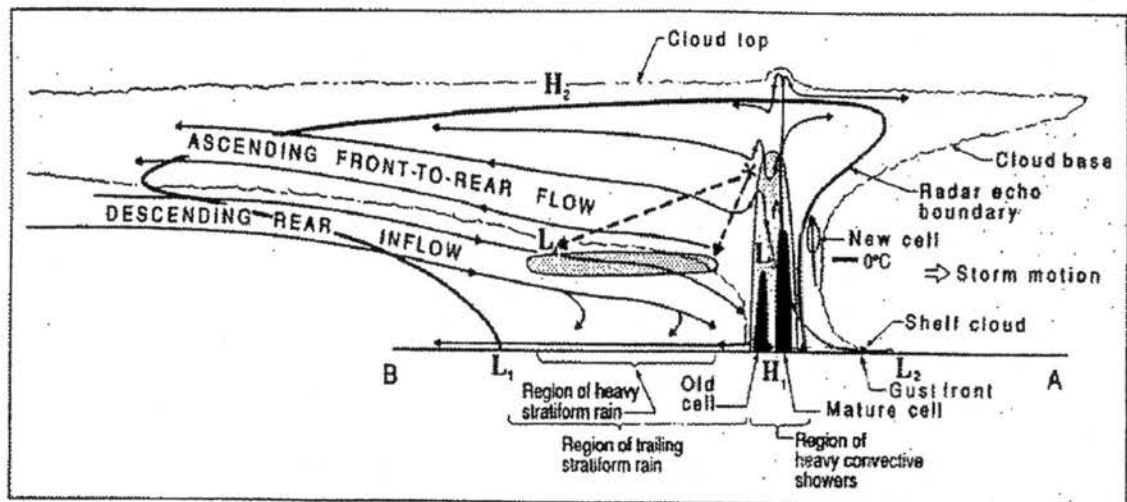
Figure 2.2: Conceptual model of a squall line with a trailing stratiform area viewed in a vertical cross section oriented perpendicular to the convective line. From Houze et al. (1989).

hydrostatic effects, associated with the cooling of the air due to evaporation and melting of hydrometeors. The meso-high is the pressure signature of the cold pool, a dome of cold air that develops under the convective line. A pressure gradient force associated with the temperature gradient causes the flow to accelerate out of the high, forming the gust front. Towards the back of the system, behind the strongest stratiform rain, a wake low forms, mainly due to subsidence warming associated with the descending RIJ. A secondary mesolow may also form ahead of the system, because part of the subsidence reaches ahead of the storm.

Several authors have described complex MCSs that organized in a very three-dimensional fashion. Skamarock et al. (1994) focus on the importance of line end effects in MCS development. Running a three-dimensional simulation in an idealized model set-up, they describe that the finite characteristics of the line are responsible for surges in the line. In the beginning stages of development, the cells located in the ends of the line are the strongest, because they have less competition for the environmental supply of unstable air. This causes the line ends to surge forward. As the system evolves, the surges migrate to the center, because the strong cold pools produced by the cells at the end of the line strengthen the neighboring cells. When the surges finally meet at the center of the line, a bow forms. This shape (Figure 2.4) is commonly observed in squall lines that develop in environments with strong shear, and has been identified in some derecho cases (Przybylinski et al. 1996).

Another important three-dimensional aspect of squall lines is the development of meso-scale convective vortices (MCVs) (Olsson and Cotton 1997a,b; Hertenstein 1996). Those vortices may attain different diameters, from 20 km (Verlinde and Cotton 1990) to hundreds of kilometers (Bartels and Maddox 1991). They usually form behind the convective line, and occupy the mid-troposphere. At times, counterrotating vortices (termed *bookend vortices* by Weisman 1992) are observed in the line ends (Scott and Rutledge 1995), while other studies show the presence of only one large cyclonic vortex on the northern end of the line (Brandes 1990). It is possible that the large cyclonic vortex evolves from the original pair of counterrotating vortices (Skamarock et al. 1994). A lot of attention has been paid to those vortices because of their longevity and ability to regenerate convection after the initial convective line has died (Raymond 1992; Fritsch et al. 1994; Davis and Weisman 1994).
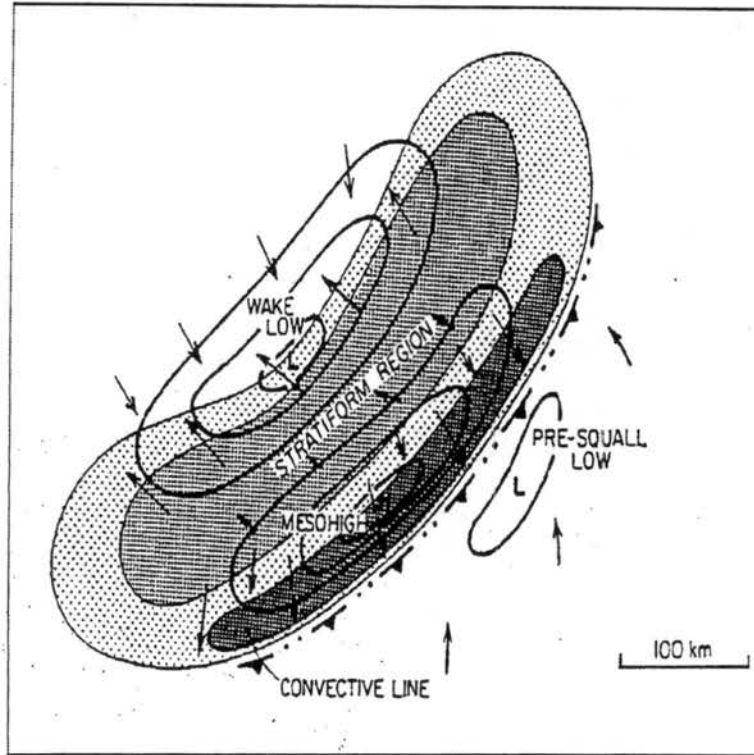
Figure 2.3: Schematic of surface pressure field (1 hPa intervals) and ground relative flow (arrows) associated with a symmetric MCS. Light and moderate shading represent radar reflectivities less than and greater than 30 dBZ, respectively. Heavy shading represents the convective line containing cells with reflectivities exceeding 40 dBZ. From Loehrer (1992).
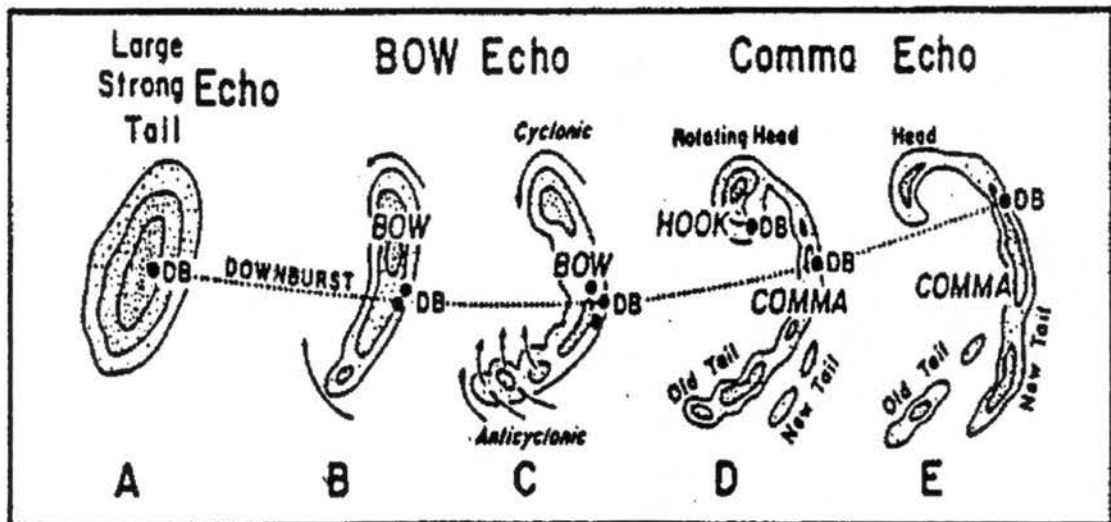
Figure 2.4: A typical morphology of radar echoes associated with strong and extensive downbursts. During the period of strongest downbursts, the echo often takes the shape of a spearhead echo pointing in the direction of motion. Adapted from Fujita (1978) by Przybylinski (1995).

Size	A. Cloud shield with IR temperature $\leq$ -32 °C must have an area $\geq$ 100,000 km^2 B. Cloud shield with IR temperature $\leq$ -52 °C must have an area $\geq$ 50,000 km^2
Initiate	Size definitions **A** and **B** are first satisfied
Duration	Size definitions **A** and **B** must be met for a period $\geq$ 6 hrs
Maximum extent	Contiguous cloud shield (IR temperature $\leq$ -32 °C) reaches maximum size
Shape	Eccentricity (minor axis/major axis) $\geq$ 0.7 at time of maximum extent
Terminate	Size definitions A and B no longer satisfied

Table 2.1: Mesoscale Convective Complex (MCC) definition. From Maddox (1980).

As mentioned before, many MCSs deviate from the leading convective line—trailing stratiform region model. Hertenstein and Schubert (1991) describe theoretically a convective line that never developed a stratiform region. Fortune et al. (1992) studied three MCSs that formed in approximately the same location on 3–4 June 1985. They had one factor in common: three-dimensionality, with convective lines that had what the authors called an "open-wave" shape, resembling a mid-latitude frontal system in miniature. Some common characteristics of squall lines, like a stratiform region, RIJ, cold pool and mesohigh could only be identified in the northwestern part of the system, probably because all anvil material produced in the southern part of the system was advected north by the ambient winds.

2.2.2 Mesoscale Convective Complexes

One special type of MCS is the *Mesoscale Convective Complex*, or MCC, that was first defined and studied by Maddox (1980) as a convective system whose anvil is very large when seen by satellite. The Maddox (1980) definition of a MCC is outlined in Table 2.1.

It might appear that the discrimination between MCSs and MCCs is arbitrary, but MCCs are a subset of MCSs that have some unique properties: the location and the environment in which they form. Figure 2.5 shows the distribution of MCCs in the Americas. While squall lines happen almost everywhere, MCCs are restricted to certain locations, because they require a special environment. Cotton et al. (1989) proposed an important
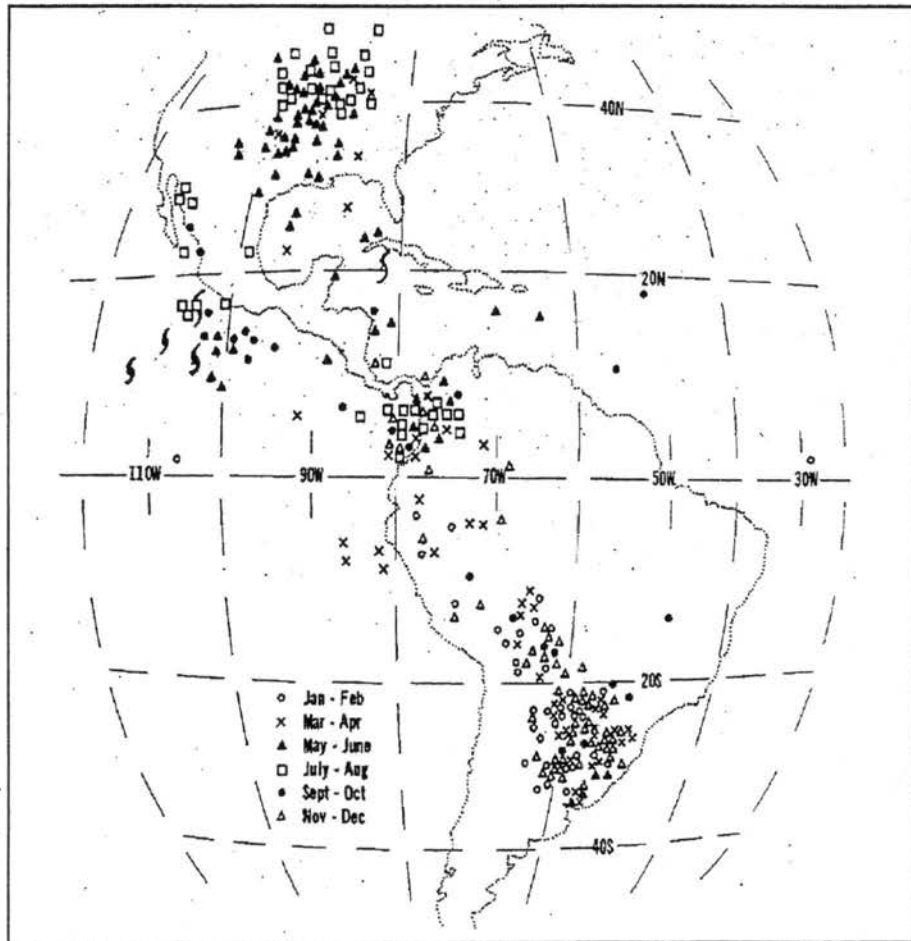
Figure 2.5: Geographic and monthly distribution of MCCs in and around the Americas. From Velasco and Fritsch (1987).

distinction between MCCs and MCSs. MCCs are a "balanced" system, whose diameter is comparable to the Rossby radius, which identifies the scale at which the inertial stability of a system becomes important. The stability is achieved through rotation, both of the Earth and of the system itself. The classification of MCCs as balanced systems was later corroborated by Olsson and Cotton (1997a,b).

Worldwide, MCCs form most often downstream of mountain chains, on the cold side of a weak frontal discontinuity, under the influence of significant westerly upper level jet and low level jet, the latter responsible for significant warm advection over the genesis region. These elements amount to some low-level baroclinicity, but strong upper-level baroclinicity is not present in most cases (Maddox 1983). However, there are definitely cases in which it is observed (Tremback 1990; Schmidt and Cotton 1989).

Another worldwide characteristic of MCCs (Velasco and Fritsch 1987; Laing and Fritsh 1993a,b) is that they are preferentially nocturnal. The development time corresponds to the formation of the nocturnal low-level jet, which is believed to play an important role.

The low-level jet

A lot of attention has been paid to the low-level jet (LLJ) in the High Plains of the United States because of its documented influence in nocturnal convection (Pitchford and London 1962; Porter et al. 1955; Augustine and Caracena 1994).

Blackadar (1957) defined the LLJ as a low-level, local maximum in the vertical profile of the horizontal wind speed. Data gathered by Blackadar using rawindsondes and by Mitchell et al. (1995) using wind profilers, shows a strong LLJ signature in the High Plains in the warm season. Mitchell et al. (1995) show that the jet is present in approximately 15 per cent of the observations in the warm season, is predominantly from the south or southwest, occurs more often between 0600 and 0900 UTC, and has an average altitude of 1000m AGL.

The dynamics of the LLJ was first studied by Blackadar (1957), who proposed a mechanism based on inertial oscillation. He considered that in a given height within the PBL the winds are slowed down during the day because of turbulent mixing. In the evening, when a stable layer forms and mixing ceases, a new balance of forces takes place, in which the winds oscillate around the geostrophic value but never converge to it.

To illustrate this, consider a situation in which the motion is completely horizontal, and the horizontal pressure gradient (and therefore the geostrophic winds) is constant in time and in a horizontal plane. In the PBL, where turbulence has acted to reduce the winds from their original geostrophic value, the horizontal momentum equations may be written as

$$\frac{\partial}{\partial t}(u - u_g) = f(v - v_g), \tag{2.1}$$

$$\frac{\partial}{\partial t}(v - v_g) = -f(u - u_g), \tag{2.2}$$

where f is the Coriolis parameter, (u, v) are the zonal and meridional components of the winds, and (u_g, v_g) are the constant zonal and meridional geostrophic winds. Defining a complex variable

$$W = (u - u_g) + i(v - v_g),$$

(2.1) and (2.2) become

$$\frac{\partial W}{\partial t} = -ifW,$$

which has the solution

$$W = W_0 e^{-ift}, \tag{2.3}$$

where W_0 = deviation from geostrophy at the initial time, taken to be before sunset.

According to (2.3), the winds will complete one clockwise circle in the northern hemisphere in the time $2\pi/f = \pi/\omega sin(\phi)$ or half a pendulum day at latitude ϕ, increasing from the value of W_0 existent at sunset.

Since the 1950's, other mechanisms have been identified as important for the development of the LLJ. One of them, the thermal wind mechanism (McNider and Pielke 1981), helps explain why, in the United States, the most prominent LLJs develop in the Plains. This is a region in which the terrain slopes gently upwards towards the west, and in which dry soils are found to the west and moist soils to the east. In this situation, a warmer and deeper boundary layer develops in the west during the day, while a cooler and shallower PBL develops in the east. In the evening the situation reverses, with the development of a cooler PBL in the west, which is topped by the residual daytime boundary layer. According

to the thermal wind relation (which is derived from geostrophic balance in the horizontal and hydrostatic balance in the vertical),

$$\frac{\partial v_g}{\partial z} = \frac{g}{fT}\frac{\partial T}{\partial x},\tag{2.4}$$

where T is the temperature, the nocturnal positive temperature gradient in the east-west direction will cause a southerly pre-existent geostrophic wind to increase with height. On top of the nocturnal PBL, where the horizontal temperature gradient reverses, the geostrophic wind starts decreasing with height. Those two processes define the height of maximum geostrophic winds as the top of the nocturnal stable boundary layer.

Other mechanisms, including air currents blocked by the Rocky Mountains, large scale baroclinicity and non-stationarity, interactions between upper-level jet streaks and diabatic processes, and interactions with synoptic systems are reviewed by Zhong et al. (1996).

2.2.3   Characteristics of Convection over a Stable Boundary Layer

MCCs are not the only form of nocturnal convection that occurs in the Plains of the United States. Pitchford and London (1962) and Porter et al. (1955) present climatologies of the occurrence of summertime nocturnal generic thunderstorms in the central US and show that they form preferentially on the days in which the LLJ is present. Wallace (1975) shows that there is a nocturnal peak in thunderstorm activity in the High Plains, and that the peak is more prominent when events with strong precipitation are selected.

Augustine and Caracena (1994) also talk about the relationship between the LLJ and the nocturnal maximum of convection in the central United States. They reiterate that MCSs form in the region where the jet decelerates and therefore creates convergence. They also recognize the importance of a previously existent frontal boundary in creating convergence for the MCS.

Trier and Parsons (1993) studied the convective events that took place on 3 and 4 June, 1985, in the Kansas–Oklahoma region. They describe a system that developed on the cold side of a front, and therefore over a stable boundary layer. The development is highly influenced by the advection of air with high equivalent potential temperature (θ_e) by the LLJ over the surface cold front (Figure 2.6). Laing (1997) and Laing and Fritsch

(1997) used a global MCC climatology to show that the LLJ is a ubiquitous feature in the environment of those systems.

One important distinction between the nocturnal system and the daytime one is that nocturnal systems are elevated, that is, the PBL under the storm is stable, and the main source of air for the system is positively buoyant air present on the top of the PBL. The air is advected to the storm region by the LLJ. In fact, elevated storms do not necessarily happen at night, but can occur whenever the PBL in a region is stable and there is an elevated source of positively buoyant air. This can happen in a localized region, for example, when a convective system leaves behind a cold pool. The next storm will not feed in that cool air, and may become an elevated thunderstorm if a source of positively buoyant air is present (e.g. Schmidt and Cotton 1989).

Elevated thunderstorms have been identified as severe weather producers. Rochette et al. (1995) performed a composite study of seven heavy-rain producing MCSs that developed in the Midwest and that had characteristics of elevated thunderstorms. They developed in different times of the day, but all formed on the cold side of a weak frontal system, a region in which the low level atmosphere was stable. Their analysis of the mesoscale environment for this type of storm shows that the source of instability for the systems is the LLJ, that advects high-θ_e air over the genesis region. They also identified some upper level support for the system, namely a short wave and positive vorticity advection (PVA) in 500 hPa and a region of divergence at 200 hPa.

Colman (1990a,b) identified a type of elevated thunderstorm that occurs in an environment without CAPE. The instability in which the storms fed was not convective instability but symmetric instability.

The development of strong surface straight-line winds has also been associated with elevated convection over a stable boundary layer (Schmidt and Cotton 1990). In Section 2.8 we will discuss observations of straight-line winds, and a hypothesis for their formation.

2.3 Individual Cumulonimbus

The individual components of the convective region of MCSs are cumulonimbus clouds, which are themselves composed of *cells*, or individual updrafts. An *ordinary* cumulonimbus,

or what Byers and Braham (1949) called an airmass thunderstorm, is short-lived (less than one hour), and may be composed of several cells. During its evolution, it goes through three stages. The first stage is called *cumulus*, and is characterized by the existence of positively buoyant updrafts. The storm reaches the *mature* stage when precipitation begins reaching the ground. The *dissipating* stage occurs when the downdrafts caused by evaporation of precipitation cut off the inflow to the storm, which is forced to ingest cold air. When this happens, the entire cloud becomes dominated by downdrafts. This type of cell occurs in environments with very weak shear and modest to weak amounts of CAPE.

Sometimes ordinary cells evolve into a *multicell* storm. This happens when the cold downdrafts of ordinary cells spread out horizontally. On the leading edge of the spreading cold pool, the convergence associated with the gust front triggers upward motion. If this is strong enough, new cells will form and move backwards in a storm relative sense (Fovell and Ogura 1988), generating a hierarchy of cells, with new cells along the leading edge of the cold pool and older cells behind it. In other cases, new cells are triggered on the right flank of the storm complex (Chisholm and Renick 1972), and either become the new center of the storm or merge into the pre-existing cells.

Another type of cumulonimbus is the *supercell*. It is long-lived, has strong rotation in the updraft, and is associated with severe weather. We will discuss its characteristics in the next section. It is important to have in mind that the distinct types of cumulonimbus presented here are in fact part of a continuum spectrum of storm types. Multicell thunderstorms sometimes evolve into supercell thunderstorms (Knupp and Cotton 1982a,b) and sometimes they present as much rotation as a classic supercell and the distinction is not obvious (Cotton and Anthes 1989).

2.3.1 Supercell Thunderstorms

Supercells are a type of convective organization associated with all types of severe weather: hail, tornadoes, strong winds, and at times heavy precipitation. They are more frequently found over of the High Plains of the United States and Canada. Their rarity in other parts of the world is attributed to the absence of the mesoscale environment that leads to its formation: very high CAPE and deep strong vertical wind shear.

There is not a unique definition of supercell accepted in the literature. Browning (1964) identifies the main characteristics of a supercell to be a rotating updraft, steadiness, and typical radar signatures. Moller et al. (1994) define supercells as storms with *mesocyclones* (regions of relative vorticity) greater then 10^{-2} s^{-1} that occupy at least one third of the depth of the storm and live for tens of minutes. Other authors use a looser definition, requiring just that the storm has a rotating updraft.

A supercell is far from symmetric around its main updraft, in fact, it is very three-dimensional. On the upshear side, usually the southwest, the supercell is commonly accompanied by a flanking line, or a line of non-precipitating cumulus cells which forms on the leading edge of the gust front caused by a downdraft. Most of the strong rain is found in its eastern portion, with hail on the western sector of the precipitation shaft (Figure 2.7). At high levels, supercells are characterized by strong divergence, and overshooting tops that penetrate the equilibrium level.

The radar signature of a supercell also distinguishes it from other types of storms. The gradient in reflectivity is very high in the southwestern part of the storm in low levels (Figure 2.8). In mid-levels (approximately 7 km), a very unique signature is found: the bounded weak echo region. This region is free of large hydrometeors and is co-located with the strong updraft, downshear of the main rain shaft. The relative absence of condensation in this region is due to the strong updraft. Condensation and growth of droplets do not happen instantaneously as parcels reach the lifting condensation level. It takes a finite amount of time for large hydrometeors to form. If the updraft is strong this process does not have time to occur until the parcels reach very high levels, and the region appears echo-free.

Since the 1970s, storm chasers have recognized that many observed supercells do not exactly match the description discussed above. The initial conceptual model formulated by Browning (1964) and Lemon and Doswell (1979) became known as a *classic supercell.* Bluestein and Parks (1983) introduced the concept of a *low-precipitation* (LP) supercell. As the name indicates, very little rain occurs with these storms. The only significant precipitation is in the form of hail, which can be large. The absence of significant rain hinders the chance for flash flooding and strong outflow winds. Also, these storms only
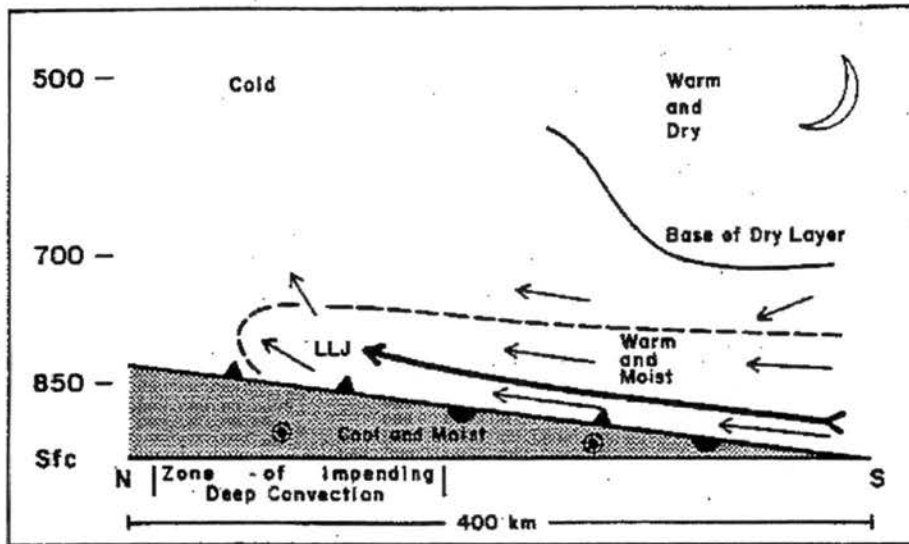
Figure 2.6: An idealized schematic north–south cross section depicting the thermodynamic and flow structure immediately prior to the development of deep convection above the wedge-shaped cold air mass (shaded). The vectors represent the flow in the x–z plane (vertical component is greatly exaggerated). The dot inside the circle represents easterly flow (out of the page) within the cool, moist air mass below the frontal surface. The dashed line represents the boundary of the warm, moist air mass transported northward above the frontal surface by the southerly LLJ whose axis is denoted by the bold streamline. From Trier and Parsons (1993).
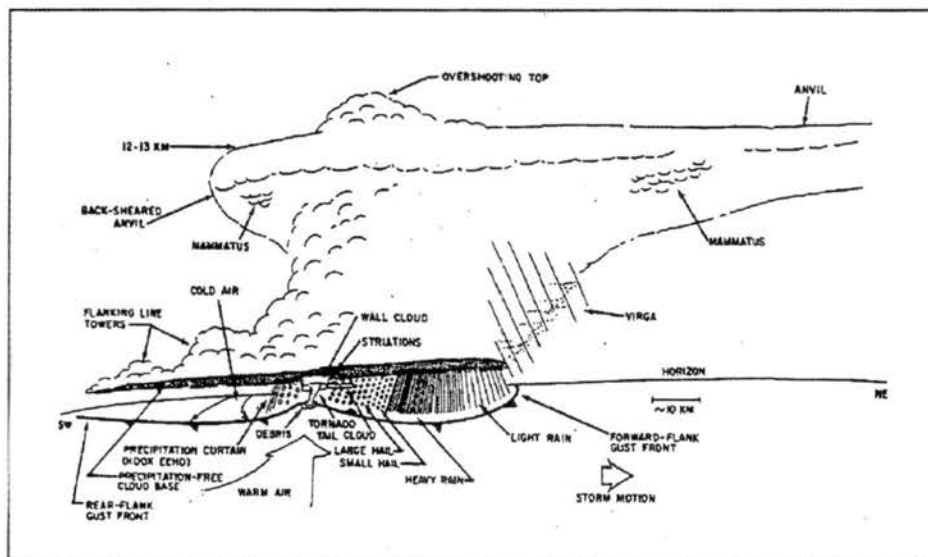
Figure 2.7: Schematic visual appearance of a supercell thunderstorm. From Houze (1993), based on U.S. National Severe Storms Laboratory publications and an unpublished manuscript of H. Bluestein.
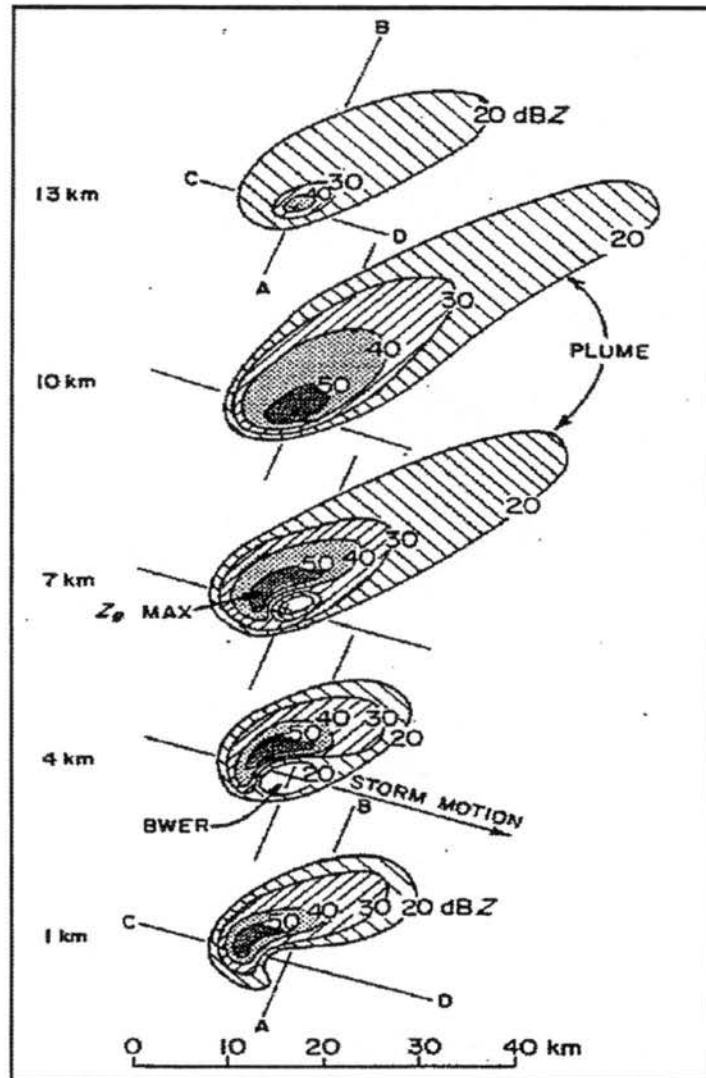
Figure 2.8: Schematic illustrating the variation of radar reflectivity patterns (dBZ) with height in supercell thunderstorms observed in Alberta, Canada. From Chisholm and Renick, 1972.

spawn occasional tornadoes, which are usually weak. The visual aspect of LP supercells is extraordinary, because the absence of rain causes the wall-cloud and occasional tornado to be very exposed and visible.

Moller and Doswell (1988) proposed still another type of supercell thunderstorm: the *high-precipitation* (HP) supercell, which is characterized by substantial precipitation in the mesocyclone, and is probably the dominant form of supercell in the United States (Johns et al. 1993). Figure 2.9 compares the characteristics of LP and HP supercells. The HP storm is larger, and has a strong rain shaft that causes very strong outflow winds and a gust front. This type of storm can also produce tornadoes, although most violent tornadoes are produced by classic supercells.

Moller et al. (1994) point out that the individual types of thunderstorms may, in certain cases, be just stages in the evolution of a single storm. Also, they mention that a HP supercell may evolve into a *bow-echo* supercell (Figure 2.10), which is an elongated supercell that retains its mesocyclone and develops a RIJ.

The classification of thunderstorms into different types is an artificial distinction in a continuum spectrum. Moller et al. emphasize that the HP supercell category is being used to encompass all thunderstorms that have strong persistent mesocyclones. It is quite possible that multicell thunderstorms are being classified under the HP category, because the multiple tornadoes spawned by HP supercells can be a consequence of updraft cycles.

2.4   What determines convective organization?

CAPE and vertical shear have traditionally been used to describe the storm's environment and to determine storm organization (Bluestein 1993).

2.4.1   Cumulonimbus organization

From observations and numerical simulations, the ideal environmental conditions for each type of cumulonimbus storm described above has been identified. A summary is presented in Table 2.2.

Because storm type depends on both CAPE and shear, the *Richardson Number* (*Ri*) can be used to classify storms (Weisman and Klemp 1984).

Vertical Shear* CAPE	Weak ≤ 15 ms^{-1}	Moderate $\sim 15\text{--}25$ ms^{-1}	Strong ≥ 25 ms^{-1}
Low (500-100 Jkg^{-1})	Ordinary cell	Ordinary cell/supercell	Ordinary cell/Supercell
Moderate ($\sim$ 1000-2500 Jkg^{-1})	Ordinary cell	Ordinary cell/supercell	Supercell
Low ($\geq$ 2500 Jkg^{-1})	Ordinary cell	Ordinary cell/supercell	Supercell

* Vertical shear over the lowest 6000 m.

Table 2.2: Storm type as a function of vertical shear and CAPE. From Bluestein, 1993.

$$Ri = \frac{CAPE}{S^2}, \qquad (2.5)$$

where,

$$S^2 = \frac{1}{2}(\bar{u}_{6000} - \bar{u}_{500})^2, \qquad (2.6)$$

where $\bar{u}_{6000}$ and $\bar{u}_{500}$ are the pressure–weighted mean–vector wind speeds in the lowest 6000m and 500m, respectively. The quantity $(\bar{u}_{6000} - \bar{u}_{500})$ can be understood as the inflow to the storm, if the storm moves with the mean wind of the lower 6000m and parcels enter the storm with $\bar{u}_{500}$.

Large Ri are therefore associated with high CAPE, which in turn determines the maximum updraft that a cloud can support. Strong updrafts in general correspond to strong downdrafts, which generate strong outflow and kill the supply of warm air to the storm, causing it to be short-lived. If Ri is moderate, there is a balance between inflow and outflow in the storm. Finally, if Ri is small, shear is large, and storms will develop rotation and be long-lived [1]. Richardson numbers of 40 or more are usually associated with ordinary cells, while smaller Ris are found when supercells or long-lived multicell storms develop. When Ri is too small (less than ~ 15) initial convection may be suppressed by the excessive shear (Weisman and Klemp 1984).

---

[1]The relationship between storm rotation and longevity was explored by Lilly (1986). He showed that in pure helical flows, non-linear advection is suppressed, and the dissipative effects of mixing are mitigated.

2.4.2 MCS organization

Observations show that convective cells often tend to group together and behave as a system that shares an anvil and has its own system scale circulation branches and pressure patterns.

The question of how and why MCS organization takes place has been a matter for intensive investigation and debate in the literature. A conclusion has not been reached yet, but some observations and numerical simulations in controlled environments have shed some light on the problem.

Sometimes MCS organization is linked to large or mesoscale forcing, such as a front, a mesoscale region of low-level convergence, an upper level short wave or a dryline, that causes several cells to form in a mesoscale region. The presence of a mesoscale convective vortex (MCV) left behind by previous convection may also aid the development of a new MCS (Raymond and Jiang 1990; Fritsch et al. 1994). Other times, only weak mesoscale forcing is present, but MCS formation is still observed. The upscale growth may be a consequence of gravity waves excited by the first cells of convection that cause the surrounding environment to be favorable to further development of convection (McAnelly et al. 1997; Nicholls et al. 1991; Mapes 1993). Blanchard et al. (1997) discuss the role of inertial instability in the upscale growth of MCSs. If divergent outflow in the upper levels of a MCS occurs in an inertially unstable region, the parcels will be displaced meridionally further away from the parent convection. This enhanced divergence acts to enhance convection because it strengthens the updraft and because it causes the compensating subsidence to occur far from the region of convection, therefore not suppressing the development of new cells.

Furthermore, given that a MCS does form, there is still a question of which type of organization that will be. According to Weisman (1993), the presence of at least 2000 Jkg^{-1} of CAPE and strong low level shear will lead to a line with a well-defined RIJ and FTRJ structure, and with well defined bookend vortices. The development of a long-lived MCV, however, is hindered by strong low level shear, and occurs preferentially in environments with weak shear (Skamarock et al. 1994). Overall, high CAPE and strong shear are taken as indicators of severe weather associated with both individual cells and squall lines.
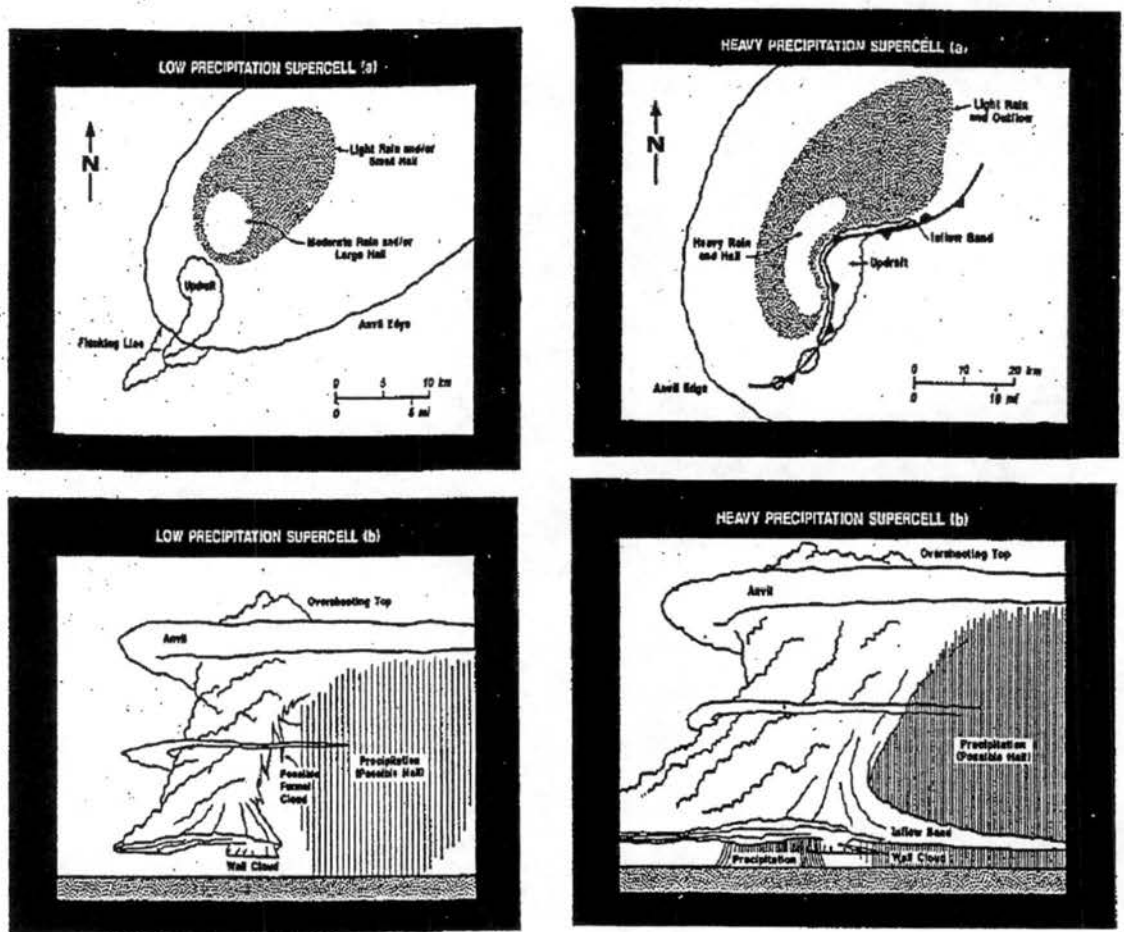
Figure 2.9: Schematic radar (top) and visual features (bottom) associated with a a) LP supercell storm and b) HP supercell. From Doswell et al. (1990).
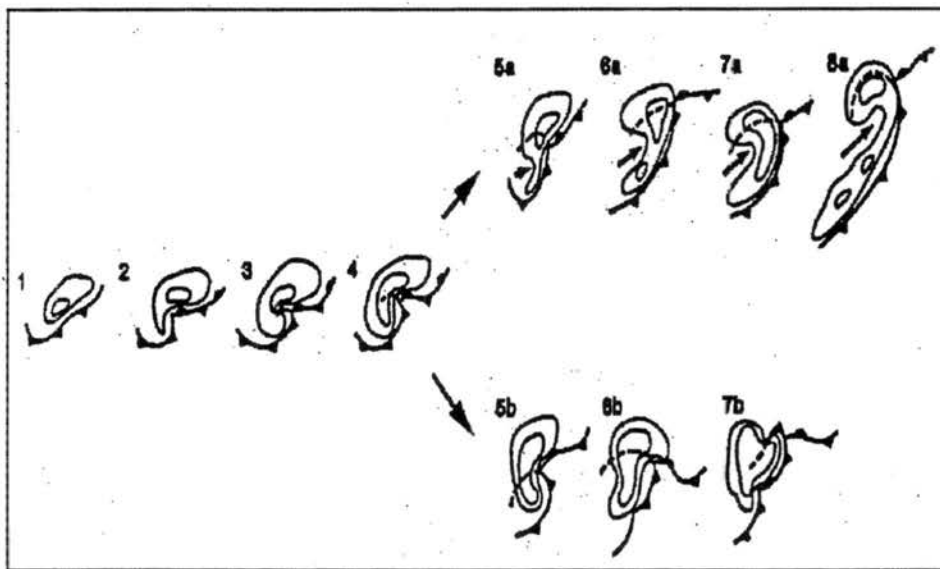
Figure 2.10: Two composite life cycles (1–8a and 1–7b) that have been identified with HP supercells. Two radar reflectivity contours and gust front positions are shown. Dark arrow in 5a–8a indicates the location of the rear inflow jet. From Moller et al. (1990).

One important issue is the choice of time and location for evaluation of the environmental parameters. Ideally, one wants the environment to represent the atmosphere just upstream of the storm, as it is forming. However, the current observational network is very limited in temporal and spatial resolution, especially for upper air sounding stations, and this can lead to a misjudgment of the environment. One typical example is the change in the environment perceived by a storm due to the presence of other convection. An outflow boundary left behind by previous convection, that gets ingested by the storm, may supply enough vertical vorticity to cause it to become tornadic. Also, environmental atmospheric structures may evolve in a matter of a few hours. A typical example is the dryline, that is strengthened during the day if a well-defined soil moisture gradient is present. Although this feature may be very important for storm development (Grasso 1996; Grasso and Cotton 1997a), it may not be present at the time the environment is measured (12 UTC — or 06 CST —is the sounding time that would operationally be used to compute environmental parameters to define afternoon convection in the High Plains).

2.5 Storm Propagation

As described by Cotton and Anthes (1989), storm propagation can be due to three mechanisms: i) advection; ii) forced propagation; and iii) autopropagation. Advection is the process through which the cloud translates as a passive solid body. In this case the storm moves with the mean speed and direction of the tropospheric winds. Forced propagation is a mechanism through which the storm does not really move, but instead it is regenerated by some external forcing, which could be a front, sea breeze, dryline etc. The net effect is that the storm changes location.

The third mechanism invokes the storm's own dynamics. The subsections below outline two ways through which this can be accomplished. A third way, related to the interaction between convection and gravity waves will be discussed in Section 2.7.

2.5.1 Pressure Gradient Force

Rotunno and Klemp (1985) describe a mechanism of storm auto-propagation. It applies to storms that develop in strongly sheared environments, in which the hodograph curves

clockwise with height. This is the typical environment of supercell thunderstorms. They derive an equation for the pressure perturbation and show that the storm (perturbation) interacts with the environment (mean-flow) to create a high-pressure center upshear of the updraft core and a low-pressure center downshear from it. The derivation of a pressure perturbation equation is done from the inviscid, Boussinesq momentum equations linearized with respect to a basic state in hydrostatic balance.

The momentum equations can be expressed as

$$\frac{du}{dt} = \frac{\partial u}{\partial t} + u\frac{\partial u}{\partial x} + v\frac{\partial u}{\partial y} + w\frac{\partial u}{\partial z} = -\frac{1}{\bar{\rho}}\frac{\partial p'}{\partial x}, \tag{2.7}$$

$$\frac{dv}{dt} = \frac{\partial v}{\partial t} + u\frac{\partial v}{\partial x} + v\frac{\partial v}{\partial y} + w\frac{\partial v}{\partial z} = -\frac{1}{\bar{\rho}}\frac{\partial p'}{\partial y}, \tag{2.8}$$

$$\frac{dw}{dt} = \frac{\partial w}{\partial t} + u\frac{\partial w}{\partial x} + v\frac{\partial w}{\partial y} + w\frac{\partial w}{\partial z} = -\frac{1}{\bar{\rho}}\frac{\partial p'}{\partial z} + B, \qquad B = -\frac{\rho'}{\bar{\rho}}g, \tag{2.9}$$

where B is the buoyancy and all the other symbols have their usual meaning.

Taking

$$\frac{\partial(2.7)}{\partial x} + \frac{\partial(2.8)}{\partial y} + \frac{\partial(2.9)}{\partial z},$$

and using the Boussinesq approximation to the continuity equation

$$\nabla \cdot \bar{\mathbf{V}} = 0,$$

one obtains

$$\frac{1}{\bar{\rho}}\nabla^2 p' = -\left[\left(\frac{\partial u}{\partial x}\right)^2 + \left(\frac{\partial v}{\partial y}\right)^2 + \left(\frac{\partial w}{\partial z}\right)^2\right] - 2\left[\frac{\partial u}{\partial y}\frac{\partial v}{\partial x} + \frac{\partial u}{\partial z}\frac{\partial w}{\partial x} + \frac{\partial v}{\partial z}\frac{\partial w}{\partial y}\right] + \frac{\partial B}{\partial z}. \tag{2.10}$$

The winds are now decomposed into a mean (horizontal average) and a perturbation part. The mean wind represents a horizontally homogeneous environment, that has no significant vertical motion, while the perturbation wind represents the storm,

$$u = \bar{u}(z) + u'(x, y, z, t), \tag{2.11}$$

$$v = \bar{v}(z) + v'(x, y, z, t), \tag{2.12}$$

$$w = w'(x, y, z, t). \tag{2.13}$$

Substituting this decomposition in (2.10) one gets

$$\frac{1}{\bar{\rho}}\nabla^2 p' = \left[\left(\frac{\partial u'}{\partial x}\right)^2 + \left(\frac{\partial v'}{\partial y}\right)^2 + \left(\frac{\partial w'}{\partial z}\right)^2\right] - 2\left[\frac{\partial u'}{\partial y}\frac{\partial v'}{\partial x} + \frac{\partial u'}{\partial z}\frac{\partial w'}{\partial x} + \frac{\partial v'}{\partial z}\frac{\partial w'}{\partial y}\right]$$
$$- 2\left[\frac{d\bar{u}}{dz}\frac{\partial w'}{\partial x} + \frac{d\bar{v}}{dz}\frac{\partial w'}{\partial y}\right]$$
$$+ \frac{\partial B}{\partial z}. \tag{2.14}$$

The pressure perturbation equation above is now decomposed in two parts, one associated with the buoyancy (p'_B) and one associated with the wind flow. The latter one, called dynamic pressure, can be further subdivided in a linear (p'_L) and a non-linear part (p'_{NL}).

$$\frac{1}{\bar{\rho}}\nabla^2 p'_B = \frac{\partial B}{\partial z}. \tag{2.15}$$

$$\frac{1}{\bar{\rho}}\nabla^2 p'_{NL} = \left[\left(\frac{\partial u'}{\partial x}\right)^2 + \left(\frac{\partial v'}{\partial y}\right)^2 + \left(\frac{\partial w'}{\partial z}\right)^2\right]$$
$$- 2\left[\frac{\partial u'}{\partial y}\frac{\partial v'}{\partial x} + \frac{\partial u'}{\partial z}\frac{\partial w'}{\partial x} + \frac{\partial v'}{\partial z}\frac{\partial w'}{\partial y}\right]. \tag{2.16}$$

$$\frac{1}{\bar{\rho}}\nabla^2 p'_L = -2\left[\frac{d\bar{u}}{dz}\frac{\partial w'}{\partial x} + \frac{d\bar{v}}{dz}\frac{\partial w'}{\partial y}\right]. \tag{2.17}$$

(2.17) can be further simplified as

$$p'_L \quad \alpha \quad \frac{d\bar{\mathbf{V}}_H}{dz} \cdot \nabla_H w', \tag{2.18}$$

a valid approximation for a function consisting of a narrow band of Fourier components.

Equation 2.18 indicates that linear processes will act to form a low pressure center downshear of the updraft. However, because the shear vector veers with height, the perturbation low and high pressure centers will not be vertically stacked. Instead, a high pressure under a low pressure will develop on the right side of the shear vector (Figure 2.11). This upward-directed pressure gradient force can be sufficient to trigger new updrafts on that side of the cell, causing the storm to propagate to the right. This mechanism seems consistent with observations of most supercell storms, that do tend to move towards the right of the mid-level mean shear vector.
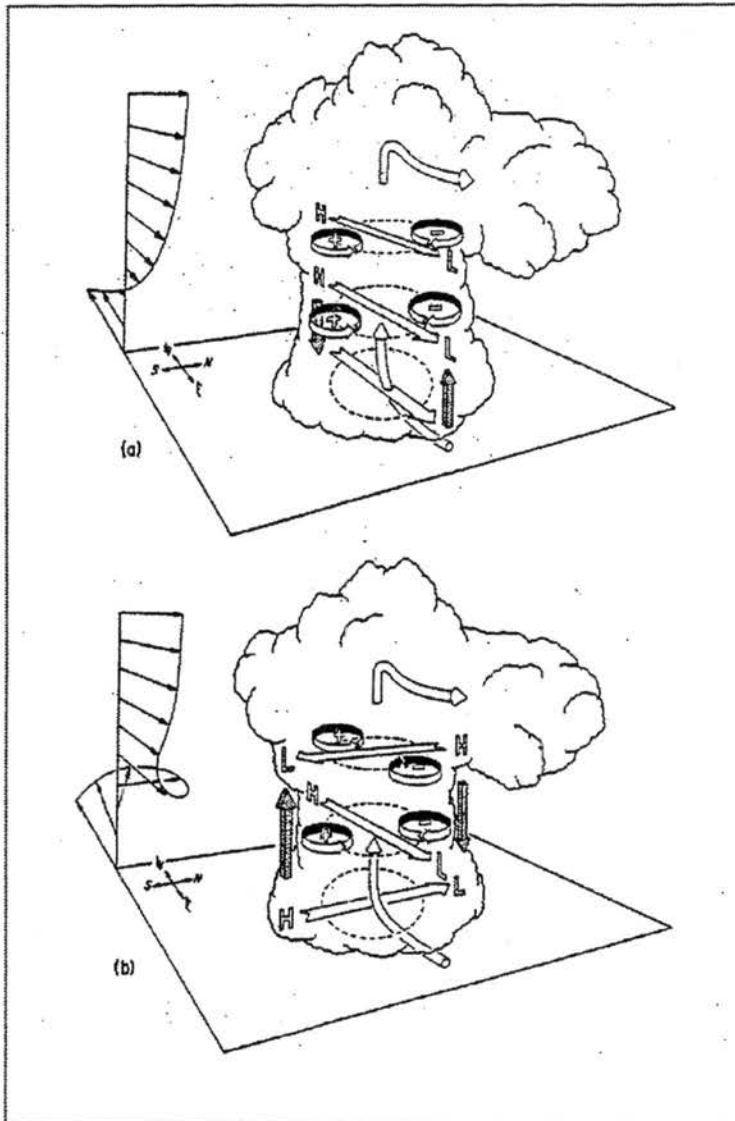
Figure 2.11: Schematic illustrating the pressure and vertical vorticity perturbations arising as an updraft interacts with an environmental wind shear that a) does not change direction with height; b) turns clockwise with height. The high (H) to low (L) horizontal pressure gradients forces parallel to the shear vectors (flat arrows) are labeled along with the preferred location of the cyclonic (+) and anticyclonic (-) vorticity. The shaded arrows depict the orientation of the resulting vertical pressure gradients. Adapted from Rotunno and Klemp (1982) by Klemp (1987).

2.5.2 Cold Pool

One classic example of auto-propagation involves the cold pool. Given the right conditions (ideally a dry, well-mixed boundary layer as will be discussed in Section 2.5.3) air under a precipitating thunderstorm will cool due to melting and evaporation of hydrometeors. This cold air tends to sink and pool under the storm forming the cold pool, which then spreads ahead of the storm. If the supply of cold air is generous, the cold pool will be deep, and a hydrostatically generated pressure gradient force (PGF) will cause its propagating speed to be significant. On the encounter of this spreading cold air, typically several hundred meters deep, and the environmental flow, boundary layer air is lifted. This can be a source of air to the storm. If the cold pool spreads too far ahead of the parent storm though, the new updraft does not feed the parent storm, but may start the development of a new cell. This is a typical situation in a multicell storm complex (Section 2.3), in which the process described above keeps repeating itself. Because new cells form ahead of the system while old ones mature and decay towards the back, the system is said to propagate forward.

2.5.3 Discussion

It is not easy to assess which of the mechanisms listed above is the most important, and probably most storms operate in a mix of the processes described. Some of the mechanisms have their importance linked to the environment in which the storm exists. For instance, the PGF mechanism requires strong deep environmental shear and strong updrafts. This environment is typical of supercells, or storms that have large mid-level rotation.

The cold-pool mechanism obviously requires the formation of a strong deep cold-pool. Here we revise the mechanism for cold-pool formation in an attempt to identify the preferred environment for this process.

As mentioned in the previous section, cooling of air parcels due to melting or evaporation will cause downdrafts. If they reach the surface while still colder than the environment, a situation typical of a well-mixed boundary layer, a cold pool will form. A different situation occurs when the environment is not neutral, but stably stratified. In this case, as the

parcel undergoes evaporation, cools and starts sinking, it will encounter a warmer environment, which will cause it to have positive buoyancy. Its descent will be hindered and the parcel may not reach the surface (Proctor 1989a,b). Therefore, a stable environment is not conducive to the development of strong cold pools.

A low-level stable layer also hinders the development of a cold pool due its support of gravity waves. Numerical experiments (Jason Nachamkin, personal communication) have shown that in some situations a cold downdraft will not reach the ground if its energy is radiated away as gravity waves.

2.6 Development of low-level downdrafts and strong winds at the surface

Low-level downdrafts and surface outflow are linked by continuity of mass and by the impermeability of the lower boundary. Descending drafts cannot go through the ground; instead they diverge very near the surface. Strong low-level downdrafts mean strong outflow. The outflow pattern will depend on the horizontal momentum of the descending parcels and on the environmental winds that the parcels encounter in low levels. The presence of environmental flow whose direction opposes the storm outflow can cause stronger low-level convergence on one side of the storm than on the other.

There are two types of downdraft associated with convective systems: mesoscale downdrafts and convective downdrafts. The defining difference between the two is the area they cover, but they can also be distinguished by intensity. While mesoscale downdrafts are a gentle descent, convective downdrafts can have large magnitudes and lead to severe weather. The most important form of mesoscale downdraft, the descending RIJ, has been addressed in Section 2.2.1. Convective downdrafts are discussed now.

Convective downdrafts are associated with individual cumulonimbus clouds. Observations report typical downdraft intensity to be 5–8 ms^{-1} and typical area to be a few kilometers in width (Byers and Braham 1949). In certain cases, however, downdrafts can be much more intense than that. In particular, Fujita (1981) coined the term *microburst*, which is a very intense downdraft that covers an area smaller than 4 km in diameter and lasts for two to five minutes.

There are two forces in the vertical momentum equation that can cause the formation of convective downdrafts: buoyancy and (PGF).

Buoyancy driven–downdrafts occur when the parcels are loaded with hydrometeors, or when liquid precipitation evaporates or solid precipitation melts below cloud base. For a given amount of rainwater, evaporation is most efficient if the diameter of the rain drops is small. Given that some evaporation takes place, air parcels below cloud base will get cooler than the environment, become negatively buoyant, and experience a downward acceleration. Parcels' descent will approximate a dry adiabatic lapse-rate if phase changes are not taking place. The efficiency of its descent will then depend on how the environmental temperature compares with the parcel's. If the environment is a neutral, well-mixed unsaturated boundary layer, the parcel will remain colder than the environment and descend in a downdraft to the ground. Johns and Hirt (1987) and Proctor (1989) pointed out that a moist low level environment, as found in wind-storm events, may favor downdrafts because a relatively dry parcel will have its negative buoyancy enhanced.

If the parcel is in a rain shaft, continuous evaporation into it may lead to a saturated downdraft. In this case the parcel will descend following a moist-adiabat, will also remain colder than the environment, and continuously sink until the surface. Precipitation loading will be an important contribution to negative buoyancy. The larger the cooling and the precipitation loading, the stronger the downdraft, and the stronger the wind outflow.

Knupp (1987, 1988) studied the downdrafts associated with High Plains ordinary cumulonimbi and concluded that the most important ones are caused by (i) entrainment of dry air in the cloud (occurs in mid and high levels); (ii) compensating subsidence (gentle descent that covers a large area around the storm; (iii) precipitation. Of the types above the only downdraft that reaches the ground with discernible speed is the one caused by precipitation. As described in the previous paragraphs, precipitation can generate a downdraft by causing evaporational cooling into a parcel and by hydrometeor loading.

The precipitation downdraft identified by Knupp (1987, 1988) has two sources of air. One is located at mid-levels and comprises air that enters the storm on its rear and right flank. The other is located in the boundary layer, and is important on the latter stages of the thunderstorm's life. The formation of this latter downdraft branch is interesting

because it relies on the presence on an upward directed PGF that lifts parcels that are negatively buoyant due to evaporation and melting of precipitation. In their trajectory, they move towards the back of the storm and cross the precipitation core, where the negative buoyancy is enhanced by water loading and melting. When the buoyancy becomes larger than the PGF, either because of loading or because the parcel has reached a region in the cloud where the PGF is not as strong, the parcel sinks. Knupp termed this sinking motion *up-down downdraft.*

Rotunno and Klemp (1982) provide an explanation for the existence of the upward PGF in a cumulonimbus that develops in an environment of high CAPE and high shear. Expanding the second bracket of the non-linear pressure term (2.16) one gets

$$
-2\left[\frac{\partial u'}{\partial y}\frac{\partial v'}{\partial x} + \frac{\partial u'}{\partial z}\frac{\partial w'}{\partial x} + \frac{\partial v'}{\partial z}\frac{\partial w'}{\partial y}\right] = -\frac{1}{2}\left[\left(\frac{\partial u'}{\partial y}+\frac{\partial v'}{\partial x}\right)^2 + \left(\frac{\partial u'}{\partial z}+\frac{\partial w'}{\partial x}\right)^2 + \right.
$$
$$
\left(\frac{\partial v'}{\partial z}+\frac{\partial w'}{\partial y}\right)^2 - \left(\frac{\partial v'}{\partial x}-\frac{\partial u'}{\partial y}\right)^2 -
$$
$$
\left.\left(\frac{\partial w'}{\partial x}-\frac{\partial u'}{\partial z}\right)^2 - \left(\frac{\partial w'}{\partial y}-\frac{\partial v'}{\partial z}\right)^2\right]. \quad (2.19)
$$

The first three terms are the square of the deformation and the last two terms are square of the horizontal vorticity. Ignoring fluid extension terms, and considering an updraft in which horizontal vorticity and deformation are zero, (2.16) reduces to

$$
\frac{1}{\rho}\nabla^2 p'_{NL} = \frac{1}{2}\zeta'^2. \quad (2.20)
$$

For purposes of qualitative analysis,

$$
-p'_{NL} \quad \alpha \quad \zeta'^2. \quad (2.21)
$$

The result above shows that a vorticity center, independent of its sign, is associated with a low pressure. Therefore, storms that have high vorticity in their cores (typically supercell thunderstorms) have a strong PGF directed upwards in the low levels. According to Knupp (1988), this PGF may be enough to lift negatively buoyant air from low levels.

Strong surface outflow may be caused by other mechanisms besides strong downdrafts, namely downward transfer of momentum and horizontal acceleration. If horizontal PGFs are present during the parcel's descent to the surface, it will experience an acceleration, which may enhance the final horizontal momentum. Schmidt and Cotton (1989) present calculations of the horizontal PGF at the rear of a MCS and conclude that this acceleration can explain a large part, if not all, of the strong winds.

Also, we can consider that when a parcel initiates its descent in the downdraft, it has not only potential energy but also has some kinetic energy, associated with its horizontal momentum, which might be retained as the parcel goes down. Barrit and Biggerstaff (1993) state that downward transfer of momentum was an important mechanism in the sustenance of the strong winds of the 10-11 June 1985 squall line.

2.7   Interaction between Convection and Gravity Waves

In this section we briefly review the theory for gravity wave propagation, discuss under which conditions the waves can be long-lived, review the production of gravity waves by convection, the influence that gravity waves have on convection and discuss a mechanism through which gravity waves can be linked to strong winds.

Schubert et al. (1989) showed that if the scale of the heating is smaller than the Rossby radius, a convective disturbance is efficient at radiating energy in the form of gravity waves. In a continuously stratified fluid, propagation will occur both in the horizontal and in the vertical. Lin and Goff (1988) describe the case of a gravity wave that propagated horizontally over 1000 km, from Tennessee to Nova Scotia, at a speed of 55 ms^{-1}. The wave maintained its characteristics for over 9 hours.

It is amazing that waves can propagate such a distance and for such a long time without getting attenuated. According to linear theory for a Boussinesq fluid, gravity waves are dispersive, that is, the components of the group velocity and wave speed differ for a given Fourier mode, causing the waves' energy to be dispersed with time if continuous forcing is not present. Under certain conditions, however, vertical propagation is hindered, and the waves can propagate for long distances in the horizontal without significant loss of

energy. The Taylor-Goldenstein equation (Holton 1992; Lindzen and Tung 1976) describes an incompressible, inviscid, Boussinesq fluid in the absence of diabatic processes:

$$\frac{d^2w}{dz^2} + \left(\frac{N^2}{[\bar{u} - c]^2} - \frac{1}{\bar{u}}\frac{d^2\bar{u}}{dz^2} \right) w = 0. \tag{2.22}$$

Proposing a solution on the form of a Fourier component, in an environment of linear wind shear $(d^2\bar{u}/dz^2 = 0)$, the vertical wave number is given by

$$m^2 = \frac{N^2}{[\bar{u}(z) - c]^2} - k^2, \tag{2.23}$$

where N is the buoyancy frequency, $\bar{u}$ is the environmental wind and c and k are the phase speed and wavenumber of a Fourier component, respectively.

Vertical propagation is hindered when the Scorer parameter decreases withheight. This occurs when stability is reduced aloft, winds in the upper levels oppose the wave motion, a jet is present which, due to curvature effects, causes m^2 to be negative aloft (Crook 1988), or the wavenumber is large. According to the first mechanism, a well-mixed (neutral) layer on top of a stable layer is an ideal situation for horizontal propagation of linear gravity waves, because their energy cannot propagate vertically in the well-mixed layer. Lindzen and Tung (1976) used linear theory to show that a stable layer near the surface, topped by a neutral layer that has a critical level (a level in which the mean wind speed and the gravity wave speed are the same) will act as an efficient wave duct. The wave duct does not necessarily need to be confined to the surface. Tripoli and Cotton (1989a,b) describe a case in which the wave is trapped below a cirrus deck generated by deep convection, made unstable because of radiative cooling. In another case, a stable layer located in the mid-troposphere acted as wave guide (Lin and Goff 1988).

Non-linear theory has also been called upon to explain the longevity of gravity waves. A wave that motivated the study of non-linear gravity waves is the Australian *Morning Glory*. This is the name given to a wave (sometimes classified as *bore* and sometimes as *solitary wave*) that forms with incredible regularity, often near dawn, during the summer months over the southern margin of the Gulf of Carpentaria in Northern Australia (Christie 1992). Its signature in the barograph can assume a variety of forms, including a family

of amplitude–ordered solitary waves or a pressure perturbation that jumps and remains elevated. The disturbance propagates in steady state for hundreds of kilometers. This wave is spectacular because it causes a roll cloud, several hundreds of kilometers long, to form and propagate steadily. A roll cloud possibly associated with solitary waves has also been observed in Oklahoma (Doviak and Ge 1984). The wave described by Lin and Goff (1988) is also a non-linear gravity wave, whose signature in the barograph is a pulse of depression. The basic idea explored by non-linear theory (Benjamin 1966, 1967; Christie et al. 1978; Christie 1989, 1992) is that non-linearity can counteract the effects of dispersion described above, so that the wave can be long-lived.

A shallow, stable layer near the surface capped by a mixed-layer also constitutes the ideal environment for the propagation of solitary waves, and it is indeed observed in Australia in association with the Morning Glory (Christie 1992). Therefore, both linear and non-linear gravity waves can benefit from the formation of a duct.

This environmental profile (a shallow stable layer near the surface capped by a layer of low static-stability above) is also sometimes found in the High Plains of the United States (Schmidt and Cotton 1990). The surface stable layer can form because of (i) radiational cooling, (ii) frontal passages, or (iii) a cold pool left by convection (Schmidt and Cotton 1989, Doviak and Ge 1984). The well-mixed layer above the stable layer can be the consequence of the eastward advection of the daytime convective boundary layer that develops in the high elevation terrain present in the west by the tropospheric westerly winds (Carlson et al. 1983).

Several processes can act as a source of gravity waves, such as shear instability in a jet streak (Uccellini and Koch 1987; Lalas and Einaudi 1976), topographical forcing (Smith 1979), convective boundary layer eddies impinging on a stable upper layer (Kuettner et al. 1987) and geostrophic adjustment (Blumen 1972; Uccellini and Koch 1987). Convection has also been identified as an important generation mechanism for gravity waves (Schubert et al. 1989; Schmidt and Cotton 1990; Lin and Goff 1988; Bretherton and Smolarkiewicz 1989; Nicholls et al. 1991; McAnelly et al. 1997; Mapes 1993; Rottman et al. 1992; Fulton et al. 1990; Doviak and Christie 1989; Doviak et al. 1991).

Nicholls et al. (1991), Mapes (1993) and McAnelly et al. (1997) discuss the generation of linear gravity waves by MCSs. Their theory is based on the typical vertical heating profile of a MCS (Hertenstein and Schubert 1991), which has two components. In the convective region the heating profile corresponds to half a wave length ($l=1$), with zero heating at the surface and at the tropopause and maximum heating in mid-levels. In the stratiform region the heating has the shape of a full wavelength ($l=2$), with cooling at low levels because of evaporation and melting of hydrometeors and heating above. The integrated heating profile is the sum of these two modes. The gravity waves excited by this heating profile will have those same vertical wavelengths and will propagate from the storm to the surroundings. The environment around the storm will receive the influence of the $l=1$ wave before the $l=2$ wave, both because of dispersive effects and because the heating profile associated with the convective line occurs before the one associated with the stratiform region.

Other studies have focused on the ability that gravity waves have to interact with convection, either to trigger it or to organize it (Carbone et al. 1990; Koch et al. 1987). The arrival of a gravity wave in a location may cause convergence and upward motion. If the upward motion is strong enough and deep enough, parcels may reach the level of free convection, and a new cloud can be initiated (Doviak and Ge 1984). Mapes (1993) and McAnelly et al. (1997) used an analytical model to show that the passage of the $l=1$ mode causes subsidence in the environment surrounding the storm. However, passage of the $l=2$ mode causes low level lifting, which acts to make the region surrounding the initial storm prone to new convective development. This mechanism can lead to the upscale growth of a MCS, since the region surrounding pre-existent convection becomes favorable to the development of new convection.

Schmidt and Cotton (1990) used a two-dimensional idealized simulation of a squall line over a stable boundary layer to show that gravity waves emanate from the region of convection both in low levels and in upper levels. The wave in upper levels plays an important role in the development of the RIJ. It acts as a block, or a region of positive pressure perturbation in upper levels that helps channel the upper-level westerlies to low levels. The low-level gravity wave also plays an important role. For certain shear profiles, Schmidt and Cotton obtained a a squall line that propagated in phase with the wave.

Waves that propagate in phase with convection have been a focus of many studies (Raymond 1984; Xu and Clark 1984). Cram et al. (1992a,b) did a primitive equation modeling study of a prefrontal squall line using bulk microphysics and cumulus parameterization. The line was triggered by a cold front, but later it propagated in phase with a gravity wave, moving faster than the cold front. They showed that the distribution of potential temperature, pressure and vertical and horizontal motions matched the structure of a deep gravity wave with a wavelength of 10 km in the vertical and 200 km in the horizontal. Bélair et al. (1995) also modeled a case in which a squall line propagated in phase with a deep gravity wave. In these cases, the gravity waves benefit from the convection which, due to the release of latent heat, acts as a continuous source of energy for the wave. The convection also benefits from the gravity wave, which causes continuous lifting of low level parcels.

The symbiotic relationship between gravity waves and convection has been explored under the name of wave-CISK (Conditional Instability of the Second Kind). Several simplified models have been constructed to study wave-CISK with some success. However, those studies have received a lot of criticism in recent years because most of them only solve the linearized set of equations (Lim et al. 1990), because they are over-sensitive to the heating profile produced by the cumulus parameterization (Raymond 1983) and because in some models the most unstable mode is always the shortest one being resolved (Davies 1979).

The presence of strong winds associated with convection and gravity waves has also been explored in several studies. In the modeling study by Schmidt and Cotton (1990) the squall line that propagated in phase with the gravity wave produced strong persistent winds. One explanation for the strong winds is that the surface pressure gradients associated with the wave accelerated the winds in low levels.

There are other observational reports of strong wind gusts associated with the passage of gravity waves (Fulton et al. 1990; Doviak and Ge 1984; Pothecary 1954). The wind pattern observed in the passage of a solitary wave is shown in Figure 2.12. In this case, described by Doviak and Ge (1984), a cloud–free solitary wave caused gusts of 27 ms^{-1} that lasted for one hour and covered a distance of tens of kilometers.

Besides the surface pressure gradient force mechanism evoked by Schmidt and Cotton (1990), gravity waves may cause strong winds because they lift parcels from the lower level stable layer. The lifting is caused by the vertical motion associated with the wave or by the passive upgliding of parcels up the isentropic surfaces that become distorted as the wave approaches a given region. As the parcels are displaced upwards, they encounter a warm environment, and are therefore negatively buoyant. Waves of higher amplitude can result in stronger vertical displacements and consequently stronger winds. If the parcels go through the precipitation core, they become loaded with hydrometeors, and their negative buoyancy is further enhanced. Very large displacements can lift parcels to their level of free convection, and cause them to be ingested into the updraft.

2.8 Strong straight-line winds

The National Weather Service recognizes three forms of severe weather: tornadoes, straight-line wind gusts of 26 ms^{-1} or more, (or damage typically associated with wind gusts of 26 ms^{-1} or more), or hail of 1.9 cm diameter or larger (McNulty 1995). In this section we focus on one particular type of strong straight-line winds: the *derecho*. This term was coined by Hinrichs (1888) and means *straight* in Spanish. The term was chosen in opposition to the Spanish word *tornado*.

Johns and Hirt (1987) define derecho as "widespread convectively induced windstorms, caused by a family of downburst clusters produced by a midlatitude mesoscale convective weather system". To be classified as a derecho event, the windstorms must have the following four characteristics:

- Concentrated area of reports consisting of convectively induced wind damage and/or convective gusts > 26 ms^{-1} (50 kt), with a major axis length of at least 400 km;

- The reports in this area must be caused by the same mesoscale convective system and be continuous in time and space, showing a pattern of chronological progression;

- Within the area there must be at least three reports, separated by 64 km or more of either F1[2] or convective gusts of 33 ms^{-1} (65 kt) or greater.

- No more than 3 hours can elapse between successive wind events.

A typical example of winds generated in a derecho event can be seen in Figure 2.13, which depicts a derecho that occurred in 8-9 July 1993 and was documented by Bentley (1995). Although each wind report is caused by a strong convective downdraft, a derecho event covers a large area.

Another definition of derecho is presented in the newly published Glossary of Weather and Climate (Geer 1996): *A widespread convective windstorm consisting of a complex of thunderstorms that develop into a long-lived squall-line or a Mesoscale Convective Complex, with straight line winds. Literally "straight ahead" to differentiate straight-line winds from wind vortices in tornadoes. Now considered as any family of downburst winds moving primarily from northwest to southeast. The area affected may extend for hundreds of kilometers along the path of the system.*

A climatological study of derechos was performed by Johns and Hirt (1987), who examined data from the warm seasons of 1980 through 1983. The climatology shows an average of 17 derecho cases observed in the United States in each season, with a maximum in the Midwest, over Indiana and Ohio.

The synoptic scale conditions associated with most derechos (Johns and Hirt 1987) include westerly or northwesterly flow aloft (500 hPa), and a quasi-stationary east-west-oriented thermal boundary at the surface, with warm advection at 850 hpa. Most derecho events form in the cold side of the thermal boundary, which may be frontal in nature, but may also be a cold pool left by previous convection (Schmidt and Cotton 1989). The preferential location for derecho occurrence corresponds to an axis of maximum frequency of northwest flow severe weather outbreak (Johns 1982, 1984), and is explained by the favored polar frontal position during the summer months. It is important to note, however,

---

[2]The F-scale for wind speed was designed by Fujita (1981).
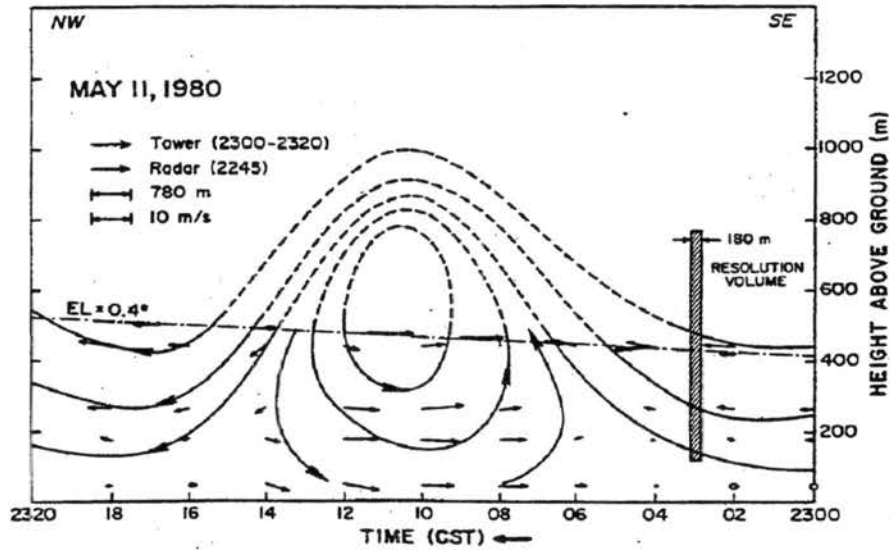
Figure 2.12: Samples of winds measured by a tower and by Doppler radar in a NW–SE cross section of an observed gust front. The dashed lines are estimated streamlines. From Doviak and Ge (1984).
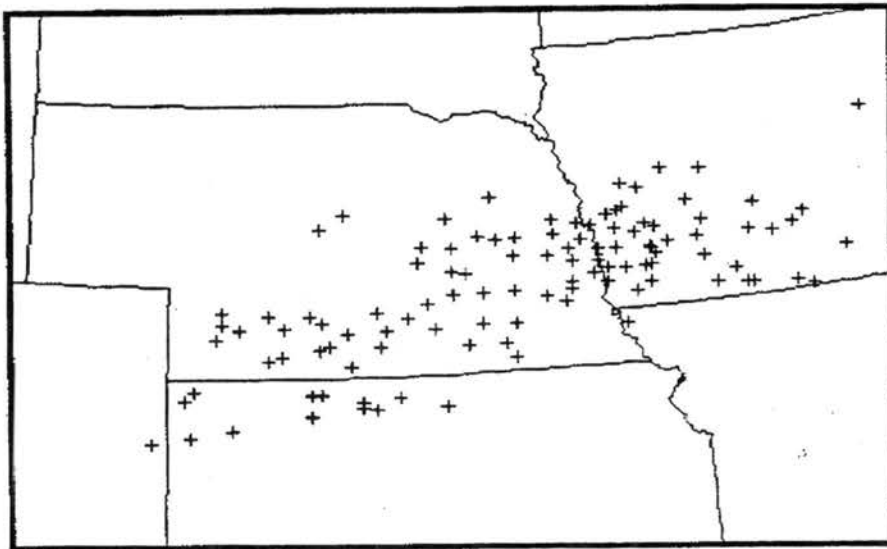
Figure 2.13: Wind reports (+) exceeding 25 ms^{-1} from 22 UTC, 8 July to 11 UTC, 9 July 1993. From Cooper and Bentley (1996).

that many derechos occur in environments that are different than that described above (Tremback 1990; Schmidt 1991; Duke and Rogash 1992), particularly because of enhanced baroclinicity.

Several authors (Johns and Hirt 1987; Przybylinski and DeCaire 1985; Funk et al. 1996; Przybylinski et al. 1996; Schmidt and Cotton 1989) have documented that the type of convective system associated with derecho events is a bow echo squall line or a line echo wave pattern. Schmidt and Cotton (1989) and Funk et al. (1996) have identified the presence of thunderstorms with mesocyclones in squall lines of derecho–producing MCSs. Moller et al. (1990) found that a number of derecho events consist of a cluster of bow-echo HP supercells. There is an important distinction between supercell scale bow-echo and squall line scale bow-echo (Moller et al. 1990; Lee et al. 1992a,b). It is unfortunate that the two systems have the same name. The supercell bow-echo has a length of around 40 km, while a squall line bow echo is composed of several cells and can reach more than 100 km. Although distinct entities, they can occur together, that is, bow echo supercells can be building blocks for bow echo squall lines that cause derecho events.

The thermodynamic aspects of derecho events have been addressed by Schmidt and Cotton (1990). From the analysis of the 19 July 1983 and the 02 August 1981 cases they concluded that derecho events occur in an environment that has (i) a stable layer at low levels (lowest 100 or 200 hPa), (ii) a 400 hPa deep neutral layer in mid levels, (iii) a layer of intermediate stability above. This thermodynamic profile has important physical significance. As mentioned in Section 2.7, a stable neutral layer near the surface is conducive to trapping of linear gravity waves and is also an environment favorable for the development of non-linear gravity waves. The waves can cause lifting of parcels from the low-level stable layer, which become negatively buoyant. After the wave passes, the parcels accelerate downwards.

Schmidt (1991) performed numerical experiments to investigate the mechanism of derecho development. He initialized a primitive equation, three-dimensional non-hydrostatic model with a horizontally homogeneous environment composed of the thermodynamic profile described in the past paragraph and ran with two types of shear: (i) unidirectional and (ii) veering with height. The experiment with a straight hodograph produced a squall line
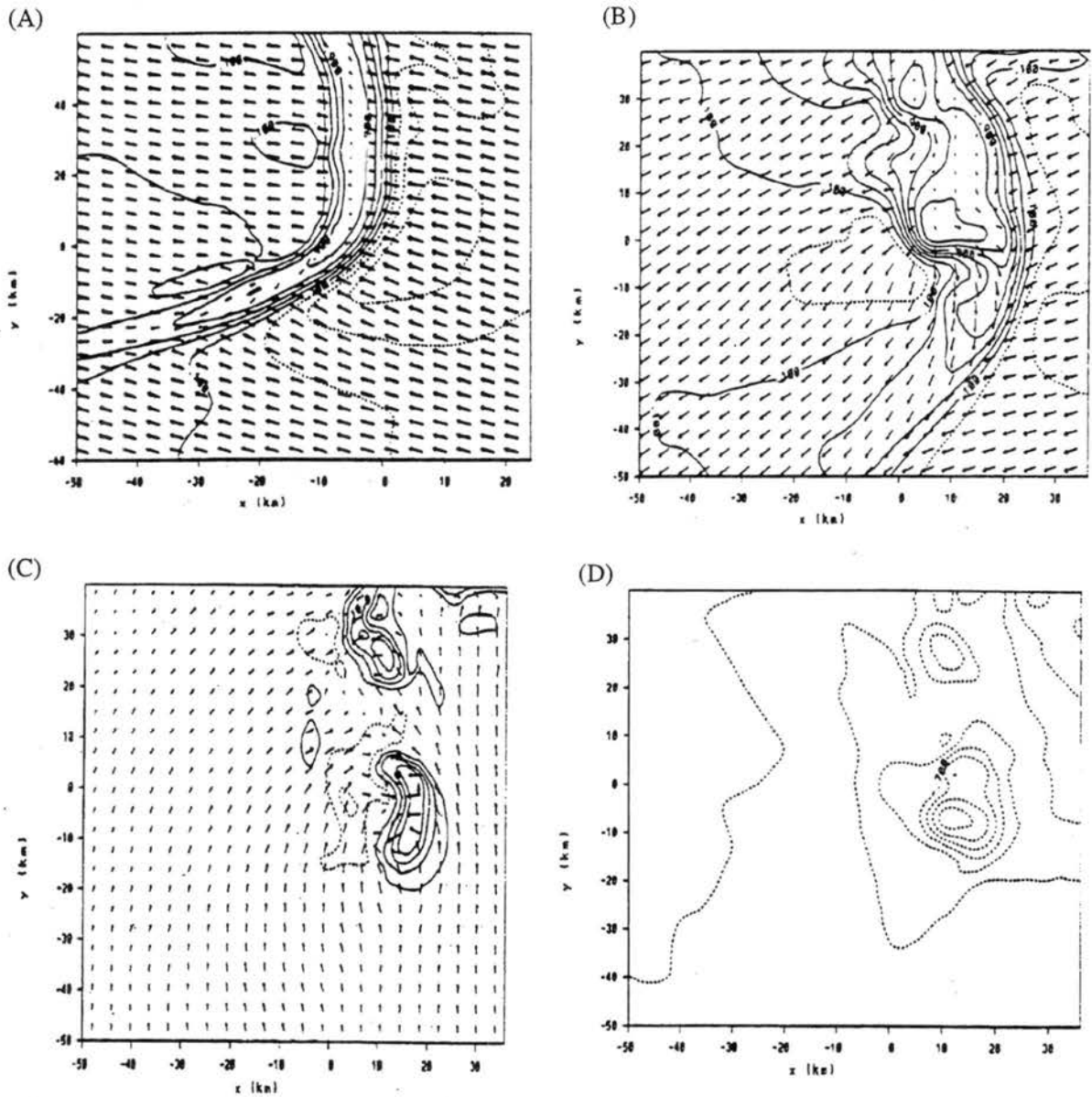
Figure 2.14: Horizontal x–y cross sections of model output three hours into the run. a) Near-surface storm relative winds and perturbation Exner function (contoured every 0.2 $Jkg^{-1}K^{-1}$) for the experiment initialized with a straight-line hodograph; b) Same as a) except for the experiment initialized with a clockwise turning hodograph; c) Mid–level vertical velocity (contours every 4.0 ms^{-1}) and storm relative winds for the experiment initialized with a clockwise turning hodograph; and d) Mid–level perturbation Exner function (contoured every 0.2 $Jkg^{-1}K^{-1}$) for the experiment initiliazed with a clockwise turning hodograph. From Schmidt (1991).

with few asymmetries and relatively weak winds (Figure 2.14a). The experiment with the curved hodograph proved to be more successful; consistent with observations, a high pressure center formed on the back of the convective line (Figure 2.14b), on its northern portion, and the strong winds had a northerly component that accelerated out of that center of high pressure. An analysis of this simulation showed that the cell associated with the strongest winds had a rotating updraft associated with a mid-level low pressure center (Figure 2.14c,d), as expected from the non-linear pressure perturbation equation described in Section 2.6. The upward PGF played a role in displacing the stable layer parcels upwards. This result shows that the combined effects of negative buoyancy generating a downdraft, and horizontal accelerations due to horizontal PGFs combined to create the strong winds.

In the previous paragraphs, physical mechanisms for the generation of strong winds were mentioned. All those involved cloud-scale circulations. However, it is important to distinguish a derecho event from isolated downbursts. A derecho is a long-lived event that covers a large area, and therefore a theory to explain derechos must explain the longevity of the system. It is possible that the derecho longevity is related to the supercell longevity, as discussed in section 2.4.1.

2.9 Approaches to Numerical Simulations of Deep Moist Convection

Different approaches have been used to perform numerical simulations of storms, and they can be separated into two major groups. The first group has examined cloud–scale dynamics in a controlled environment, while the second has examined the effect of adding a realistic variable environment to the simulations.

In the first group (Klemp and Wilhelmson 1978; Weisman and Klemp 1984; Weisman 1992, 1993; Skamarock et al. 1994; Rotunno and Klemp 1982, 1985; Schmidt and Cotton 1990; Grasso and Cotton 1995), a primitive equation model that does not contain radiation or boundary layer physics is used. Hence fluxes of heat and moisture are neglected. Also, flat topography is employed. The grid spacings used are small, on the order of 1 km, and predictive equations for microphysics are incorporated, with different degrees of detail. The models are initialized with only one sounding, representative of the pre-convective environment, and an artificial method is used to trigger convection, such as one or more

warm or cold bubbles [3]. The advantage of this controlled environment is that sensitivity experiments are easily performed. Therefore, vertical shear and the thermodynamic profile can be altered, and the impacts on the storm can be assessed. Although these experiments are *self-consistent*, i.e., they represent a correct solution to the problem posed, it is not obvious that the problem posed is the correct one. Is the idealized environment proposed in the experiments representative of the environment in which an MCS forms in nature? Can the conclusions drawn from those experiments be extended to the real storms? Crook and Moncrieff (1988) state that the presence of large-scale convergence in the environment, a process not present in most idealized simulations initiated with bubbles, has a large impact in convection generation, maintenance and propagation.

Another point is that the initialization of the model using a bubble is based on the assumption that the evolution of the storm from then on is independent of the original perturbation. However, this approach has been questioned by Brooks and Wilhelmson (1992) who noted that by initiating the model with a buoyant bubble smaller than usual their numerical simulation of a LP supercell was more successful.

The second avenue of study employs a much larger grid spacing. It usually has a first grid with spacing on the order of 80 km, and one or more nested grids, with a smaller grid spacing on the order of 20 km. The model is initialized with realistic topography, observed atmospheric data, and in some cases, also real physiographic data. Because of the relatively large grid spacing, individual storms are not resolved, and instead of employing a bulk microphysics parameterization, these simulations employ a cumulus parameterization (Zhang et al. 1989; Tremback 1990; Schmidt 1991). Cumulus parameterizations are built to *parameterize* the effects of convection in the environment, and not to represent convection itself. Therefore, this type of approach is obviously not suitable for the study of convection itself. It can be used to study the mesoscale environment in which storms develop. As a realtime forecasting tool, this type of modeling approach has been commonly used because limited computer power, time constraints, and the necessity of producing a forecast for a vast

---

[3]Bubbles are small regions in a model in which the thermodynamic fields are altered. They act as perturbations to trigger convective instability.

area have limited grid spacings to around 10 kilometers. The use of this type of model as a research tool has the inconvenience of being difficult to interpret, due to the complex realistic initialization and the presence of several physical processes occurring simultaneously. The obvious advantage of this approach is that there is less doubt about the applicability of the results, because they represent how MCSs evolve in a realistic environment.

More recently, a hybrid approach of the two types of simulation has been attempted (Nair et al. 1995; Grasso 1997a,b; Nachamkin and Cotton 1996, Olsson and Cotton 1997a; Cram et al. 1992a; Alexander and Cotton 1997). These are simulations in which relatively small grid spacings were used, so thunderstorms could be resolved, but the model was still initialized with realistic data. This was accomplished by the use of several nested grids in powerful computers, and allowed the study of thunderstorms in a realistic set-up.

2.10 Summary

In the previous sections we reviewed some of the most important forms of convective organization in the High Plains of the United States, focusing on the ones associated with wind storms. We showed that at least some strong straight line winds are associated with HP supercells, which can be organized in squall lines, usually with bow-echo shape. We also showed that several episodes of derecho and of other forms of severe weather occur at night, on the cold side of a front, under the influence of the LLJ. This environment is conducive to the development of long-lived gravity waves, and is favorable for the development of up-down downdrafts, two mechanisms that can lead to strong surface winds.

In this work, we studied in detail a derecho event that took place on 13 May 1985, whose winds were associated with a MCS that formed in southeast Colorado, and propagated towards the northeast during the night. Although the MCS formed in the afternoon, the first severe winds only were reported after midnight. The environment in which this derecho developed had some of the important "ingredients" for strong winds discussed in this chapter. The system formed on the cold side of a weak summer stationary front, a region in which the lower levels got very stable at night, and where a significant LLJ was present.

Previous modeling studies of derechos have not used a variable initialization, and have therefore not been able to study the interactions between convection and an evolving environment. In this study, this multi–scale problem was approached through a multi-grid numerical simulation, in which motions from the synoptic scale down to cloud scale were resolved. The results from the high-resolution grid were used to study the HP supercell that, in the simulation, was responsible for the strongest winds. The importance of the different mechanisms that can generate strong sustained winds near the surface was then evaluated.

Chapter 3

CASE DESCRIPTION

In this chapter the evolution of the MCS that was studied is described using observations from surface and upper air stations, radar, satellite and special observations recorded in Storm Data (1985). This MCS was chosen because it was an event of severe straight line winds. From the observations available, the event could not be classified in the derecho definition proposed by Johns and Hirt (1987) and discussed in Section 2.8 because the number of high wind reports was insufficient. However, we do believe this was a derecho event. The scarcity of observations can be attributed to the low population density in this rural area and to the nocturnal character of the system.

The fact that the system was nocturnal brought our attention to this case. A nocturnal system typically develops over a stable lower boundary layer that forms due to radiational cooling. In this case, the boundary layer was particularly stable because the MCS developed on the cold side of a front. As discussed in the last chapter, a stable layer is not usually thought of as a good ingredient for strong convective downdrafts or strong surface winds. Therefore, mechanisms other than buoyancy–driven downdrafts must have taken place. The longevity of the system also made it intriguing and worthy of investigation. The low level stable layer hinders the formation of a surface–based cold pool, so propagation and longevity are probably not associated with the cold pool.

The strong winds in this case were first recorded at 0600 UTC[1] of 13 May 1985, but the convective system itself formed in the afternoon. At 0035 UTC only light precipitation existed over southeast CO, as can be seen in the radar summary (Figure 3.1). At 0130 UTC

---

[1] To convert from UTC to CST subtract 6 hours. Therefore, 06 UTC is 00 CST.
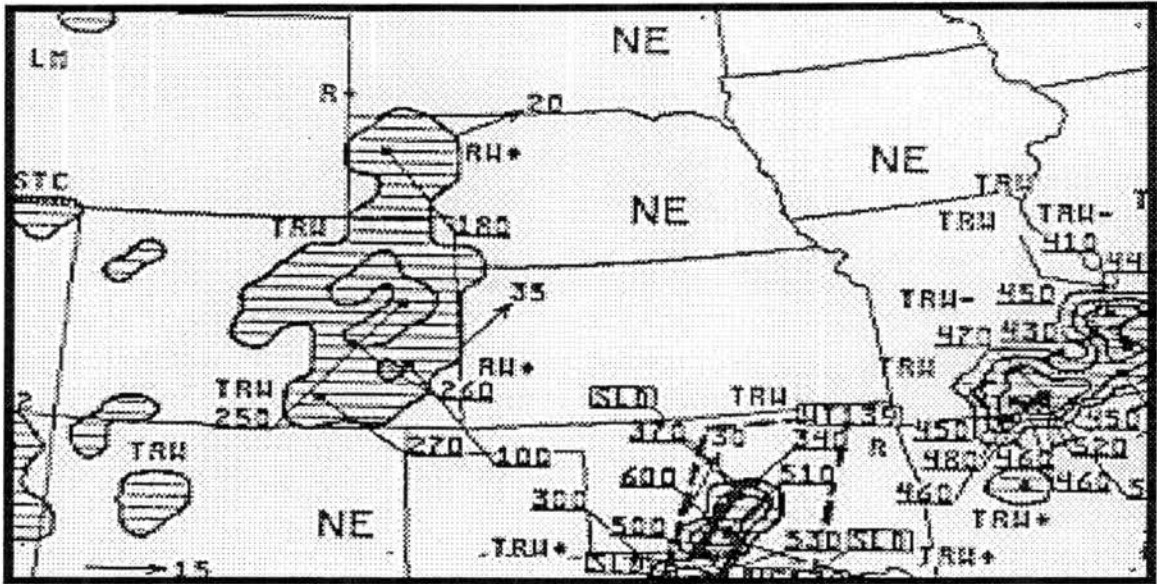
Figure 3.1: Radar Summary at 0035 UTC on 5/13.
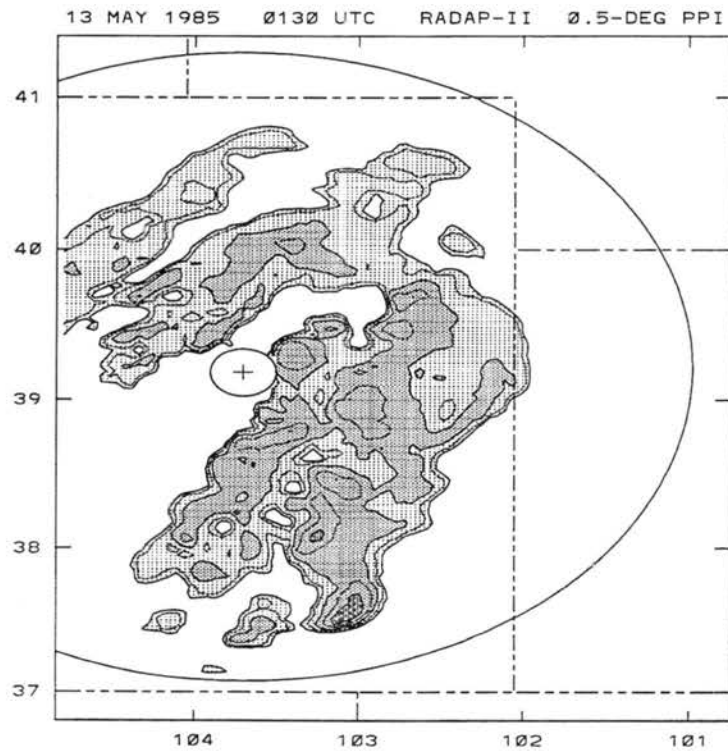
Figure 3.2: PPI from Limon Radar at 0130 UTC on 5/13. Contours begin at 15.0 dBZ and are at 7.5 dBZ intervals. Shading begins at 15.0 dBZ and increases at 15.0 dBZ intervals.
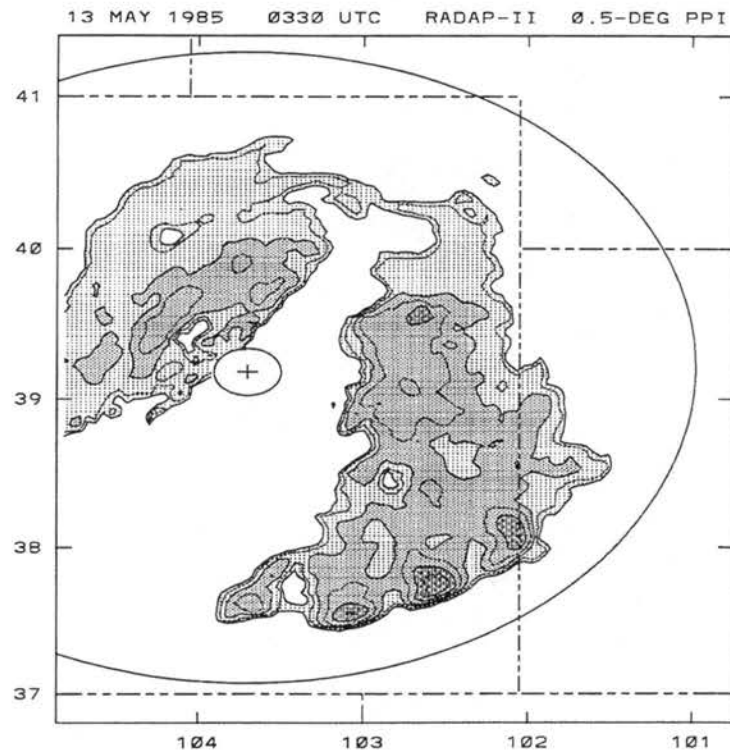
Figure 3.3: PPI from Limon Radar at 0330 UTC on 5/13. Contours begin at 15.0 dBZ and are at 7.5 dBZ intervals. Shading begins at 15.0 dBZ and increases at 15.0 dBZ intervals.
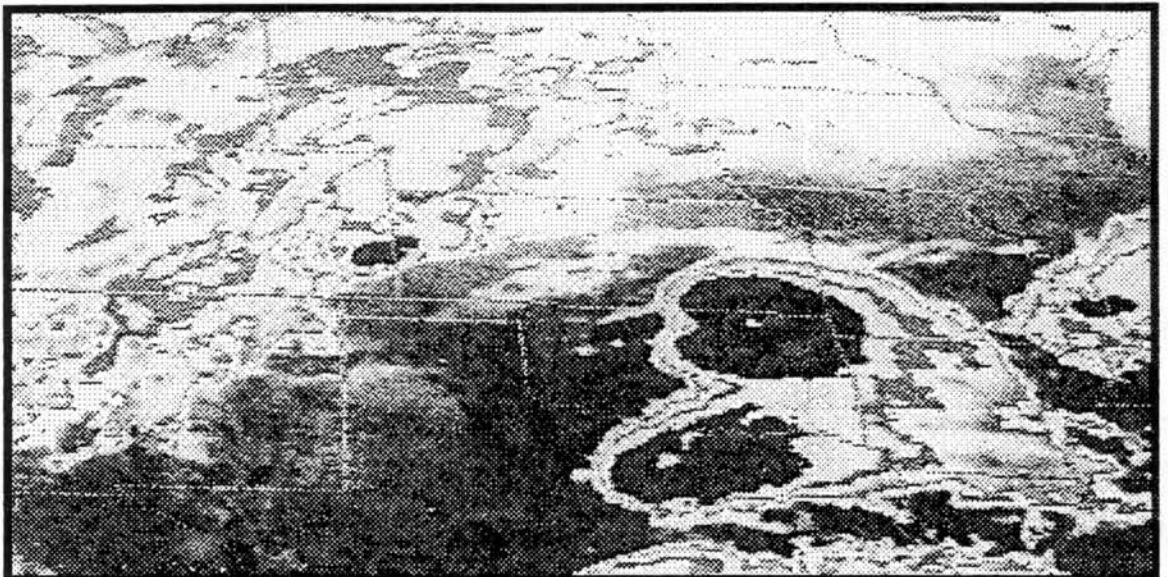
Figure 3.4: Infrared satellite image at 0330 UTC on 5/13.

the Limon radar showed two strong cells in southeast CO (Figure 3.2), associated with an area of lighter precipitation to the north. By 0330 (Figure 3.3) several cells had formed in southeast Colorado, aligned approximately in the southwest–northeast direction. A region of stratiform precipitation was located to the north of the convective line. The cells were moving towards the northeast. The infrared satellite image at that same time (Figure 3.4) showed deep clouds on the Colorado–Kansas border. Also, two convective systems with large anvils can be seen in eastern Oklahoma.

As the system moved farther towards the northeast into Kansas (KS), it exited the scope of the Limon radar. Its evolution can be followed using the radar summaries. At 0535 UTC (Figure 3.5) the cells that had formed in CO had entered KS, and by 0835 UTC (Figure 3.6) the cells were located in northern KS. A tornado watch box issued by the National Weather Service at 0735 UTC can be seen over the region of strong convection. At 1035 UTC some cells of the MCS were moving over the Kansas–Nebraska border. Convection started to weaken after sunrise.

The swath of damage left behind by this system can be seen in Figure 3.7. Reports of strong winds compiled by Storm Data (1985) began at 0530 UTC in Syracuse (KS) with 70 kt winds, and progressed towards the northeast. The last reports came from the Kansas–Nebraska border at 1015 UTC, with 80 kt. One weak (F0 in the Fujita 1981 scale) tornado was reported associated with this MCS in Scott City (KS).

Although this case occurred during the PRE-STORM experiment (Meitín and Cunning 1985), this MCS did not pass over the array of dense surface and upper-air observations located in the KS–OK border. Therefore, we will use data from the regular National Weather Service network to describe the environment in which the MCS formed and developed.

At 00 UTC a semi-stationary surface front extended from the Texas (TX) panhandle through OK towards the east (Figure 3.8). A low pressure center of 1000 hPa was located on the border of the TX panhandle and New Mexico (NM). A dryline [2] extended south from the center of low pressure, separating the moist air on the east from the dry air to the

---

[2]A dryline is a narrow zone of very sharp horizontal gradient of moisture in the planetary boundary layer. It is commonly found over Texas during the spring months.
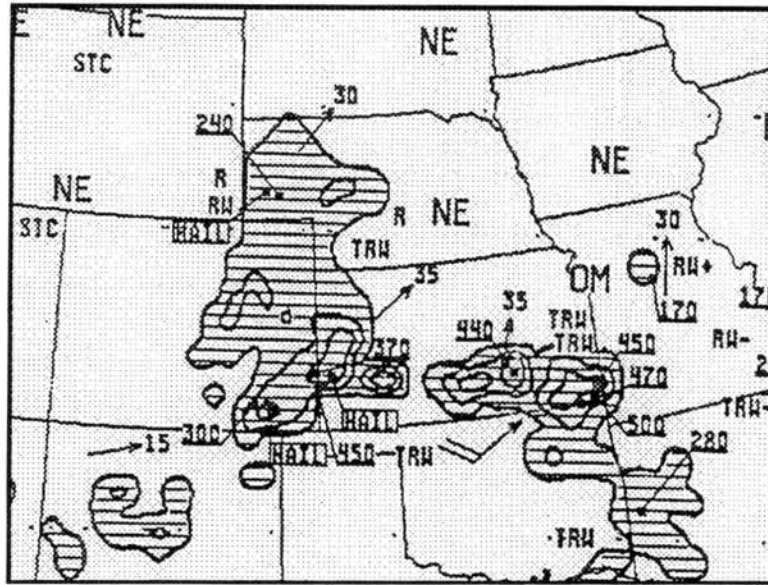
Figure 3.5: Radar Summary at 0535 UTC on 5/13.
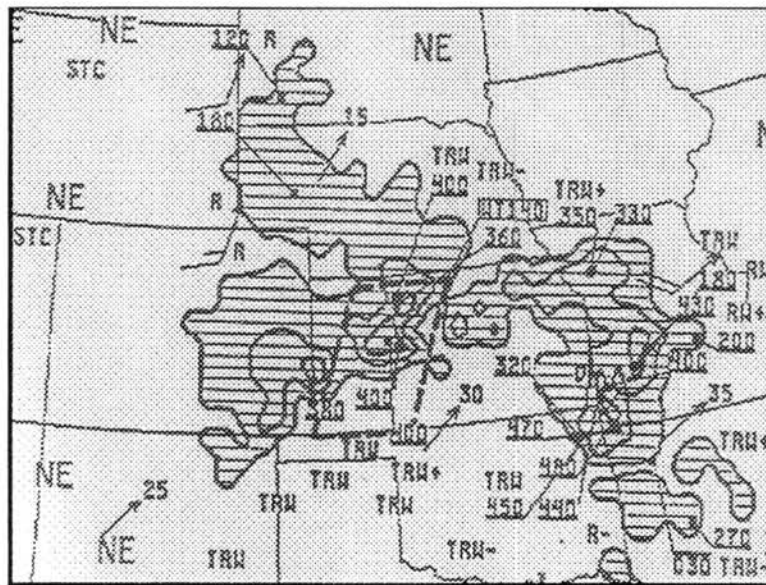
Figure 3.6: Radar Summary at 0835 UTC on 5/13.
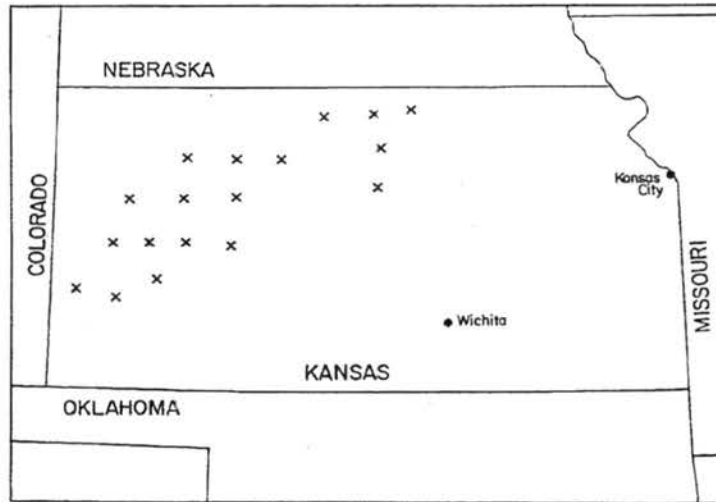
Figure 3.7: High wind reports between 0534 and 1130 UTC.
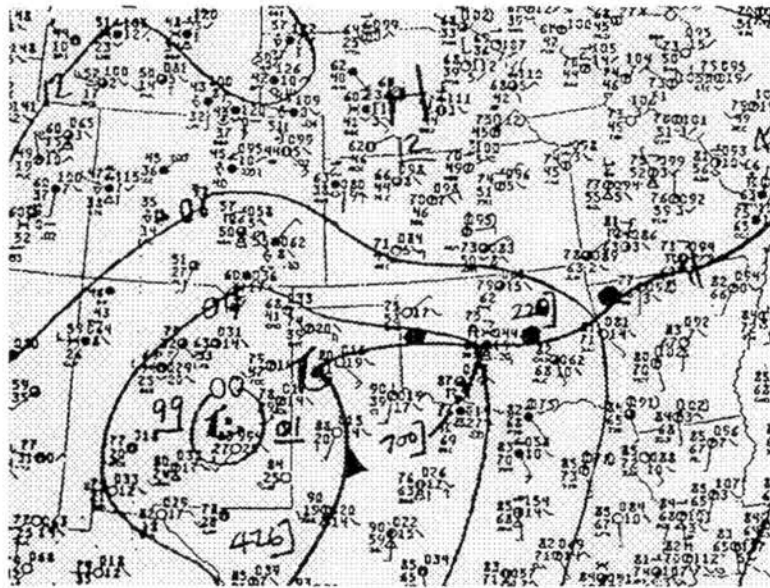
Figure 3.8: Surface analysis at 00 UTC on 5/13.

west. The winds turned cyclonically around the low, therefore flow in southeast CO was from the northeast, and in KS, from the east. A weak center of high pressure was located over Nebraska.

In upper-levels, a center of low geopotential was present in 850 hPa over the surface low, causing southwest winds over the MCS genesis region. At higher levels (Figures 3.9a,b), a closed low did not exist over the southwest United States, but a trough whose axis tilted westward with height was present. Therefore the mean wind in upper levels was from the southwest, and the MCS developed on the downwind side of a trough, a region prone to large scale upward motion. Figure 3.10 shows a Skew-T diagram for a location near Dodge City (lat=37.8N, lon=100.2W) at 00 UTC. This figure was obtained by interpolation of soundings to a model grid point. A deep, relatively dry, and well-mixed boundary layer extended up to 720 hPa, and was capped by an inversion. The winds are from the east up to 780 hPa, where they begin to veer considerably.

During the evening, the position of the surface low remained unaltered, but it deepened slightly and reached 998 hPa by 12 UTC (Figure 3.11). The semi–stationary front moved north and by 12 UTC was along the KS–OK border. The high pressure center migrated to the east and at 12 UTC was over southern Minnesota. It contributed with the establishment of easterly winds over KS, that fed the convective system.

At the 850 and 700 hPa levels the low was closed at 12 UTC (Figure 3.12), and significant southerlies can be seen in those levels over KS. The winds in 850 hPa over OK increased from 20 kt to 40 kt from 00 UTC to 12 UTC. Figure 3.13 shows a Skew-T diagram for (lat=37.8N, lon=100.2W) at 12 UTC. A very stable layer with northeast winds is present from the surface up to 800 hPa. A layer of intermediate instability is present from 800 to 720 hPa, capped by an inversion. The winds are from the south upwards of 820 hPa. A comparison of Figures 3.13 and 3.10, reveals that the winds have strengthened and become more southerly in the layer from 820 to 700 hPa between 00 and 12 UTC, and that the 800 hPa temperatures have increased by a few degrees Celsius during the same period. This evolution in the sounding has the signature of a LLJ, and will be discussed further in Chapter 5.

Figure 3.9: Station plot, geopotential height (solid lines) and temperature (dashed lines) at a) 700 hPa and b) 500 hPa at 00 UTC on 5/13.
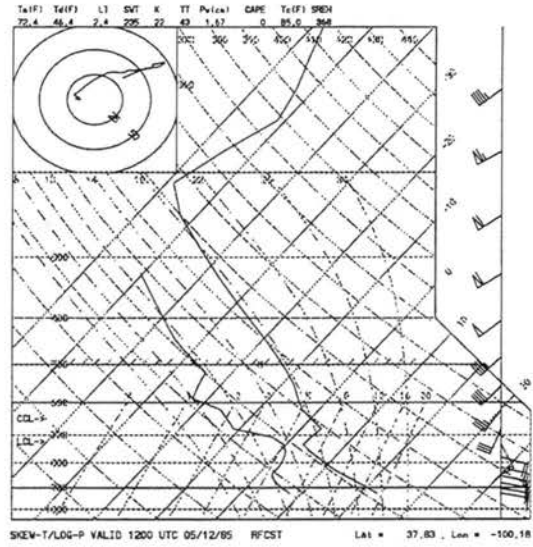
Figure 3.10: Skew-T diagram for lat=37.8N and lon=100.2W at 00 UTC on 5/13. Obtained from observations interpolated to a model column.
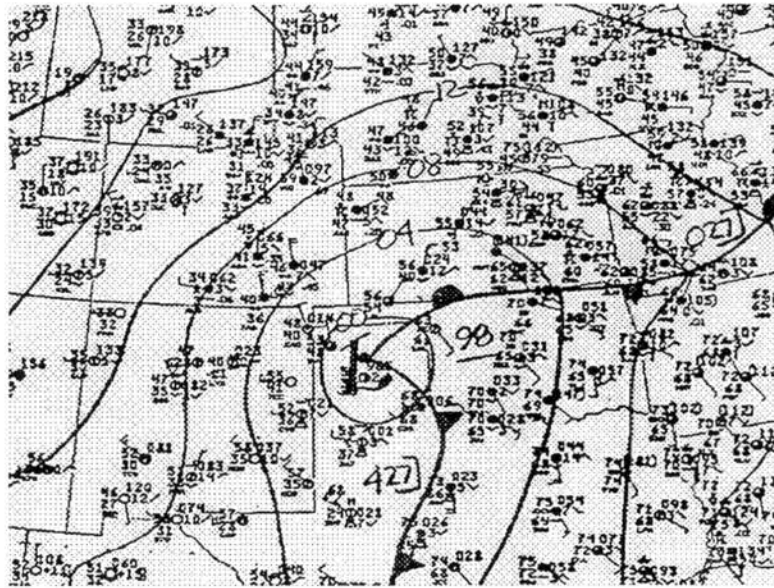
Figure 3.11: Surface analysis at 12 UTC on 5/13.

Figure 3.12: Station plot, geopotential height (solid lines) and temperature (dashed lines) at 700 hPa at 12 UTC on 5/13.

Figure 3.13: Skew-T diagram for lat=37.8N and lon=100.2W at 12 UTC on 5/13. Obtained from observations interpolated to a model column.

In summary, we will study a MCS that began forming at night in southeast Colorado, and propagated towards the northeast during the night, generating strong winds. The system evolved on top of a stable boundary layer, under the presence of a LLJ.

In the next chapter, the numerical model used to study this case will be described, and in Chapter 5 the results of the multi-grid simulation of this case will be presented.

Chapter 4

MODEL OVERVIEW

The simulations described in this dissertation were performed using version 3b of the Regional Atmospheric Modeling System (RAMS) developed at Colorado State University. This model is very versatile and may be set up in many ways, depending on the intended application. In this section we will limit the description to the parts of the numerics and physics that were actually used in our simulations.

4.1 Experimental set-up

The model was integrated for a total of 24 hours and four grids were used in this simulation. Three grids were telescopically nested within the first grid. The coarsest three grids were initialized in the beginning of the simulation, while the fourth grid was initialized eight hours into the run. All grids use a rotated polar-stereographic projection, in which the pole of the projection is located near the center of the domain of the coarsest grid (latitude=42.1N, longitude=107.1W).

The main characteristics of the model set-up are described in Table 4.1. The horizontal grid spacings used in Grids # 1 through 4 were 80, 40, 10 and 2 km, respectively. The type of grid used in the model is Arakawa–C (Messinger and Arakawa 1976). All thermodynamic and moisture variables are defined at the same point and the velocity components, u, v and w are staggered half a grid point in the x, y and z directions respectively. The location of the grids at the time they were initialized is displayed in Figure 4.1.

All grids have 38 vertical levels, and the top of the domain is at a height of 21 km. The vertical coordinate used in the model follows the terrain and is called *sigma* (σ). The height of each σ-level is given by

	Grid #1	Grid #2	Grid #3	Grid #4
Grid spacing (km)	80	40	10	2
Domain (x × y km)	4560×3760	1960×1560	490×490	182×182
Vertical Levels (#)	38	38	38	38
Timestep (s)	90	45	22.5	7.5
Initial at t (hrs)	0	0	0	8

Table 4.1: Model configuration.

$$\sigma = \frac{(z - z_b)}{(z_t - z_b)} z_t, \tag{4.1}$$

where z_b is the topographical height of a grid point, z_t is the height of the top of the domain, and z is the physical height of a vertical levels.

The vertical grid spacing for a column located over a zero terrain elevation was 100m near the ground, stretching at a rate of 1.1, up to a maximum Δz of 1000m. Therefore, above a height of 10 km, the vertical grid spacing was a constant 1000m. In grid points located over elevated terrain the vertical grid spacing was less than that, as described by (4.1).

Below we list briefly some of the numerical and physical characteristics of the model. A more general description of the model can be found in Pielke et al. (1992), Cotton et al. (1994), Walko et al. (1995a,b) and references therein.

4.1.1 Initialization

The model was initialized at 1200 UTC of 12 May 1985 and run for 24 hours. The data to initialize the model were obtained from the National Center for Atmospheric Research (NCAR) and consisted of 3 files: (i) surface observations; (ii) rawindsonde data; (iii) model data, in isobaric surfaces (called *pressure data*, from time zero, used to initialize the National Meteorological Center (NMC — now known as National Center for Environmental Prediction) model.

These data were input to the model's initialization package (Tremback 1990). In this package, the pressure data are initially interpolated to the model's Grid # 1 horizontal mesh. Next, the pressure data were interpolated to σ-surfaces near the ground and to

isentropic surfaces above 5 km. Then, the surface and upper-air data were ingested and interpolated in the vertical to the $\sigma-$ and isentropic surfaces. A Barnes (1973) analysis was then performed to interpolate the irregularly spaced observations to the Grid # 1 horizontal mesh. The final step was the vertical interpolation of the data to the model's vertical grid.

Data for the times of 00 and 12 UTC of 13 May 1985 were also run through the initialization package, to produce data files to be used as boundary conditions, as described in Section 4.1.2.

Datasets of topography and vegetation were also used to initialize the model. Topography was interpolated from a USGS dataset to Grids # 1 and # 2 (Figure 4.2), and from Grid # 2 to Grids # 3 and # 4. The dataset had spacing of 30 seconds of degree over the United States, and 10 minutes of degree over Canada and Mexico. Vegetation was initialized from a file with a 1 degree resolution (Loveland et al. 1991).

4.1.2 Grid Nesting and Boundary Conditions

The horizontal boundaries of Grid # 1 and the vertical boundary of all grids were updated using a technique called *nudging* (Davies 1983) in which an extra term is added to the prognostic equations of the model. This extra term forces the variables computed in the model to relax to the observed state. Nudging was applied to 5 grid points in each horizontal border and to 6 grid points in the upper part of the domain.

The boundaries of the nested grids were simply obtained from the next coarser grid. The nesting system was two-way (Clark and Farley 1984; Clark and Hall 1991). The parent grid furnishes boundary conditions to the nested grid, and the region of the parent grid that is covered by a nested grid has its information replaced by an average of the values of the nested grid.

Grids # 3 and # 4 moved to follow the track of the MCS. A grid movement direction and speed was specified subjectively to best follow the convective system. Grid movement is accomplished by a redefinition of the grid location. Information in locations no longer covered by the fine grid was lost, and information in new regions of the fine grid was interpolated from the parent grid (Walko et al. 1995b).
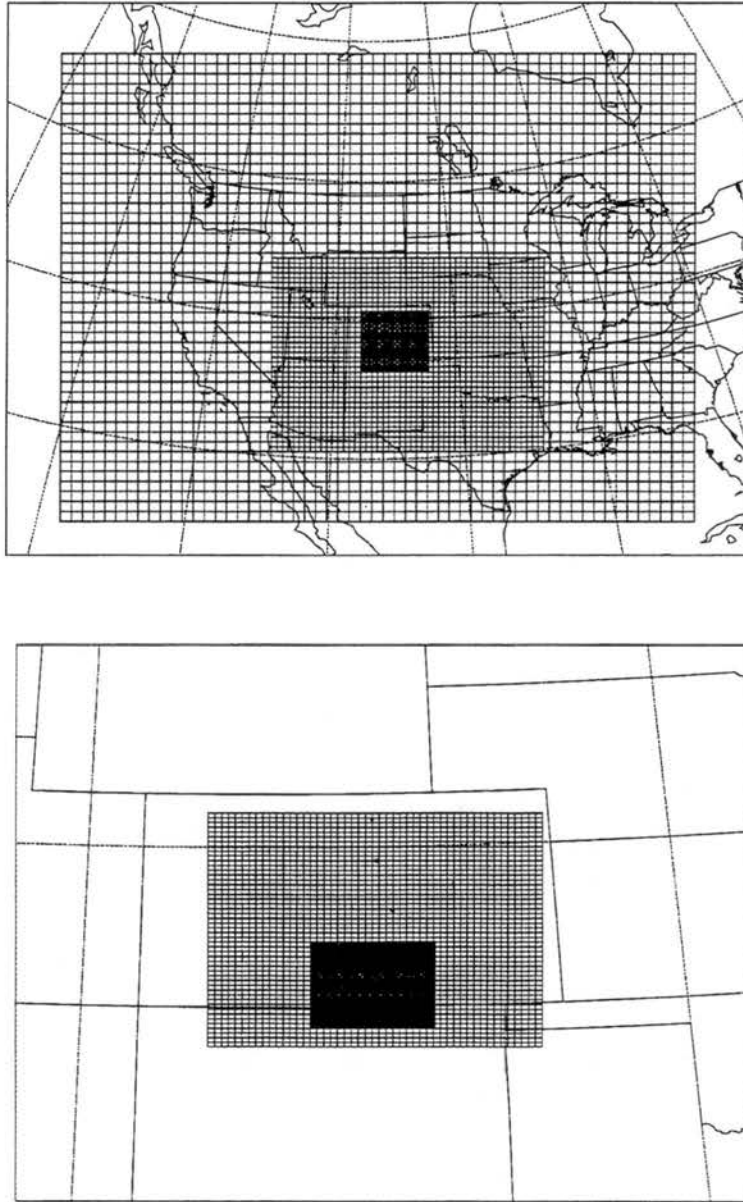
Figure 4.1: Location of the grids at t=20 UTC. a) Grids 1, 2 and 3; b) Grids 3 and 4.
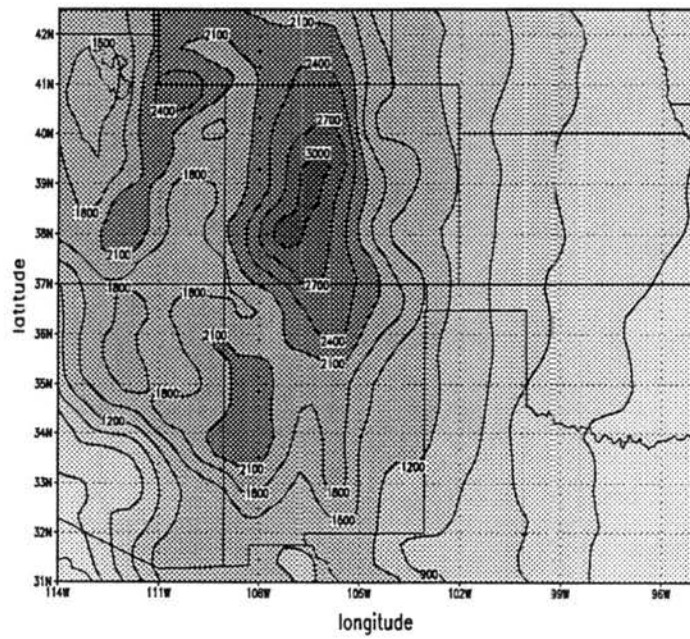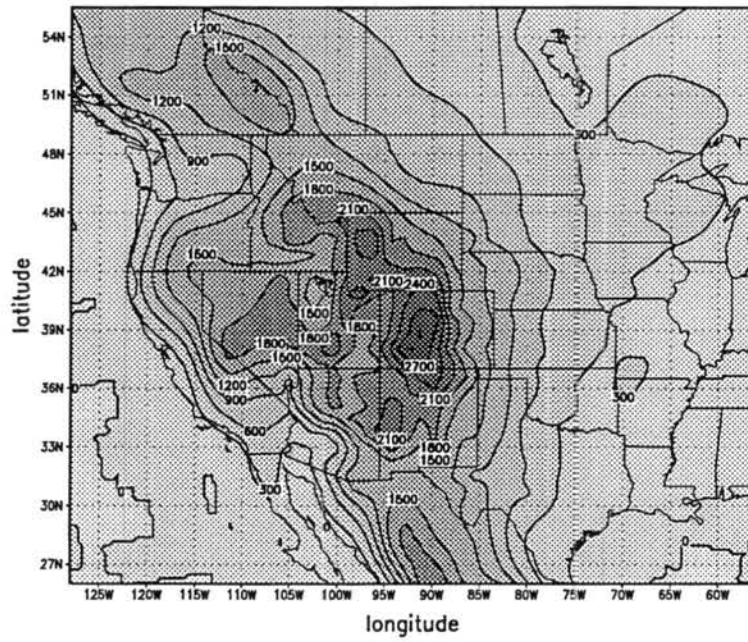
Figure 4.2: Topography (m) in Grids a) # 1; b) # 2.

4.1.3 Time and Space Differencing

The non-hydrostatic, compressible version of the model was integrated for 24 hours using a hybrid scheme, which consists of leapfrog time differencing for the momentum and continuity equations and forward differencing for the thermodynamic and moisture equations. Advection was done using a second order scheme.

To save computer time, the timestep was split. A short timestep was used to compute terms in the prognostic equations that are responsible for the generation of acoustic waves (Klemp and Wilhelmson 1978). All other processes were computed using the longer timestep listed in Table 4.1.

4.1.4 Long-wave and short-wave radiation

The radiation scheme used was developed by Mahrer and Pielke (1977). The short-wave scheme accounts for the absorption and scattering by oxygen, ozone and carbon dioxide and for the absortivity of water vapor in an empirical manner. It treats absorption by water vapor but ignores the presence of condensed water. The long-wave scheme accounts for the infrared emission and absorption of water vapor and carbon dioxide, but also ignores condensed water. The scheme takes into account the longitudinal variation of short-wave radiation reaching the top of the atmosphere. The tendencies to the thermodynamic equation due to radiation were updated every 15 minutes.

4.1.5 Surface Layer

The surface fluxes of heat, moisture and momentum were computed using the scheme of Louis et al. (1981). The fluxes depend on the roughness length, on the Richardson number and on the differences of wind speed, temperature and moisture between the ground and the air. The wind speed at the ground is always zero, and the temperature and moisture are supplied by the soil and vegetation model. The surface in each grid box is subdivided in percentages of water cover, vegetation, shaded soil and bare soil. The fluxes are computed separately for each type of surface and then averaged.

The soil model (Tremback and Kessler 1985) used 11 levels (going down to half a meter in depth) on which temperature and moisture were prognosed. The vegetation model

(Avissar and Pielke 1989) was run using a variable vegetation initialization (Loveland et al. 1991).

4.1.6 Diffusion

Eddy diffusion was parameterized using the Smagorinski (1963) deformation–K scheme. The vertical diffusion scheme was modified by Hill (1974) to include a dependency on the Brünt-Vaisalla frequency and by Lilly (1962) to include a dependency on the Richardson number. A minimal horizontal diffusion was used for numerical purposes even when physical diffusion was small or zero.

4.1.7 Microphysics

A bulk microphysics parameterization (Walko et al. 1995a) was used, with prognostic equations for the mixing ratios of rain, pristine ice, snow, aggregates, graupel and hail. Cloud water was diagnosed and pristine ice mixing ratio was prognosed.

No cumulus parameterization was employed.

Chapter 5

EVOLUTION OF THE SIMULATED MCS

In this section we will discuss the multi-scale evolution of the simulation of the 12–13 May 1985 MCS that led to the strong winds described in Chapter 3.

As mentioned before, this simulation was initialized at 12 UTC (06 CST), 12 May and integrated for 24 hours. The coarsest 3 grids ($\Delta x = \Delta y = 80/40/10$ km) were present for the full period of integration. Grid # 4 ($\Delta x = \Delta y = 2$ km) was initialized 8 hours into the run, after the first evidence of convection was noted on Grid # 3. This was also the time when the microphysics parameterization was turned on. All other physical processes were on during the whole time.

We will begin the description at 00 UTC of 13 May, 12 hours into the run, when the initial convection from the MCS had already begun.

Except where specified, the x–y cross sections are shown on the model's σ-surfaces. The word *surface* refers to the lowest model level, which is located one Δz above the ground for vertical velocity and half a Δz for the other variables. As discussed in Chapter 3 (Equation 4.1), Δz is compressed over regions of non-zero topography. Therefore, the height of a given σ-surface is larger over regions of lower topography. In this dissertation, *height* refers to the height of a σ-surface over a grid point of zero topography.

5.1 MCS at 00 UTC

5.1.1 Large Scale Environment

At 00 UTC the stationary front stretched along the OK-KS border. The front at the surface was better defined as a moisture gradient and as a wind shift than as a temperature gradient (Figure 5.1). Moist air was carried from the south by the southerlies, and pooled over southern OK, accentuating the moisture contrast along the front. A strong east–west
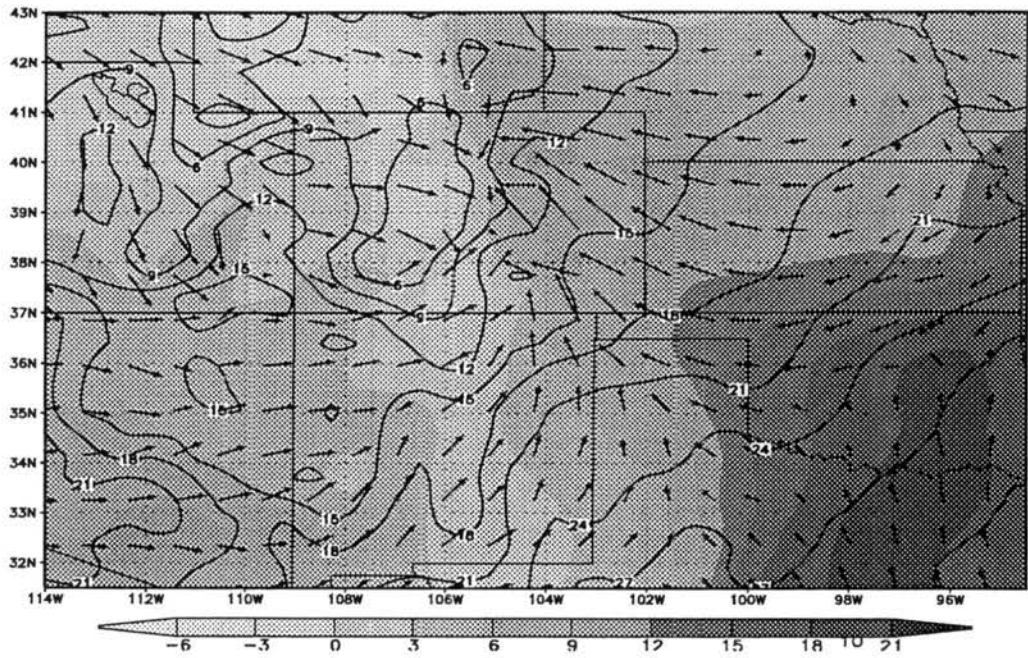
Figure 5.1: Dew point temperature (shaded) (C), temperature (contoured) (C) and horizontal wind vectors at σ=48m and t=00 UTC on Grid #2.

(A)
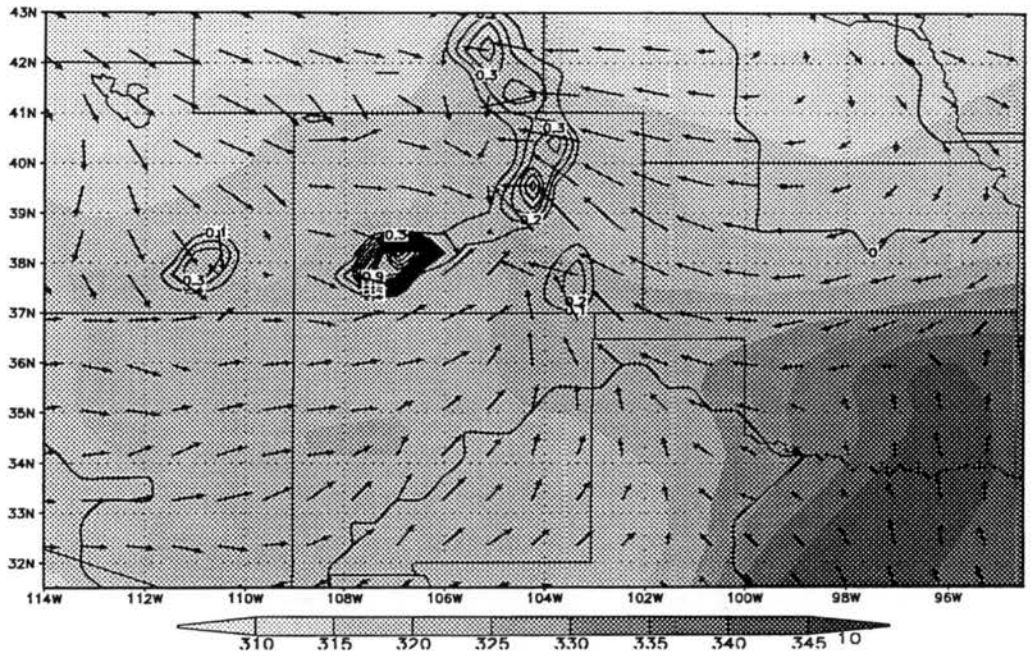
(B)
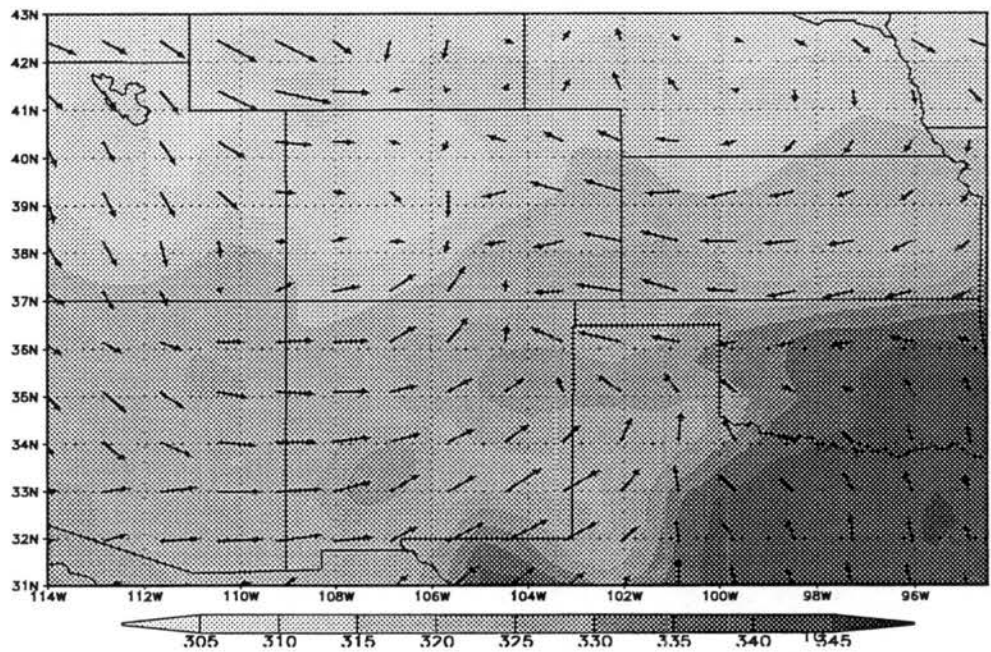
Figure 5.2: a) Equivalent potential temperature (shaded) (K), condensate mixing ratio (contoured) (gkg^{-1}) and horizontal wind vectors at σ=48m and t=00 UTC on Grid #2; b) Observed equivalent potential temperature (K) and horizontal wind vectors at σ=48m and t=00 UTC, interpolated to Grid #1.
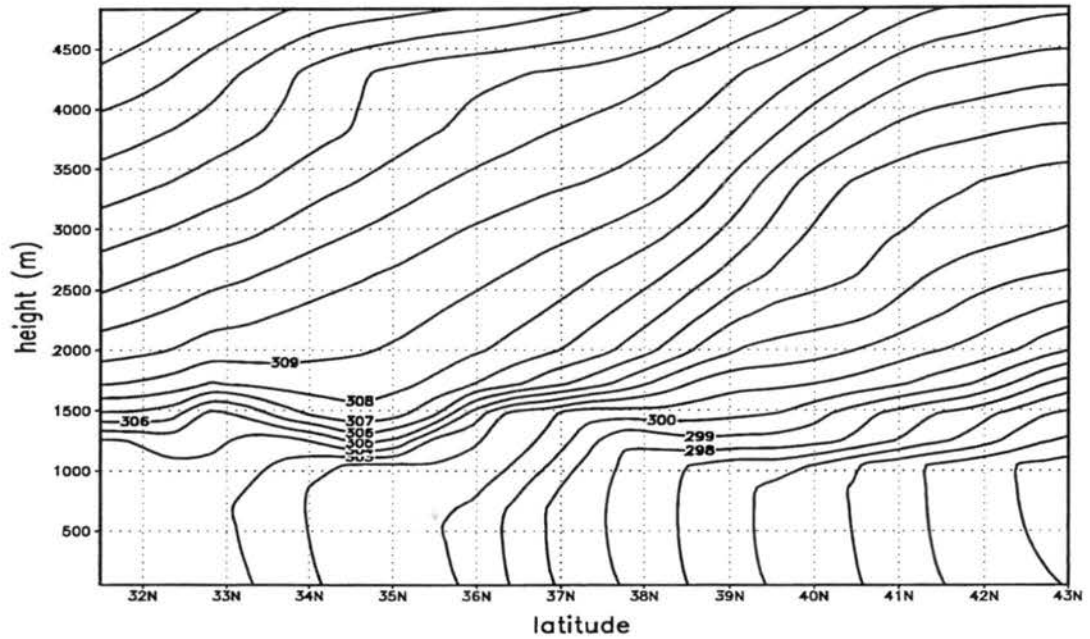
Figure 5.3: Vertical cross section through lon=97.5W of potential temperature (K) at t=00 UTC on Grid #2.
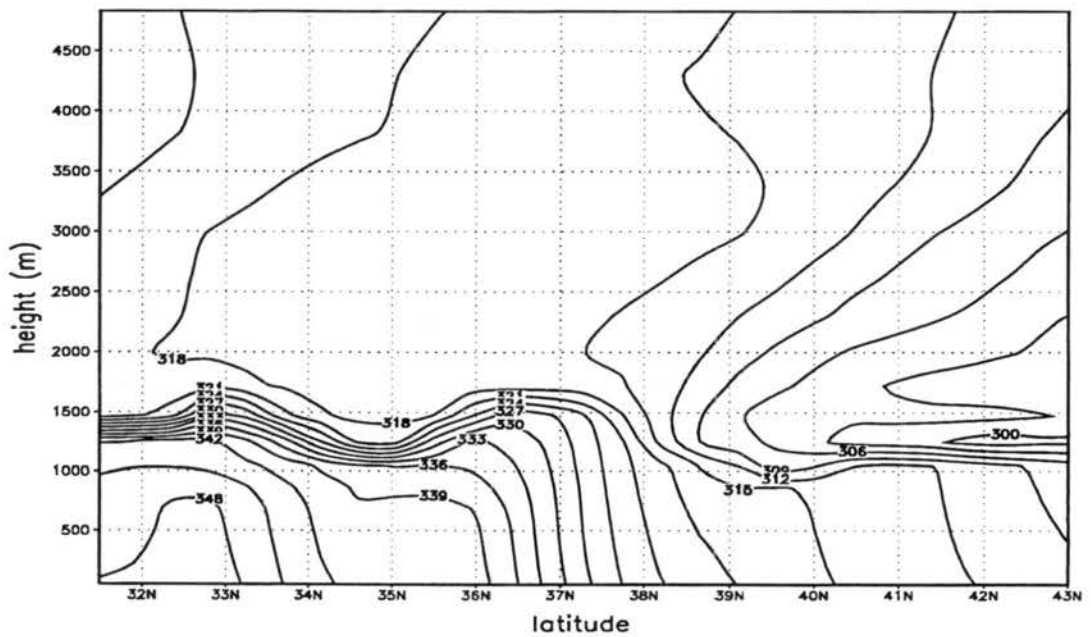
Figure 5.4: Vertical cross section through lon=97.5W of equivalent potential temperature (K) at t=00 UTC on Grid #2.
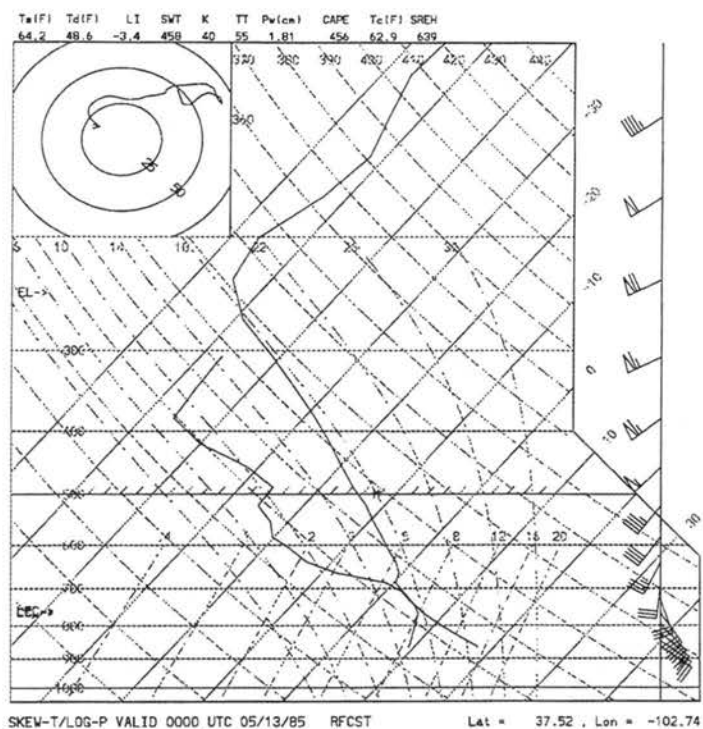
Figure 5.5: Skew-T diagram for lat=37.5N, lon=102.7W from Grid # 4 at t=00 UTC.
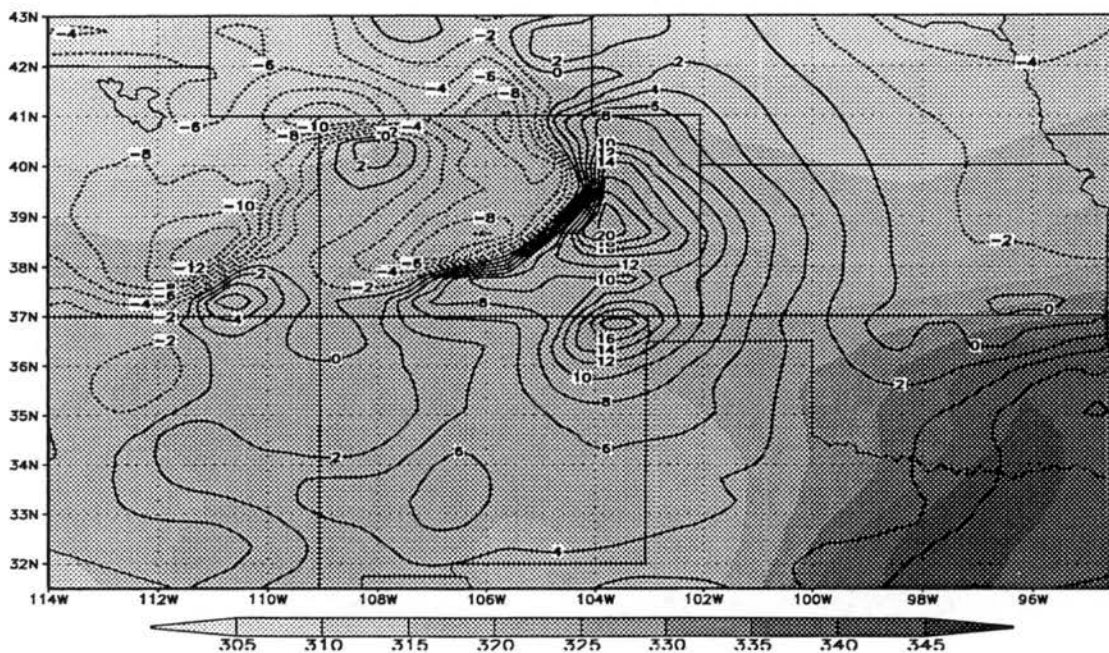
Figure 5.6: Equivalent potential temperature (shaded) (K) and meridional speed (contoured) (ms^{-1}) at σ=689m and t=00 UTC on Grid #2.

(A)
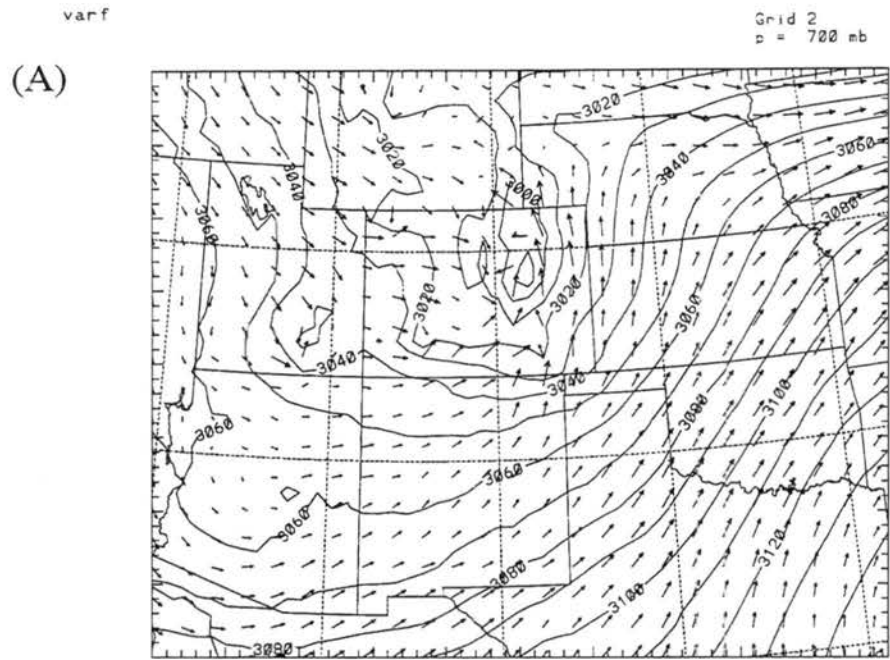
GEOPOTENTIAL HEI
'2HR FCST VALID 0000 UTC 05/13/85
Contours from   2980.0   to   3140.0   Contour interval   10.000

.221E+02
MAXIMUM VECTOR

(B)
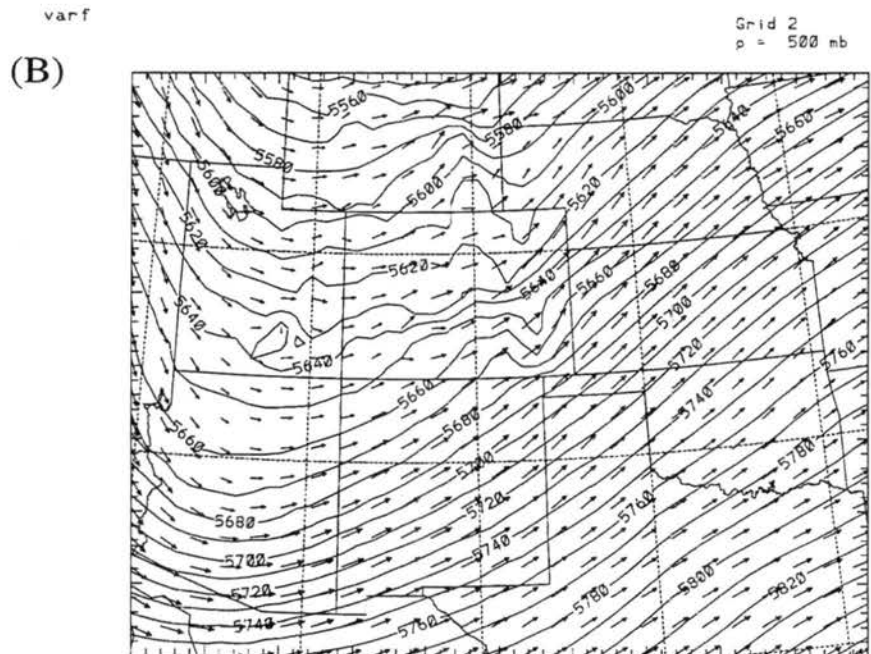
GEOPOTENTIAL HEI
12HR FCST VALID 0000 UTC 05/13/85
Contours from   5540.0   to   5850.0   Contour interval   10.000

.299E+02
MAXIMUM VECTOR

Figure 5.7: Geopotential (m) and horizontal wind vectors at t=00 UTC on Grid #2 at a) p=700hPa; b) p=500hPa.
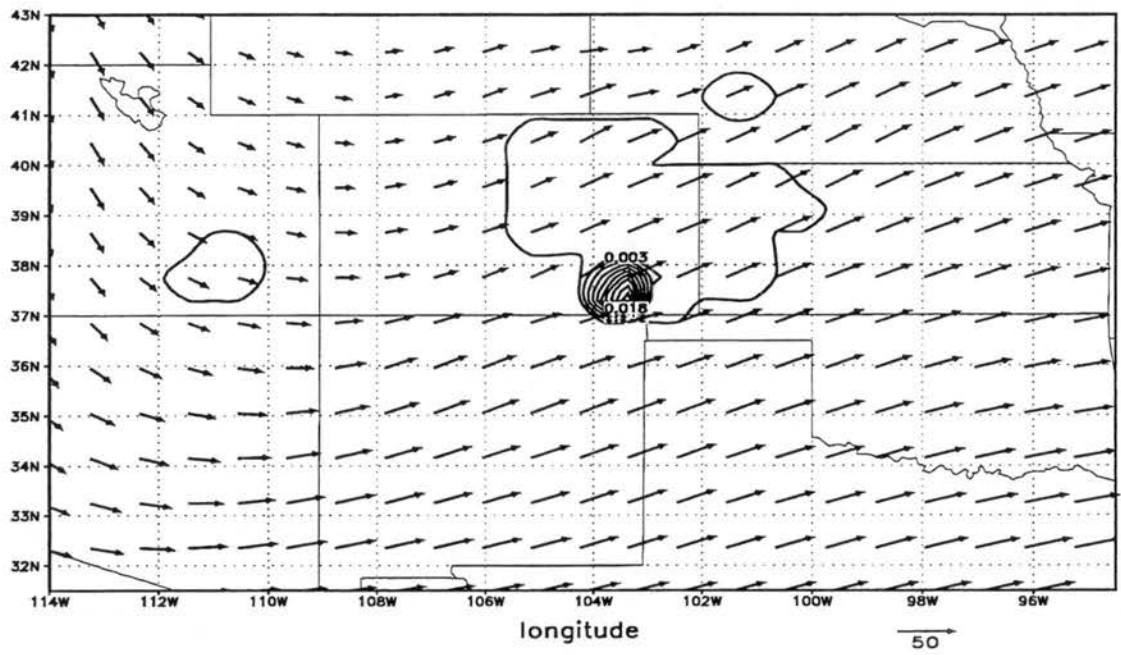
Figure 5.8: Condensate mixing ratio (kgkg^{-1}) and horizontal wind vectors at σ=11334m and t=00 UTC on Grid #2.

dew point gradient was present over Texas, indicating the position of the dryline. Equivalent potential temperature (θ_e) is a useful variable to define the position of the front and of the dryline (Figure 5.2a), because it incorporates the effects of both temperature and moisture. Surface and upper-air observations from 00 UTC were interpolated to Grid # 1 and used to compute θ_e (Figure 5.2b). A comparison of 5.2a and 5.2b shows that the model captured well the θ_e gradient and the wind shift across the surface front, as well as the position and location of the dryline over TX. Observations showed the dryline extending over the southern border of NM, but this feature was not captured by the model.

South of the front, surface winds were from the south, while north of the front they were from the east. Surface winds in southeast CO, the genesis region of the MCS, were southeast. They were driven by the synoptic patterns and enhanced by a mountain–plains solenoid that developed during the day on the eastern side of the Rocky Mountains. This solenoid had been identified before (e.g., Tripoli and Cotton 1989a) as important in the generation of deep convection in eastern CO.

North-South cross sections of potential temperature (θ) and θ_e on Grid #2 are shown in Figures 5.3 and 5.4, respectively. At 00 UTC, just before sunset, a well mixed boundary layer with a height of 1.5 km was present over the whole domain. The boundary layer cooled towards the north. The position of the front is not easily identifiable in the potential temperature plot, but it is clearly visible in the θ_e plot, indicating again that the front was better defined as a moisture contrast than as a temperature contrast at this time. The boundary layer was well mixed everywhere in θ_e, but had higher θ_e's in the south.

A sounding (Figure 5.5) taken just ahead of the incipient storm (lat=37.5N, lon=102.7W) showed that the boundary layer was well-mixed. In this situation the source of air to the storm is expected to be located close to the ground.

Figure 5.6 shows that at σ=689m (850 hPa over central Kansas) the θ_e gradient was still present along the KS/OK border.

In upper levels, a pronounced trough was present at 700 hPa (Figure 5.7a — compare with observations displayed in Figure 3.9), bringing southerly winds to the genesis region in SE CO. At 500 hPa (Figure 5.7b) the winds were SW. From quasi-geostrophic dynamics, which is valid at the spatial scale discussed here, we know that the genesis region, on

the downwind part of a trough, is favorable for upward motion and convective development (Holton 1992). It is interesting to note that this is not very common in episodes of MCC formation. According to Maddox (1983), the most common environment for MCC development is beneath a 500 hPa ridge, under the influence of a small short wave.

At this time, the MCS on which we will focus was beginning to develop. Deep convection was already present in SE CO, as seen in the plot of condensate mixing ratio at a height of 11334 m (Figure 5.8). At the surface (Figure 5.2a), condensate mixing ratio was associated with the developing MCS and with convection in the western slope of the Rocky Mountains. Some condensation was also present in northern CO, associated with the upslope flow in that location.

5.1.2   MCS on Grid #4 at 00 UTC

In this section we will examine the characteristics of the MCS on the cloud scale. To do that, we will focus on the results on Grid #4.

Figures ?? and ?? show the condensate mixing ratio at the surface, for t=23 UTC on 5/12 and 00 UTC on 5/13, respectively. The incipient MCS was composed of several cells. At 00 UTC, two strong cells could be seen. The vertical motion on the top of the PBL (1473 m) and in mid-levels (6056 m) is shown in Figures ?? and ??, respectively. The vertical motion cells were roughly co-located with the cells of surface condensate. The vertical motion was elongated in low levels, and more cellular in upper levels. This feature is commonly observed in modeling studies of convection. In low levels forcing occurs in a band, caused either by mesoscale forcing, or by a cold pool (as in this case). Although the forcing occupies a large region, only a subset of that region evolves into deep convection.

A comparison of Figures ?? and ?? shows that the southern cell at 00 UTC was the product of the merger of two previously independent cells, triggered by vertical motion that developed on the edge of each cell's cold pool. The cold pools were quite strong: 4°C colder than the environment. This can be attributed to the large condensate mixing ratio at the
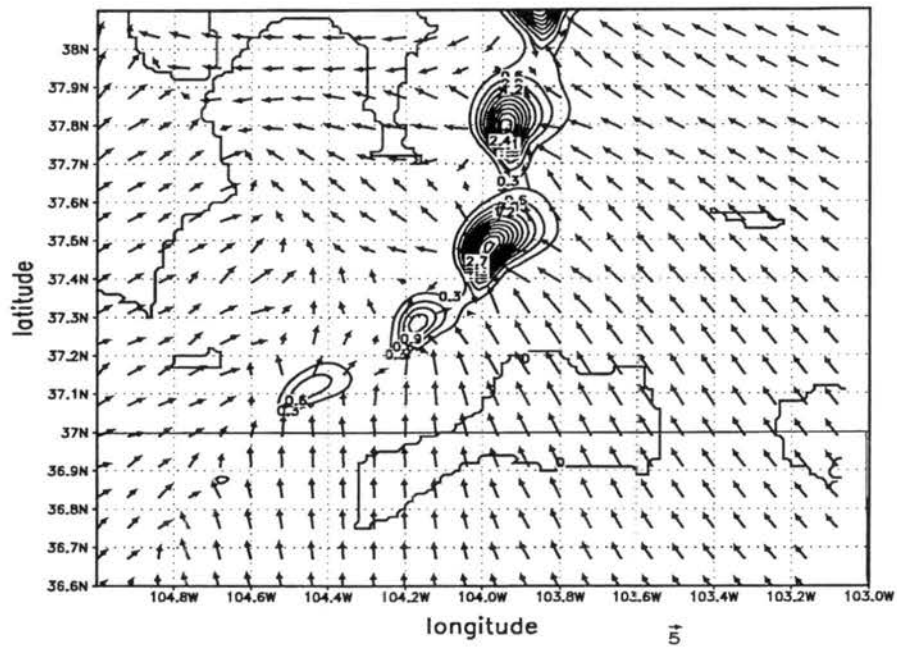
Figure 5.9: Condensate mixing ratio (contoured) (gkg^{-1}) and horizontal wind vectors at σ=48m and t=23 UTC of 5/12 on Grid #4.
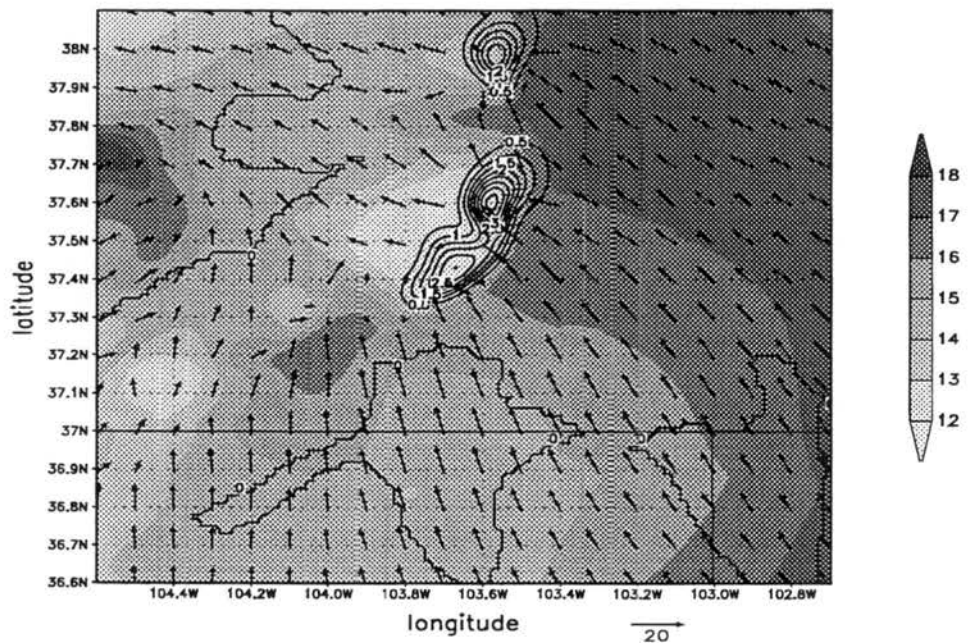
Figure 5.10: Temperature (shaded) (C), condensate mixing ratio (contoured) (gkg^{-1}) and horizontal winds vectors at σ=48m and t=00 UTC on Grid #4.
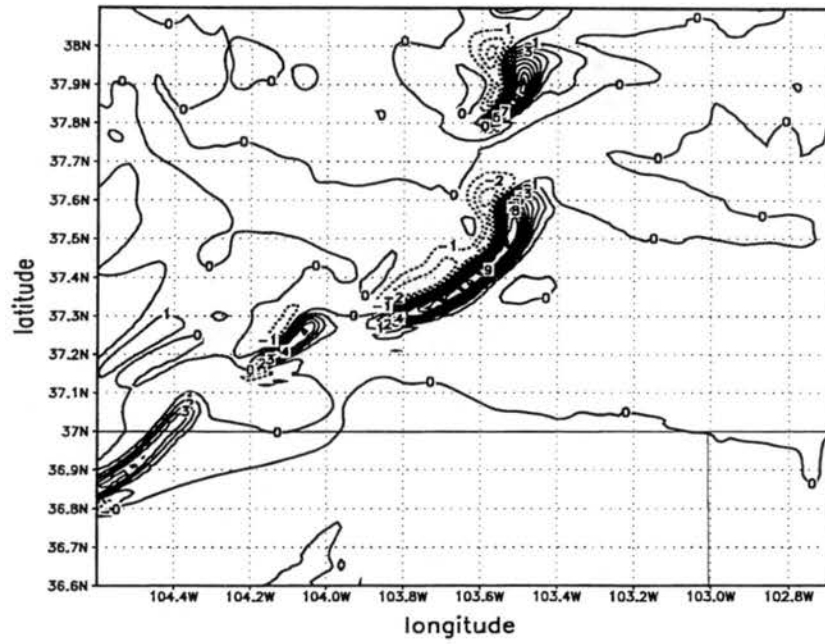
Figure 5.11: Vertical velocity at σ=1473m (ms^{-1}) and t=00 UTC on Grid #4.
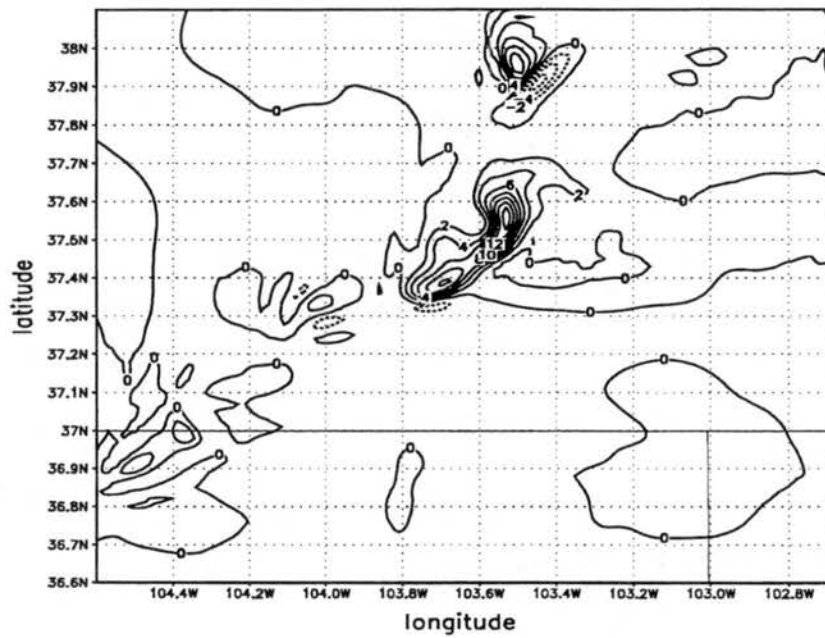
Figure 5.12: Vertical velocity at σ=6056m (ms^{-1}) and t=00 UTC on Grid #4.
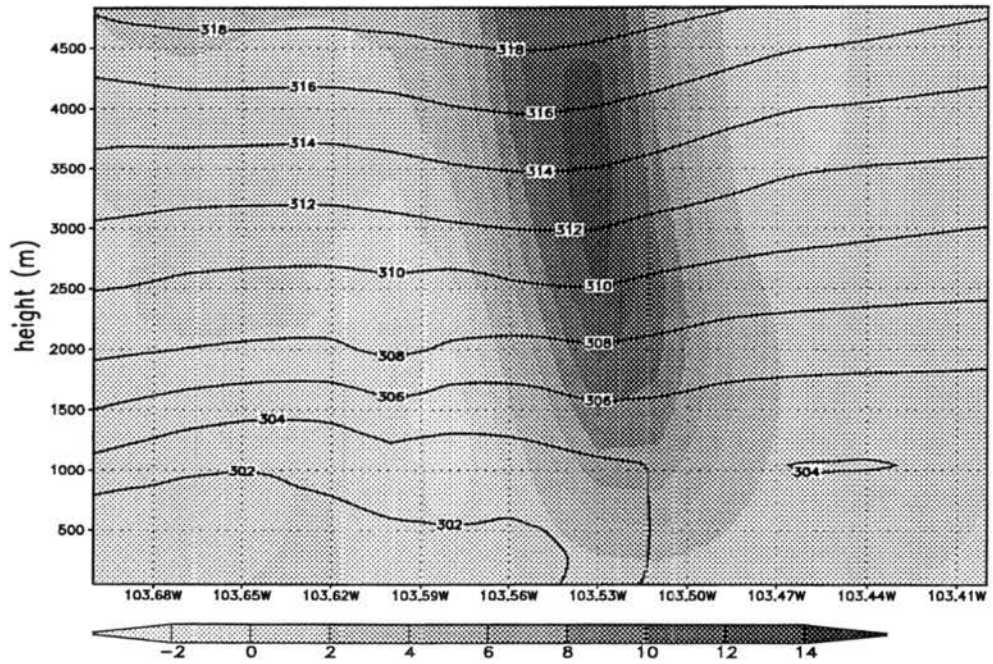
Figure 5.13: Vertical cross section through lat=37.5N of vertical velocity (shaded) (ms^{-1}) and potential temperature (contoured) (K) at t=00 UTC on Grid #4.
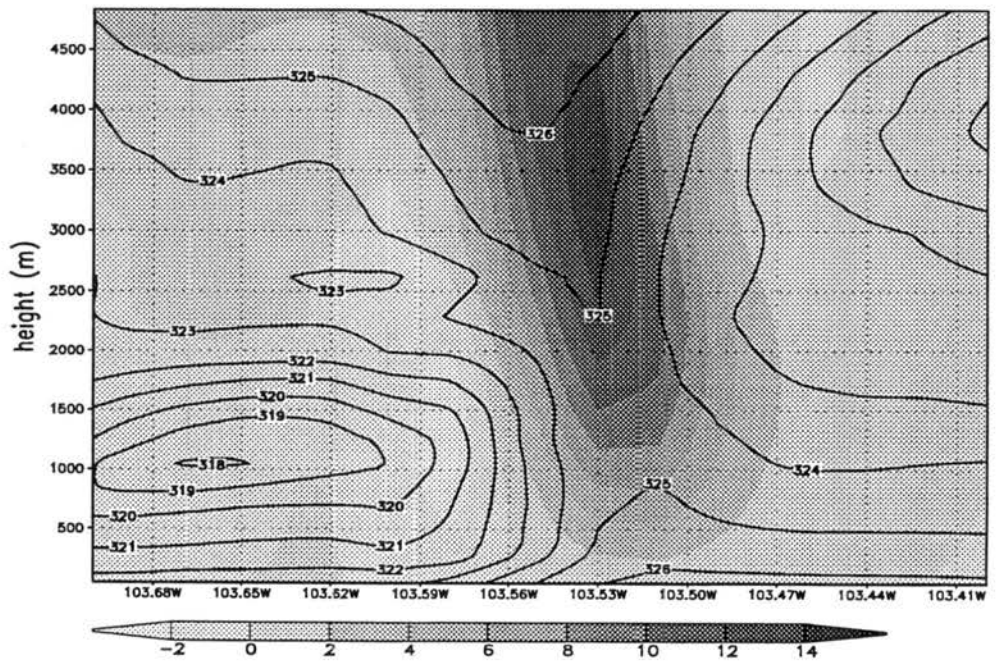
Figure 5.14: Vertical cross section through lat=37.5N of vertical velocity (shaded) (ms^{-1}) and equivalent potential temperature (contoured) (K) t=00 UTC on Grid #4.
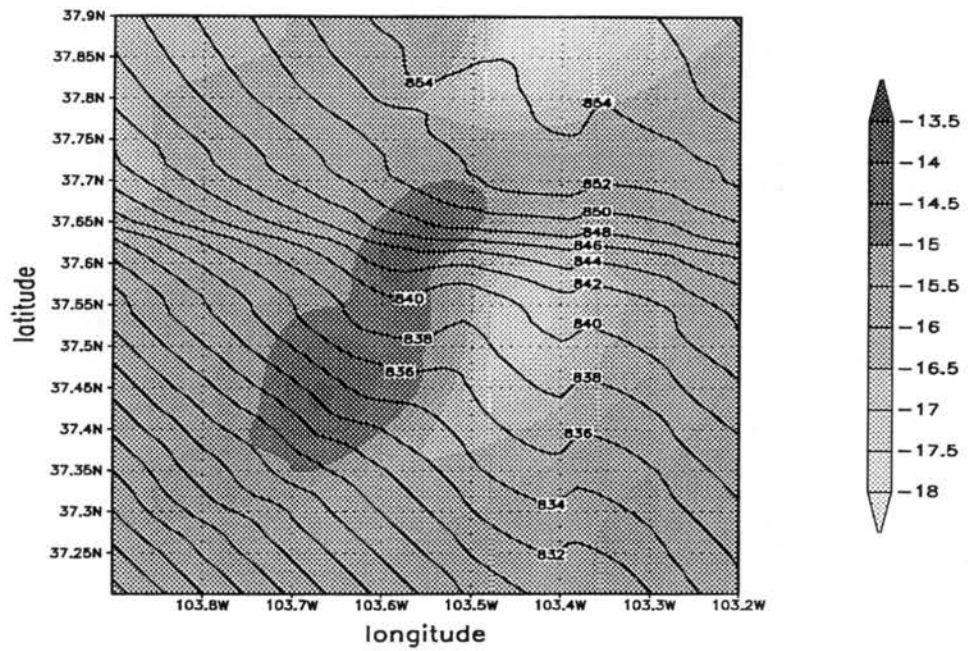
Figure 5.15: Perturbation pressure (shaded) and hydrostatic pressure (contoured) (hPa) at σ=48m and t=00 UTC on Grid #4.
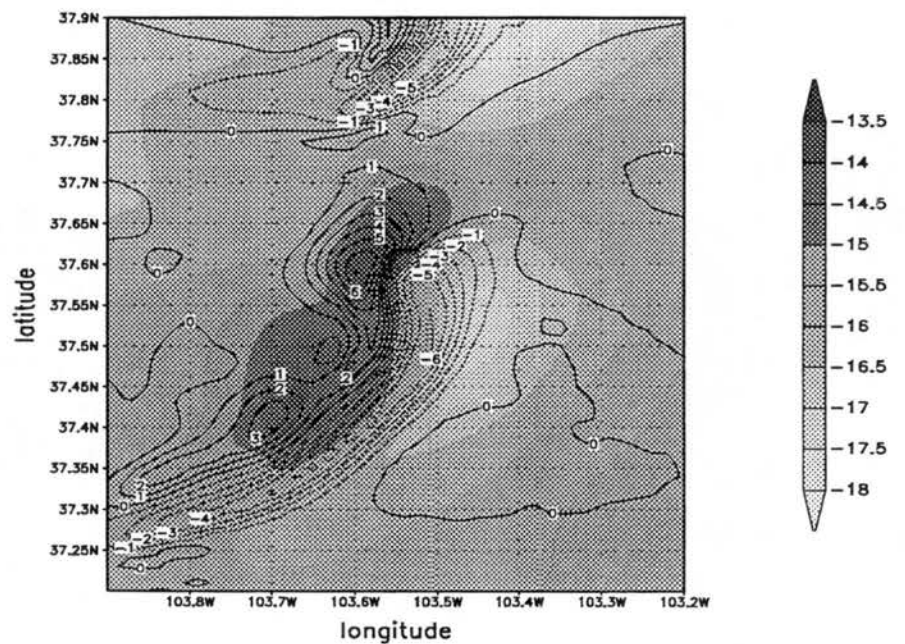
Figure 5.16: Perturbation pressure (shaded) (hPa) and horizontal divergence (contoured) $((1000s)^{-1}))$ at σ=48m and t=00 UTC on Grid #4.
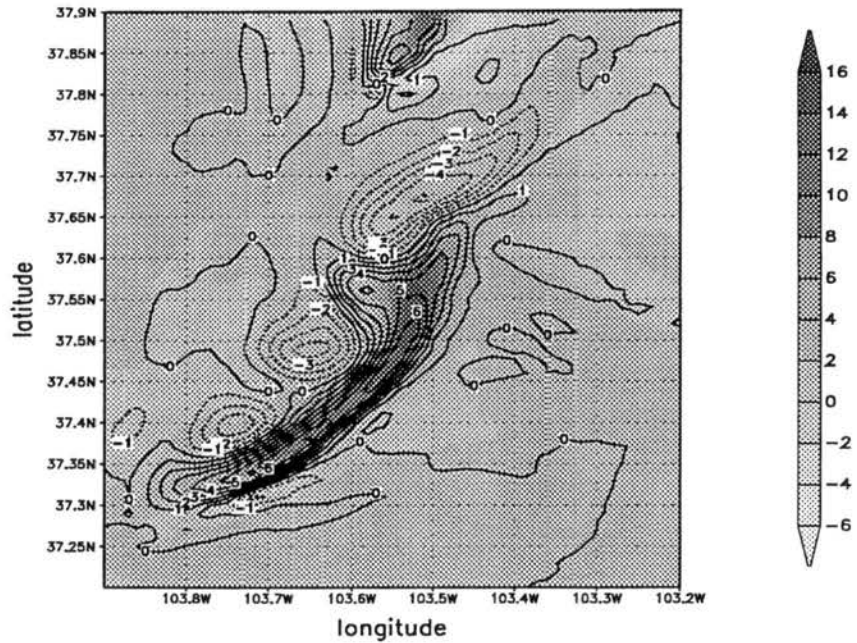
Figure 5.17: Vertical velocity (shaded) (ms^{-1}) and vertical vorticity ((1000s)$^{-1}$) at σ=3381m and t=00 UTC in Grid #4.
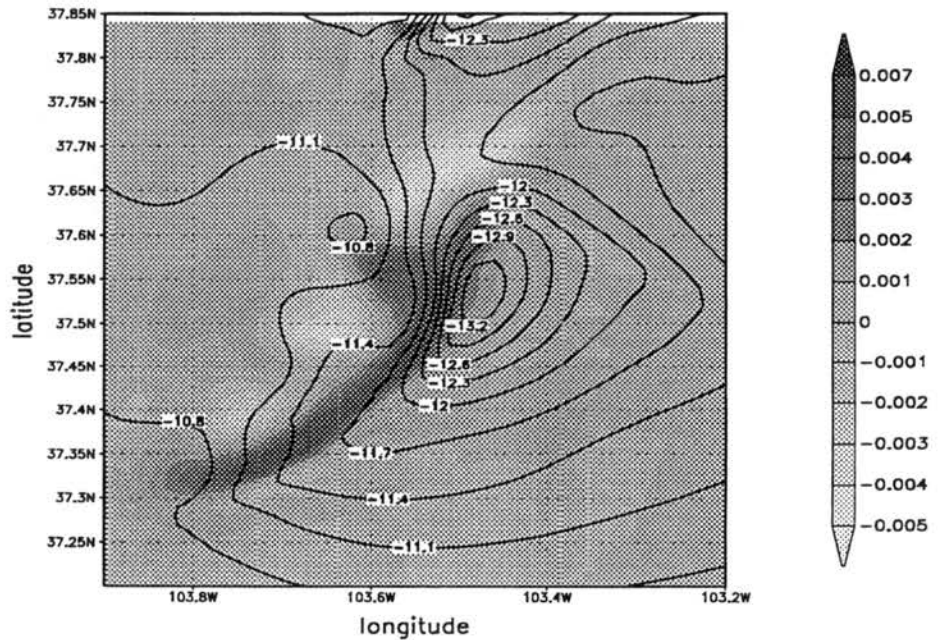
Figure 5.18: Vertical vorticity (shaded) (s^{-1}) and pressure perturbation (contoured) (hPa) at σ=3381m and t=00 UTC on Grid #4.
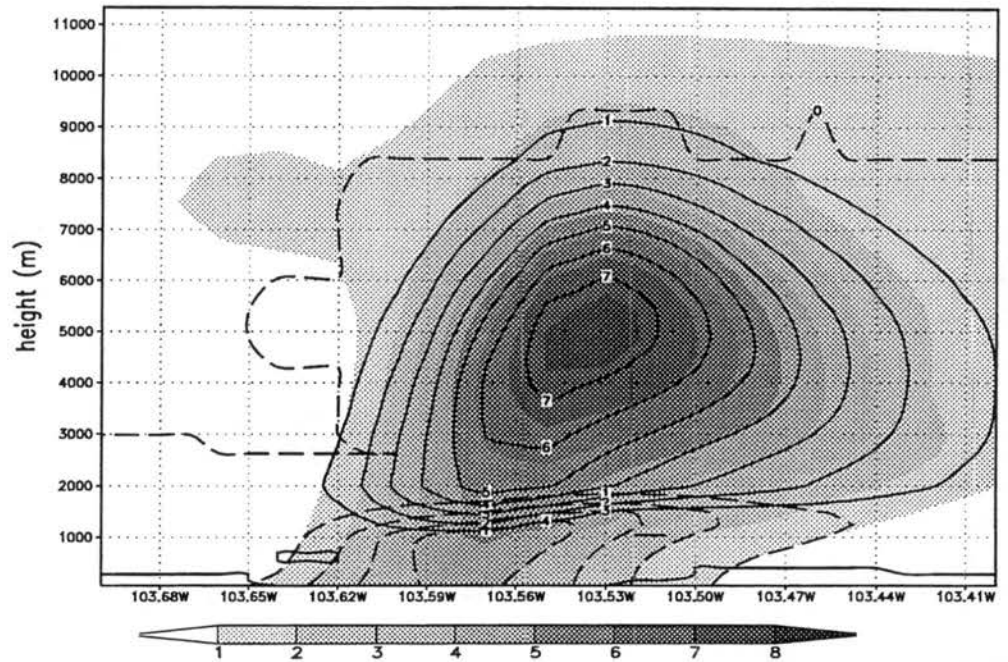
Figure 5.19: Vertical cross–section through latitude 37.6N of condensate mixing ratio (shaded) (gkg^{-1}), hail mixing ratio (solid contours) (gkg^{-1}) and rain mixing ratio (dashed contours) (gkg^{-1}) at=00 UTC on Grid #4.
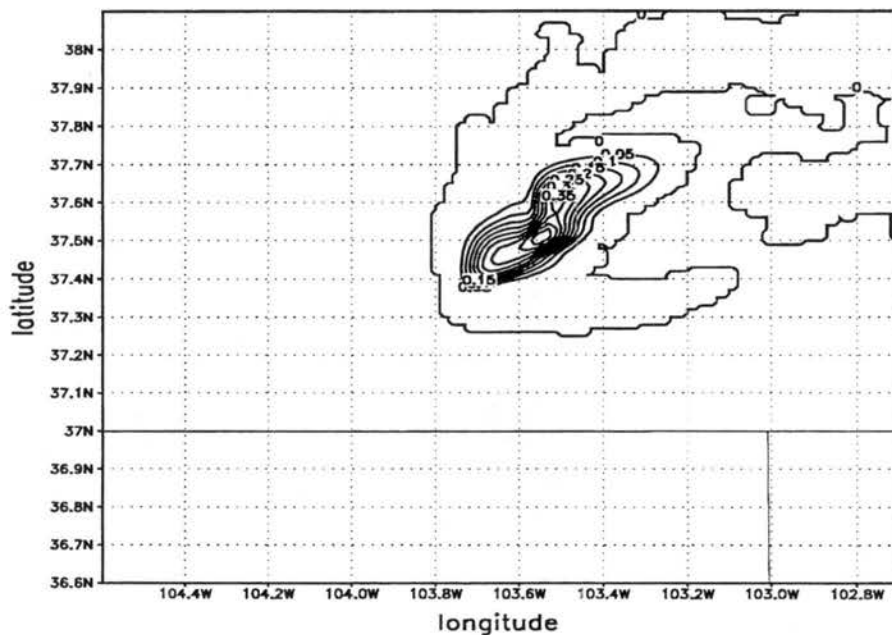
Figure 5.20: Condensate mixing ratio (gkg^{-1}) at σ=11334m and t=00 UTC on Grid #4.

the ground at this time (Figure 5.10), which has a maximum of 4.2 gkg^{-1}, corresponding to a rain rate[1] of 111.6 mmh^{-1}.

The edge of the cold pool was very well defined on the east and southeast sides of the storm (Figure 5.10) and poorly defined towards the back of the storm. The sharp gradient on the east side of the storm was due to the convergence of the environmental flow with the storm outflow. The environmental flow was from the southeast at 7 ms^{-1}. Inflow to the storm occurred along its eastern leading edge. The outflow diverged from the center of the cold pool with a maximum speed of 17.6 ms^{-1} (Figure 5.10). Divergence was stronger from the north part of the cold pool, and spread towards the north and back of the storm, and also against the southeast inflow.

In order to examine more closely the characteristics of the dominant cell, the next figures will be presented on a subdomain of Grid #4. Another view of the cold pool is presented in Figure 5.13, an east-west cross-section through the coldest part of the pool, showing potential temperature and vertical motion. Again, we note the cold pool was 4°C colder than the environment. The cold pool was most intense up to 500 m above the ground, but its influence extended up to 1200 m. The vertical motion at low levels was located at the leading edge of the cold-pool, indicating that triggering of vertical motion by the cold pool was an important mechanism in the dynamics of the storm at this time. The vertical motion leaned slightly upwind with height.

A plot of θ_e (Figure 5.14) through the same cross-section shows that the high values present in the cloud ($\sim 326K$) were also present in the lower boundary layer ahead of the storm, indicating that the source of air for the storm was located close to the surface. Although θ_e is not strictly a conservative variable due to ice physics, precipitation and turbulence, it can be used as a qualitative tracer. A region of low-valued θ_e, indicative of the cold pool, was present just behind the main updraft.

---

[1] To convert rain mixing ratio to rainfall rate, we use the density of the air and water, and the fall speed of the hydrometeors. The expression used is $R = q \frac{\rho_{H_2O}}{\rho_{air}} V_t \frac{3600s}{1hr} \frac{1000mm}{1m}$; where R is the rain rate in $\frac{mm}{h}$, q is the dimensionless rain mixing ratio and V_t is the terminal fall speed of the rain hydrometeors.

The pressure perturbation[2] pattern at the surface was composed of two mesohighs associated with condensational cooling due to the previously distinct storms, and one large mesolow ahead of the two mesohighs (Figure 5.15). This mesolow had both hydrostatic and non-hydrostatic components [3]. A hydrostatic pressure trough was present on the western side of the mesolow, due to the warm column corresponding to the convective cloud. This hydrostatic low pressure at the surface accelerated the winds in the horizontal, towards the cloud. The acceleration caused a wind divergence east of the hydrostatic low, and mass evacuation in low levels (Figure 5.16). The non-hydrostatic component of the low was associated with this mass evacuation.

In mid levels (3381 m) an updraft with magnitude of 17 ms^{-1} and a vorticity band with magnitudes up to 6.0×10^{-3}s^{-1} (Figure 5.17) were present. Several mechanisms can be responsible for the high vorticity obtained. There was some previously existent vertical vorticity in the environment, both earth's vorticity and relative vorticity, since the system developed on the downwind side of an upper level trough. The environmental vorticity could have been stretched in the cloud to yield at least part of the high positive vorticity observed. However, negative relative and absolute vorticity existed upshear of the band of positive vorticity, indicating that stretching was not the only mechanism to cause the high values of vorticity present. The second mechanism is tilting of environmental horizontal vorticity. This storm developed in an environment with strong shear (Figure 5.5). Winds were easterly at the surface, southerly at low levels and southwesterly at upper levels. The shear therefore had a westerly component and, in low levels, also a southerly component. The vorticity associated with this shear pointed north in upper levels and east in low levels. As discussed by Davies–Jones (1984), this low level vorticity can be tilted by an easterly storm inflow to produce vorticity that is positively correlated with the vertical motion, that

---

[2]Pressure perturbation is the total pressure in a given grid point minus the reference state pressure in that grid point. By subtracting the reference state, the influence of topography on the pressure is eliminated. The actual millibar value of the pressure perturbation is meaningless, since the reference state is arbitrary, but the pressure perturbation gradient does represent meteorological features.

[3]Using the model density, a hydrostatic pressure was computed ($P_H = \int_{sfc}^{top} \rho g dz$). When this is subtracted from the total pressure, a non-hydrostatic component of pressure is obtained.

is, positive/negative vorticity co–located with the updraft/downdraft. Convective updrafts and downdrafts may also have tilted storm generated shear. The rear inflow that developed in the storm amounted to westerly shear between the surface and the maximum inflow and easterly shear above it. Davis and Weisman (1994) noted that this shear was tilted in the formation of bookend vortices in a squall line. Finally, baroclinically generated vorticity may have been produced in the edge of the cold pool and tilted up, as discussed by Weisman et al. (1996). Although this mechanism may have been important during the development of the MCS discussed here, it probably was not active in its nocturnal phase, when a cold pool was not present, as will be discussed later in this Chapter.

At this time a pressure perturbation minimum of (2 hPa lower than the surroundings) was present in mid-levels in the center of the storm (Figure 5.18). The pressure, which had hydrostatic and non-hydrostatic components, was co-located with the northern part of the band of high relative vorticity, and extended ahead of it.

A cross-section through lat=37.6N revealed the distribution of some microphysical species within the storm. More than 8.0 gkg^{-1} of condensate existed in the core of the cloud at a height of 5 km (Figure 5.19). The liquid species were cloud water (not shown) and rain. Rain, only present below 2 km, was a large contribution to total condensate at low levels, and was the only microphysical species to reach the ground. Cloud water existed in the core of the updraft, up to a height of 9 km. This was the height of the $-40°$C isotherm. In colder temperatures homogeneous freezing occurs, so liquid water was not found. The most important species in the core of the cloud was hail, which is the only mixed–phase species in the parameterization. Melting and shedding of hail are the most important sources of rain water. The other species (snow, aggregates, graupel and pristine ice) appeared in much smaller quantities. Although in smaller quantities, they were important constituents of the mid and upper level anvil. The anvil's top was at a height of 11 km and (using a threshold of 0.2 gkg^{-1}) extended mainly to the frontal flank of the storm. Another view of the anvil can be seen in Figure 5.20, a plot of total condensate at upper levels.

5.2 Evolution of the storm from 00 to 06 UTC

From 00 to 06 UTC the cell described in the last section persisted as a long-lived evolving entity.

The first important evolution was the consolidation of the merger of the two cells that occurred between 23 and 00 UTC. The northern cell in the merger became the dominant one, and the southern cell lost strength, so the system became more round, with what looked like an appendage on the southern end (01 UTC) (Figure 5.21). Between 02 and 05 UTC, the cell grew in horizontal dimensions, to become more elongated in the north-south direction (Figures 5.22 through 5.25). The surface condensate mixing ratios for the dominant cell increased during this period, from a maximum of 4.2 gkg^{-1} (111.0 $mmhr^{-1}$) at 00 UTC to a maximum of 5.4 gkg^{-1} (144.0 $mmhr^{-1}$) at 05 UTC. The dominant cell moved from 252° with a speed of 12.6 ms^{-1}. However, each different cell present in Grid #4 moved with its own velocity, so the cell organization changed shape. By 23 UTC (Figure 5.9) the cells were aligned almost in the north-south direction. Differential motion between the cells caused the alignment to be almost east-west by 04 UTC (Figure 5.24a).

A comparison with the radar observations (Figure 3.3) showed that the model captured successfully the presence of three cells of deep convection on the CO-KS border, although it did not capture the area of light rain reaching the surface to the north of the line of convective cells. The location of the anvil, displayed in a plot of upper level condensate (Figure 5.26) compared well with the satellite image (Figure 3.4), which indicated deep clouds in the CO-KS border.

At mid-levels (z=3381m), the condensate mixing ratio in the dominant cell also increased, from 7.3 gkg^{-1} at 00 UTC to 8.3 gkg^{-1} at 06 UTC. Since after 03 UTC (Figure 5.27) a bulge forward in the condensate was quite prevalent. Also, the cloud developed a comma shape, with a horizontally broader region of condensate to the north and a narrow extension to the south. A region of well-defined rear inflow separated the comma head from the tail. Actually, there is a striking resemblance between the morphology of the storm depicted in Figures 5.22 through 5.25 and the bow-echo HP supercell shown in Figure 2.10, especially frames 5a and 6a.

Figure 5.21: Condensate mixing ratio (gkg^{-1}) and horizontal wind vectors at σ=48m and t=01UTC on Grid #4.
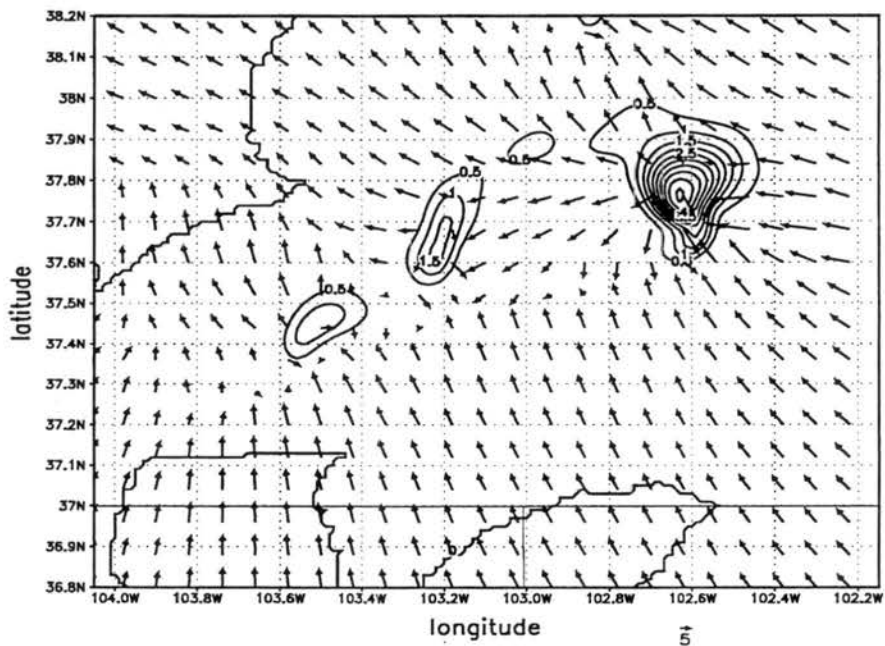
Figure 5.22: Condensate mixing ratio (gkg^{-1}) and horizontal wind vectors at σ=48m and t=02UTC on Grid #4.
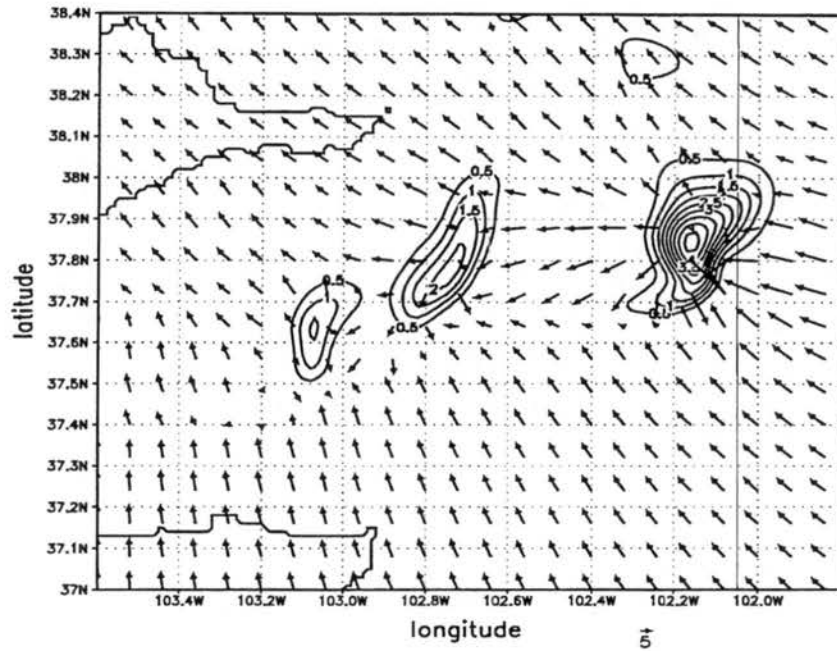
Figure 5.23: Condensate mixing ratio (gkg^{-1}) and horizontal wind vectors at σ=48m and t=03UTC on Grid #4.
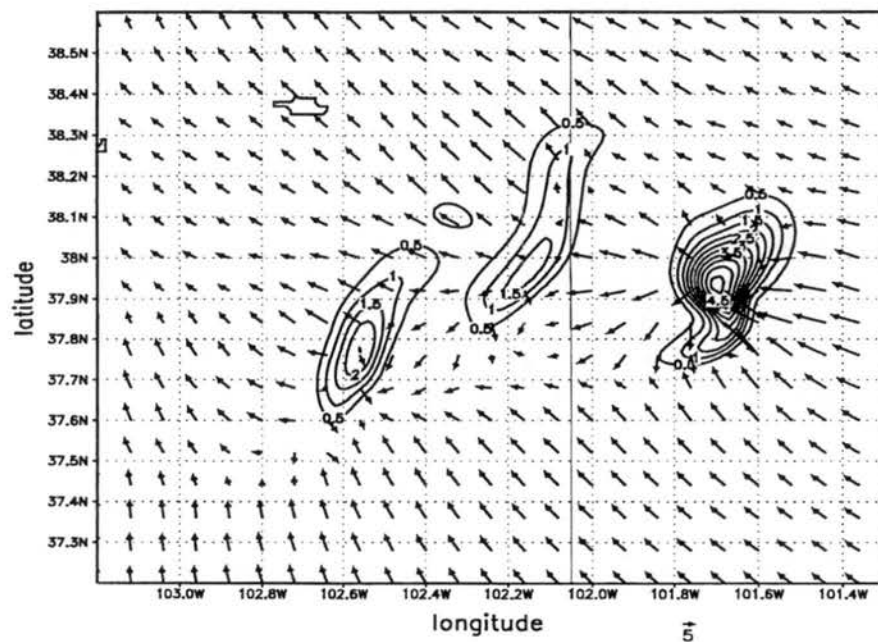
Figure 5.24: Condensate mixing ratio (gkg^{-1}) and also horizontal wind vectors at σ=48m and t=04UTC on Grid #4
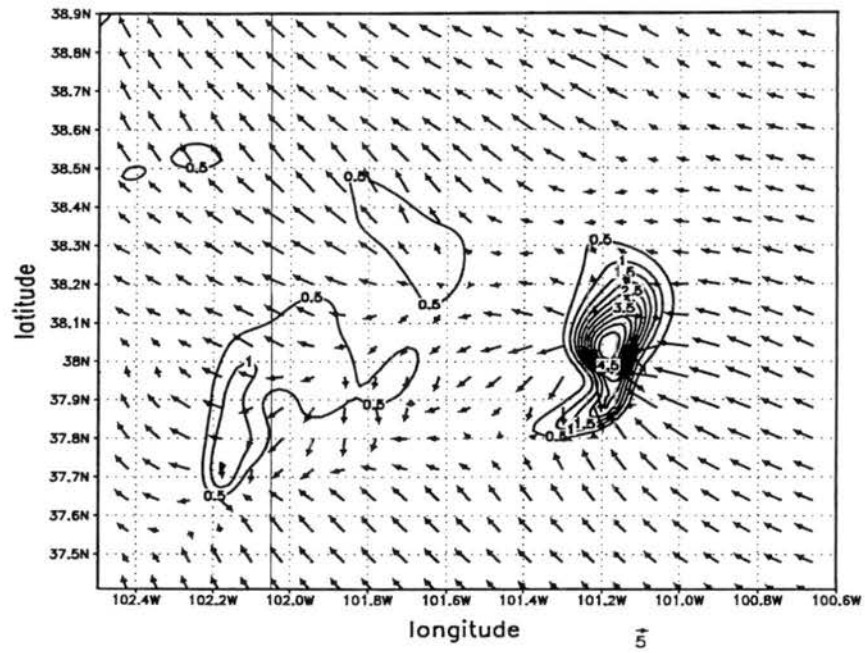
Figure 5.25: Condensate mixing ratio (gkg^{-1}) and horizontal wind vectors at σ=48m and t=05UTC on Grid #4.
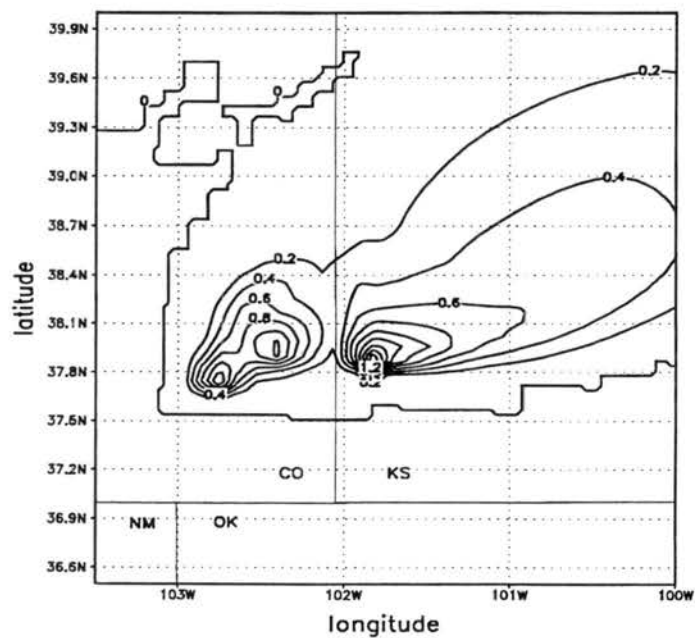
Figure 5.26: Condensate mixing ratio (gkg^{-1}) at σ=10,334m and t=0330UTC on Grid #3.
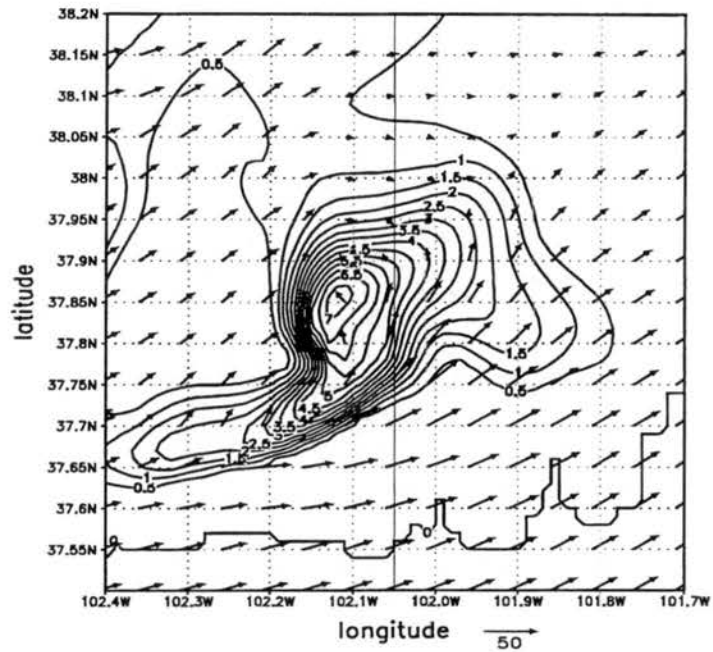
Figure 5.27: Condensate mixing ratio (gkg^{-1}) and horizontal wind vectors at σ=3381m and t=03UTC on Grid #4.
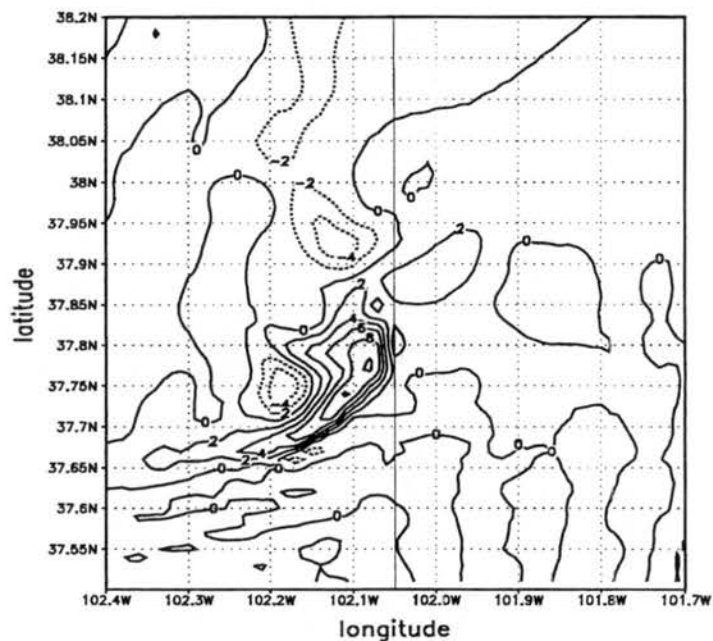
Figure 5.28: Vertical vorticity (contoured) ((1000s)$^{-1}$) at σ=3381m and t=03UTC on Grid #4.

Figure 5.29: Hydrostatic Pressure (shaded), pressure perturbation (contoured) (hPa) and horizontal wind vectors at σ=3381m and t=03UTC on Grid #4.

Figure 5.30: Time series of winds at σ=48m on Grid #4. The closed circles represent the maximum speed in the horizontal domain and the open circles, the maximum speed found in convective outflow. After 03 UTC they coincide.

During this period, the vorticity in the mesocyclone of the storm increased. At 00 UTC the maximum vorticity at $\sigma=3381$m was $5.0 \times 10^{-3}\text{s}^{-1}$ (Figure 5.33, and that increased to $9.0 \times 10^{-3}\text{s}^{-1}$ by 03 UTC (Figure 5.44).

Together with the changes in mid-level vorticity, came changes in perturbation pressure. At 03 UTC, the pressure perturbation in the center of the storm at a height of 3381m was 5 hPa lower than the surroundings (Figure 5.45). Roughly 2 hPa out of those 5 could be traced to hydrostatic pressure. Although a deepening in the low pressure and an increase in vertical vorticity occurred, their centers were not co-located, which would be expected if the non-linear process described by Equation 2.21 was predominant. The linear process (Equation 2.18) and other processes that were neglected in the derivation of those two equations were also acting, causing a complex superposition of effects.

A time series of the strongest surface winds in Grid #4 is shown in Figure 5.46. The outflow winds increased almost steadily from 15.5 ms^{-1} at sunset (02 UTC) to 25.0 ms^{-1} at 0330 UTC, The winds then remained high, and reached a maximum at 06 UTC with 26.5 ms^{-1} from the northwest, decaying after 0930 UTC. The observed strong winds reported by STORM DATA started only at 0530 UTC and lasted through 1030 UTC, therefore the model was a few hours early in the production of strong winds.

5.3 MCS at 06 UTC

5.3.1 Large Scale Environment

By 06 UTC (midnight local time) the temperatures had cooled considerably, both north and south of the front (Figure 5.47). The surface front remained quasi-stationary along the KS-OK border. Significant changes occurred in the lower troposphere over northern TX, OK and KS. Stronger southerly winds developed, causing northward advection of high-θ_e air.

Figures 5.48 and 5.49, cross-sections of θ and θ_e respectively, show that the PBL had become more stable, and that air with high θ_e was being advected north on top of the surface stable air by the southerly low level jet.
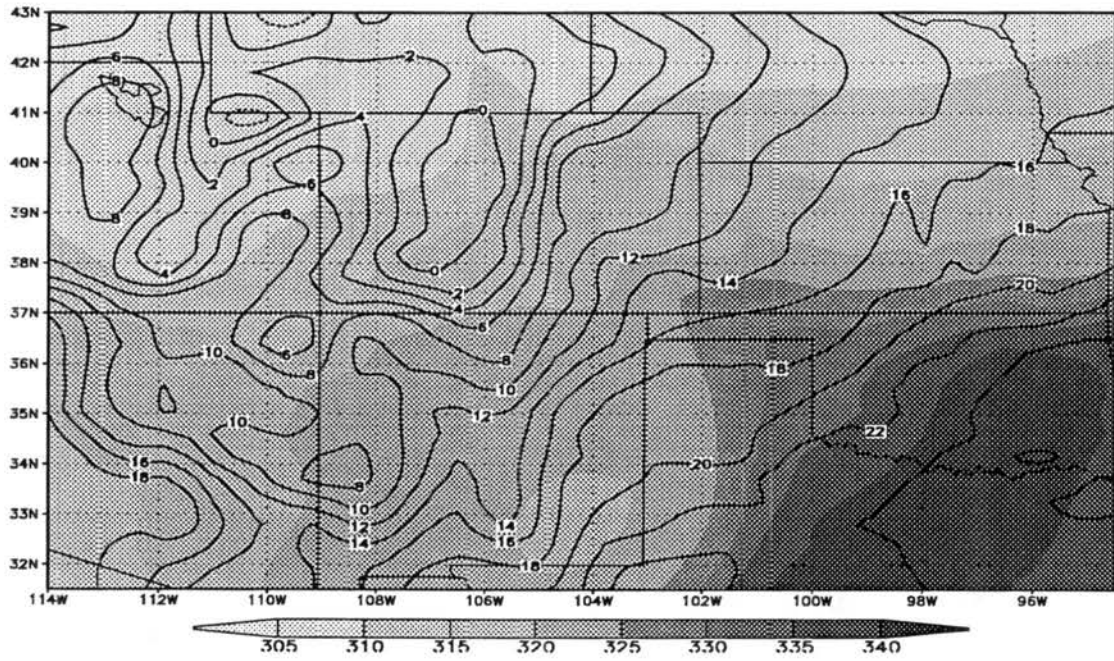
Figure 5.31: Equivalent potential temperature (shaded) (K) and temperature (contoured) (C) at σ=48m and t=06 UTC on Grid #2.
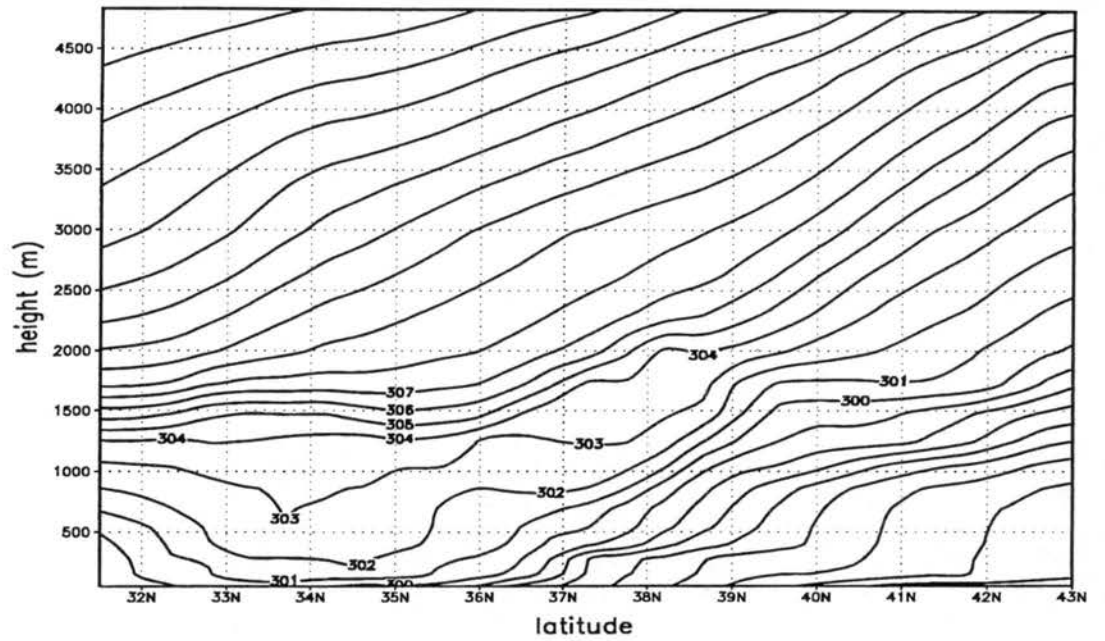
Figure 5.32: Vertical cross section through lon=97.5W of potential temperature (K) at t=06 UTC on Grid #2.
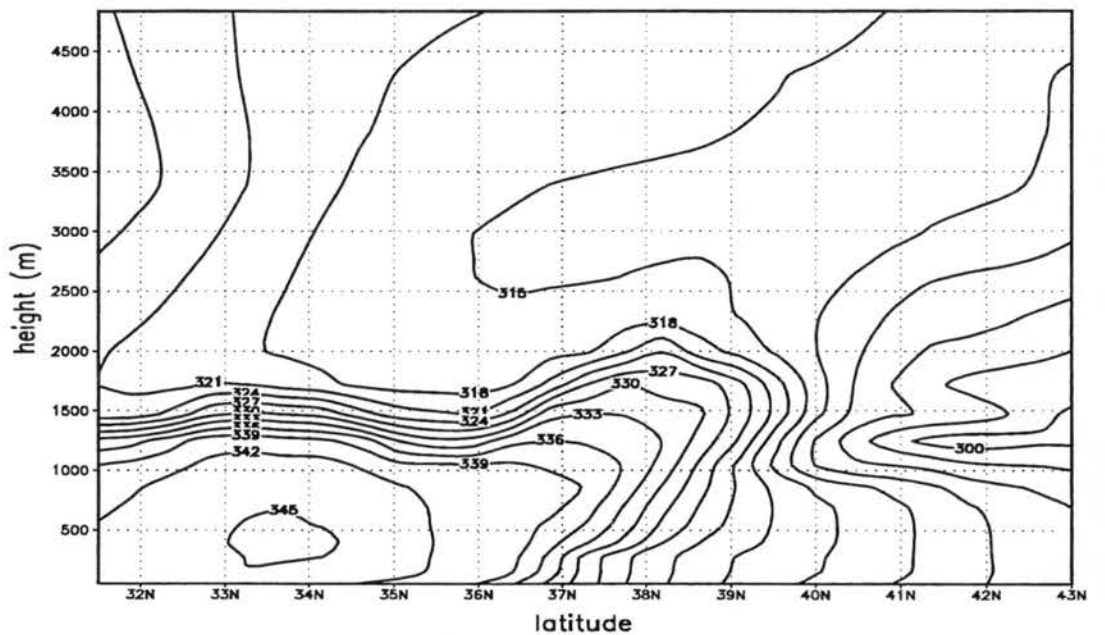
Figure 5.33: Vertical cross section through lon=97.5W of equivalent potential temperature (K) at t=06 UTC on Grid #2.
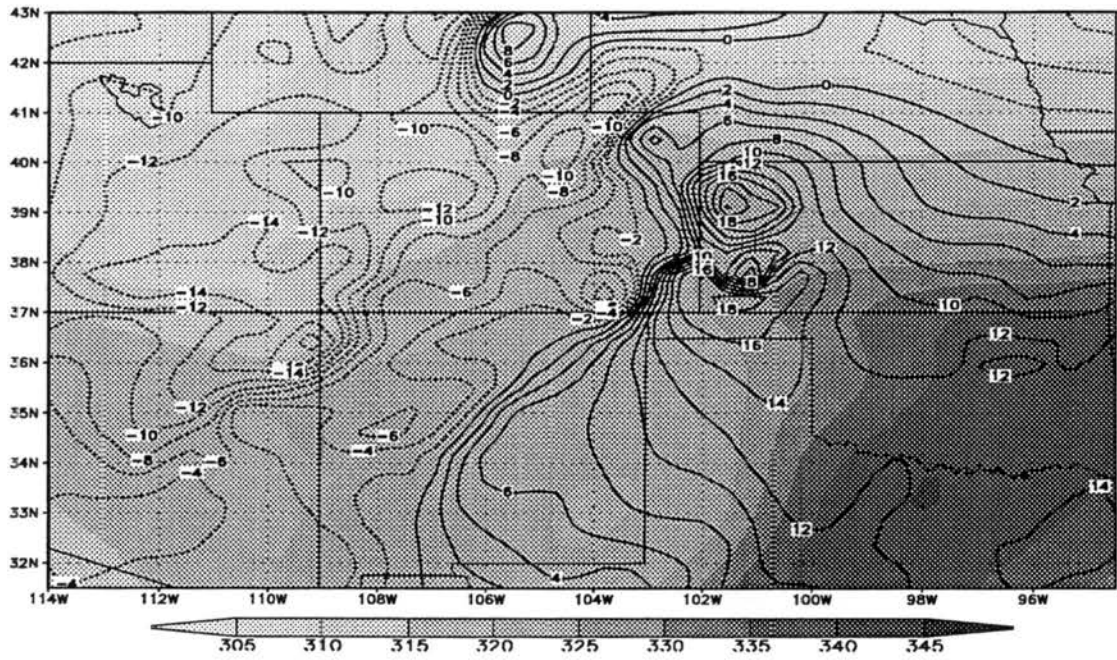
Figure 5.34: Equivalent potential temperature (shaded) (K) and meridional speed (contoured) (ms^{-1}) at σ=689m and t=06 UTC on Grid #2.
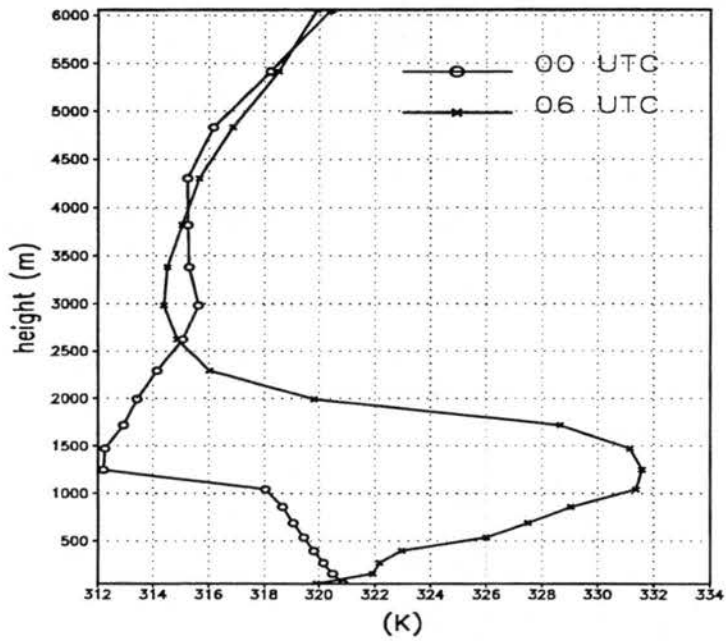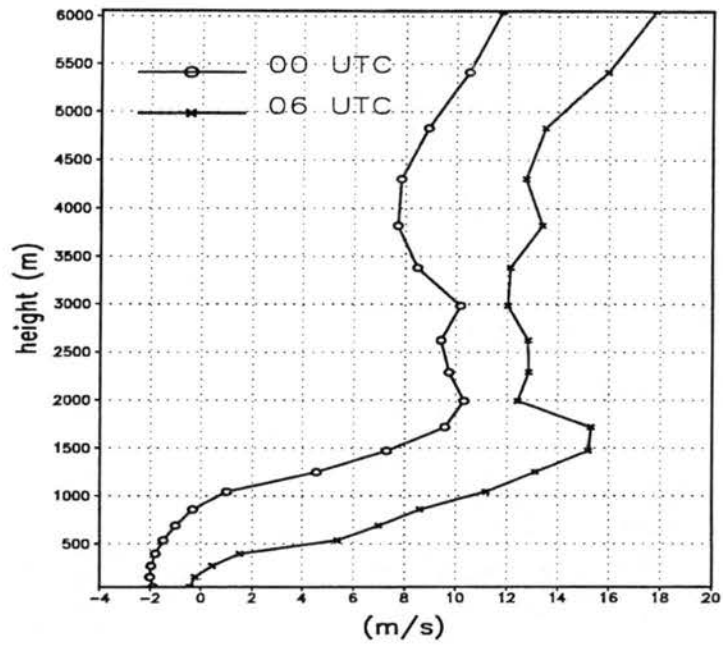
Figure 5.35: Vertical profile at lat=38N, lon=98W at times 00 and 12 UTC on 5/13 from Grid # 4 of a) Meridional wind (ms^{-1}), b) Equivalent potential temperature (K).
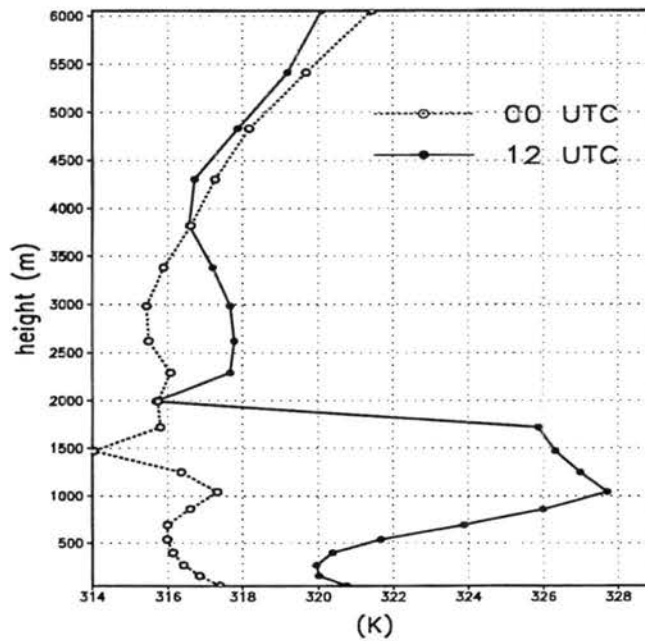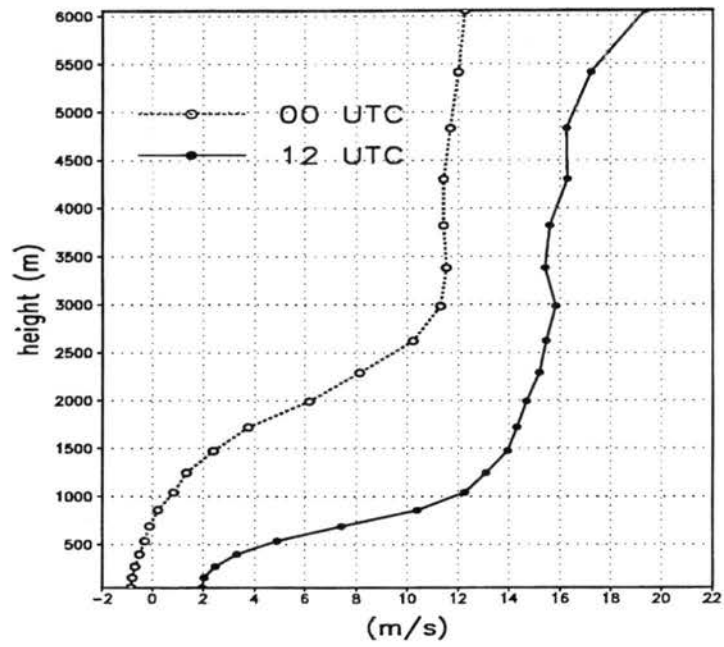
Figure 5.36: Vertical profile of observations interpolated to lat=38N, lon=98W at times 00 and 12 UTC on 5/13 of a) Meridional wind (ms^{-1}), b) Equivalent potential temperature (K).

Plots of meridional wind and θ_e at a height of 689 m (equivalent to 850 hPa over central KS) are shown in Figure 5.34. Comparison with the same plots at 00 UTC (Figure 5.6) shows that the winds increased about 5 ms^{-1} over Kansas, while θ_e increased around 4K.

The development of the jet is easily seen in Figure 5.35a, which shows a vertical profile of meridional winds at lat=38N and lon=98W. Between 00 and 06 UTC, meridional winds increased at all heights due to the eastward movement of the upper level trough. At 1200 m AGL, the meridional wind increased by 8.5 ms^{-1}. This had a large impact in θ_e, which increased by 19K at this level (Figure 5.35b). The large θ_e increase occurred between the surface and 2500 AGL. Above that level, the θ_e profile remained unaltered. This increase is comparable to the observed. Figure 5.35 can be compared with Figure 5.36, which shows observed rawindsonde data interpolated to a model column at the same latitude and longitude. A comparison shows that the model represented well the observed environment, with a local maximum increase in meridional winds and θ_e between 1000 and 1500m. The figures are useful only for a qualitative comparison however, because there are no observations at 06 UTC, so the 12 UTC data were used, and also because rawindsonde data were spatially smoothed by an interpolation to the model's Grid # 1.

5.3.2 MCS on Grid #4 at 06 UTC

We now focus on the characteristics of convection at 06 UTC.

A plot of condensate at the surface (Figure 5.37) shows three cells aligned E-W across the CO-KS border. A comparison of this plot with the radar summary for 0535 UTC, which also depicted three regions of deep convection on the border (Figure 3.5), indicates that the model was representing well the dominant patterns of convection. At the surface, the leading cell was characterized by large amounts of rain mixing ratio (5.4 gkg^{-1} or 114 mmh^{-1}.

The vertical motion at the heights of 1473 and 6056 m is shown in Figure 5.38. The vertical motion in the leading cell increased considerably since 00 UTC. Again, features like condensate water and vertical motion are elongated near the surface and more cellular in upper levels.

A cold pool was not present in low levels at this time. As shown in Figure 5.39, some cold air has been left behind during the afternoon phase of the system, but at this time there was an area of warm temperatures associated with the main downdraft of the dominant cell. A cross section through this warm spot (Figure 5.40) showed that the downdraft is co-located with the pocket of high temperatures. Therefore, the warm spot can be attributed to subsidence warming. Similar warm spots have been observed by other authors (e.g., Bernstein and Johnson 1994) in situations of convection over a stable boundary layer.

Figure 5.41 shows a cross-section through latitude 38.1N on Grid #4, depicting θ and vertical motion up to a height of 4.6 km. The PBL was stably stratified and a cold pool was not present. Therefore, cold-pool dynamics is not too dominant as the mechanism responsible for storm propagation at this time.

One interesting characteristic of this cell can be seen in a θ_e plot (Figure 5.42). In the convective cloud, a very high θ_e core was present at mid-levels ($\sim$ 328 K). At the surface, a region of relatively low θ_e was present ($\sim$ 324 K), both ahead and behind the storm. The low θ_e ahead of the storm, in low levels, indicated that surface air was not being ingested by the storm. This situation contrasts with that obtained at 00 UTC (Figure 5.14), in which similar values of θ_e were found on the surface ahead of the storm and in the core of the storm. At this time, values of θ_e consistent with those found in the core of the storm existed at the top of the shallow stable layer, suggesting that the storm had an elevated source of air.

Strong surface outflow (26 ms^{-1}) (Figure 5.43) was found in the region where the down-draft reached the ground. The pattern of the outflow was not as symmetric as it was at 00 UTC (Figure 5.10). Instead, the prevalent outflow was from the northwest, converging with the southeast environmental winds ahead of the storm. Some of the divergent winds also had a northeast direction. Outflow to the north was almost non-existent at this time. This pattern is consistent with that found in the derecho case of 2–3 August, 1981 documented by Schmidt and Cotton (1989) and modeled by Schmidt (1991), as shown in Figure 2.14b.

Figure 5.43 shows the pressure perturbation and the surface winds. The strongest out-flow originated on a meso-high located on the northwest side of the storm, and accelerated towards a mesolow located just ahead of the main rain shaft. The outflow did not converge
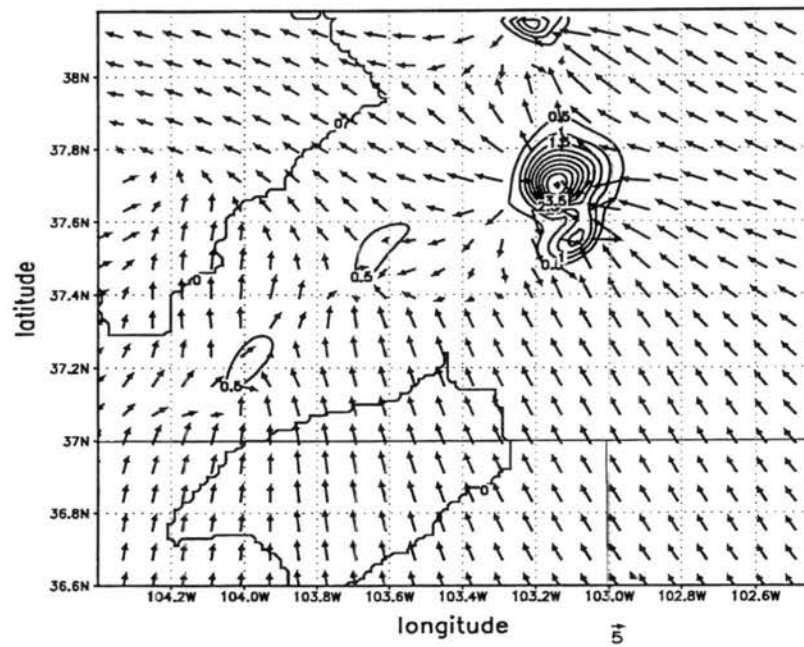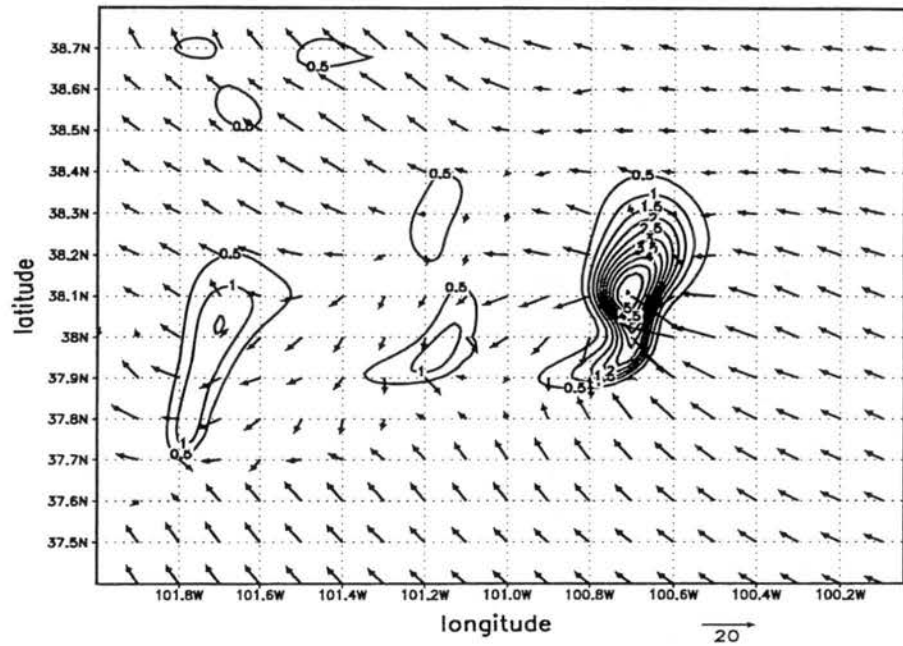
Figure 5.37: Condensate mixing ratio (gkg^{-1}) and horizontal wind vectors at σ=48m at t=06 UTC on Grid #4.
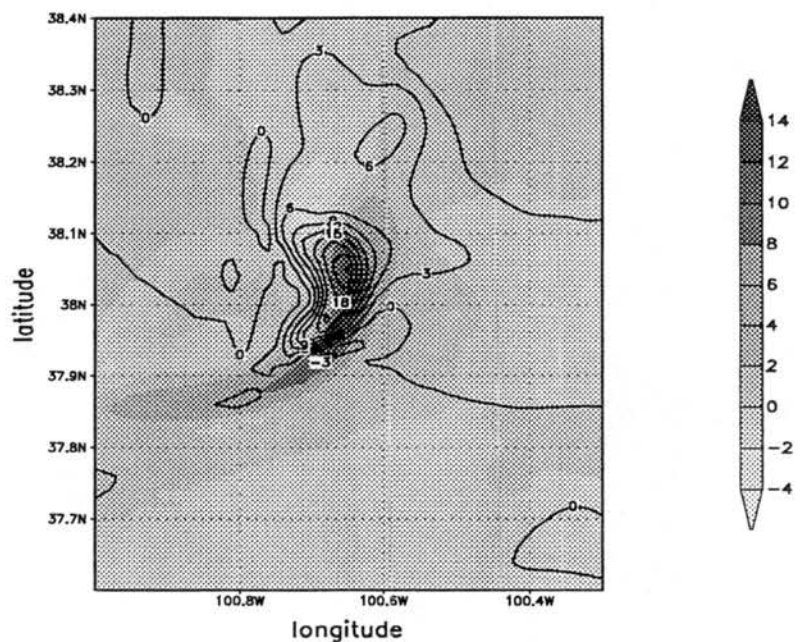
Figure 5.38: Vertical velocity at σ=1473m (shaded) and σ=6056m (contoured) (ms^{-1}) at t=06 UTC on Grid #4.
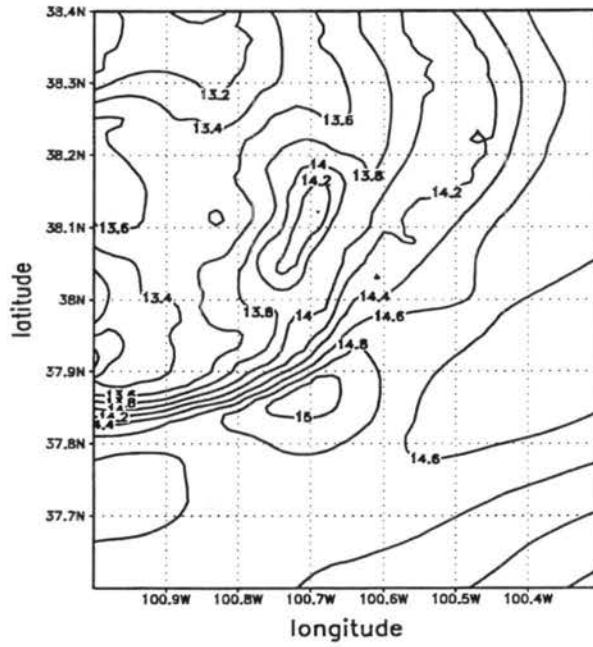
Figure 5.39: Temperature (C) σ=48m at t=06 UTC on Grid #4.
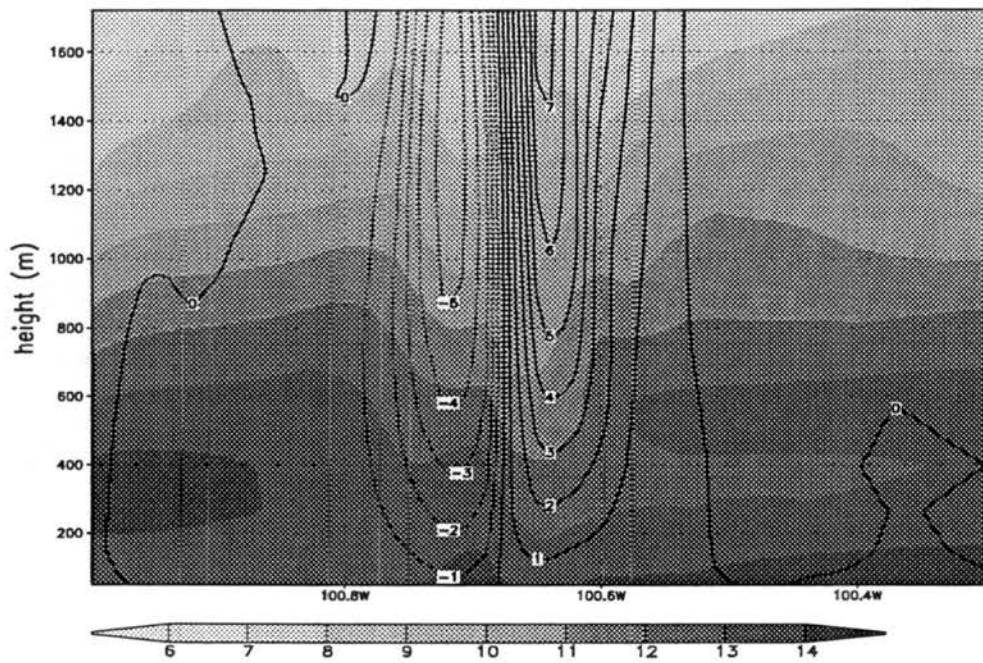
Figure 5.40: Vertical cross section through lat=38.1N of temperature (shaded) (C) and vertical velocity (ms^{-1}) at t=06 UTC on Grid #4.

98
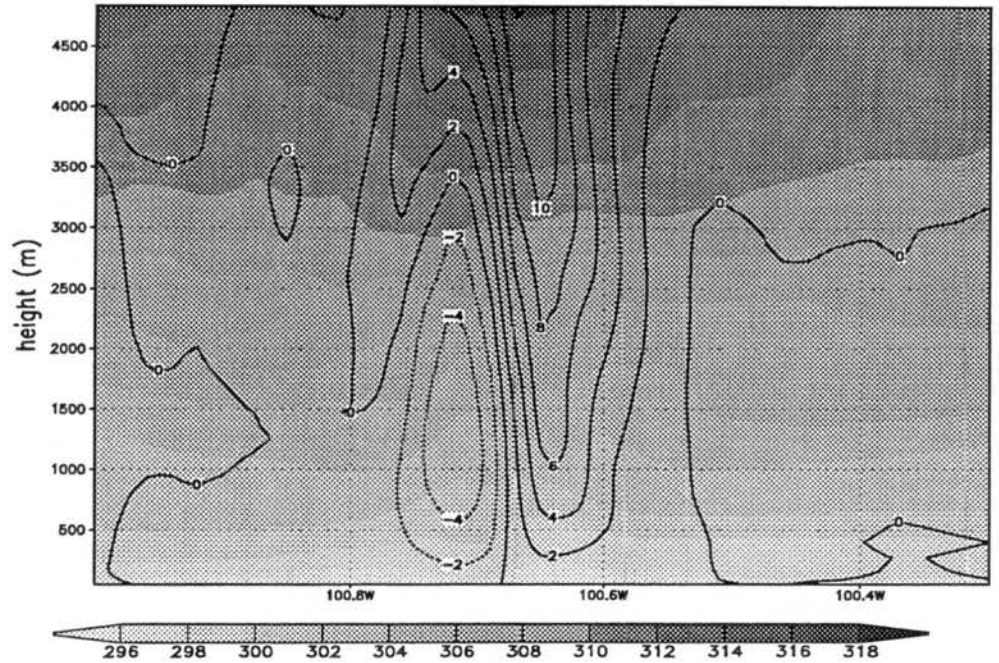
Figure 5.41: Vertical cross section through lat=38.1N of potential temperature (shaded) (K) and vertical velocity (ms^{-1}) at t=06 UTC on Grid #4.
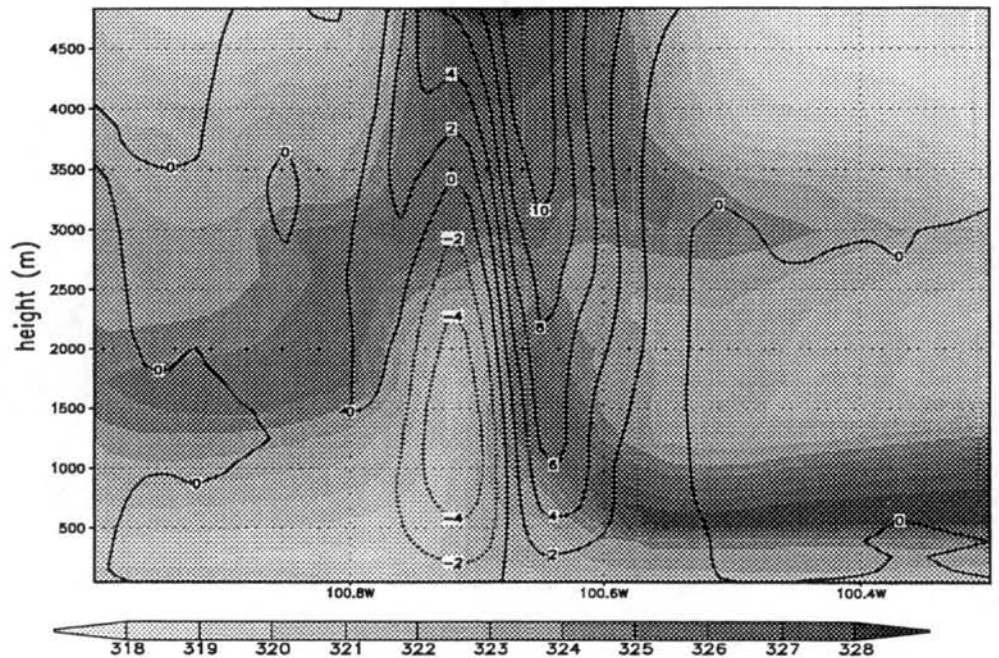
Figure 5.42: Vertical cross section through lat=38.1N of equivalent potential temperature (shaded) (K) and vertical velocity (ms^{-1}) at t=06 UTC on Grid #4.
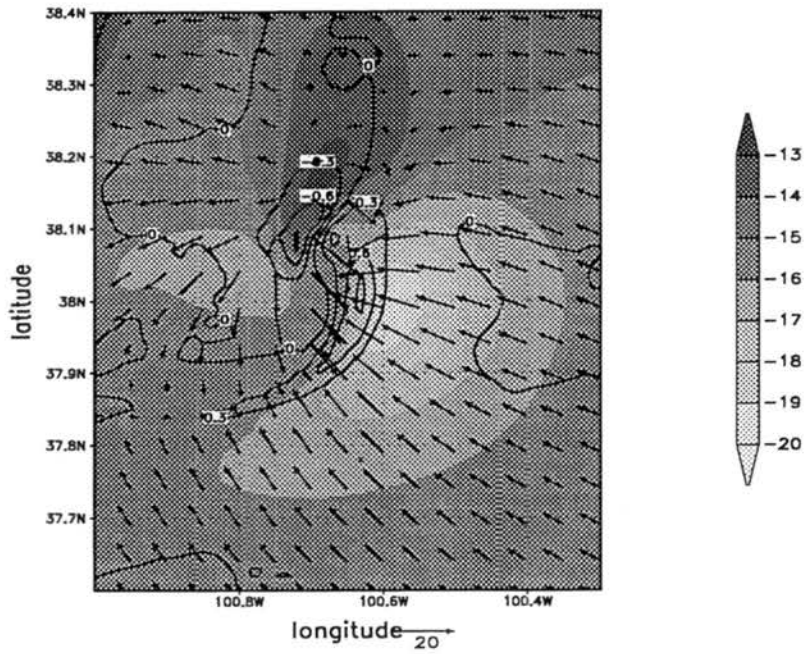
Figure 5.43: Perturbation pressure (shaded) (hPa), vertical velocity (ms^{-1}) and horizontal wind vectors at σ=48 and t=06 UTC on Grid #4.
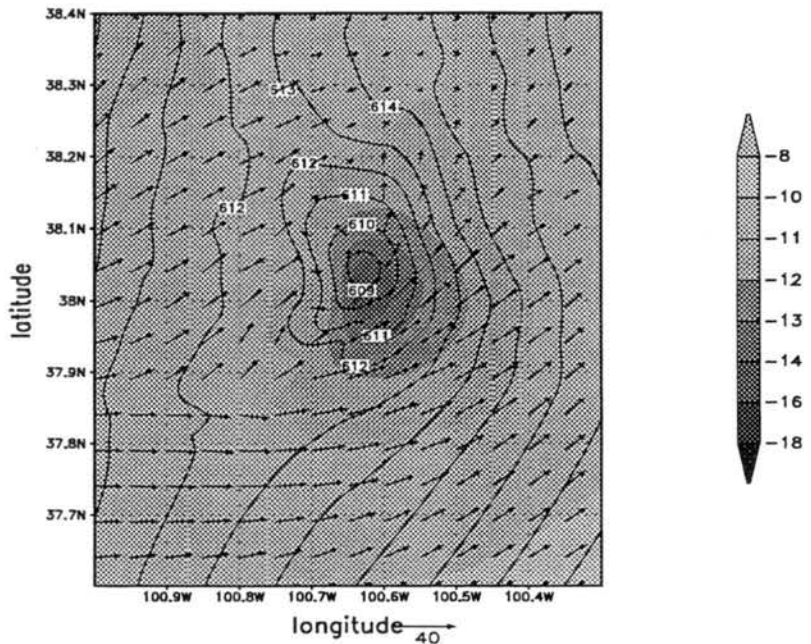
Figure 5.44: Perturbation pressure (shaded), hydrostatic pressure (contoured) (hPa) and horizontal wind vectors at σ=3381m and t=06 UTC on Grid #4.
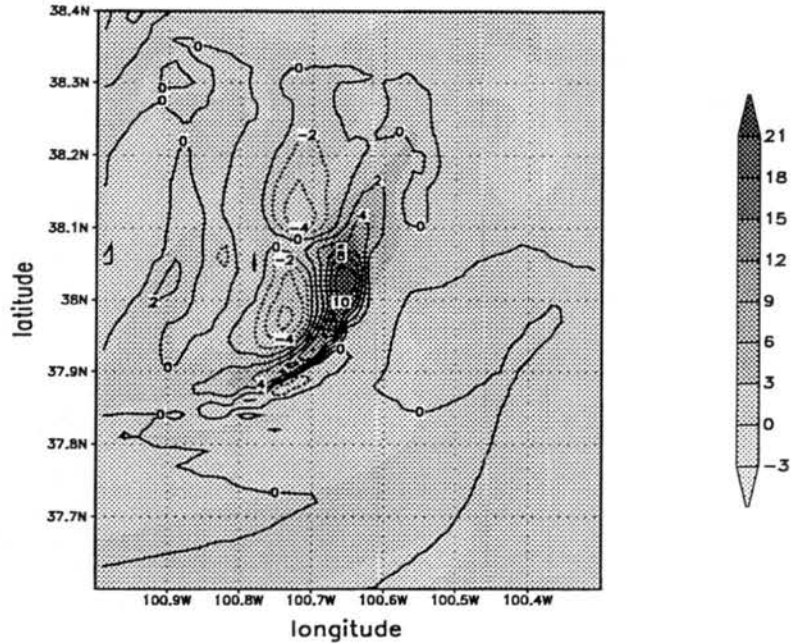
Figure 5.45: Vertical velocity (shaded) (ms^{-1}) and vertical vorticity ((1000s)$^{-1}$) at σ=3381m and t=06 UTC on Grid #4.

all the way to the center of the mesolow because of the strong opposing environmental winds. One might find surprising that the mesohigh at the surface roughly corresponds to the pocket of warm air, because in a MCS the mesohigh is commonly associated with air cooled by evaporation. However, the main contribution to this center of high pressure was dynamic and not hydrostatic. The dynamic pressure was associated with the strong deceleration of the downdraft. Wakimoto (1982) observed a similar increase in dynamic pressure at the surface, ahead of a spreading cold pool, caused by the deceleration of the cold air outflow.

In mid levels (3381m), the core of the storm was dominated by a center of low pressure 4.0 hPa lower than the surroundings (Figure 5.44). Hydrostatic effects were responsible for 3.0 hPa, while the remaining 1.0 hPa are due to dynamic effects.

At σ=4831m, a mesocyclone with vorticity of 1.0×10^{-2}s^{-1} was present (Figure 5.45) and co-located with the updraft. A center of negative vorticity was present behind the mesocyclone, with magnitude of -5.0×10^{-3}s^{-1}.

5.4 Summary

An overview of the simulation of the 12–13 May, 1985 MCS, responsible for strong winds in western Kansas, was presented in this chapter. The system began to develop in SE CO in the afternoon, and moved E-NE during the night at approximately 12.6 ms^{-1}. The system formed on the cold side of a front, on the downwind side of an upper level trough. During the afternoon, the PBL was warm and well mixed, and the storm fed on surface air.

During the night, radiative cooling caused the boundary layer to become stable. At this time, the source of air to the storm shifted from the surface to the top of the boundary layer. The air at the top of the boundary layer became much warmer and moister during the night due to the development of a nocturnal elevated jet, that transported high-θ_e air from lower latitudes.

The transition described above is mainly determined by radiative cooling and its influence on PBL characteristics. The radiative cooling becomes more important after sunset, when shortwave radiation at the surface ceases. The time series of the strongest surface winds (Figure 5.30) shows that the strongest winds began steadily increasing at 02 UTC. Considering that the sunset in central KS at this time of the year occurs at 02 UTC, a relationship might be expected between the environment, the storm structure and the strong outflow. This relationship will be explored in the next chapter.

Chapter 6

ANALYSIS

6.1 Introduction

In this chapter we examine the source of air for the updrafts and downdrafts of the modeled convective system, and the physical processes that led to the strong surface winds.

The source of air was determined using a Lagrangian (parcel) model. Parcels were initialized in the updraft and downdraft of the storm at different times, and advected backwards in time, so their origin could be assessed. Along the trajectories, properties of the parcel and balances of forces were computed. This aided understanding the path the parcels took and the physical mechanisms involved.

6.2 Trajectory model

A Lagrangian model (LM) was used to compute backwards parcel trajectories in the convective system. The LM was adapted from previous versions developed by Cotton et al. (1995) and Grasso (1996).

The winds used by the LM to advect the parcels are generated by the Eulerian model (RAMS). The analysis described here focused on two periods referred to as daytime and night-time. In each period, trajectories were followed for 30 to 45 minutes. When RAMS was run for each period, the values of the wind components in the Eulerian Grid # 4 were recorded every 15 seconds, which corresponds to twice the timestep on Grid # 4 (see Table 4.1).

Given the calculated winds at 15 second intervals, trajectories could be computed for any number of parcels. The trajectories for each parcel are referred to as P1, P2 etc.

The initial position of a parcel P in the Eulerian grid is given by $[x_P(t = 0), y_P(t = 0), z_P(t = 0)]$. The subsequent positions of the parcel are given by

$$x_P(t + \Delta t) = x_P(t) + u_P(t)\Delta t, \tag{6.1}$$

$$y_P(t + \Delta t) = y_P(t) + v_P(t)\Delta t, \tag{6.2}$$

$$z_P(t + \Delta t) = z_P(t) + w_P(t)\Delta t, \tag{6.3}$$

where (u, v, w) is the velocity at the position of the parcel, and Δt is the timestep for integration of the Lagrangian model, chosen to be 15s for the analysis done here. Δt is chosen to be small enough so that significant errors are not introduced by the use of the velocity from the beginning of the timestep (instead of some average between the beginning and end of timestep) and a convergence method is not necessary. To avoid errors, Δt is chosen sufficiently small so that the trajectories become independent of Δt.

The (u, v, w) to be used in Equations 6.1–6.3 are obtained from the Eulerian Grid. A tri-linear interpolation in space is done to provide values of (u, v, w) at the exact parcel position. Because we chose to have the timestep of the LM the same as the time interval in which the Eulerian data were recorded (15 seconds), interpolation in time of Eulerian data was not necessary. The LM took into account eventual grid movements of Grid #4, by computing the position of the parcel with respect to a stationary reference frame and not with respect to Grid #4.

The trajectories discussed in the following sections are representative of a larger set of trajectories that compose the updraft or the downdraft. Initially, hundreds of trajectories were computed for each time and location. As an example, Figure 6.1 shows 82 trajectories (out of 825 computed) of parcels that compose the night-time downdraft. Of this set, four were chosen to be discussed in Section 6.4.1.

Trajectories are displayed graphically by projections on the horizontal or vertical planes. In certain cases, Eulerian model fields will be superimposed on the trajectories to give a better idea of the position of the parcel with respect to the convective system (e.g., Figure 6.2). The reader must be cautious interpreting this last type of plot. The Eulerian model fields are a snapshot in time, while the trajectories may occur over a time period as long
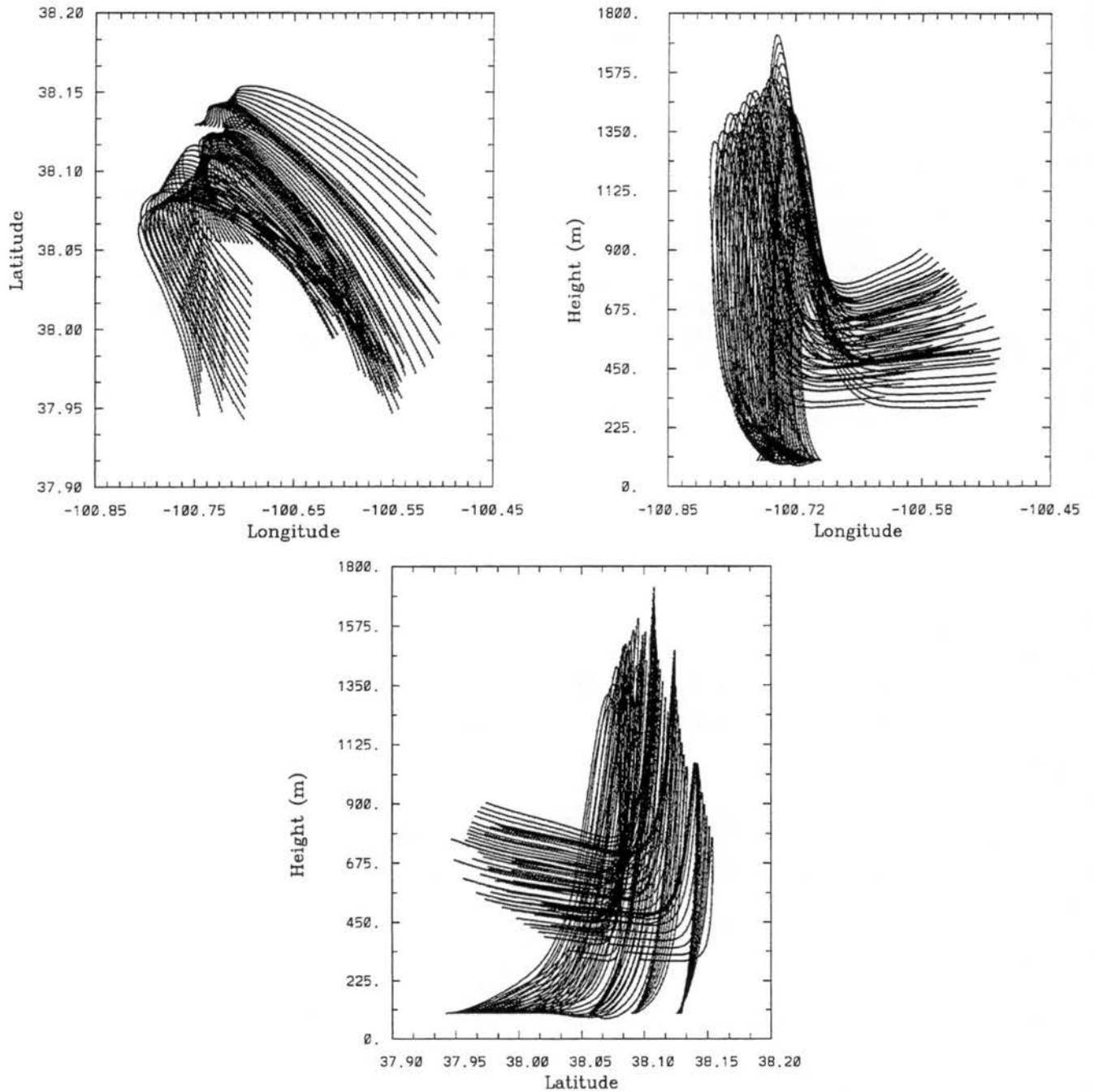
Figure 6.1: Projection of 82 trajectories of downdraft parcels t=0530 UTC to t=0600 UTC on the a) xy plane; b) xz plane; c) yz plane.

as 45 minutes. Therefore, the parcel was subject to the displayed Eulerian field only at a given instant during its trajectory. In general, the convective system is moving east, so if the storm were in steady state, the Eulerian model fields early in the lifetime of the parcel would be further west than late in the lifetime of the parcel.

6.3 Daytime Trajectories

In this section we will describe two sets of trajectories ending at 0045 UTC one terminating on a surface downdraft, and one terminating on a mid-level updraft, each lasting 45 minutes.

6.3.1 Daytime Downdraft

At the ground there are two separate regions of downdraft, as shown in Figure 6.2. One is located to the north and will be referred to as the Northern Downdraft (ND). The other covers a smaller area and resides in the bow region of the echo. It will referred to as Bow Downdraft (BD). These two downdrafts together resemble the rear flank downdraft (RFD) in a classic supercell thunderstorm. This convective cell does not have a forward flank downdraft (FFD), that is, a downdraft at the surface located ahead of the storm. This is due to the absence of precipitation ahead of the main updraft. In the BD, speed and downdraft are well-correlated but to the northwest, the highest surface speed occurs between the ND and the updraft.

The trajectory analysis shows that parcels that end up in the ND and BD have different histories. Figure 6.3 shows three trajectories, P1 through P3, superimposed on the surface vertical motion and condensate mixing ratio. The thick lines in the figure are the projection, on the horizontal plane, of the parcels' trajectories. P1 and P2 end up in the ND, and P3 ends up in the BD.

Projections of the 3 parcels' trajectories on the xy, xz and yz planes are shown in Figure 6.4. Parcels that end up in the ND (P1 and P2) start their trajectories east of the storm, and follow the southeast flow. P3, that ends up in the BD, originates closer to the storm. It initially moves towards the northwest, then makes a loop. This is due to the mesocyclone of the storm. Figure 6.5 shows the winds and vertical motion at a height of

535m, at 0045 UTC with P3 superimposed on it. Early in the lifetime of this parcel, it passes through a region where the winds are turning counterclockwise. Although the center of the mesocyclone is in a region of updraft, it expands to the surrounding areas, occupying also downdraft regions.

Figure 6.4 shows that P1 and P2 initially flow horizontally then sink in the ND. P1, which ends up more to the north, undergoes the shallowest trajectory: it starts at 321m. P2 comes from as high as 1255 m, and P3 starts around 550m. P3 sinks at its westernmost position, and then returns to the east at low levels. This shows that although the high winds in the bow region are co-located with the BD, P3 is in fact descending the most in the ND. We will explore this idea further in Section 6.6.1, through an analysis of properties of this parcel.

6.3.2 Daytime Updraft

In this section we present some trajectories that compose the updraft of this storm. The projection on the horizontal plane of 5 trajectories superimposed on the vertical motion are shown in Figure 6.6. They all terminate at a height of 6400 m, at 0045 UTC. Projections of the trajectories on the xy, xz and yz planes are shown in Figure 6.7. All parcels have similar trajectories. P5 starts the closest to the ground. P1, that ends up furthest north, initiates its trajectory to the west of the other parcels, and travels at higher levels. Parcels that travel at low levels follow the surface southeast flow, while parcels that travel at higher levels, follow the upper level southerlies and southwesterlies associated with the upper-level trough. P5 can also be seen in a vertical cross-section in Figure 6.8. This parcel comes from the southeast at a height of approximately 500m, and then gets ingested in the updraft, ascending rapidly towards the northeast.

6.4 Night-Time trajectories

In this section we describe two sets of nocturnal trajectories. In Section 6.4.1 we describe a set that ends at 0600 UTC and terminates on surface downdraft, and in Section 6.4.2, a set that ends at 0615 UTC on midlevel updraft. The integration for the downdraft lasted 30 minutes and the integration for the updraft lasted 32 minutes.

6.4.1 Night–time Downdraft

Several trajectories were integrated beginning at 0600 UTC. At this time strong winds were occurring, with the largest horizontal speeds (up to 26.5 ms^{-1}) located just east of the main downdraft, between the surface downdraft and updraft. Figure 6.9 shows the projection of Parcels 1–4 on the horizontal plane, superimposed on the horizontal wind speed. The 4 parcels end their trajectories on the region of strongest winds. Figure 6.10 shows the same trajectories, but superimposed to the vertical velocity and horizontal wind vectors. We note that the strongest winds are from the northwest and are co-located with the downdraft. At this time the distinction made in Section 6.3.1 between the ND and BD, although present, is not as evident.

Figures 6.11a–c show the projection of all 4 trajectories on the horizontal, xz and yz planes, respectively. From these figures, we note all parcels approach the storm from the southeast, do a cyclonic turn as they get embedded in the storm's mesocyclone, and sink in the downdraft.

The parcels originate at different levels. P4 originates in fairly low levels, 200m, and undergoes a trajectory that has almost no net east-west component. The other three parcels originate between 350 and 600m.

All 4 parcels ascend for a while before descending in the downdraft. P4 ascends up to 600m, while P1 and P2 ascend to 900 and 1100m, respectively.

6.4.2 Night–time Updraft

Several parcels were initiated at a height of 3819 m, in the core of the updraft at 0615 UTC. Figure 6.12 shows the projection on the horizontal plane of P1, P3 and P5 with respect to the updraft. Projections of P1 through P5 on the xy, xz and yz planes are shown in Figure 6.13. All parcels come from the south, and ascend in the updraft. Their original height varies. Some come from very near the ground (around 100 m), while others come
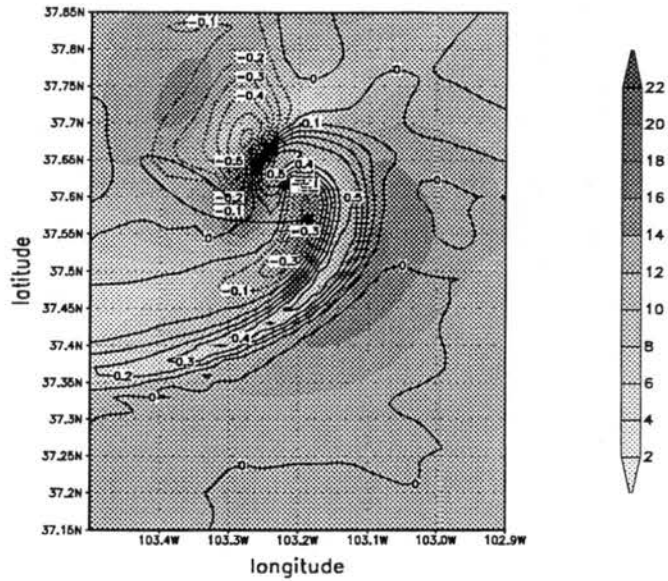
Figure 6.2: Horizontal wind speed (shaded) (ms^{-1}) and vertical velocity (contoured) (ms^{-1}) at σ=48m and t=0045 UTC. The thick line is the projection of the downdraft P3's trajectory on the horizontal plane for t=0000 UTC to t=0045 UTC. The dot indicates the position of the parcel at t=0045 UTC.
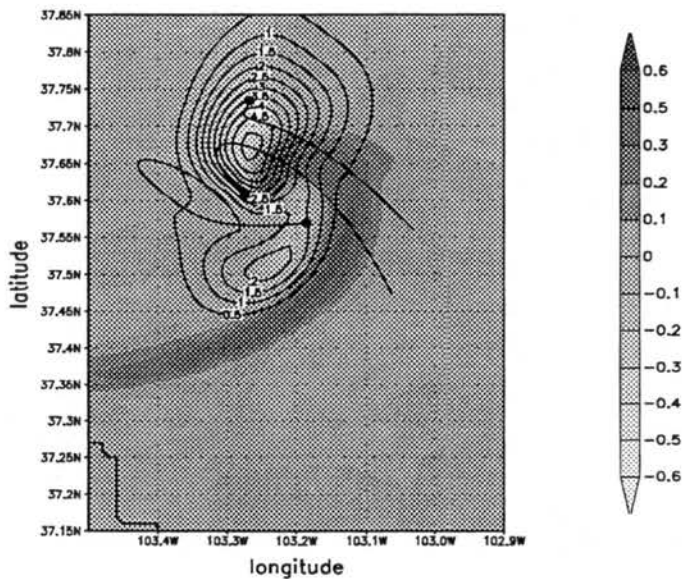
Figure 6.3: Vertical velocity (shaded) (ms^{-1}) and condensate mixing ratio (contoured) (gkg^{-1}) at σ=48m and t=0045 UTC. The thick lines are the projection of the trajectories of downdraft parcels 1—3 on the horizontal plane for t=000 UTC to t=0045 UTC. The dots indicate the position of the parcels at t=0045 UTC.
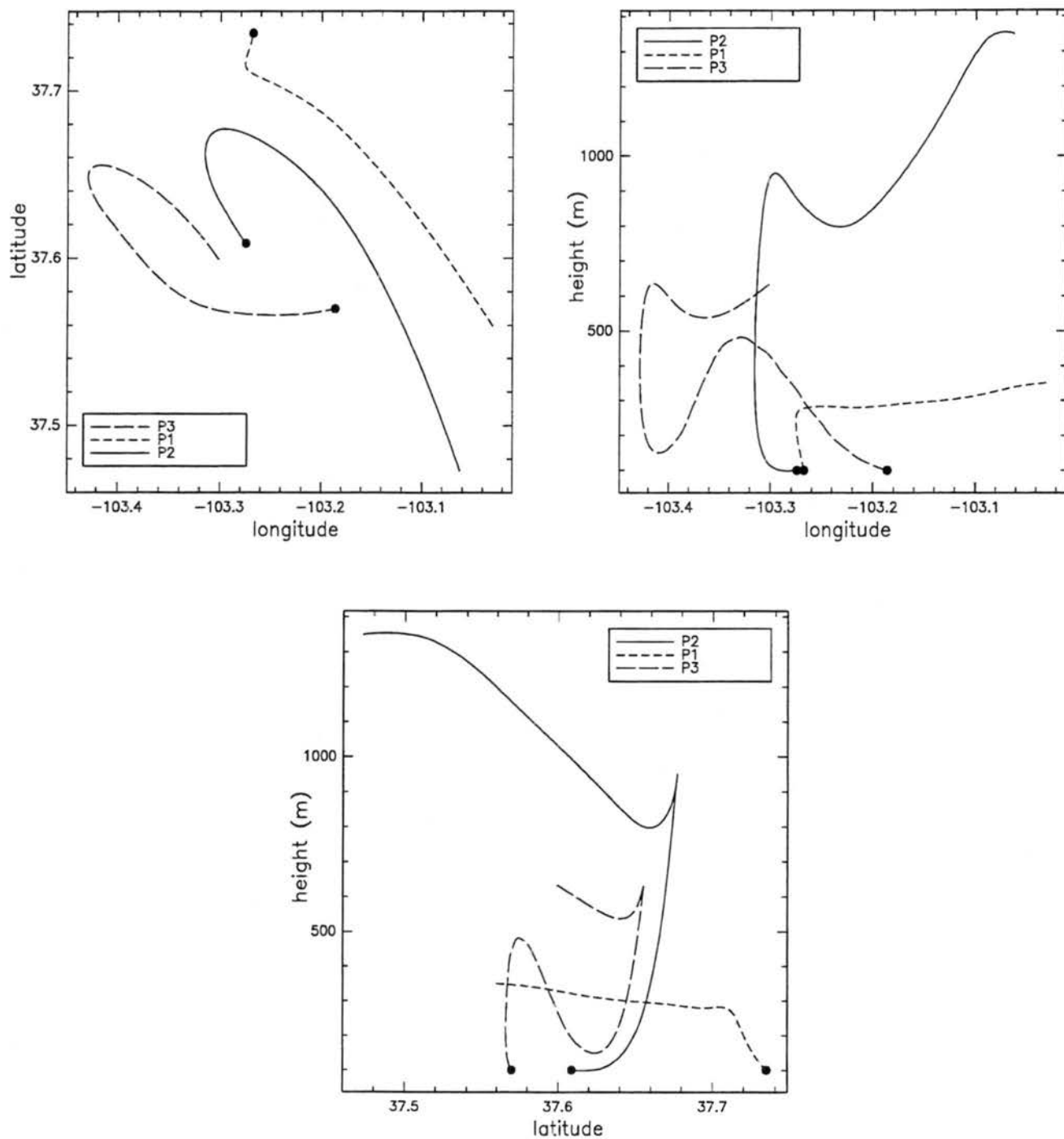
Figure 6.4: Projection of the trajectories of downdraft parcels P1—P3 from t=0000 UTC to t=0045 UTC on the a) xy plane; b) xz plane; c) yz plane.
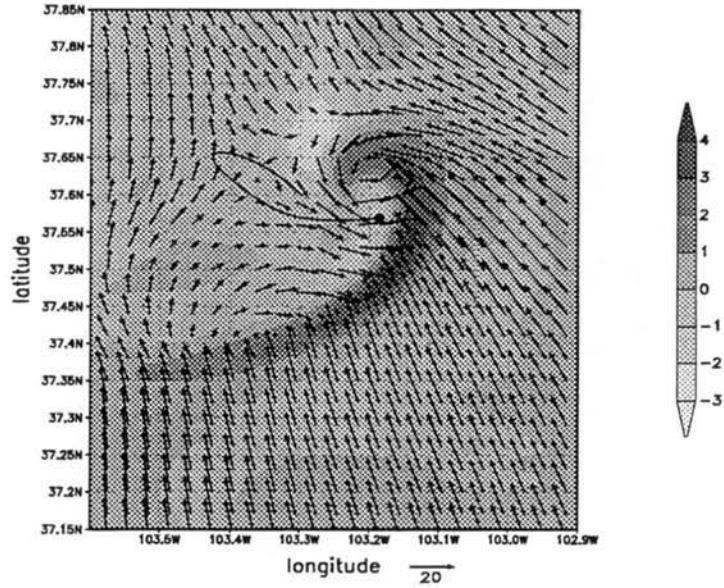
Figure 6.5: Vertical velocity (shaded) (ms^{-1}) and horizontal wind vectors at σ=535m and t=0045 UTC. The thick line is the projection of the downdraft P4's trajectory on the horizontal plane for t=0000 UTC to t=0045 UTC. The dot indicates the position of the parcel at t=0045 UTC.
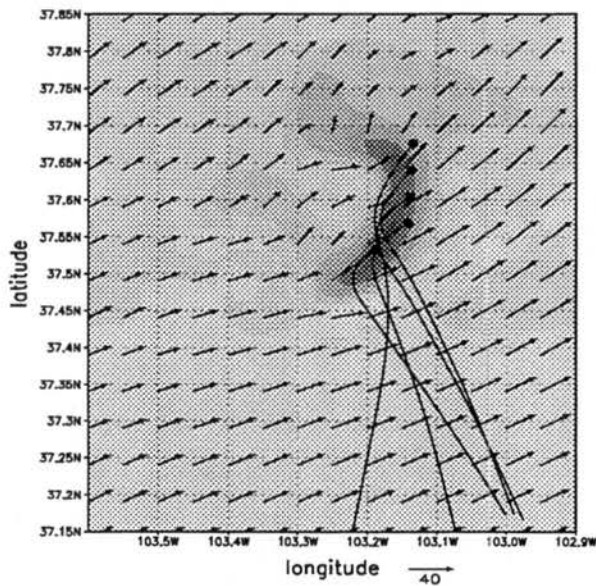
Figure 6.6: Vertical velocity (shaded) (ms^{-1}) and horizontal wind vectors at σ=6055m and t=0045 UTC. The thick lines are the projection of the trajectories of updraft parcels 1—5 on the horizontal plane for t=0000 UTC to t=0045 UTC. The dots indicate the position of the parcels at t=0045 UTC.
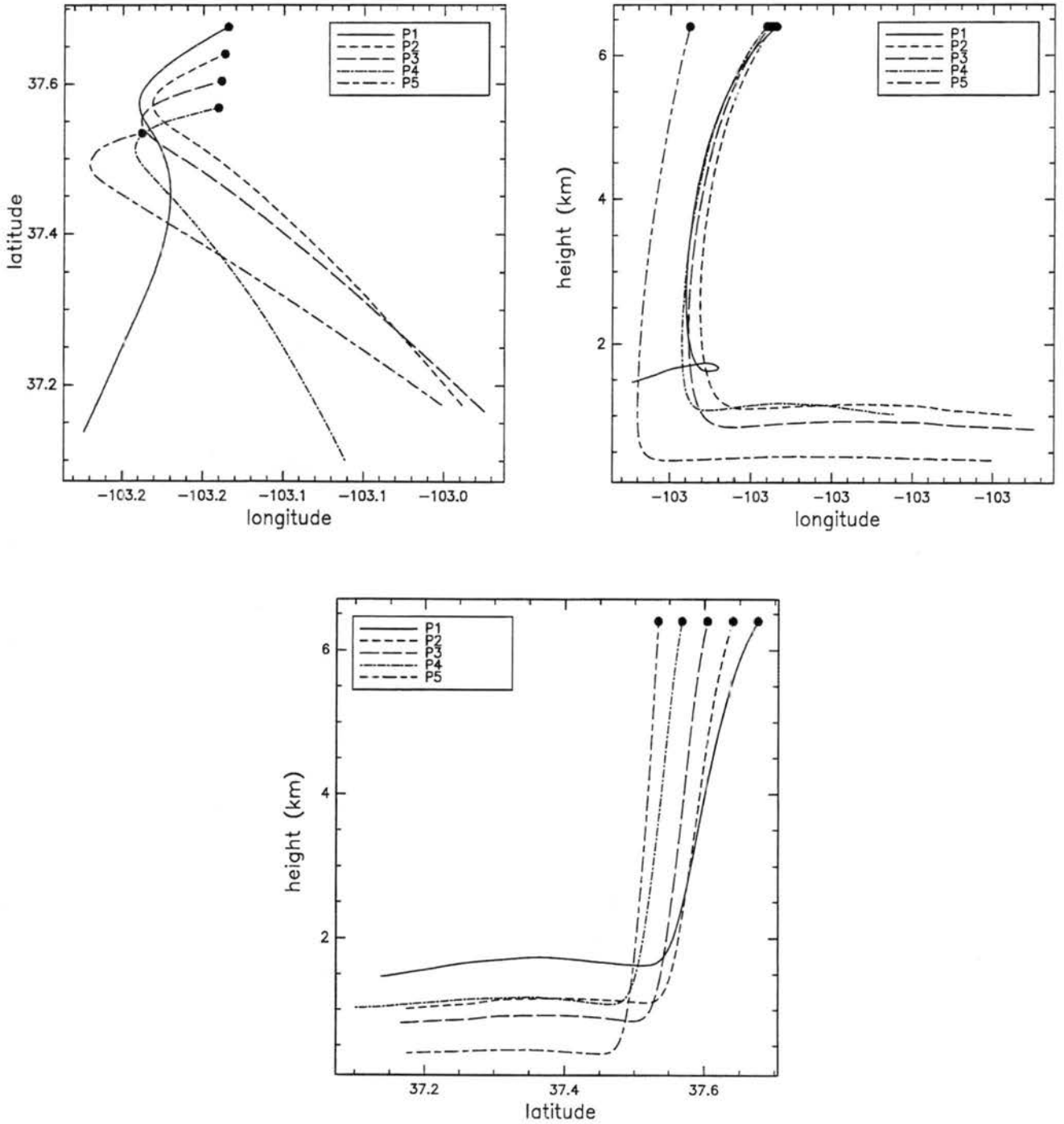
Figure 6.7: Projection of the trajectories of updraft parcels P1—P5 from t=0000 UTC to t=0045 UTC on the a) xy plane; b) xz plane; c) yz plane.
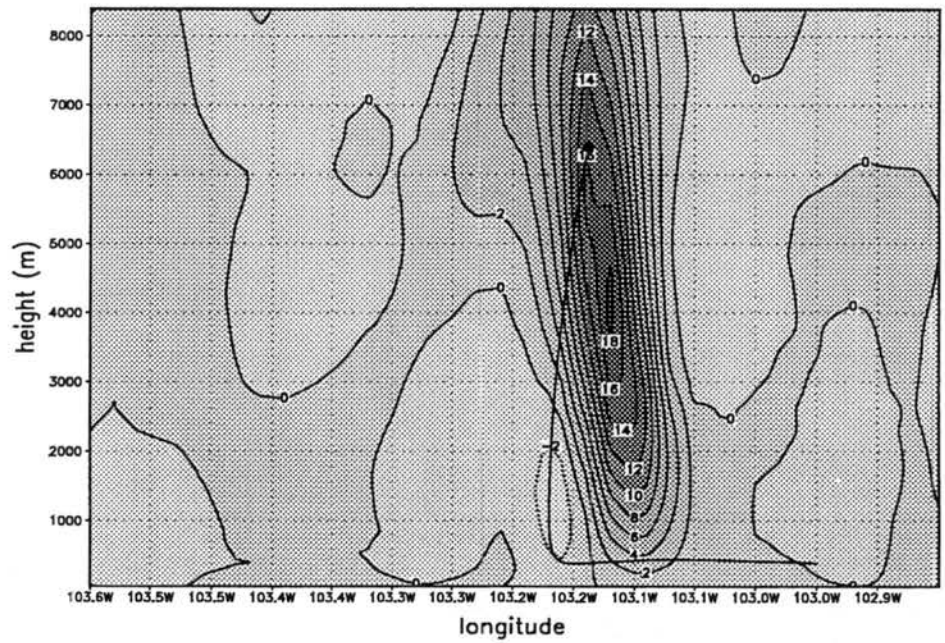
Figure 6.8: Vertical cross-section of vertical velocity (ms^{-1}) through latitude 37.53N at t=0045 UTC. The thick line is the projection of the updraft P5's trajectory on the xz plane for t=0000 UTC to t=0045 UTC. The dot indicates the position of the parcel at t=0045 UTC.
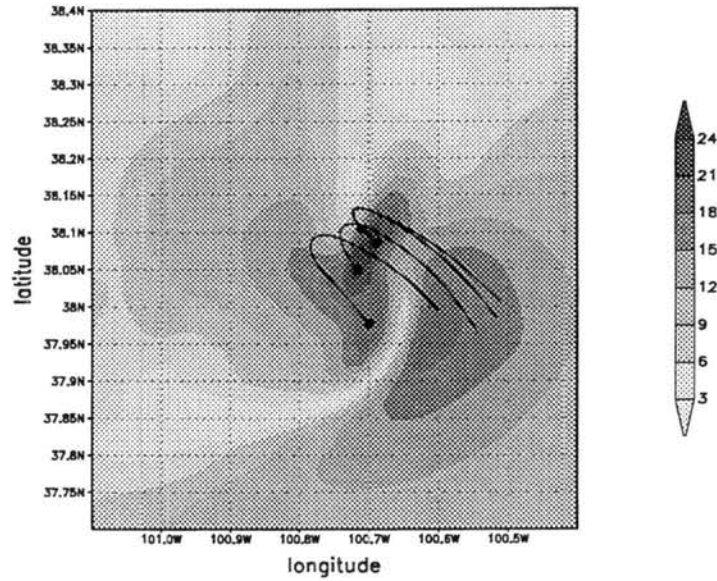
Figure 6.9: Horizontal wind speed (shaded) (ms^{-1}) σ=48m and t=68400s. The thick lines are the projection of the downdraft trajectories P1—P4 on the horizontal plane for t=0530 UTC to t=0600 UTC. The dots indicate the position of the parcels at t=0600 UTC.
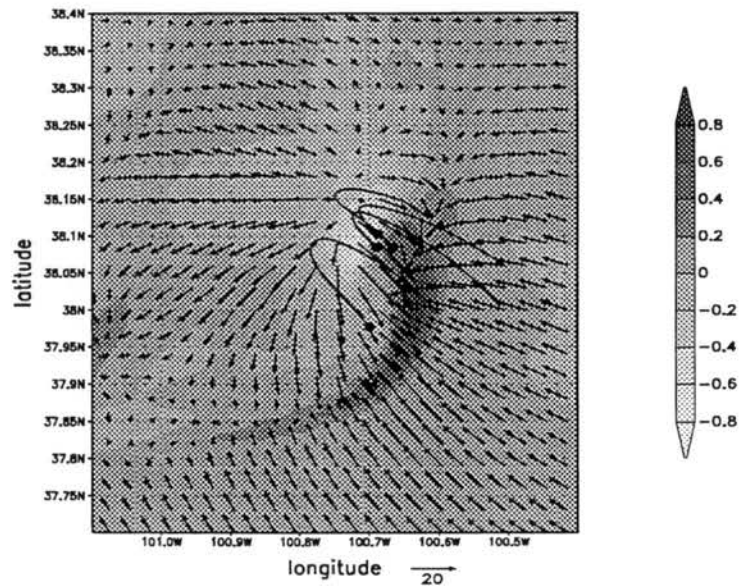
Figure 6.10: Vertical velocity (ms^{-1}) and horizontal wind vectors at σ=48m and t=0600 UTC. The thick lines are the projection of the downdraft trajectories P1—P4 on the horizontal plane for t=0530 UTC to t=0600 UTC. The dots indicate the position of the parcels at t=0600 UTC.
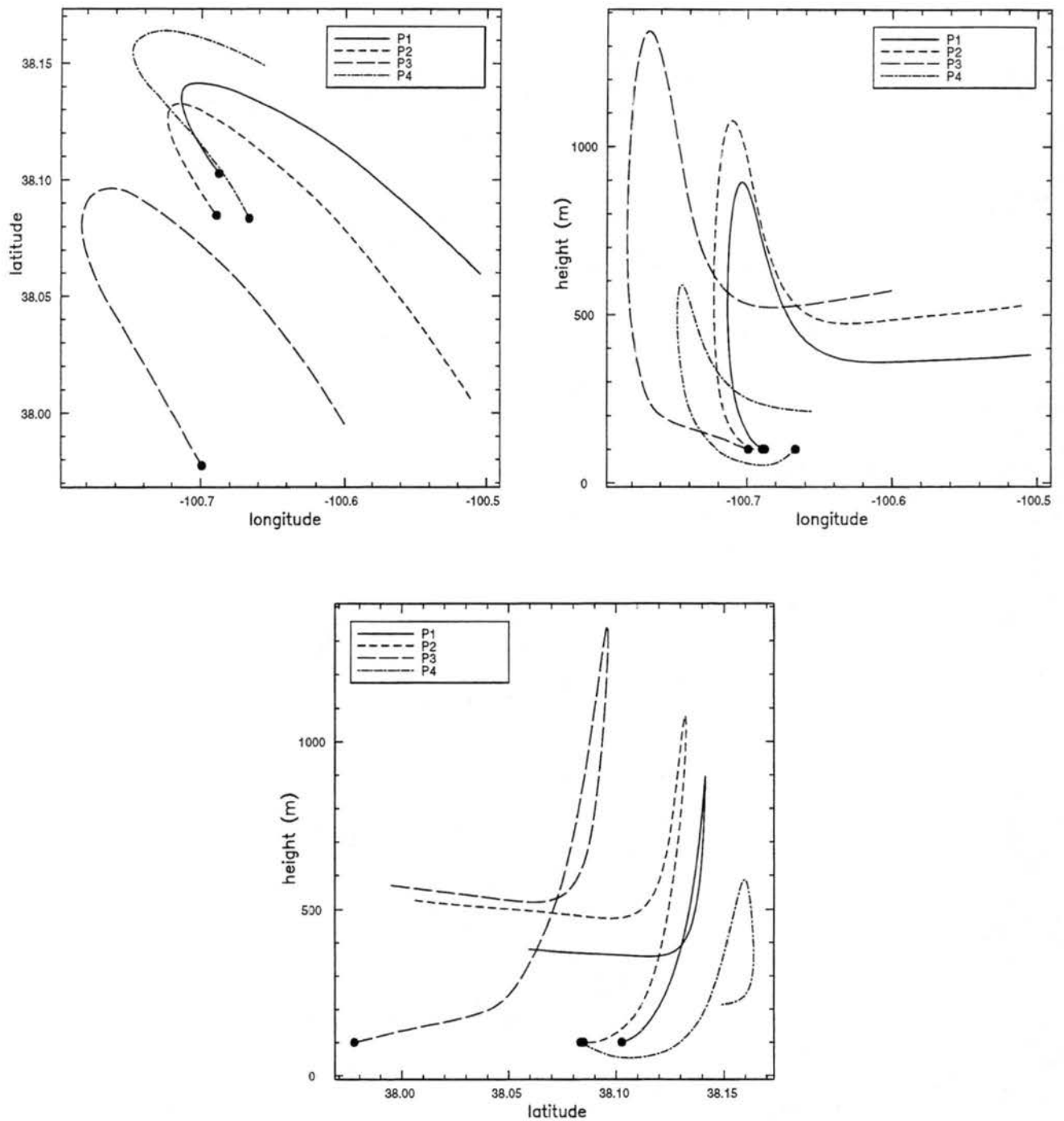
Figure 6.11: Projection of the trajectories of downdraft parcels P1—P4 from t=0530 UTC to t=0600 UTC on the a) xy plane; b) xz plane; c) yz plane.
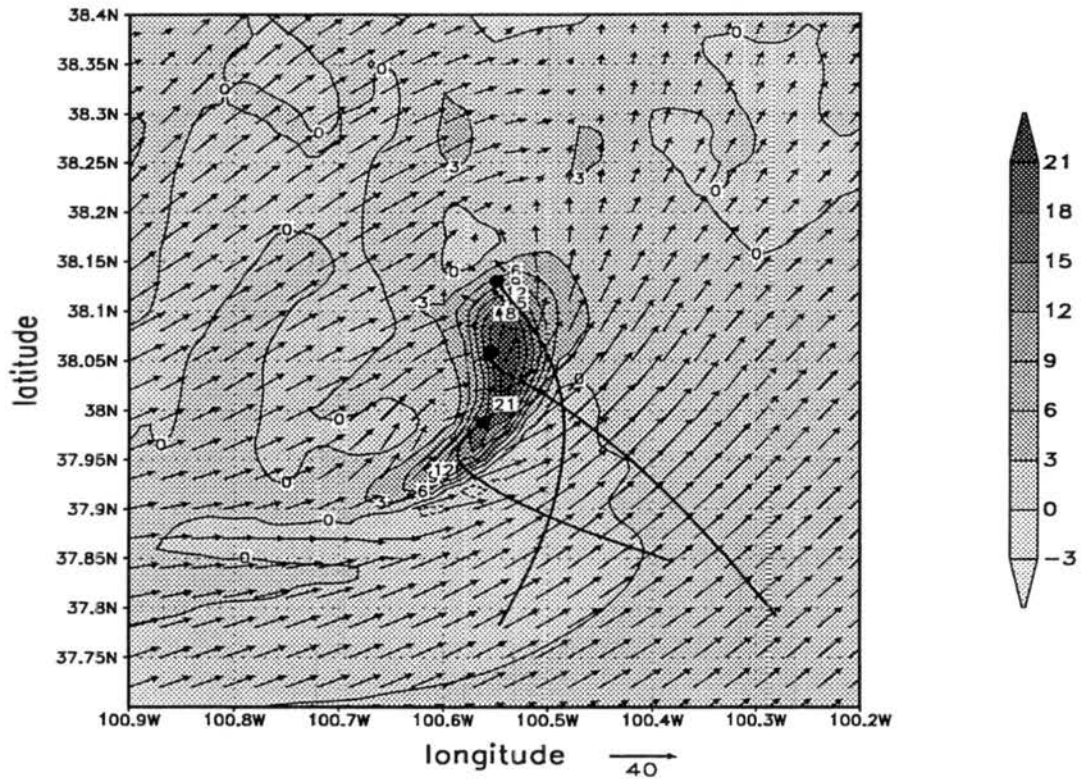
Figure 6.12: Vertical velocity (ms^{-1}) and horizontal wind vectors at σ=3819m and t=0615 UTC. The thick lines are the projection of the updraft trajectories P1, P3 and P5 on the horizontal plane for t=0543 UTC to t=0615 UTC. The dots indicate the position of the parcels at t=0615 UTC.
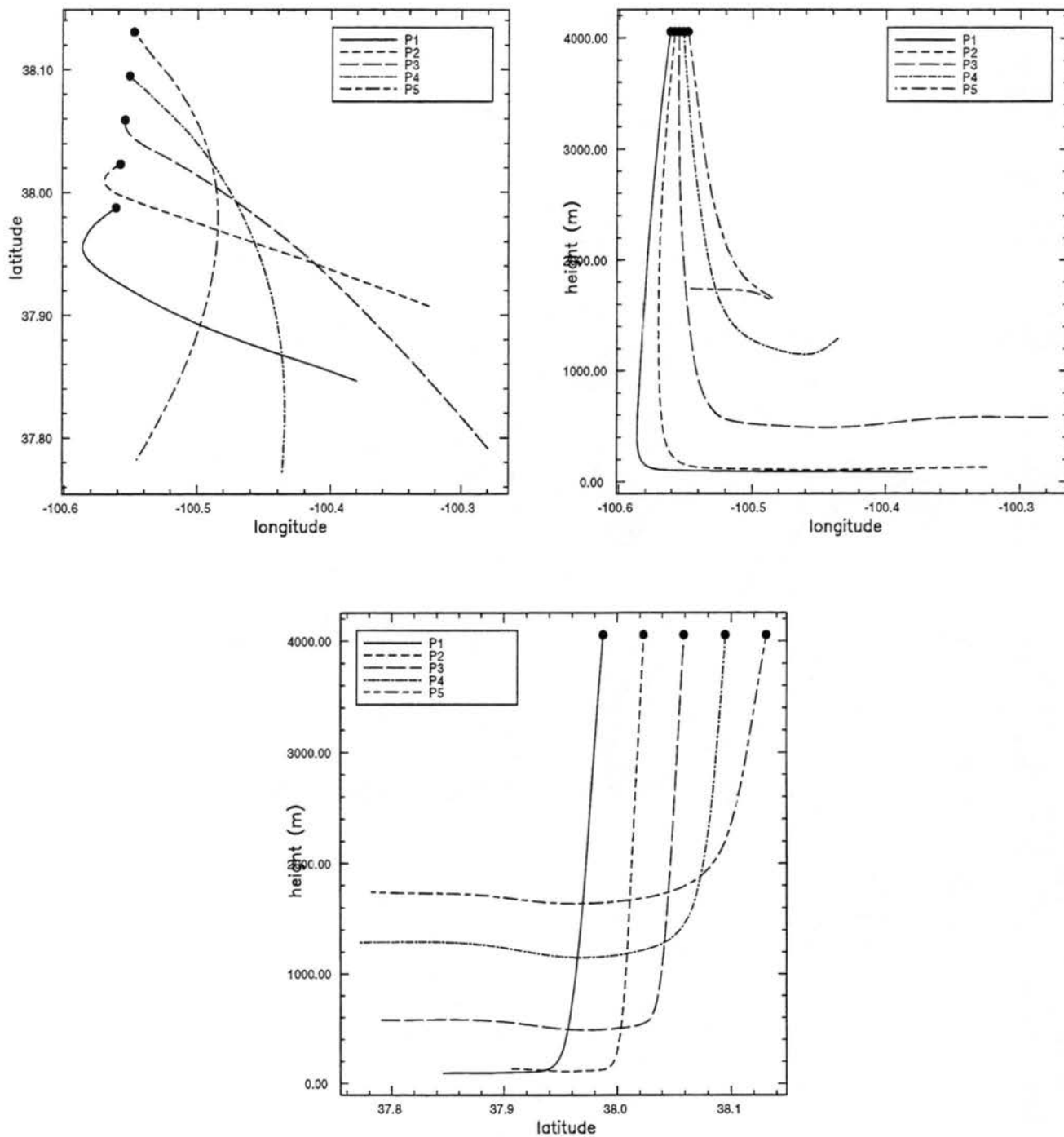
Figure 6.13: Projection of the trajectories of updraft parcels P1—P5 from t=0543 UTC to t=0615 UTC on the a) xy plane; b) xz plane; c) yz plane.
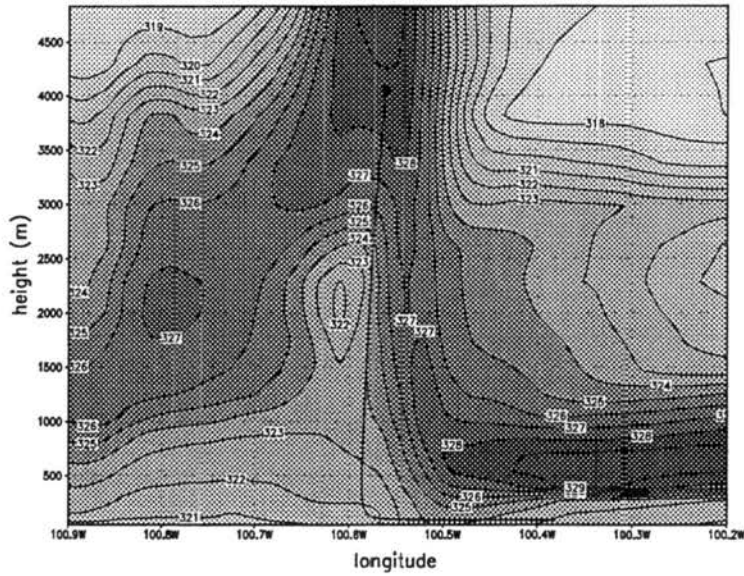
Figure 6.14: Vertical cross section of equivalent potential temperature (K) through lat=37.99N at t=0615 UTC. The thick line is the projection of the updraft P1's trajectory on the xz plane for t=0543 UTC to t=0615 UTC. The dot indicates the position of the parcel at t=0615 UTC.
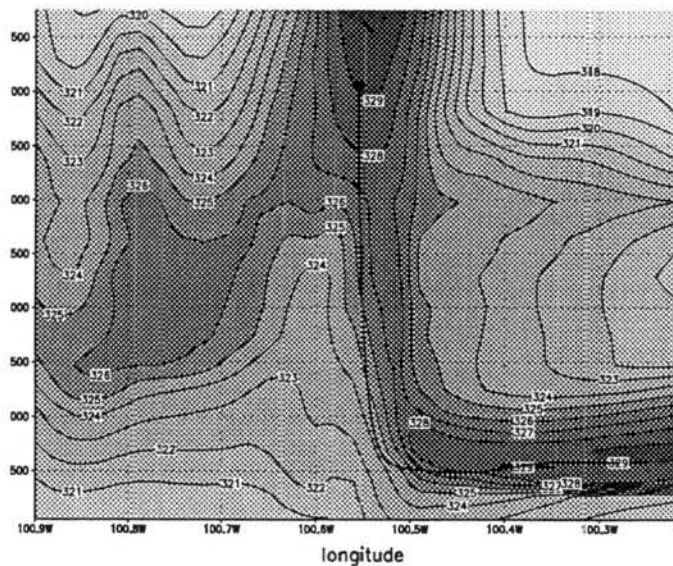
Figure 6.15: Vertical cross section of equivalent potential temperature (K) through lat=38.06N at t=0615 UTC. The thick line is the projection of the updraft P3's trajectory on the xz plane for t=0543 UTC to t=0615 UTC. The dot indicates the position of the parcel at t=0615 UTC.

from as high as 1800m. The ones that originate in low levels come from the southeast, under the influence of the low level flow. Parcels that originate in upper levels follow the southerlies associated with the nocturnal LLJ.

Vertical cross sections of θ_e superimposed on P1 and P3 (Figures 6.14 and 6.15) show that P3 comes from the elevated tongue of high θ_e air, while P1 originates in the lower θ_e underneath it.

6.5 Force Balances and Physical Properties along Trajectories

To understand the trajectories taken by the parcels, several dynamic and thermodynamic properties of the parcels were studied, and will be discussed in the following sections. Some of the properties, such as height of the parcel, are obtained straight from the trajectories themselves. Other properties, such as the three components of velocity, potential temperature and mixing ratio, are interpolated from the Eulerian grid to the parcel's position.

The forces in the vertical momentum equation, used to accelerate the parcel in the Eulerian model, are also interpolated to the parcel location. We now explain how these forces were obtained. The vertical momentum equation in RAMS is written as

$$
\frac{dw}{dt} = \underbrace{-\theta_{v0}\frac{\partial \pi'}{\partial z}}_{PGF} + \underbrace{g\frac{\theta_v'}{\theta_{v0}}}_{BUO} \quad \underbrace{-g(r_t - r_v)}_{LOA}
$$

$$
+ \underbrace{\frac{\partial}{\partial x}\left(K_m\frac{\partial w}{\partial x}\right) + \frac{\partial}{\partial y}\left(K_m\frac{\partial w}{\partial y}\right) + \frac{\partial}{\partial z}\left(K_m\frac{\partial w}{\partial z}\right)}_{DIF}, \tag{6.4}
$$

where, on the right-hand side (RHS), the first term is the π-gradient force (PGF), the second is the moist buoyancy (BUO), the third is the condensate loading (LOA), and the remaining ones are eddy diffusion (DIF). The description of the symbols can be found in Table 6.1.

In particular,

$$
\theta_v' = \theta_v - \theta_{v0}, \tag{6.5}
$$

$$
\pi' = \pi - \pi_0, \tag{6.6}
$$

θ_v	Virtual potential temperature.
θ_{v0}	Virtual potential temperature of the reference state.
θ'_v	Perturbation virtual potential temperature.
π	Exner function $= c_p \left(\frac{p}{p_0}\right)^{\frac{R}{c_p}}$.
π'	Perturbation Exner function.
π_0	Exner function of the reference state.
c_p	Specific heat for dry air at constant pressure.
K_m	Eddy diffusion coefficient for momentum.
p	Pressure.
p_0	1000 hPa.
r_t	Total mixing ratio.
r_v	Vapor mixing ratio.
R	Gas constant for dry air.
w	Vertical velocity.

Table 6.1: Symbols used in Chapter 6.

where θ_{v0} and π_0 are the virtual potential temperature and the Exner function of the reference state, respectively. Therefore, the buoyancy and PGF in (6.4) depend on the choice of reference state. However, the total acceleration ($\frac{dw}{dt}$), and in particular the sum of the PGF force with the buoyancy do not depend on the reference state. Equation 6.4 is derived from the original continuous vertical momentum equation

$$\frac{dw}{dt} = -\theta_v \frac{\partial \pi}{\partial z} - g \tag{6.7}$$

and $\frac{dw}{dt}$ is the same for any choice of decomposition of θ_v and π, as long as the reference state is in hydrostatic balance and perturbations are small enough so their product can be neglected.

We will call the sum of the π-gradient force and the buoyancy in (6.4) A. It represents accelerations in vertical velocity neglecting diffusion and loading:

$$PGF + BUO = A. \tag{6.8}$$

Since the model results do not depend on the choice of reference state, that state is arbitrary. In RAMS it is chosen at the time of model initialization (06 UTC of 5/12 in this case) as the model column with the lowest topography in the Grid #1 (in this simulation a

column over the Pacific Ocean). This reference state is therefore *NOT* representative of the storm environment, which makes it physically meaningless. To discuss the individual PGF and BUO as provided by the equation 6.4, we have redefined the buoyancy acceleration (BUO^{new}) to be a physically meaningful quantity. We chose a sounding, representative of the environment close to the convective system at each analysis time, and called that sounding the new reference state. The soundings chosen for the daytime and night-time analysis are shown in Figures 6.16 and 6.17, respectively, and were obtained through an average of 726 model columns ahead of the convective system. As the parcel ascended or descended, virtual potential temperature perturbations were computed with respect to this new reference state, and (BUO^{new}) was obtained.

The new PGF (PGF^{new}) to balance the newly defined reference state was then simply diagnosed.

$$PGF^{new} = A - BUO^{new}. \tag{6.9}$$

With this method we guarantee that BUO^{new} and PGF^{new} are self-consistent and physically meaningful quantities that can be used to gain understanding of the physical processes that determine the parcels' trajectories.

6.6 Results for Daytime

In this section we present the physical properties and the force balances for some trajectories discussed in Section 6.3.

6.6.1 Daytime Downdraft

Parcel 2 (Figure 6.4) begins its trajectory at a height of 1350m (Figure 6.18a). It descends monotonically, except for a brief period of 08 minutes between 0025 and 0033 UTC. In its final descent it attains a downward speed of -2.2 ms^{-1} (Figure 6.18b), and reaches the ground with a horizontal speed of 23.3 ms^{-1} (Figure 6.18c). The parcel contains liquid condensate (Figure 6.18d) from the time the parcel begins its brief ascent period.

Figure 6.18e shows the 5 terms in Equation 6.4. It indicates that the accumulation of condensate in the parcel is necessary to start the final descent period. But when the parcel

is getting close to the ground, its condensate loading starts decreasing, probably because the adiabatic warming leads to some evaporation. Figure 6.18f shows that the potential temperature increases when the parcel is close to the surface, probably because of mixing with the warmer environment. Evaporation on this final stretch causes the vapor mixing ratio of the parcel to increase (Figure 6.18d). In a saturated descent, the parcel's potential temperature decreases because evaporation is taking place. This has opposing effects on moist buoyancy: cooler potential temperature leads to decreased buoyancy, while larger vapor amounts lead to increased buoyancy. However, the effect of cooling by far exceeds the effect of moistening, and the net effect of evaporation is negative buoyancy, as shown in Figure 6.18e.

Parcel 1 (Figure 6.4) has a history similar to that of Parcel 2, except that it descends from a height of just 350m (Figure 6.19a). P1 ends up in the northernmost portion of ND, and only attains a downward speed of -0.4 ms^{-1} (Figure 6.19b) and a final horizontal wind speed of 8.0 ms^{-1} (Figure 6.19c). Its descent occurs under negative buoyancy and significant condensate loading (Figure 6.19d). The negative buoyancy can be seen in Figure 6.19e, which indicates that the parcel becomes progressively colder as it descends. It also shows that the potential temperature of the environment is almost constant, indicating a well-mixed boundary layer, consistent with the Skew-T diagram shown in Figure 6.16 and the results of Chapter 5.

Parcel 4 (Figure 6.4) has a very interesting history. Most of its descent occurs earlier in its lifetime (from 635m to 150m) (Figure 6.20a), and it is then that it reaches the highest horizontal speed: 20ms^{-1} (Figure 6.20b). After that, the parcel ascends to 481m, to finally descend in the BD. Comparing Figure 6.20 with P4's projection on the horizontal plane (Figure 6.4), we note that the most significant descent occurred in the ND! After sinking in the ND, the parcel migrated to the BD. The parcel's trajectory contains condensate all times (Figure 6.20c), which leads to a strong negative vertical acceleration due to condensate loading (Figure 6.20d).

6.6.2 Daytime Updraft

Figure 6.21 shows properties of P5 (Figure 6.7) along its trajectory. The height plot (Figure 6.21a) and the velocity plots (Figures 6.21b,c) indicate that the parcel follows a

horizontal trajectory at a height of 400 m with constant speed in the beginning, accelerates when it gets close to the storm, and gets ingested in the updraft. Its vertical velocity increases from zero to 17.3 ms^{-1} in a few minutes, causing it to ascend from 500 to 6400 m. As the parcel ascends, condensation takes place. Figure 6.21d shows that the vapor mixing ratio of the parcel decreases from 8.1 gkg^{-1} at low levels to 1.5 gkg^{-1} in upper levels, and its total mixing ratio increases from 8.1 gkg^{-1} to 9.4 gkg^{-1}. This indicates that the parcel is exchanging mass with its environment, otherwise the parcel's total water would remain constant. The increase of total water mixing ratio can be due either to mixing or to the accumulation of precipitation falling from above. As the parcel ascends, its potential temperature increases, as can be seen in Figure 6.21e. A comparison of the parcel's potential temperature with the reference state potential temperature shows that the difference is small, which implies small buoyancy. The parcel's potential temperature only becomes higher than the ambient's above 4300m.

The balance of vertical forces for this parcel is presented in Figure 6.21f. At the beginning of the trajectory, a small negative buoyancy acceleration is balanced by an upward directed PGF. Condensate loading and dissipation are near zero. As the parcel approaches the storm, a PGF accelerates it upwards. Moist buoyancy remains negative until the parcel attains a height of 3815m. But loading becomes large then and the parcel stops accelerating. As the parcel attains higher speeds, eddy viscosity becomes an important negative acceleration.

Figure 6.21g shows a verification of w. The solid curve shows w obtained from the Eulerian model (w^{diag}) and interpolated to the parcel's position. w^{diag} is the quantity used to move the parcels in the LM. The dashed curve shows the vertical motion prognosed using the tendencies listed in Figure 6.21f and Equation 6.4, according to

$$w^{prog}(t=0) \;=\; w^{diag}(t=0)$$
$$w^{prog}(t+\Delta t) \;=\; w^{prog}(t) + \Delta t * (BUO^{new} + PGF^{new} + LOA + DIF).$$

There is good agreement between w^{diag} and w^{prog}. The quality of the agreement is good for most parcels, but in a few cases it is several meters per second off. When that

happens in a case of small vertical velocities, the percent error becomes large. Even if discrepancies occur between the diagnosed and prognosed vertical velocity, that does not invalidate the tendency analysis described in Figure 6.21f. Discrepancies occur because small errors accumulate over a period of 45 minutes. At each individual point in time, the errors are never very large.

Figure 6.22 illustrates the properties of P1. Overall, the history is similar to that described for P5. The parcel approaches the storm with a constant height of 1500m (Figure 6.22a). Its speed increases as it gets closer to the storm (Figure 6.22b). The parcel gets ingested in the updraft (Figure 6.22c), condensate matter forms (Figure 6.22d), initially as liquid water, then as ice. The main acceleration to drive the parcel upwards is PGF (Figure 6.22e). Moist buoyancy is negative up to a height of 4170m, when it becomes large and positive. However, by then, condensate loading is very large, and the net acceleration is negative. Nonetheless, the parcel continues its ascent, with its vertical velocity decreasing from the 12.2ms^{-1} peak to smaller values, around 3.5 ms^{-1}.

The main difference between the updraft and the downdraft parcels is that the parcels in the downdraft have a very large negative buoyancy, which causes a downward net acceleration.

6.7 Results for Night-Time

In this section we present physical characteristics and balances of forces for some trajectories shown in Section 6.4, that are present in the night-time phase of the convection.

6.7.1 Night–time Downdraft

We will examine two parcels in the downdraft, parcels 2 and 4 from Figure 6.11.

Parcel 4 starts north of the downdraft and has a trajectory of half a circle. It starts at a height of 213m and ascends to a height of 588 m, before descending in the downdraft (Figure 6.23a). On the ascent it reaches a vertical velocity of 0.9 ms^{-1} and on the descent, -1.1 ms^{-1} (Figure 6.23b). It reaches the ground with a horizontal speed of 23 ms^{-1} (Figure 6.23c). Figure 6.23d shows that during the ascent the parcel warms up, but the environment warms up faster, so the parcel develops a strong negative buoyancy as it ascends (Figure 6.23e).

The negative buoyancy is partly overcome by a positive PGF, but because condensate loading is very large, the net acceleration is downwards. Figure 6.23f shows that the parcel's total mixing ratio increases by 5.0 gkg^{-1} during its trajectory, indicating that the parcel is receiving condensate water from its environment. The figure shows that no ice phase exists in the downdraft, since it occurs at low levels.

Parcel 2 arrives at the ground with a very high horizontal wind speed: 30 ms^{-1} (Figure 6.24a). It starts its trajectory at a height of 526 m and ascends to 1077 m before descending in the downdraft (Figure 6.24b). It reaches an upward velocity of 2.6 ms^{-1} on its way up and -2.9 m/s on its way down (Figure 6.24c). Buoyancy is not very large during the parcel's ascent, because the parcel gains potential temperature at roughly the same rate as the environment (Figure 6.24d). The accelerations shown in Figure 6.24e emphasize the importance of condensate loading, without which the upward–directed PGF would dominate the tendency to vertical velocity. Figure 6.24f shows that the parcel gains 4.5 gkg^{-1} from the surroundings, and that 1.5 gkg^{-1} of its own moisture condenses on the ascent. Again, as expected, no ice phase is present.

The plots of speed, height and kinetic energy (Figures 6.24a,b,c) can be used to investigate the importance of downward transfer of momentum and its contribution to the strong surface winds. P2 originates at a height of 526 m, well below the level of local maximum winds associated with the LLJ, located at 1500m (Figure 5.35). Its speed and kinetic energy decrease during the first moments of descent, but then increase considerably. The parcel's final kinetic energy is more than twice its initial value, indicating that negative buoyancy and loading are indeed important in increasing the parcel's momentum.

The analysis of these parcels implies that there are different sources of air for the downdraft at this time. All parcels have in common a low–level origin, with trajectories that originate lower than 600 m. They are forced up by a PGF, and sink due to negative buoyancy and condensate loading. Parcels that originate closer to the ground, acquire more negative buoyancy as they ascend. However, even parcels that originate near the top of the stable layer can reach significant downward motions and horizontal accelerations.
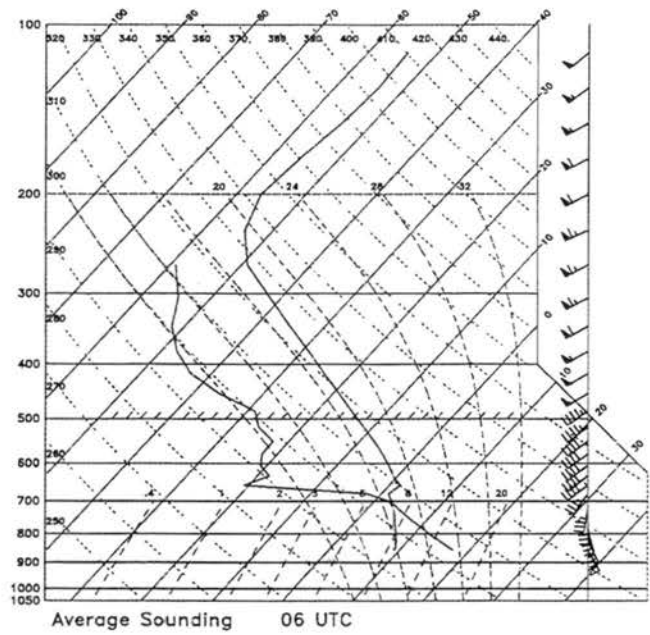
Figure 6.16: Skew-T diagram used as reference state in the calculation of daytime buoyancy and pressure gradient force. Obtained from point (61,31) of the Eulerian model's Grid #4 at t=0030 UTC.
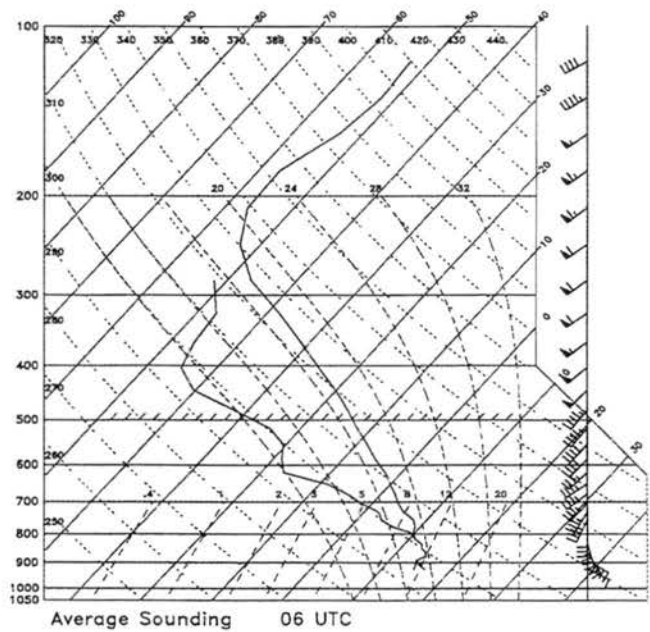
Figure 6.17: Skew-T diagram used as reference state in the calculation of night-time buoyancy and pressure gradient force. Obtained from point (85,20) of the Eulerian model's Grid #4 at t=0545 UTC.
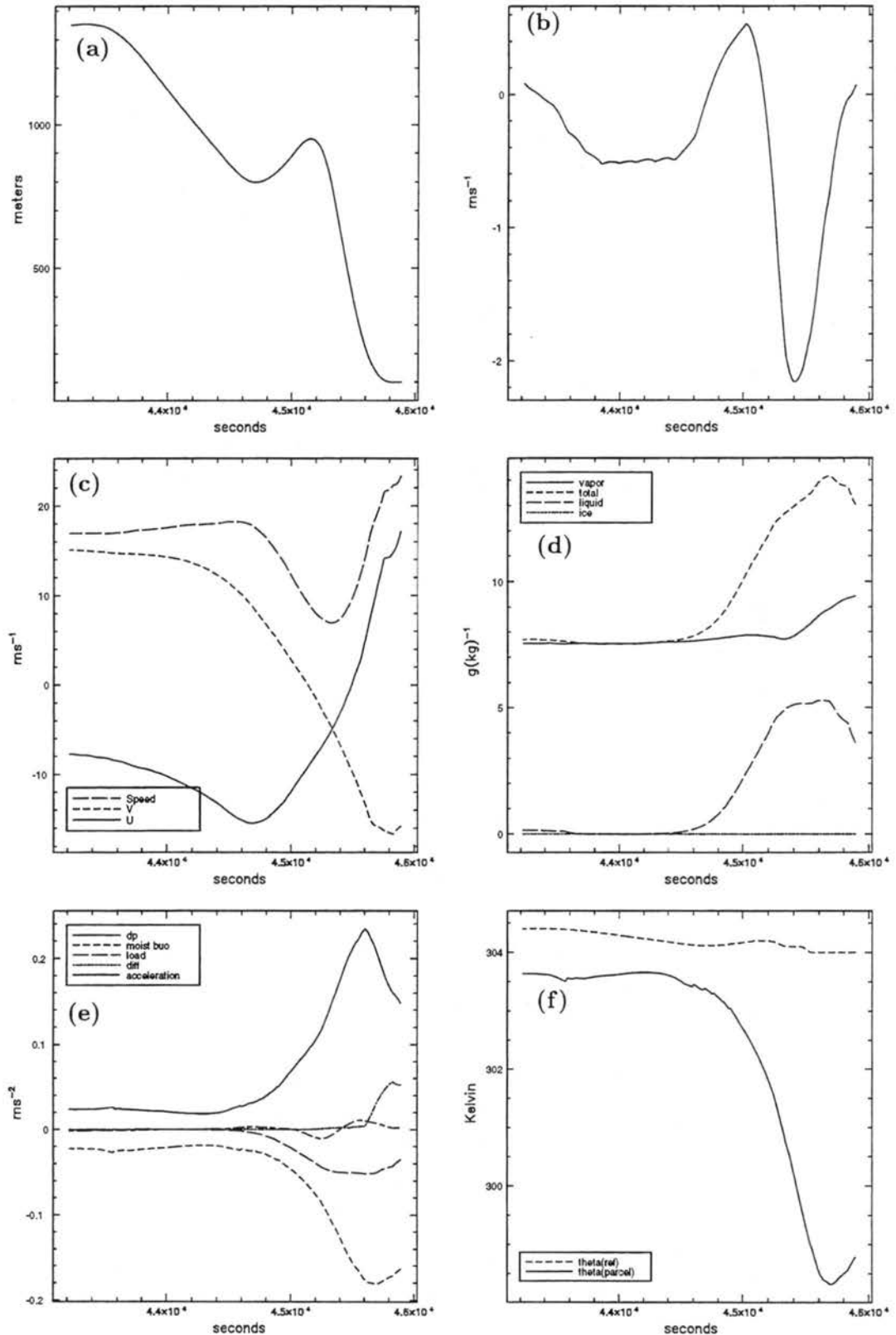
Figure 6.18: Time series (0000–0045 UTC) for daytime downdraft parcel P2. a) height; b) vertical velocity; c) horizontal wind components and speed; d) vapor, total, liquid and ice mixing ratios; e) terms of vertical momentum equation; f) parcel's and reference state's potential temperature.
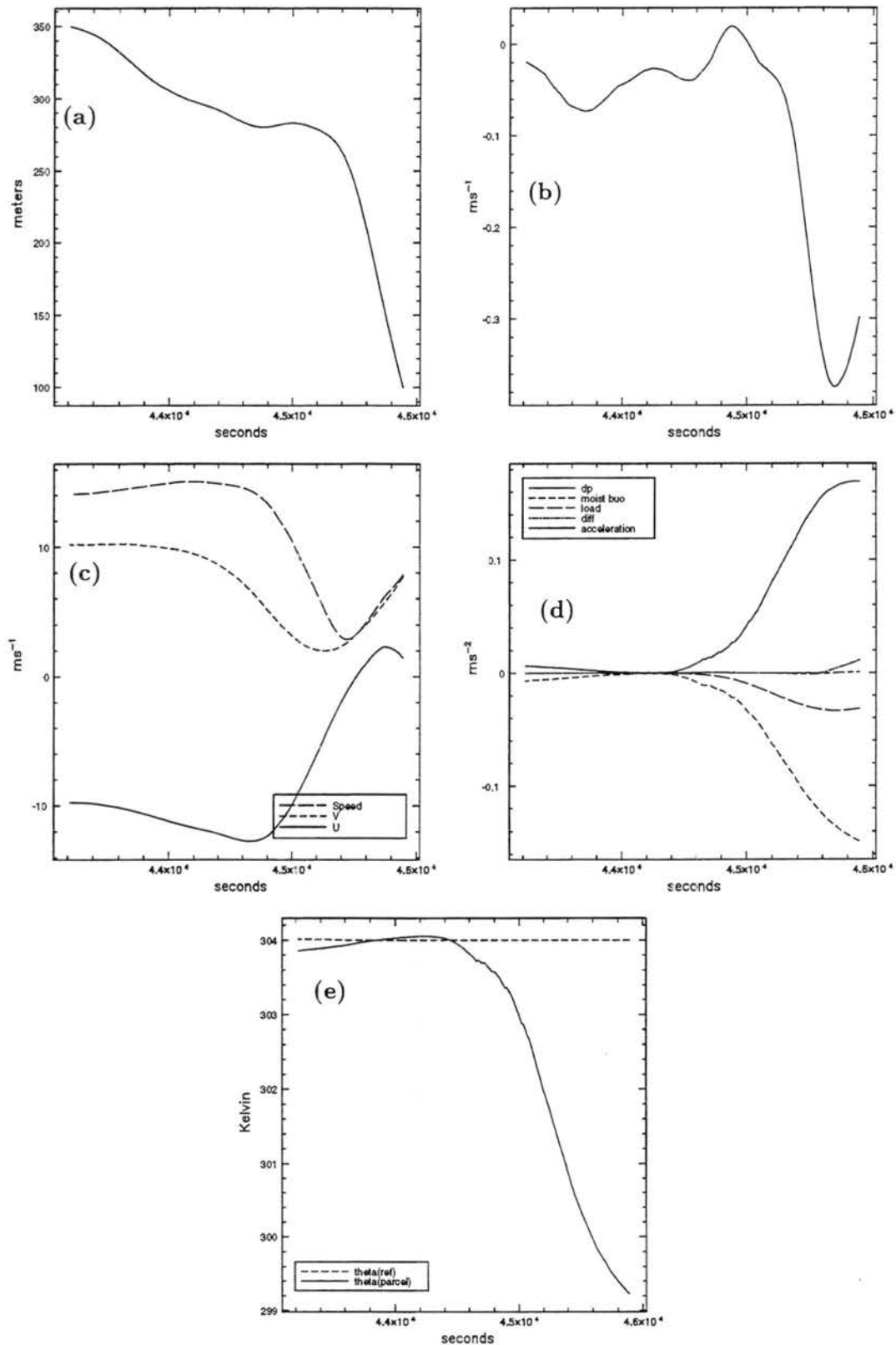
Figure 6.19: Time series (0000–0045 UTC) for daytime downdraft parcel P1. a) height; b) vertical velocity; c) horizontal wind components and speed; d) terms of vertical momentum equation; e) parcel's and reference state's potential temperature.
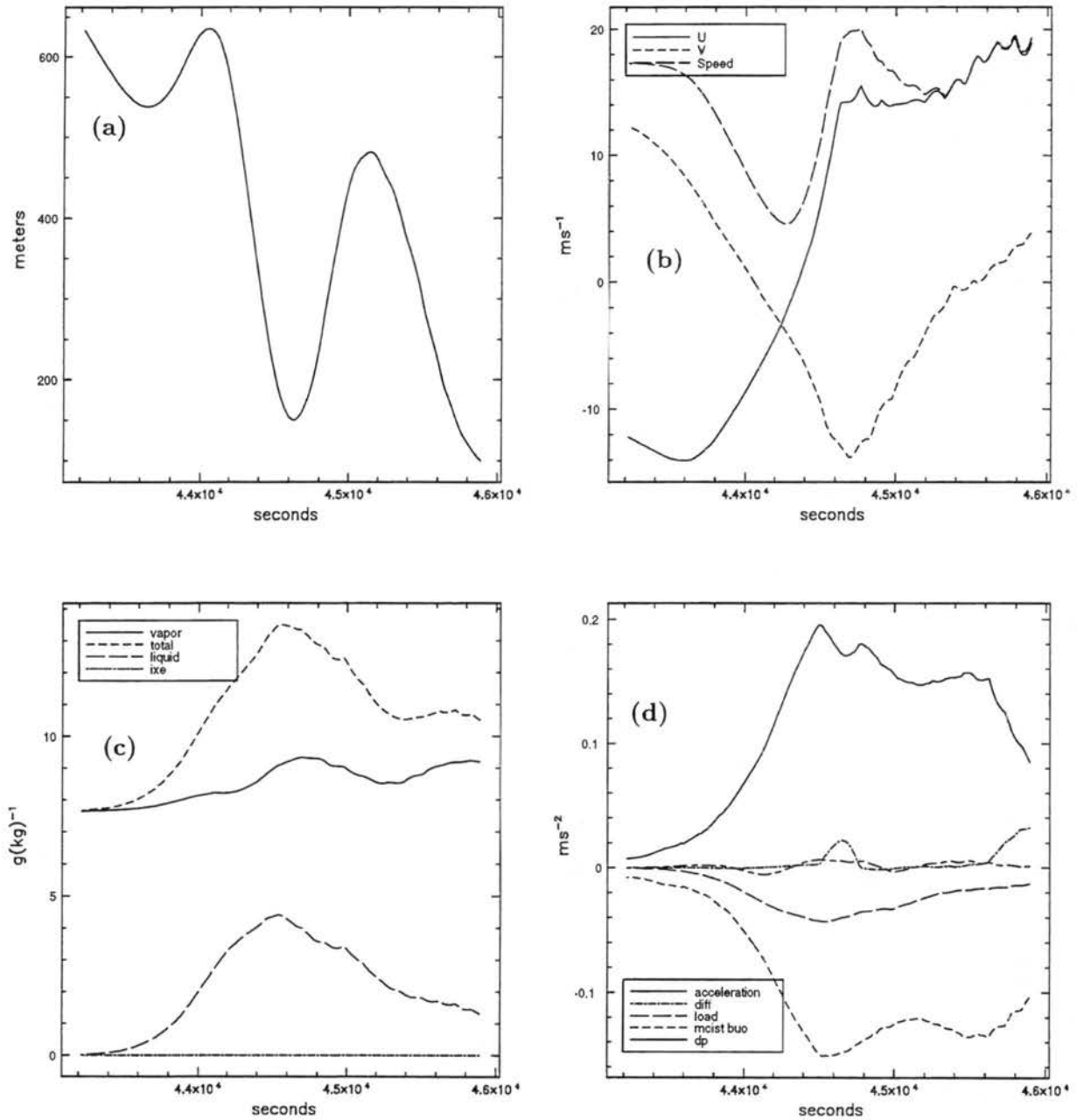
Figure 6.20: Time series (0000–0045 UTC) for daytime downdraft parcel P3. a) height; b) horizontal wind components and speed; c) vapor, total, liquid and ice mixing ratio; d) terms of vertical momentum equation.
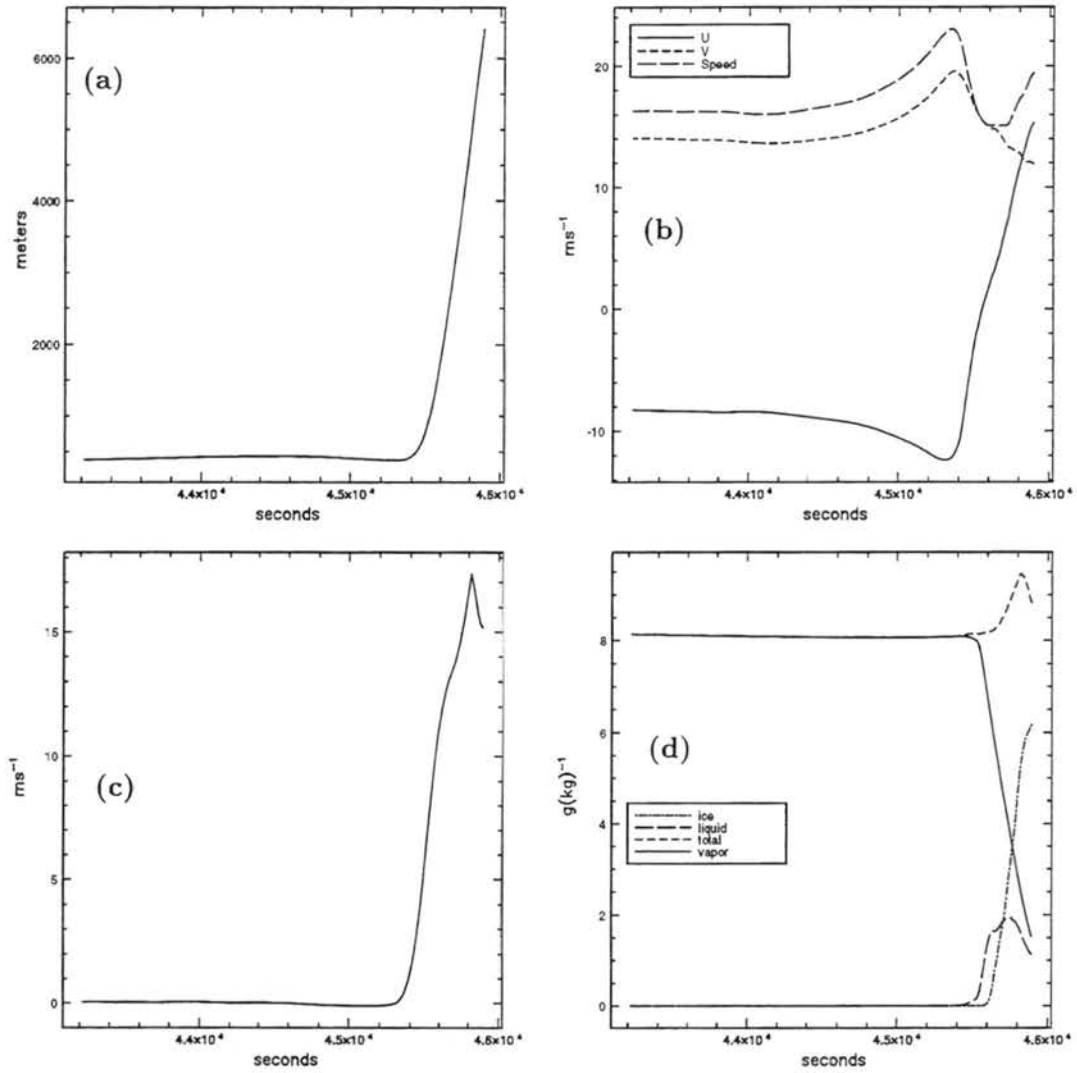
Figure 6.21: Time series (0000–0045 UTC) for daytime updraft parcel P5. a) height; b) horizontal wind components and speed; c) vertical velocity; d) vapor, total, liquid and ice mixing ratios — continues on the next page.
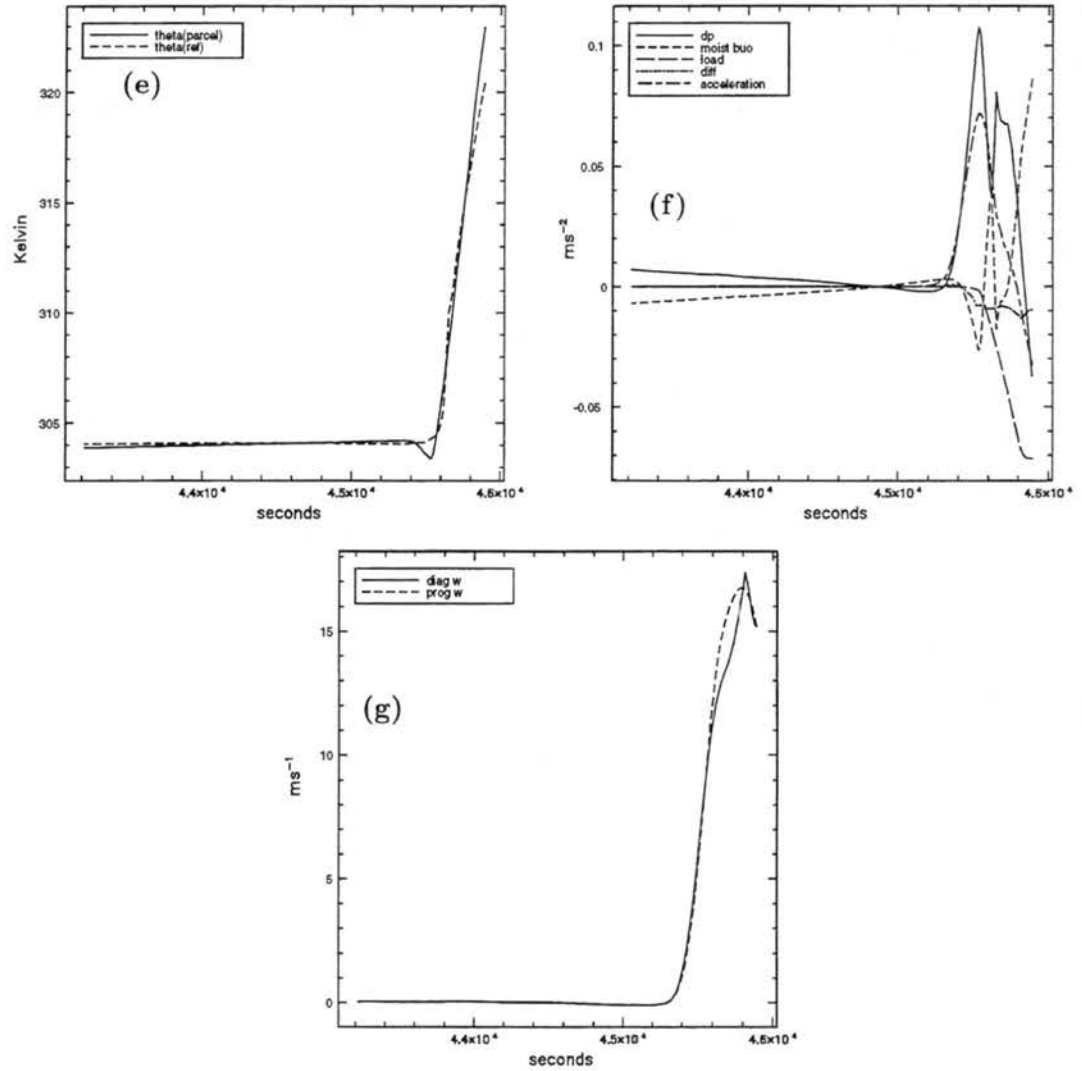
Figure 6.21: — continuation. e) parcel's and reference state's potential temperature; f) terms of vertical momentum equation; g) diagnostic and prognostic vertical velocities.
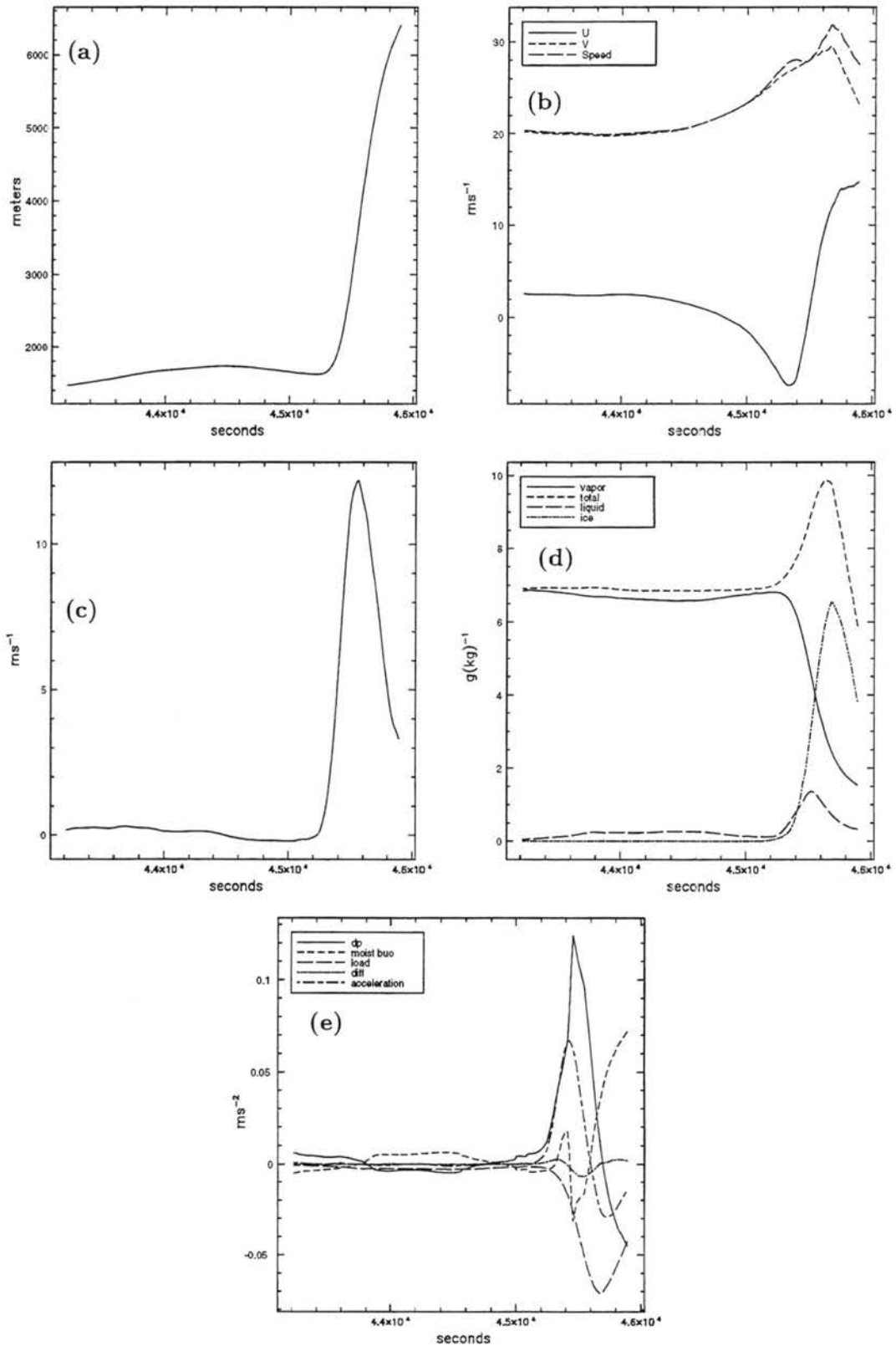
Figure 6.22: Time series (0000–0045 UTC) for daytime updraft parcel P1. a) height; b) horizontal wind components and speed; c) vertical velocity; d) vapor, total, liquid and ice mixing ratios; e) terms of vertical momentum equation.
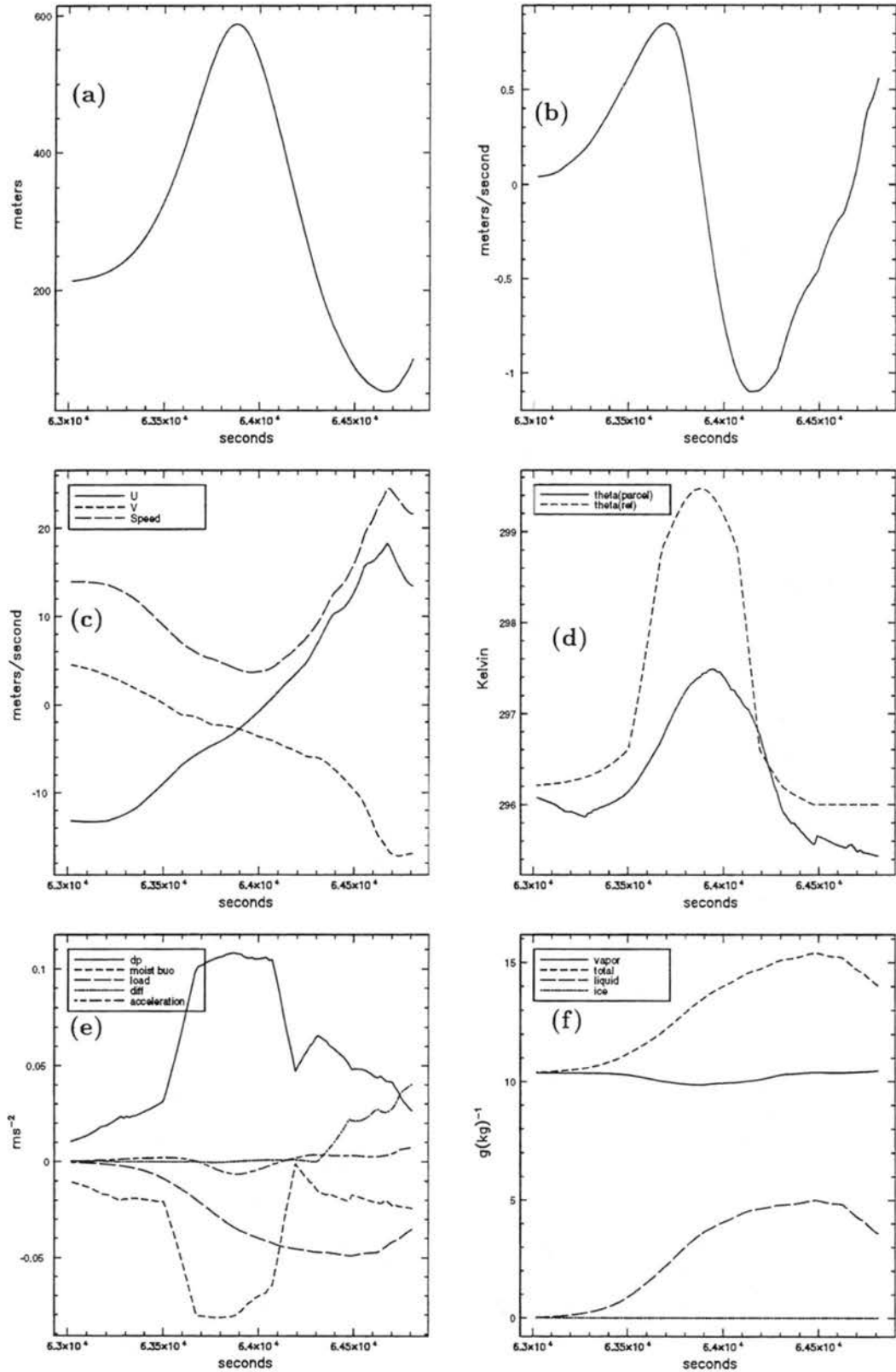
Figure 6.23: Time series (0530–0600 UTC) for night-time downdraft parcel P4. a) height; b) vertical velocity; c) horizontal wind components and speed; d) parcel's and reference state's potential temperature; e) terms of vertical momentum equation; f) vapor, total, liquid and ice mixing ratios.
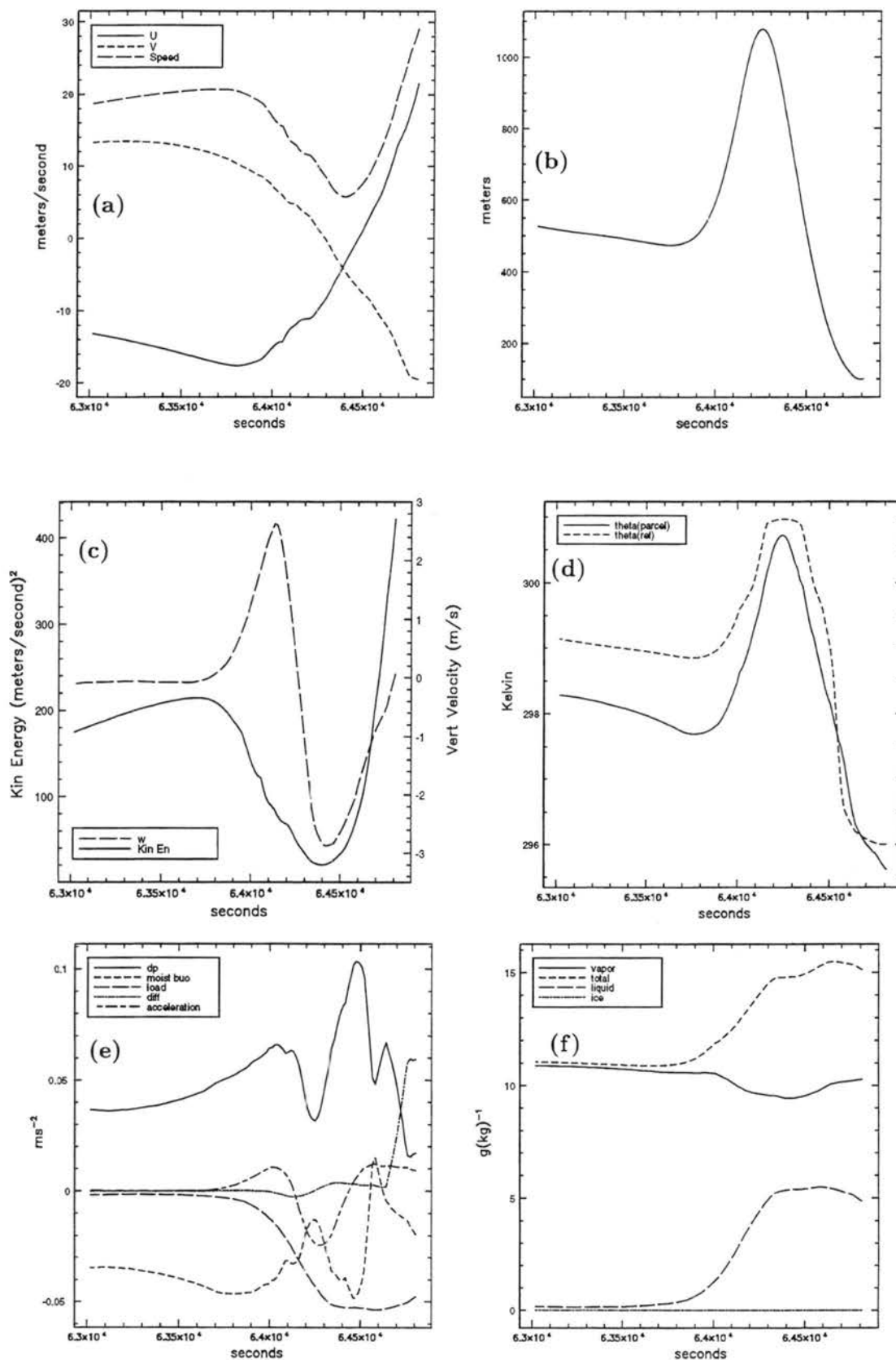
Figure 6.24: Time series (0530–0600 UTC) for night-time downdraft parcel P2. a) horizontal wind components and speed; b) height; c) vertical velocity and kinetic energy; d) parcel's and reference state's potential temperature; e) terms of vertical momentum equation; f). vapor, total, liquid and ice mixing ratios.
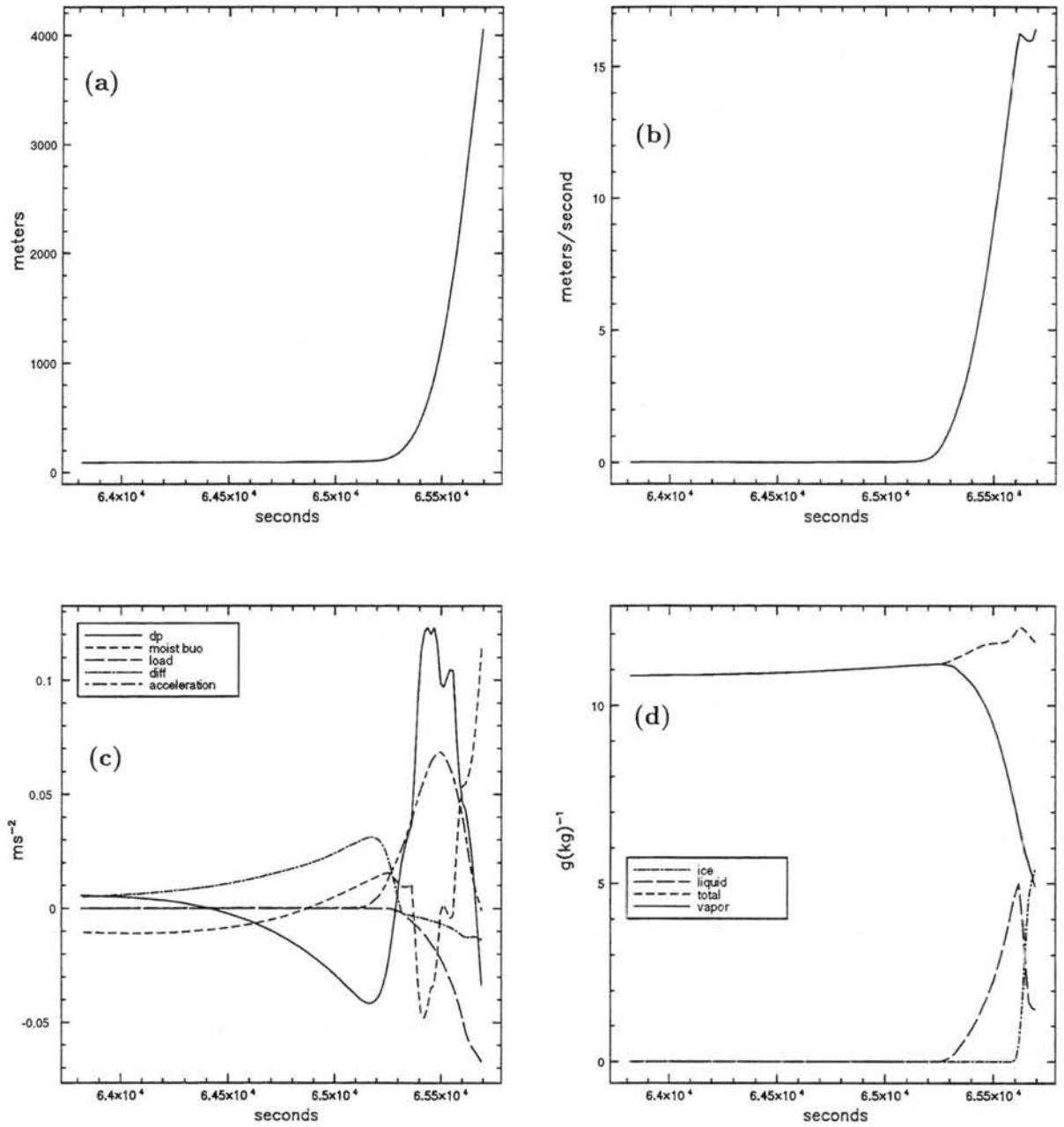
Figure 6.25: Time series (0543–0615 UTC) for night-time updraft parcel P1. a) height; b) vertical velocity; c) terms of vertical momentum equation; d) vapor, total, liquid and ice mixing ratios.
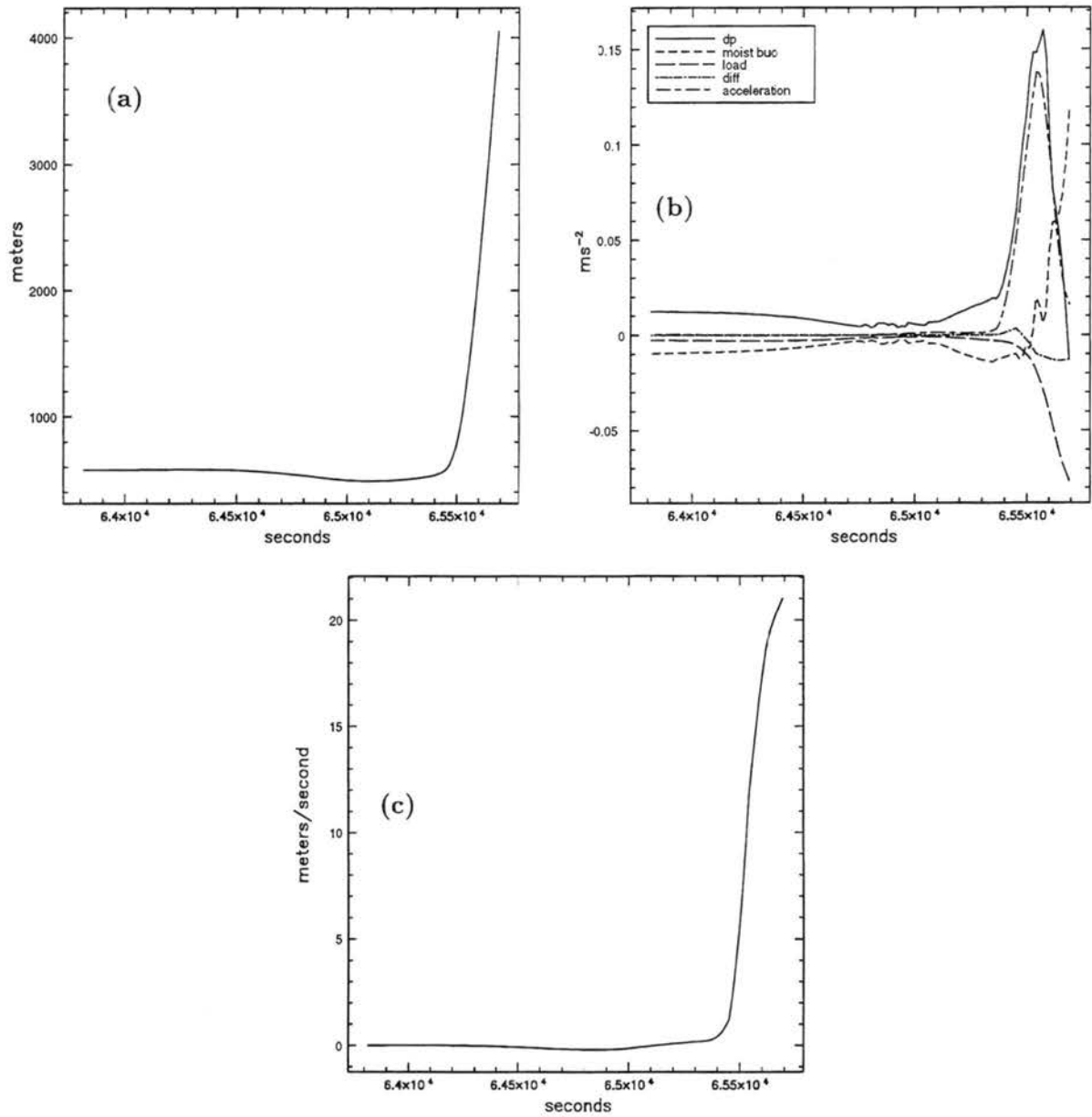
Figure 6.26: Time series (0543–0615 UTC) for night-time updraft parcel P3. a) height; b) terms of vertical momentum equation; c) vertical velocity.

6.7.2 Night–time Updraft

In this section we will discuss trajectories P1 and P3 (Figure 6.13) that compose the updraft at this time. P1 originates close to the ground and ends up in the southern part of the updraft, while P3 originates within the tongue of moist air flowing on top of the nocturnal stable layer.

P1 flows horizontally at a height of 100m (Figure 6.25a) towards the northwest, until it begins to ascend in the updraft, attaining an upward speed of 16.0 ms^{-1} (Figure 6.25b).

Figure 6.25c shows that P1's ascent is caused by a strong PGF. At 0607 UTC, and therefore before it starts ascending (which does not happen until 0608 UTC), P1 begins to experience an increasingly high PGF. In a few minutes, this force increases by 0.16 ms^{-2}. It is this very strong PGF that is responsible for pulling this parcel off the low level stable layer, leading it to reach the level of free convection. As it ascends, condensation occurs (Figure 6.25b) and 5.9 gkg^{-1} are transferred from vapor to condensate matter. The total water mixing ratio remains almost constant, indicating that mixing and precipitation processes are not very important. Up to 0613 UTC, or a height of 2600 m, all condensed water is in liquid form. After that, the liquid water content starts decreasing and the ice phase content increases. The balance of forces (Figure 6.25c) shows that in the initial portion of the ascent, through the stable layer, the buoyancy decreases sharply and becomes negative. As the parcel exits the stable layer, its buoyancy becomes large and positive. Buoyancy and PGF are strong enough to overcome loading, which increases as the parcel ascends and condensation takes place.

Parcel 3, that starts its trajectory further south (Figure 6.13) has a different history. As it begins to ascend (Figure 6.26a), its buoyancy becomes increasingly positive (Figure 6.26b), because it starts with high θ_e. The large buoyancy combines with an upward directed PGF to produce large accelerations and a vertical velocity of 21 ms^{-1} (Figure 6.26c).

6.8 Summary

As expected, the source of air for the regions of strong surface winds and for the updrafts and downdrafts of the storm is very complex. Usually, multiple sources of air are present, and in the previous sections representative trajectories were discussed.

The results show that the sources of air for the downdraft are different in the daytime phase of the system than in the night-time phase.

In the afternoon, two regions of downdraft were identified. They were classified according to their location as Northern Downdraft (ND) and Bow Downdraft (BD) in Section 6.3.1. The source of air for the ND is low level air from ahead of the storm, that is just at the saturation mixing ratio. As the air enters the storm, it gets loaded with rain and sinks. The source of air for the BD is located closer to the storm. Parcels get caught in the mesocyclone present at cloud base, undergo a path of half a circle in the counterclockwise sense, descend in the ND and then move to the BD. The highest horizontal speeds are actually located in the ND.

At night, the source of air for the downdrafts is located on the eastern flank of the storm. Parcels are strongly influenced by the low level mesocyclone. Their origin is in general quite low: not higher than 600m. The parcels ascend as they get close to the storm due to the upward π-gradient force. As they ascend, their buoyancy becomes negative (Figure 6.23e) and condensate loading also becomes an important negative acceleration. When the parcel is no longer under the influence of such a strong PGF, sinking occurs. This process closely resembles the *up-down* downdraft described by Knupp (1987, 1988).

The analysis also showed differences in the source of air for the updraft according to the time of the day. During the afternoon, because the PBL is well-mixed, parcels that originate at different heights within the PBL have the same buoyancy. Therefore, when subject to a PGF, they all have the same likelihood of ascending. During the ascent, the trajectories are subject to similar forces, regardless of where they initiated.

At night, the presence of a stable PBL influences the source of air to the updraft. Parcels originally within the stable layer have less buoyancy than parcels that originate above it. It is interesting to note, however, that in spite of the difference in buoyancy, the updraft is constituted by parcels that originate in both regions. The low pressure associated with the cloud core is capable of extracting parcels from the stable boundary layer, overcoming buoyancy and condensate loading.

One question that arises from this analysis is: if the PGF is strong enough to pull parcels off the nocturnal stable layer and incorporate them in the updraft, what differentiates

those parcels from the ones that also originate in the stable layer but end up constituting downdraft air?

Our analysis shows that the main difference is in the location of the parcels with respect to the the low level water condensate field. Parcels that originate in the stable PBL and end up constituting downdraft and updraft air are shown in Figures 6.9 and 6.12, respectively. Downdraft air originates ahead of the storm, and *crosses the bulk of the storm towards its back.* Therefore, it crosses the bulk of the precipitation field and becomes heavily loaded with precipitation. Figure 6.23f shows that for the downdraft parcel P4, total mixing ratio increases by 5.0 gkg^{-1} during its lifetime, indicating that the parcel is being highly influenced by its environment. The consequence of this increase in condensate is a strong downward acceleration due to loading: -0.05 ms^{-2}.

On the other hand, updraft air originates ahead of the storm, gets ingested on its eastern flank, and does not cross a region of the storm where high condensate mixing ratios exist. The lifetime of such a parcel can be divided in two parts: 1) the parcel is within the stable boundary layer; 2) the parcel has reached the level of free convection. While updraft parcel P1 (Figure 6.25) is *within* the stable layer, its total mixing ratio only increases by 1 gkg^{-1} and its condensate loading does not exceed -0.01 ms^{-2}. Therefore, the existent PGF is enough to counteract both negative buoyancy and condensate loading. As P1 exits the stable layer, its condensate loading continues to increase. From Figure 6.25 we note that the condensate mixing ratio reaches a maximum of 7.0 gkg^{-1}, which corresponds to a downward acceleration of -0.07 ms^{-2}. Since the total mixing ratio remains almost constant, it is clear that the condensate does not come from an exchange of mass with the environment, but from condensation within the parcel. Although the condensate loading reaches high values, the parcel achieves high positive buoyancy when it exits the stable layer. This is enough to compensate the loading and the result is a positive acceleration.

Chapter 7

THE ROLE OF THE STABLE BOUNDARY LAYER IN DERECHO DEVELOPMENT

7.1 Review of the Numerical Simulation

The goal of this research was to propose an explanation for the existence of strong, persistent strong line winds at the surface, associated with convective systems. To investigate this phenomenon, we focused on a case that took place on May 12 and 13, 1985. In this event, a convective system formed in SE Colorado in the afternoon, and propagated towards the northeast during the night, decaying over south Nebraska in the early morning. The system moved along a stationary front. Strong winds associated with the convective system were reported between midnight local time and sunrise.

Previous studies of derechos were used to identify which elements were most common to derecho cases: the presence of a stable boundary layer and of the LLJ. Our research then focused on those elements and on how they could physically explain the strong winds.

The problem of derecho development and maintenance is inherently multi-scale. Convective winds and downdrafts depend on synoptic and mesoscale characteristics. To incorporate the different scales, four telescopically nested grids were used in a primitive equation Eulerian model to do a simulation of this case. The grids resolved circulations from the synoptic scale down to cloud scale. A bulk microphysics parameterization was used to represent the moist processes, and no cumulus parameterization was employed.

The model represented well the mesoscale environment of the storm, as well as storm characteristics. Lack of data on the storm scale prevented a more thorough comparison of model results with observations.

The simulation showed that the system began developing on the afternoon of May 12 and persisted through the evening. It formed on the eastern side of an upper level trough,

a baroclinic region in which vertical shear was significant and the upper level winds were strong, a situation favorable for large scale upward motion. A weak stationary front was present at the surface, and the convective system developed on its cold side, a region of moderate vertical instability during the day.

The system was composed of several cells. Initially (e.g. at 00 UTC), the cells were aligned in the north-south direction and all cells had roughly the same intensity. Later (e.g. at 03 UTC), the cells were aligned on the east-west direction, and the easternmost cell was the most intense. This cell produced the strong winds in the simulation, which were sustained above 22 ms^{-1} from 03 to 10:30 UTC.

The cell that was responsible for the strong winds had characteristics of a HP supercell. In the afternoon it had moderate mid-level vertical vorticity, up to 5.5×10^{-3}s^{-1}. In the evening, the vorticity increased to 10^{-2}s^{-1}. The cell had a comma shape, with a large head on its northern portion. The southern part of the cell presented a bulge forward, with rear inflow on the upshear side. Figure 7.1 shows conceptual models of the daytime and night–time phases of the storm, illustrating the main circulation branches.

The strongest surface winds were northwest outflow winds on the back of the storm. Their direction follows the mid-level northwest branch of the mesocyclone, indicating that some downward momentum transfer is taking place. This transfer is not essential for the strong wind development, though. Horizontal wind speed and kinetic energy increase in the downdraft as the parcel gets close to the surface, indicating that local generation of momentum is important. This process will be discussed further in Section 7.3.

7.2 Night-time environment and its influence on storm scale circulations

In Chapter 5 we showed that this persistent storm was under the influence of two distinct environments, one during the day and one at night. During the day a well mixed deep and dry boundary layer was present. At night, the surface cooled, and a LLJ developed, causing a low level inversion to form. This inversion was 700m deep in the model, and determined the top of a cool, moist boundary layer.

This change in environment had a large impact in cloud scale circulations. The trajectory analysis presented in Chapter 6 showed that, during the day, downdraft air came from mid levels, and sank due to evaporative cooling and condensate loading. The downdrafts
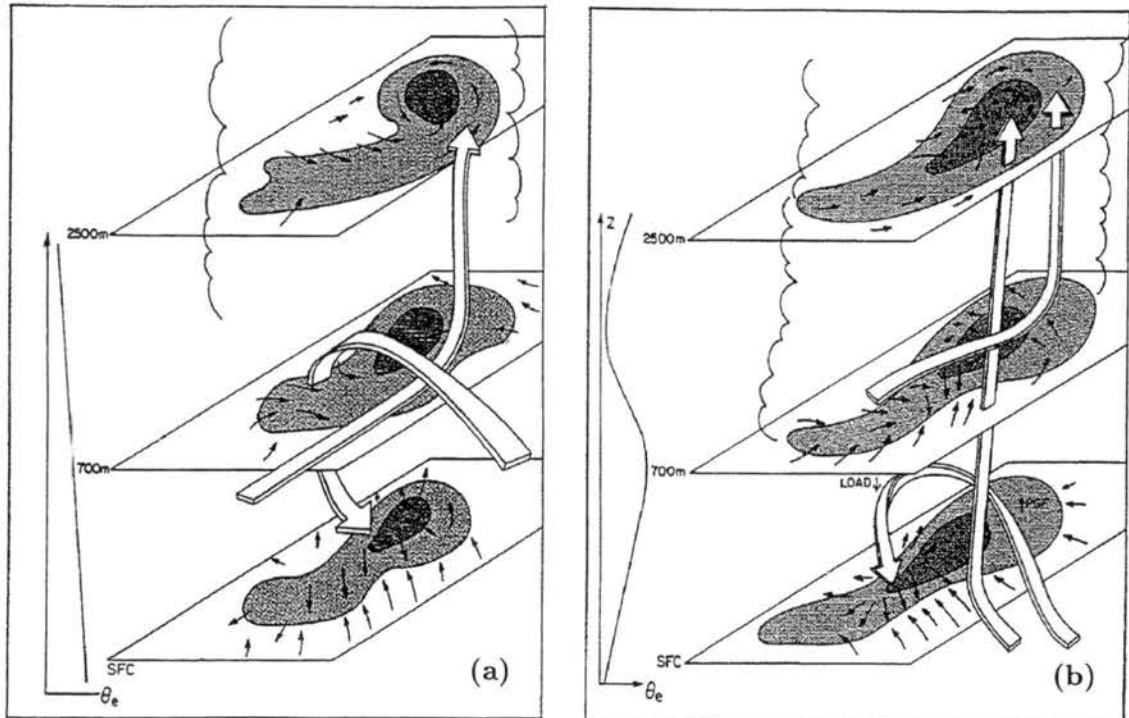
Figure 7.1: Conceptual model of the a) daytime and b) night-time phases of the MCS. The three planes are located at the surface, 700m and 2500m height. The shaded field in each plane is the condensate mixing ratio and the thin arrows are the ground relative winds. The thick arrows represent the main branches of the updraft and of the downdraft. The plot on the left of each sketch depicts the vertical profile of equivalent potential temperature. In b) the locations of the upward π-gradient force and condensate loading that act on the up–down downdraft are noted.
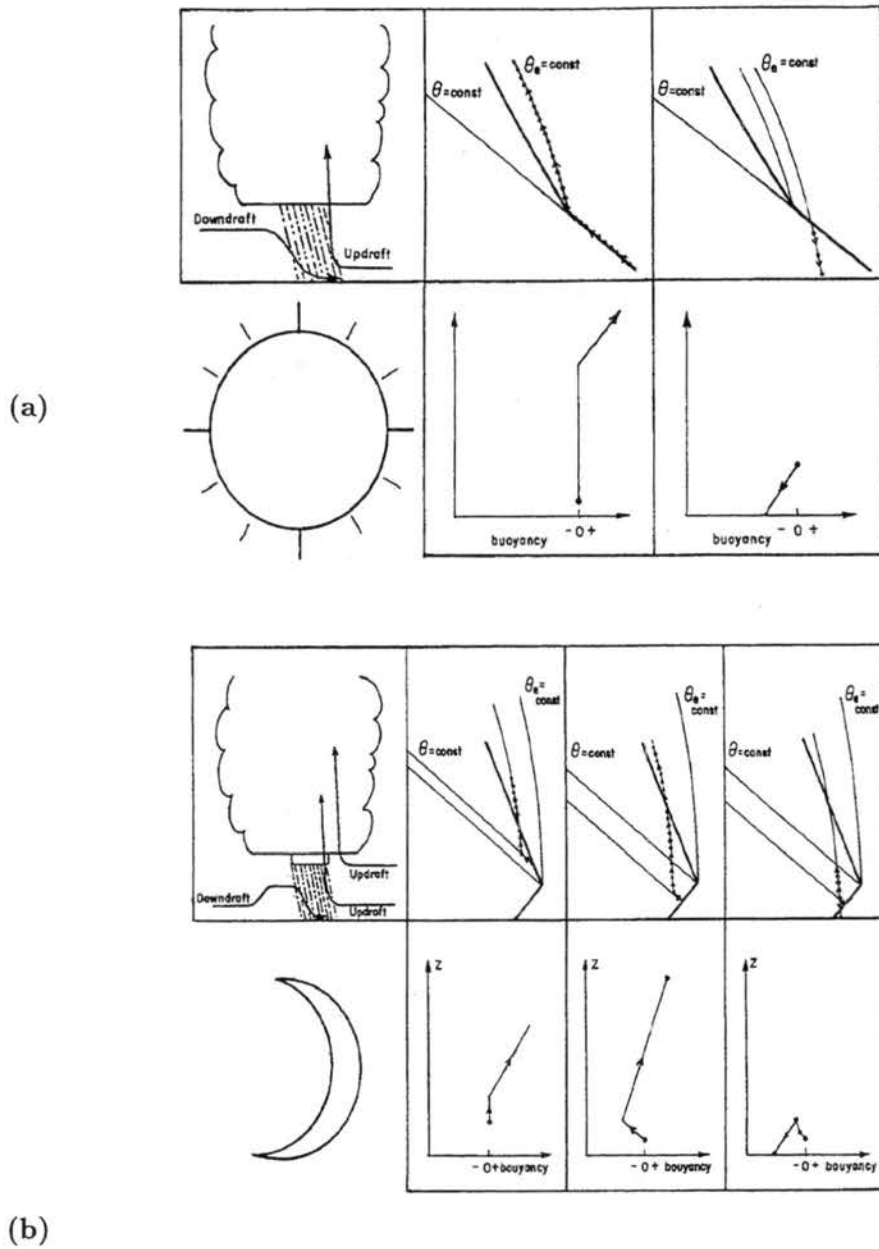
Figure 7.2: Diagram illustrating properties of idealized updraft and downdraft parcels at a) daytime and b) night-time. The trajectory location with respect to the cloud is shown on the left. The top right sketches are Skew-T diagrams, illustrating thermodynamic properties of the environment and of the parcels, whose trajectories is represented by dots and arrows. The bottom right sketches are vertical profiles of total buoyancy (including vapor effects and condensate loading) along the parcels' paths.

were saturated, and became colder than their environment as they descended.

At night the source of downdraft air shifted to near the ground. Parcels ascended through the stable boundary layer because a strong upward–directed pressure gradient force was present. As they ascended, they became colder than the surrounding environment. Also, they became loaded with condensate and those two processes acted to increase the parcels' negative buoyancy. Once the loading became too large, or the parcels reached a region of the storm in which the PGF was not as strong, they sank. As they sank, they warmed up, which caused their buoyancy to become near zero or even sometimes positive, but not positive enough to reverse their vertical velocity. Indeed, some of the parcels studied here arrived at the ground warmer than the environment.

This process is illustrated in Figure 7.2, which shows idealized environmental temperature profiles and parcel trajectories for daytime and night-time. During the day (Figure 7.2a), a well mixed PBL existed under cloud base. Updraft and downdraft parcels originated there. Updraft parcels became positively buoyant once they condensed and reached the level of free convection. Downdraft parcels were negatively buoyant because of evaporative cooling and condensate loading.

During the night (Figure 7.2b), a low level stable boundary layer developed, topped by a layer of reduced stability. The figure shows two different parcels that composed the updraft, and one that composed the downdraft. Updraft air sometimes initiated above the stable layer, and the parcels immediately became positively buoyant. Some of it also started within the stable layer. In that case, it had to overcome a stretch of negative buoyancy before it could freely ascend. Downdraft air also originated within the stable layer, but because of the rain shaft, condensate loading occurred on the parcel, its negative buoyancy became very large, it never exited the stable layer and ended up sinking.

It is interesting to contrast the process of downdraft formation described here with the one described by Bernstein and Johnson (1994) as responsible for the "heat bursts", episodes of sudden warming associated with MCSs that also occur in an environment of low level stability. In the case described by them, a well-mixed layer existed on top of the stable layer. In their conceptual model, they showed a branch of the MCS circulation that entered the storm at mid-levels. Parcels in this lateral-inflow were cooled due to the evaporation

of precipitation and sank, acquiring enough momentum to go through the stable layer and reach the surface. Although Bernstein and Johnson (1994) did not address this point, it is possible that in the case studied by them some up–down downdraft dynamics was taking place.

It is also worth pointing out the differences between the case we present and the situations discussed by Knupp (1987, 1988). The up-down trajectories discussed by him occurred in daytime cases in which the boundary layer was dry and well-mixed (see Figure 16 of Knupp 1988). Therefore, as the parcels ascended in the upward branch of the up-down downdraft, their negative buoyancy was caused by evaporation and melting of precipitation. In our case those processes are less important because the low levels are very moist and the ascent is saturated. This can be seen in Figure 6.23 which shows that as the parcel ascends, its potential temperature increases due to condensation. Negative buoyancy occurs because the ascent takes place in a stable PBL, in other words, it is mainly due to a change in the environment and not in the parcel.

7.3 Generation of strong winds

The strong surface winds during the night were from the northwest, and diverged out of a center of high pressure located at the surface (Figure 5.43). The high pressure was co-located with the downdraft, and was dynamically caused by a deceleration of the downward motion. A center of hydrostatically-induced low pressure was located at the surface east of the region of the strong winds, ahead of the band of surface updraft. This low pressure, however, did not act to accelerate the outflow winds, responsible for the derecho. As can be seen in Figure 5.43 the winds over the low-pressure center were from the southeast, according to the environmental winds at the surface. When the parcels associated with the environmental southeasterlies reached the western part of the low, they were decelerated, but their direction was not reversed. This flow met the northwest downdraft outflow *to the west of* the pressure gradient associated with the hydrostatic low. Parcels that descended in the downdraft did not reach the gradient associated with the hydrostatic low and therefore were not influenced by it.
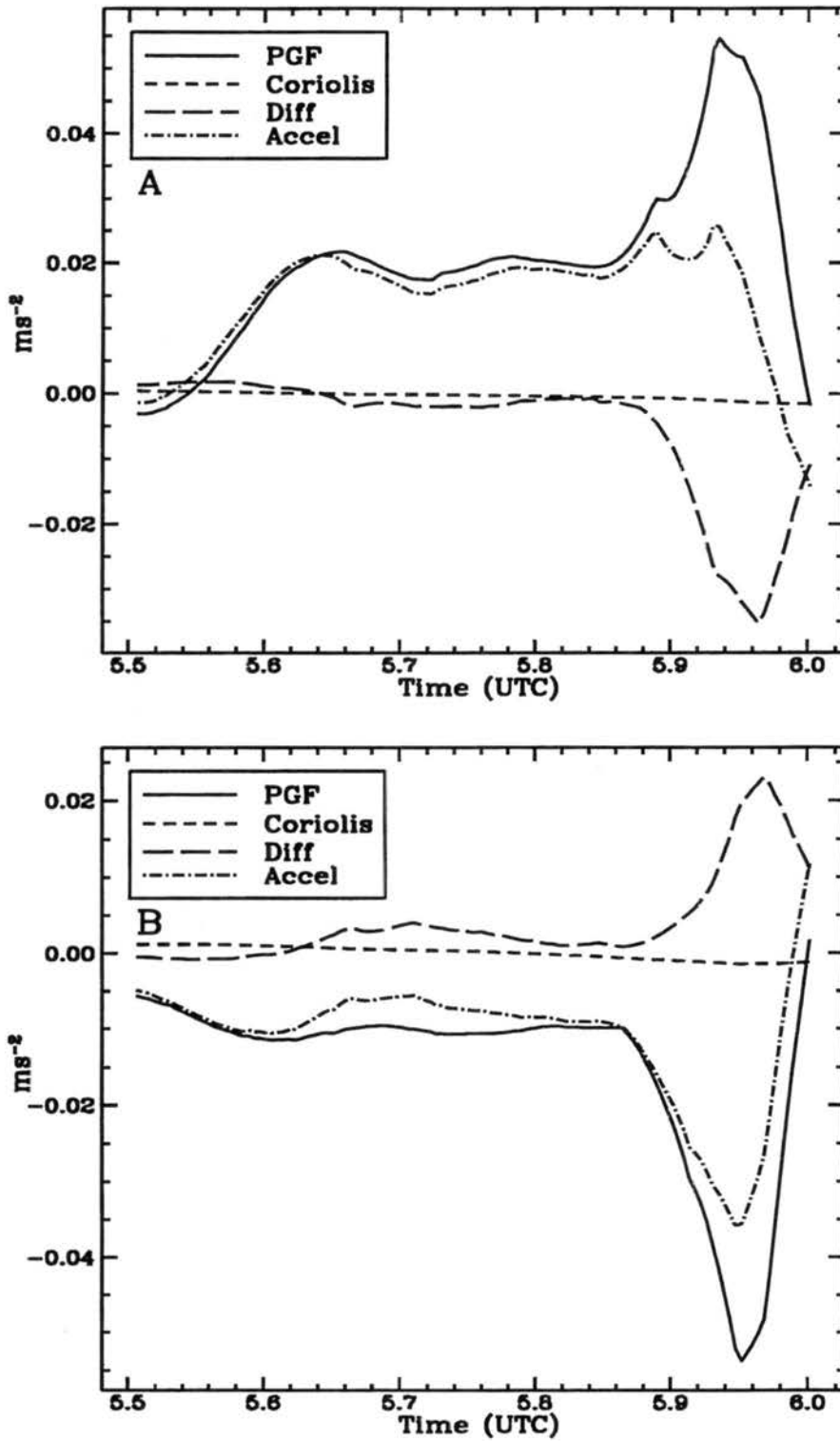
Figure 7.3: Time series (0530–0600 UTC) for night–time downdraft parcel P4. a) Terms of the zonal momentum equation; b) Terms of the meridional momentum equation.

To illustrate this idea, nocturnal downdraft P4's trajectory may be taken as an example. The parcel started its descent at 0545 UTC, and between 0546 and 0558 its horizontal speed increased from 4 to 25 ms^{-1} (Figure 6.23c). The horizontal acceleration acting on this parcel may be expressed as

$$\frac{du}{dt} = PGF + CORIOLIS + DIF,$$
$$\frac{dv}{dt} = PGF + CORIOLIS + DIF,$$

which are equations similar to the previously presented vertical balance of forces 6.4.

Figure 7.3a,b shows the terms of the equations above for P4. The parcel accelerated due to a PGF, which had peak values of 0.055 ms^{-2} in the x–direction and -0.055 ms^{-2} in the y–direction. If those were the only forces present, the parcel would have accelerated a lot during the 30 minutes its trajectory lasted. The Coriolis acceleration gave a very small contribution to the horizontal balance of forces, as is expected in this small scale. But diffusion acted strongly to reduce the wind speed, and therefore peak net accelerations were 0.025 ms^{-2} in the x–direction and -0.035 ms^{-2} in the y–direction, enough to accelerate the parcel by 21 ms^{-1}.

The horizontal PGF can be seen again in Figure 7.4a,b, which shows horizontal cross-sections of the perturbation pressure field at 0549 and 0557 UTC, respectively. Superposed on the Eulerian field is nocturnal downdraft trajectory P4. The square mark on the trajectory represents the location of the parcel at each time. The cross-sections were taken at the height of the parcel at each time: 48 m in a) and 396 m in b). This figure supports the idea that the parcel was accelerated by the pressure gradient associated with the high pressure on the northern part of the cell, and not by the mesolow ahead of the storm.

The origin of the horizontal PGF was investigated using the technique described in Chapter 2 (Equations 2.15—2.19), in which the Laplacian of the pressure perturbation is decomposed into 2 main terms, one associated with buoyancy and the other with the wind field. The part associated with the wind field is decomposed into a linear and a non-linear part. The latter is further decomposed into terms associated with horizontal vorticity, vertical vorticity, deformation, and fluid extension.
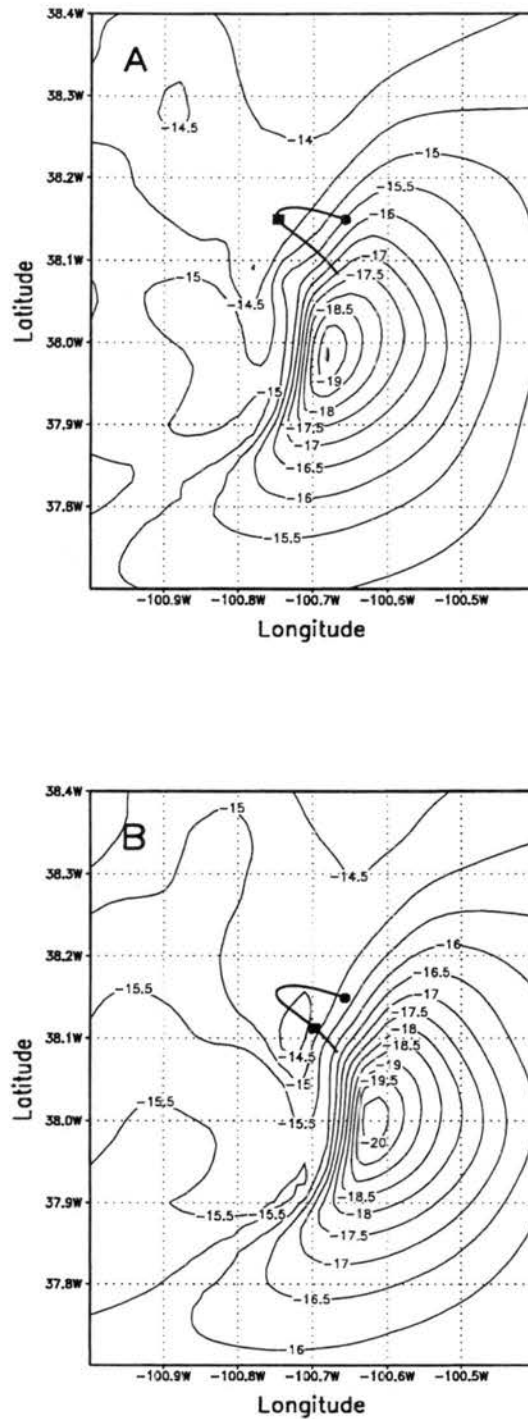
Figure 7.4: Pressure perturbation (hPa) at a) 0549 UTC and $\sigma=232$m and b) 0557 UTC and $\sigma=48$m. The thick line is the projection of the trajectory of night–time trajectory P4 from t=0530 to t=0600 UTC. The circle marks the beginning of the trajectory, and the square marks the position of the parcel at the time the pressure field is depicted.

Figure 7.5: Pressure perturbation (hPa) obtained from the model (shaded) and a) sum of forcing terms of the pressure perturbation equation (contoured); b) fluid extension term of the pressure perturbation equation (contoured) at 0600 UTC and σ=48m.
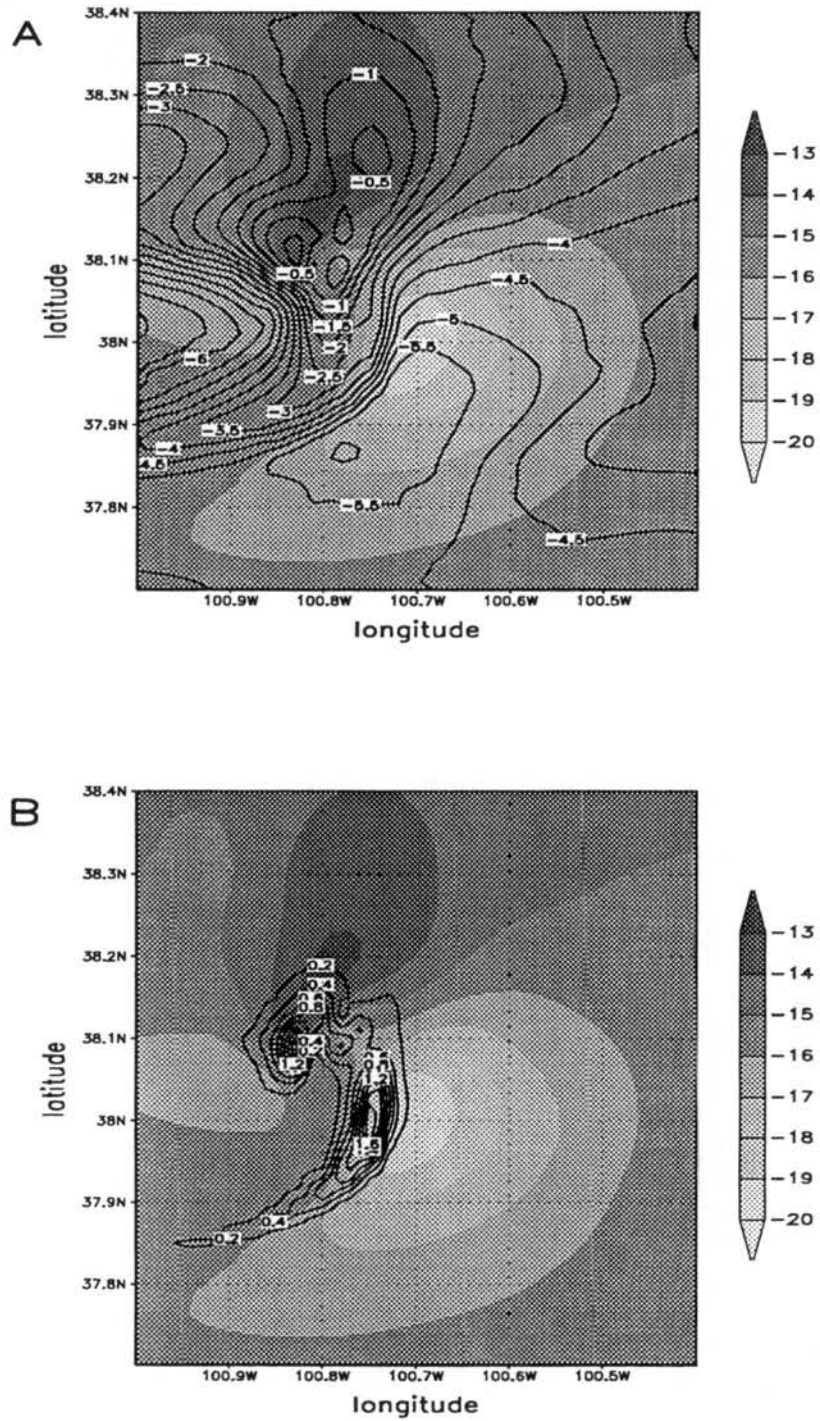
$$P' \quad \alpha \quad P'_{VVORT} + P'_{HVORT} + P'_{DEF} + P'_{EXT} + P'_{LINEAR} + P'_{BUO}. \tag{7.1}$$

Figure 7.5a shows a comparison between the pressure perturbation computed by the model and the one retrieved from the equation above. Although the derivation of this form of the pressure perturbation equation assumes an inviscid, incompressible fluid, the decomposition represents well the model's pressure perturbation gradients. An inspection of the different forcing terms shows that the largest contribution to the southern part of the surface high pressure (which is associated with the strong winds) comes from the fluid extension term, related to the deceleration of the downdraft (Figure 7.5b).

7.4 Buoyancy

In this section, a detailed analysis of the buoyancy and other terms of the vertical momentum equation for nocturnal downdraft parcel P4 are presented. This parcel originated at a height of 213m, ascended to 588m and then descended to the surface. As it started it did not have significant condensate mixing ratio; it was just at saturation, with a total mixing ratio of 10.4 gkg^{-1}. As it ascended, its total mixing ratio increased to 15.4 gkg^{-1} and its condensate mixing ratio amounted to 5.0 gkg^{-1}. During the ascent, about 0.5 gkg^{-1} from the parcel condensed into liquid water. As a consequence, the parcel's temperature, originally at 296.1 K increased 1.4 K.

To simplify this analysis, we assume here that the parcel undergoes isobaric condensation. In the absence of mixing, precipitation or other diabatic processes, its temperature increases due to the release of latent heat, its vapor content decreases and its condensate mixing ratio increases, such as to keep the total water constant. These three factors affect buoyancy, that undergoes a positive tendency due to warming and a negative tendency due to the shift of water from vapor to condensate. The overall effect of this process is an increase in buoyancy, as shown in the derivation below.

Total buoyancy, B_T is given by

$$B_T = g \left[\frac{\theta_v - \bar{\theta}_v}{\bar{\theta}_v} - r_{co} \right]$$

$$= g\left[\frac{\theta(1+0.61r_v)-\bar{\theta}_v}{\bar{\theta}_v}-r_{co}\right]$$

$$= g\left[\frac{\theta+0.61\theta r_v-\bar{\theta}_v}{\bar{\theta}_v}-r_{co}\right]$$

$$= g\left[\frac{\theta}{\bar{\theta}_v}+\frac{0.61\theta r_v}{\bar{\theta}_v}-r_{co}-1\right]. \tag{7.2}$$

To obtain a *back-of-the-envelope* estimation of the amounts involved, we took the partial derivatives of 7.2 and plugged in representative amounts.

$$\frac{\partial B_T}{\partial \theta} = g\left(\frac{1+0.61r_v}{\bar{\theta}_v}\right). \tag{7.3}$$

$$\frac{\partial B_T}{\partial r_v} = g\left(\frac{0.61\theta}{\bar{\theta}_v}\right). \tag{7.4}$$

$$\frac{\partial B_T}{\partial r_{co}} = g. \tag{7.5}$$

Using downdraft parcel P4 as an example, a potential temperature of θ=296K, vapor mixing ratio of r_v=10.5 gkg^{-1} and no condensate were used. The virtual potential temperature of this parcel was therefore θ_v=297.89K, which was also the virtual potential temperature of the environment ($\bar{\theta}_v$).

Using these numbers Equations (7.3—7.5) become

$$\frac{\partial B_T}{\partial \theta} = 9.8\frac{1+0.61\times0.0105}{297.89}$$

$$= 3.33\times10^{-2}\text{ms}^{-2}\text{K}^{-1}. \tag{7.6}$$

$$\frac{\partial B_T}{\partial r_v} = \frac{9.8\times0.61\times296.0}{297.89}$$

$$= 5.94\text{ms}^{-2}(\text{kgkg}^{-1})^{-1}. \tag{7.7}$$

$$\frac{\partial B_T}{\partial r_{co}} = -9.8\text{ms}^{-2}(\text{kgkg}^{-1})^{-1}. \tag{7.8}$$

This parcel underwent isobaric condensation on its ascent, and 0.5 g of total water mixing ratio left the vapor category to the condensate category. The amount of heat released (ΔQ) by this process is given by the latent heat of condensation $L = 2.5 \times 10^6$ Jkg^{-1}. The associated warming of the parcel (dT) is given by

$$
\begin{aligned}
dT &= \frac{\Delta Q}{m_{air} c_p} \\
&= \frac{L m_{vapor}}{m_{air} c_p} \\
&= \frac{2.5 \times 10^6 J kg^{-1} \times 0.5 \times 10^{-3} kg}{1 kg \times 10^3 J kg^{-1} K^{-1}} \\
&= 1.25 K.
\end{aligned}
$$

Since the process is isobaric, $dT = d\theta$ and Equations (7.6)–(7.8) become

$$
\begin{aligned}
\Delta B_T^{\theta} &= 3.3 \times 10^{-2} \text{ms}^{-2} \text{K}^{-1} \times 1.25 K = 4.125 \times 10^{-2} \text{ms}^{-2}. \\
\Delta B_T^{r_v} &= 5.94 \text{ms}^{-2} \text{kgkg}^{-1} \times (-0.0005) = -2.97 \times 10^{-3} \text{ms}^{-2}. \\
\Delta B_T^{r_{co}} &= -9.8 \text{ms}^{-2} \text{kgkg}^{-1} \times 0.0005 = -4.9 \times 10^{-3} \text{ms}^{-2}.
\end{aligned}
$$

These numbers show that the process of condensation alone tended to increase buoyancy:

$$
\begin{aligned}
\Delta B_T^{total} &= \Delta B_T^{\theta} + \Delta B_T^{r_v} + \Delta B_T^{r_{co}} \\
&= 4.125 \times 10^{-2} - 2.97 \times 10^{-3} - 4.9 \times 10^{-3} \\
&= 3.33 10^{-2} \text{ms}^{-2}.
\end{aligned}
$$

However, in the night-time downdraft trajectories discussed in Chapter 6, two other processes were taking place. One is that the parcel ascended in a stable boundary layer. Therefore, $\bar{\theta}_v$ was not constant, but increased with height, which caused the parcel's buoyancy to decrease as it ascended.

The second process taking place involved mixing. The parcel contained zero or almost zero condensate mixing ratio when it was far from the cloud. As it got near the cloud, it underwent mixing with air that had large condensate amounts and went through a precipitation shaft. Those two processes caused the total mixing ratio of the parcel to increase.

Indeed, these processes can be seen in our results. Referring back to Figure 6.23, as that parcel ascended, from t=0530 to 0545 UTC, its potential temperature did increase by

1.4K (from 296.1 to 297.5K). But the environment's potential temperature increased much faster: by 3.3K, from 296.2 to 299.5K. Also, in that same period, the total water mixing ratio of the parcel increased by 3.5 gkg^{-1}, from 10.2 to 13.7 gkg^{-1}.

The result is that seen on Figure 6.23e, total buoyancy (including condensate loading) decreased by 0.105 ms^{-2}. The parcel's cooling with respect to its environment contributed more to the development of negative buoyancy than condensate loading during the ascent period. This was valid for all downdraft parcels that originated near the ground, and demonstrates that the process of saturated ascent within a rain shaft in a stable environment led to the accumulation of large negative buoyancy. The stable layer played a fundamental role as an "infinite" supply of stable air and the limiting factor for this downdraft process is the presence of a thunderstorm above the stable boundary layer. And that is guaranteed, as discussed before, by the elevated LLJ that destabilizes the thermodynamic profile.

7.5 The updraft

The key to determine whether a parcel that originated within the stable layer ended up composing updraft or downdraft air is the precipitation. If the parcel remained too long within a rain shaft, it ended up with large negative buoyancy and sank.

During the day, because the boundary layer was well-mixed, saturated parcels that ascended became positively buoyant. This is the traditional concept of updraft formation. Parcels only needed to ascend up to the lifting condensation level, because it coincided with the level of free convection. No further forced lifting was required.

During the night, a different process occurred. Free ascent in conditions of positive buoyancy occurred only for parcels that originated above the stable layer. With the development of the nocturnal LLJ, high equivalent potential temperature air was present above the PBL, and those parcels could ascend freely. But not all updraft parcels originated above the PBL. Contrary to our original expectations, we did find that some parcels originated within the stable layer.

Parcels that originated within the stable layer, be they updraft or downdraft parcels, experienced negative buoyancy as they ascended. What differentiated the two parcels was condensate loading. Updraft parcels originated ahead of the storm and got ingested in their

eastern flank. They did not go through the precipitation shaft and did not get loaded with condensate. Therefore, only a weak mid-level PGF was needed in order to pull the parcels off the stable layer.

7.6 The source of the upward pressure gradient force

One question that we are leaving unanswered is the origin of the pressure gradient force that pulls the parcels off the stable boundary layer. In this section we speculate about its origin, based on the results of our simulation and of other work in the literature. There are 3 possible explanations for this force: 1) A hydrostatic mid-level low pressure associated with the warm column represented by the cloud; 2) A dynamic low pressure associated with the flow field in the storm; or 3) A low level gravity wave.

All three are plausible explanations. A horizontal cross-section of pressure through the storm at mid-levels, shows that it corresponds to a region of low hydrostatic pressure. This occurs because as parcels ascend in the updraft, condensation and freezing release latent heat, causing the thickness of the column to expand. This process translates to the development of a low level pressure deficit. In our simulation, this caused parcels that were approaching the storm with the low level southeasterlies to accelerate horizontally towards the storm and to be ingested by it.

Rotation in the storm can also lead to a low-level upward-directed PGF. From Rotunno and Klemp's (1982) work (see Chapter 2), we know that mesocyclones are associated with regions of low pressure. They used this argument to explain thunderstorm splitting. In his studies of derechos, Schmidt (1991) performed three-dimensional numerical experiments initialized with a horizontally homogeneous environment, using either a straight–line hodograph or a turning hodograph. The experiment with the rotating hodograph generated a rotating storm that had asymmetric surface patterns, including strong NW winds on the back of the storm, as the observations had shown. With the straight line hodograph, the storm did not develop rotation, the outflow winds were westerlies and not as strong.

Our simulation revealed that in the 12–13 May 1985 case a storm with strong rotation developed (vorticity up to $10^{-2}s^{-1}$). To assess the importance of the dynamic pressure in our simulation, we compared the location of the mesocyclone with that of the pressure

minimum, just above cloud base. The two features were not obviously co-located. Large values of vorticity occurred in an elongated band that matched the updraft of the storm. Lowest pressure was found in a region approximately circular, on the northern part of the storm. This indicated that while rotation may have had an impact in lowering the pressure in the storm, it was not the only mechanism.

A gravity wave is also a possible mechanism to lift the parcels off the stable layer. The convective system developed within a stable layer, which is an environment favorable for a gravity wave. Schmidt and Cotton (1990) performed two-dimensional experiments using the thermodynamic profile of a pre-derecho environment in North Dakota. They showed that a gravity wave propagated in low levels within the stable layer. Depending on the shear profile used, the gravity wave would propagate away from the storm, or remain in phase with the storm. If the wave stays in phase, it can force parcels off the boundary layer and through a region of high condensate mixing ratio. As the parcel migrates towards the back of the storm and recedes from the influence of the gravity wave, the negative buoyancy associated with the sinking translates into a strong downdraft.

As discussed in Chapter 2, Schmidt and Cotton (1990) attributed the low-level gravity wave to the presence of an adiabatic layer on top of the stable layer, which would act to prevent the upward propagation of the wave. It is important to notice that in this case, a deep adiabatic layer was *not* present (Figure 6.17). Therefore, a possible gravity wave present here has a trapping mechanism different than the one proposed by Schmidt and Cotton (1990) (see discussion in section 2.7.

In the next section, a preliminary attempt to investigate the nature of the gravity waves supported by this environment is presented. But before that, the nature of the pressure perturbation we will addressed using the decomposition discussed in Chapter 2 and expressed in Equation 7.1. Figure 7.4a shows a comparison of the pressure perturbation from the model and the one retrieved from Equation 7.1. The agreement is best in the region of the mesolow, and loses quality to the southwest of the mesolow. The forcing terms of the pressure perturbation equation are shown in Figure 7.4b–g. The only terms
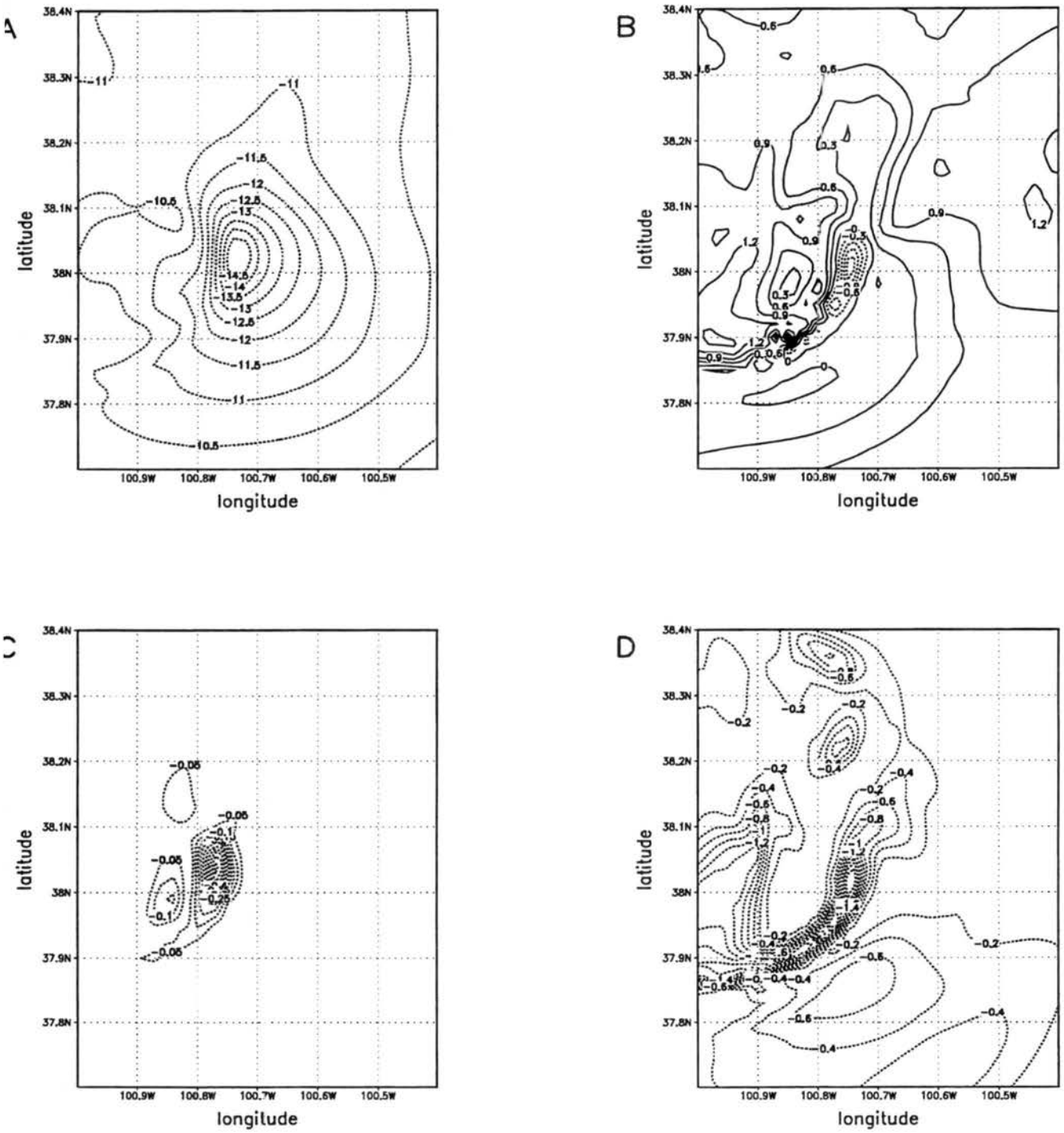
Figure 7.6: a) Pressure perturbation (hPa) from the model; b) Sum of forcing terms of the pressure perturbation equation; c) Vertical vorticity forcing; d) Horizontal vorticity forcing; — continues on the next page.
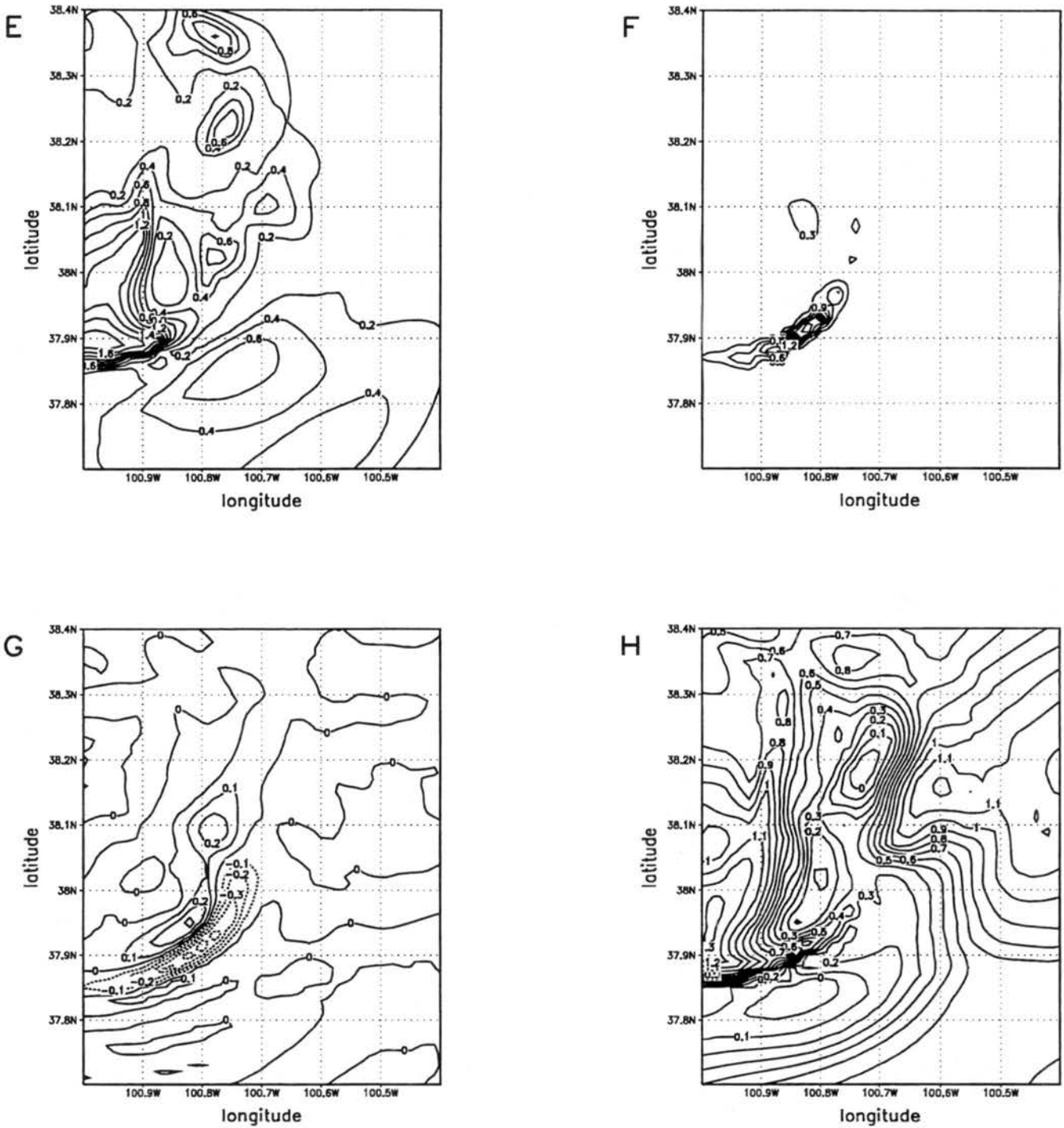
Figure 7.4: — continuation. e) Deformation forcing; f) Fluid extension forcing; g) Linear forcing; h) Buoyancy forcing at t= 0600 UTC and σ=3381m.. All forcing fields are in $10^{-4}s^{-2}$.

that can contribute to a negative pressure perturbation are P'_{VVORT}, P'_{HVORT}, P'_{LINEAR} and P'_{BUO}, since P'_{DEF} and P'_{EXT} are the square of a quantity. The figure shows that the terms associated with the perturbation vertical and horizontal vorticity are the most important term associated with the mesolow, pointing to the importance of the mesocyclone and of the shear associated with the updraft in lowering the pressure. The third term in importance is the linear term, which is associated with a low pressure perturbation downshear of the updraft. Finally, buoyancy acts only to produce positive pressure perturbation at these levels. In the region of the mesolow, the contribution from buoyancy is not very large though.

7.6.1 Idealized Simulation to Investigate Gravity Waves

To investigate the possibility of gravity waves in the nocturnal environment of the storm, a two-dimensional version of the RAMS model was initialized horizontally homogeneous with the thermodynamic sounding depicted in Figure 6.17. Only the zonal component of the winds from the sounding was included in the initialization. The grid spacing used was identical to that of the three-dimensional simulation described in Chapters 4 and 5.

To simplify the problem, several physical parameterizations were omitted. The model had no soil or vegetation model, no surface fluxes of latent and sensible heat, no topography, no radiation and no microphysics. The cloud was simply represented as an erect heat and cooling source, following Pandya and Durran (1996).

The model was integrated for two hours, and the results showed the propagation of two deep tropospheric gravity waves away from the region of heating, in the positive and negative x-directions. These waves occupied the whole depth of the troposphere (h_t) and had a vertical wavelength of ($2h_t$). They are similar to the waves that Nicholls et al. (1991), Mapes (1993) and McAnelly et al. (1997) termed the $n1$ mode.

Following the first waves, two other waves began to propagate horizontally, with a wavelength of (h_t). They were analogous to the $n2$ mode described by the authors above. It was interesting to note that only the wave that was moving in the negative x–direction moved away from the cloud. The wave that was moving in the positive x–direction remained

co-located with the storm. The net effect of this stationary wave at low levels was an upward bulge in the the low level isentropes, and consequent upgliding of air.

This experiment shows that this environment was supportive of gravity waves and that they may have played a role in lifting the parcels off the stable layer. These waves, as discussed by Mapes (1993) are quasi–horizontal and differ from the oscillatory simple view of a monochromatic gravity wave. The gravity wave emitted was not confined to the lower stable layer, but occupied the whole depth of the troposphere. Bretherton and Smolarkiewicz (1989) point out that these waves with little vertical structure are well described by the hydrostatic approximation and are therefore almost non-dispersive. This can explain their longevity, even in the absence of an adiabatic layer in the mid-troposphere.

Chapter 8

SUMMARY AND FUTURE WORK

In this chapter, we outline the most important findings of our work and some possibilities for future work.

8.1 Summary

- The three-dimensional synoptic-scale and meso-scale environments, which include the low-level jet, fronts and synoptic scale troughs, are very important to convective organization and to the characterization of cloud dynamics in this case. Differences between the daytime and night-time environments determine two "phases" of the MCS, termed "daytime" and "night-time" phases.

- After the MCS forms in mid-afternoon in eastern Colorado, it goes through the daytime phase. It is composed of a series of convective cells of similar strength, aligned roughly in a north–south line, propagating in a region where the boundary layer is well mixed. Only small amounts of rotation are present in the storms.

- In the day-time phase, downdrafts are generated as air within the boundary layer approaches the storm and cools due to evaporation and melting of hydrometeors. The lower temperature of the cooled parcels and the presence of condensate loading contribute to negative buoyancy, which causes the parcels to descend in a downdraft. The negative buoyancy is maintained all the way to the ground, because the boundary layer has constant potential temperature.

- The cold downdraft air reaches the surface, forming a cold pool which spreads slightly ahead of the parent convective cloud. Surface parcels are lifted on the leading edge of the cold pool, where the outflow converges with the environmental flow. The

lifted parcels rise neutrally on the boundary layer, and become positively buoyant as condensation and latent heat release take place.

- As the sun sets, the surface starts to cool due to the loss of longwave radiation. A shallow stable layer develops on the north side of the cold front. Also, a low level jet develops and flows on top of the surface front, transporting warm, moist air to higher latitudes.

- The low–level jet arrives at the MCS region one kilometer above the ground. It contributes greatly to storm intensity by maintaining a source of energy for this storm.

- With this new environment, the convective system enters its nocturnal phase. The convective cells become organized in an east-west line that moves east, with the leading cell being the strongest one. Strong mid-level rotation develops in this storm. The rain pattern develops a bow shape with midlevel inflow in the back, and the storm resembles a high-precipitation supercell.

- At this time, the most important source of air to the convection is located on top of the boundary layer. Although the main source of air for the cloud is elevated, some boundary layer air gets displaced upwards due to a pressure gradient force. As this air ascends through the stable boundary layer, it undergoes condensation. However, the latent heat release is not enough to overcome the effects of the stable layer, and the air parcels become colder than their environment and therefore negatively buoyant.

- If the parcels remain under the influence of the pressure gradient force long enough to move upwards and exit the stable layer, they may become positively buoyant and end up composing the cloud's updraft. Therefore, the night-time phase updraft is composed of air from the top of the PBL and air that originates in an elevated layer.

- If the parcels do not remain under the influence of the pressure gradient force long enough, or if they cross a precipitation shaft and become loaded with hydrometeors, negative buoyancy becomes the predominant acceleration in the vertical momentum equation, and the parcels sink. This is the main mechanism of downdraft generation at night–time.

- The deceleration of the downdraft generates a region of high-pressure perturbation in the lowest kilometer of the atmosphere. As parcels go through the up–down trajectory, they spend ten or more minutes in a region of strong horizontal pressure gradient associated with this meso-high, and accelerate to strong horizontal wind speeds.

- Results indicate that the midlevel pressure gradient force that pulls the parcels out of the stable boundary layer is partially caused by rotation associated with the meso-cyclone of the storm. It also receives contributions from perturbation horizontal vorticity and from the interaction between the environmental shear and the updraft. It is possible that perturbation winds associated with a gravity wave are responsible for part of the negative pressure perturbation.

8.2 Future Work

- In this study, we have identified the mechanism of strong wind generation for one case. Other cases must be modeled to establish if this mechanism is relevant to a majority of cases. In particular, it would be of interest to study a case that formed under a more typical environment of derecho, that is, under 500 hPa northwest flow.

- Further observational studies should be performed. Several studies of the synoptic and mesoscale environment of derechos can be found in the literature, both with a climatological perspective and with a case study approach. The type of study lacking is the one addressing cloud scale characteristics. Because routine observations are not available on such small scales, they have to come from special observations or field projects. Dual Doppler radar observations, describing both reflectivity and winds within the clouds, such as used in the studies of Knupp (1987a) and Schmidt and Cotton (1989) would contribute greatly to further understanding these systems. The use of airborne radar measurements, such as the ones made with the ELDORA (Electra Doppler Radar) in TOGA-COARE (Tropical Oceans–Global Atmosphere Coupled Ocean–Atmosphere Response Experiment) (Hildebrand et al. 1996) would be of great value.

- It would be of great interest to further study the origin of the pressure gradient force that lifts the parcels out of the stable boundary layer, and is instrumental in developing the up–down branch of the nocturnal downdraft. One possible avenue is to develop a non-hydrostatic balanced model, which would be an extension of the hydrostatic models by Raymond and Jiang (1990) and Olsson and Cotton (1997b). Such a model would filter out gravity waves and allow one to determine the magnitude of the pressure gradient force associated with the mesocyclone. Comparison of the upward pressure gradient force for a balanced mesocyclone and that of a numerical prediction would then determine if the force is indeed associated with the rotating storm. This approach may be very challenging because such a non–hydrostatic non-linear model has not been formulated, and because the features in which we are interested are located very close to the lower boundary of the model where friction, which will not be represented by a balanced model, is an important acceleration. Also, the choice of boundary conditions for the invertibility principle can contaminate the solution near the ground.

- An obvious application of this research is in weather forecasting. Johns and Hirt (1987) have developed a set of forecasting rules for derecho events. Although these constituted an advancement in forecasting, they are far from comprehensive, and would have failed in the prediction of the system studied here, since it developed under a 500 hPa flow which had too much of a southerly component and the surface front was not parallel to the 500 hPa flow. Therefore, forecasting rules must be revised in light of the several case studies performed in the last ten years. Our work suggests that the existence of a bow–echo–shaped cell with an embedded mesocyclone that exists on top of a nocturnal boundary layer or some other stable layer may be a key feature of derechos. WSR88D radar data should be scrutinized to see if this is indeed the case.

Chapter 9

REFERENCES

Alexander, G. D. and W. R. Cotton, 1997. The use of cloud-resolving simulations of mesoscale convective systems to build a convective parameterization scheme. Conditionally accepted for publication by *J. Atmos. Sci.*

Augustine, J. A. and F. Caracena, 1994. Lower-tropospheric precursors to nocturnal MCS development over the central United States. *Wea. Forec.*, **9**, 116–135.

Avissar, R. and R. A. Pielke, 1989. A parameterization of heterogeneous land surface for the atmospheric numerical models and its impact on regional meteorology. *Mon. Wea. Rev.*, **114**, 330–343.

Barnes, S. L. 1973. Mesoscale objective map analysis using weighted time–series observations. NOAA Tech. Memo. ERL NSSL-62 [NTIS COM-73-10781], March, National Severe Storms Laboratory, Norman, Oklahoma, 60 pp.

Barrit, R. C. and M. I. Biggerstaff, 1993. Kinematic structure of a long–track severe straight–line wind storm. *17th Conference on Severe Local Storms*, St. Louis, MO, 577-581.

Bartels, D. L. and R. A. Maddox, 1991. Midlevel cyclonic vortices generated by mesoscale convective systems. *Mon. Wea. Rev.*, **119**, 104–118.

Bélair, S., D.-L. Zhang and J. Mailhot, 1995. Numerical prediction of an intense convective system associated with the July 1987 Montreal Flood. Part I: Gravity waves and the squall line. *Atmos.-Ocean*, **33**, 447–473.

Benjamin, T. B., 1966. Internal waves of finite amplitude and permanent form. *J. Fluid Mech.*, **25**, 241–270.

Benjamin, T. B., 1967. Internal waves of permanent form in fluids of great depth. *J. Fluid Mech.*, **29**, 559–592.

Bentley, M. L., 1995. The 8 July 1993 Nebraska derecho: An observational study and comparison with the climatology of related mesoconvective systems. M.A. Thesis, Univ. of Nebraska, Lincoln.

Bernstein, B. C. and R. H. Johnson, 1995. A dual-Doppler radar study of an OK PRE-STORM heat burst event. *Mon. Wea. Rev.*, **122**, 259–273.

Blackadar, A., 1957. Boundary layer wind maxima and their significance for the growth of nocturnal inversion. *Bull. Amer. Metor. Soc.*, **38**, 283–290.

Blanchard, D. O., W. R. Cotton and J. M. Brown, 1997. Mesoscale circulation growth under conditions of weak inertial instability. *Mon. Wea. Rev.*, accepted for publication.

Bluestein, H. B., 1993. *Synoptic–Dynamic meteorology in midlatitudes. Volume II: Observations and Theory of Weather Systems*. Oxford University Press, New York, 594 pp.

Bluestein, H. B. and C. R. Parks, 1983. A synoptic and photographic climatology of low–precipitation severe thunderstorms in the Southern Plains. *Mon. Wea. Rev.*, **118**, 1640–1664.

Blumen, W., 1972. Geostrophic adjustment. *Rev. Geophys. Space Phys.*, **10**, 485–528.

Brandes, E. A., 1990. Evolution and structure of the 6–7 May 1985 mesoscale convective system and associated vortex. *Mon. Wea. Rev.*, **118**, 109–127.

Bretherton, C. S. and P. K. Smolarkiewicz, 1989. Gravity waves, compensating subsidence and detrainment around cumulus clouds. *J. Atmos Sci.*, **46**, 740–759.

Brooks, H. E. and R. B Wilhelmson, 1992. Numerical simulation of a low-precipitation supercell thunderstorm. *Meteor. Atmos. Phys.*, **49**, 3–17.

Browning, K. A., 1964. Airflow and precipitation trajectories within severe local storms which travel to the right of the winds. *J. Atmos Sci.*, **21**, 634–639.

Byers, H. R. and R. R. Braham, 1949. The thunderstorm. U. S. Government Printing Office, Washington D. C., 287 pp.

Carbone, R. E., J. W. Conway, N. A. Crook and M. W. Moncrieff, 1990. The generation and propagation of a nocturnal squall line. Part I: Observations and implications to mesoscale predictability. *Mon. Wea. Rev.*, **118**, 26–48.

Carlson, T. N., S. G. Benjamin and G. S. Forbes, 1983. Elevated mixed layers in the regional severe storm environment: Conceptual model and case studies. *Mon. Wea. Rev.*, **111**, 1453–1473.

Chisholm, A. J. and J. H. Renick, 1972. Supercell and multicell hailstorms. *International Cloud Physics Conference*, London, England, 1–8.

Christie, D. R. 1989. Long nonlinear waves in the lower atmosphere. *J. Atmos Sci.*, **46**, 1462–1491.

Christie, D. R., 1992. The morning glory of the Gulf of Carpentaria: A paradigm for non–linear waves in the lower atmosphere. *Aust. Met. Mag*, **41**, 21–60.

Christie, D. R., K. J. Muirhead and A. L. Hales, 1978. On solitary waves in the atmosphere. *J. Atmos Sci.*, **35**, 805–825.

Clark, T. L. and R. D. Farley, 1984. Severe downslope windstorm calculations in two and three spatial dimensions using anelastic interactive grid nesting: A possible mechanism for gustiness. *J. Atmos Sci.*, **41**, 329–350.

Clark, T. L. and W. D. Hall, 1991. Multi–domain simulations of the time dependent Navier-Stokes equations: Benchmark error analysis of some nesting procedures. *J. Comput. Phys.*, **92**, 456–481.

Colman, B. R., 1990a. Thunderstorms above frontal surfaces in environments without positive CAPE. Part I: Climatology. *Mon. Wea. Rev.*, **118**, 1103–1121.

Colman, B. R., 1990b. Thunderstorms above frontal surfaces in environments without positive CAPE. Part II: Organization and instability mechanisms. *Mon. Wea. Rev.*, **118**, 1103–1121.

Cooper, S. R. and M. L. Bentley, 1996. A case study of the 8–9 July 1993 Great Plains derecho. *18th Conf. on Severe Local Storms*, San Francisco, CA, Amer. Meteor. Soc., 531–535.

Cotton, W. R., G. D. Alexander, R. Hertenstein, R. L. Walko, R. L. McAnelly and M. Nicholls, 1995. Cloud venting — A review and some new global annual estimates. *Earth–Science Reviews*, **39**, 169–206.

Cotton, W. R. and R. A. Anthes, 1989. *Storm and Cloud Dynamics*. Academic Press, 883 pp.

Cotton, M. Lin, R. L. McAnelly, and C. J. Tremback, 1989. A composite model of mesoscale convective complex. *Mon. Wea. Rev.*, **117**, 765–783.

Cotton, W. R., G. Thompson and P. W. Mielke, 1994. Real-time mesoscale prediction on workstations. *Bull. Amer. Meteor. Soc.*, **75**, 349–362.

Cram, J. M., R. A. Pielke and W. R. Cotton, 1992a. Numerical simulation and analysis of a pre-frontal squall line. Part I: Observations and basic simulation results. *J. Atmos Sci.*, **49**, 189–208.

Cram, J. M., R. A. Pielke and W. R. Cotton, 1992b. Numerical simulation and analysis of a pre-frontal squall line. Part I: Propagation of the squall line as an internal gravity wave. *J. Atmos Sci.*, **49**, 210–225.

Crook, N. A. and M. W. Moncrieff, 1988. The effect of large-scale convergence on the generation and maintenance of deep moist convection. *J. Atmos Sci.*, **45**, 3606–3624.

Davies, H. C., 1979. Phase-lagged wave-CISK. *Quart. J. Royal Met. Soc.*, **105**, 325–353.

Davies, H. C., 1983. Limitations of some common lateral boundary schemes used in regional NWP models. *Mon. Wea. Rev.*, **111**, 1002–1012.

Davies–Jones, R., 1984. Streamwise vorticity: The origin of updraft rotation in supercell storms. *J. Atmos Sci.*, **41**, 2991–3006.

Davis, C. A. and M. L. Weisman, 1994. Balanced dynamics of mesoscale vortices produced in simulated convective systems. *J. Atmos Sci.*, **51**, 2005–2030.

Doswell, C. A., A. R. Moller and R. Pryzybilinski, 1990. A unified set of conceptual models for variations on the supercell theme. *16th. Conf. on Severe Local Storms*, Kanannaskis Park, Alberta, Canada, Amer. Meteor. Soc., 40–45.

Doviak, R. J., S. S. Chen and D. R. Christie, 1991. A thunderstorm–generated solitary wave observation compared with theory for nonlinear waves in a sheared atmosphere. *J. Atmos Sci.*, **48**, 87–111.

Doviak, R. J. and D. R. Christie, 1989. Thunderstorm–generated gravity waves: a wind shear hazard. *J. Aircraft*, **26**, 423–431.

Doviak, R. J. and R. Ge, 1984. An atmospheric solitary gust observed with a Doppler radar, a tall tower and a surface network. *J. Atmos Sci.*, **41**, 2559-2573.

Duke, J. W. and J. A. Rogash, 1992. Multiscale review of the development and early evolution of the 9 April 1991 derecho. *Wea. Forec.*, **7**, 623–635.

Fortune, M. A., W. R. Cotton and R. L. McAnelly, 1992. Frontal–wave–like evolution in some mesoscale convective complexes. *Mon. Wea. Rev.*, **120**, 1279–1300.

Fovell, R. G. and Y. Ogura, 1988. Numerical simulation of a midlatitude squall line in two dimensions. *J. Atmos Sci.*, **45**, 3846–3879.

Fritsh, J. M., J. D. Murphy and J. S. Kain, 1994. Warm–core vortex amplification over land. *J. Atmos Sci.*, **51**, 1780–1807.

Fujita, T. T., 1978. Manual of downburst identification for project NIMROD. Satellite and Meteorology Research Paper No. 156, Dept. of Geophysical Sciences, Univ. of Chicago, 104 pp.

Fujita, T. T., 1981. Tornadoes and downbursts in the context of generalized planetary scales. *J. Atmos Sci.*, **38**, 1511–1534.

Fulton, R., D. S. Zrnić and R. J. Doviak, 1990. Initiation of a solitary wave family in the demise of a nocturnal thunderstorm density current. *J. Atmos Sci.*, **47**, 319–337.

Funk, T. W., K. E. Darmofal, J. D. Kirkpatrick, M. T. Shields, R. W. Przybylinski, Y.-J. Lin, G. K. Schmocker and T. J. Shea, 1996. Storm reflectivity and meso-cyclone evolution associated with the 15 April 1994 derecho. Part II: storm structure and evolution over Kentucky and southern Indiana. *18th Conf. on Severe Local Storms*, San Francisco, CA, Amer. Meteor. Soc., 516–520.

Geer, I. W., Editor, 1996. *Glossary of weather and climate with related oceanic and hydrologic terms.* Amer. Meteor. Soc., 272 pp.

Grasso, L. D., 1996. Numerical simulation of the May 15 and April 26, 1991 tornadic thunderstorms. Atmospheric Science Paper No. 596, 151pp. [Available from Department of Atmospheric Science, Colorado State University, Fort Collins, CO 80523].

Grasso. L. D. and W. R. Cotton, 1995. Numerical simulation of a tornado vortex. *J. Atmos Sci.*, **52**, 1192–1203.

Grasso, L. D. and W. R. Cotton, 1997a. The simulation of two tornadic thunderstorms initiated by dry line dynamics. Part I: Simulated dry lines and thunderstorms. Submitted to *J. Atmos Sci.*.

Grasso, L. D. and W. R. Cotton, 1997b. The simulation of two tornadic thunderstorms initiated by dry line dynamics. Part II: Simulated tornadoes. Submitted to *J. Atmos Sci.*.

Hertenstein, R. A., 1996. Evolution of potential vorticity associated with mesoscale convective systems. Atmospheric Science Paper No. 599, 170pp. [Available from Department of Atmospheric Science, Colorado State University, Fort Collins, CO 80523].

Hertenstein, R. F. A. and W. H. Schubert, 1991. Potential vorticity anomalies associated with squall lines. *Mon. Wea. Rev.*, **119**, 1663–1672.

Hildebrandt, P. H., W-C Lee, C. A. Walther, C. Frush, M. Randall, E. Loew, R. Neitzel, R. Parsons, J. Testud, F. Baudin and A. LeCornec, 1996. *Bull. Amer. Meteor. Soc.*, **77**, 213–242.

Hill, G. E., 1974. Factors controlling the size and spacing of cumulus clouds as revealed by numerical experiments. *J. Atmos Sci.*, **31**, 646–673.

Hinrichs, G. Tornadoes and derechoes, 1888. *Amer. Meteor. J.*, **5**, 306–317, 341–349.

Holton, J. R., 1992. *An introduction to dynamic meteorology.* Academic Press, 3rd. edition, 511 pp.

Houze, R. A., 1993. *Cloud dynamics.* Academic Press, 573pp.

Houze, R. A., S. A. Rutledge, M. I. Biggerstaff and B. F. Smull, 1989. Interpretation of Doppler weather radar displays of midlatitude mesoscale convective systems. *Bull. Amer. Meteor. Soc.*, **70**, 608–619.

Houze, R. A., B. F. Smull and P. Dodge, 1990. Mesoscale organization of springtime rainstorms in Oklahoma. *Mon. Wea. Rev.*, **117**, 613–654.

Johns, R. H., 1982. A synoptic climatology of northwest flow severe weather outbreaks. Part I: Nature and significance. *Mon. Wea. Rev.*, **110**, 1653–1663.

Johns, R. H., 1984. A synoptic climatology of northwest flow severe weather outbreaks. Part II: Meteorological parameters and synoptic patterns. *Mon. Wea. Rev.*, **112**, 449–464.

Johns, R. H., J. M. Davies and P. W. Leftwich, 1993. Some wind and instability parameters associated with strong and violent tornadoes. Part II: Variations in the combinations of wind and instability parameters. *The Tornado: Its structure, Dynamics, Prediction and Hazards, Geophys. Monogr.*, No. 79, Amer. Geophys. Union, 583–590.

Johns, R. H. and Hart, J. A., 1993. Differentiating between types of severe thunderstorm outbreaks: A preliminary investigation. *17th. Conference on Severe Local Storms*, St Louis, MO, 46–50.

Johns, R. H. and W. D. Hirt, 1987. Derecho: widespread convectively induced windstorms. *Wea. Forec.*, **2**, 32–49.

Johnson, R. H. and P. J. Hamilton, 1988. The relationship of surface pressure features to the precipitation and airflow structure of an intense midlatitude squall line. *Mon. Wea. Rev.*, **116**, 1444–1472.

Klemp, J. B., 1987. Dynamics of tornadic thunderstorms. Ann. Rev. Fluid Mech., **19**, 369–402.

Klemp, J. B. and R. B. Wilhelmson, 1978. The simulation of three-dimensional convective storm dynamics. *J. Atmos Sci.*, **35**, 1070–1096.

Knupp, K. R., 1987. Downdrafts within High Plains cumulonimbi. Part I: General kinematic structure. *J. Atmos Sci.*, **44**, 988–1008.

Knupp, K. R., 1988. Downdrafts within High Plains cumulonimbi. Part II: Dynamics and thermodynamics. *J. Atmos. Sci.*, **45**, 3965–3982.

Knupp, K. R. and W. R. Cotton, 1982a. An intense, quasi-steady thunderstorm over mountainous terrain. Part II: Doppler radar observations of the storm morphological structure. *J. Atmos Sci.*, **39**, 343–358.

Knupp, K. R. and W. R. Cotton, 1982b. An intense, quasi-steady thunderstorm over mountainous terrain. Part III: Doppler radar observations of the turbulence structure. *J. Atmos Sci.*, **39**, 359–368.

Koch, S. E., R. E. Golus and P. B. Dorian, 1987. A mesoscale gravity wave event observed during CCOPE. Part II: Interactions between mesoscale convective systems and antecedent waves. *Mon. Wea. Rev.*, **116**, 2545–2569.

Kuettner, J. P., P. A. Hildebrand and T. L. Clark, 1987. Convection waves: Observations of gravity wave systems over convectively active boundary layers. *Quart. J. Royal Met. Soc.*, **113**, 445–467.

Laing, A. G., 1997. The large scale environment of mesoscale convective complexes: comparison with other deep convective weather systems. *22nd Conference on Hurricanes and Tropical Meteorology*, Fort Collins, CO, Amer. Meteor. Soc., 415–416.

Laing, A. G. and J. M. Fritsch, 1993a. Mesoscale convective complexes over the Indian monsoon region. *J. Clim.*, **6**, 911–919.

Laing, A. G. and J. M. Fritsch, 1993b. Mesoscale convective complexes in Africa. *Mon. Wea. Rev.*, **121**, 2254–2263.

Laing, A. G. and J. M. Fritsch, 1997. The global population of mesoscale convective complexes. *Quart. J. Royal Met. Soc.*, **123**, 389–405.

Lalas, D. P. and F. Einaudi, 1976. On the characteristics of gravity waves generated by atmospheric shear layers. *J. Atmos Sci.*, **33**, 1248–1259.

Lee, W-C., R. E. Carbone and R. M. Wakimoto, 1992a. The evolution and structure of a "bow-echo–microburst" event. Part I: The microburst. *Mon. Wea. Rev.*, **120**, 2188–2210.

Lee, W-C., R. M. Wakimoto and R. E. Carbone, 1992b. The evolution and structure of a "bow-echo–microburst" event. Part II: The bow echo. *Mon. Wea. Rev.*, **120**, 2211–2225.

Lemon, L. R. and Doswell, 1979. Severe thunderstorm evolution and mesocyclone structure as related to tornadogenesis. *Mon. Wea. Rev.*, **107**, 1184–1197.

Lilly, D. K., 1962. On the numerical simulation of buoyant convection. *Tellus*, **2**, 148–172.

Lilly, D. K., 1986. The Structure, energetics and propagation of rotating convective storms. Part II: Helicity and storm stabilization. *J. Atmos Sci.*, **43**, 126–140.

Lim, H., T.-K. Lim, and C.-P. Chang, 1990. Reexamination of wave-CISK theory: existence and properties of nonlinear wave-CISK modes. *J. Atmos Sci.*, **47**, 3078–3091.

Lin, Y-L. and R. C. Goff, 1988. A study of a mesoscale solitary wave in the atmosphere originating near a region of deep convection. *J. Atmos Sci.*, **45**, 194–205.

Lindzen, R. S. and K. K. Tung, 1976. Banded convective activity and ducted gravity waves. *Mon. Wea. Rev.*, **104**, 1602–1617.

Loehrer, S. M., 1992. The surface pressure features and precipitation structure of PRE-STORM mesoscale convective systems. Atmospheric Science Paper No. 518, 296 pp. [Available from Department of Atmospheric Science, Colorado State University, Fort Collins, CO 80523].

Louis, J. F., M. Tiedke and J.-F. Geleyn 1981. A short history of the PBL parameterization at the ECMWF. Workshop on Planetary Boundary layer parameterization, Shinfield Park, Reading, United Kingdom, ECMWF, 59–80.

Loveland, T. R., J. W. Merchant, D. O. Ohlen and J. F. Brown, 1991. Development of a land-cover characteristics database for the conterminous U.S.. *Photo. Eng. Rem. Sens.*, **57**, 1453–1463.

Maddox, R. A., 1979. Synoptic and Meso-α scale aspects of flash flood events. *Bull. Amer. Meteor. Soc.*, **60**, 115–123.

Maddox, R. A., 1980. Mesoscale Convective Complexes. *Bull. Amer. Meteor. Soc.*, **61**, 1374–1387.

Maddox, R. A., 1983. Large-scale meteorological conditions associated with midlatitude, mesoscale convective complexes. *Mon. Wea. Rev.*, **111**, 1475–1493.

Mahrer, Y. and R. A. Pielke, 1977. A numerical study of the airflow over irregular terrain. *Beitr. Phys. Atmos.*, **50**, 98–113.

Mapes, B., 1993. Gregarious tropical convection. *J. Atmos Sci.*, **50**, 2026–2037.

McAnelly, R. L. and W. R. Cotton, 1986. Meso-beta-scale characteristics of an episode of meso-alpha-scale convective complexes. *Mon. Wea. Rev.*, **114**, 1740–1770.

McAnnely, R. L., J. E. Nachamkin, W. R. Cotton and M. E. Nicholls, 1997. Upscale evolution of MCSs: Doppler radar analysis and analytical investigation. *Mon. Wea. Rev.*, **125**, 1083–1110.

McNider, R. T. and R. A. Pielke, 1981. Diurnal boundary-layer development over sloping terrain. *J. Atmos. Sci.*, **38**, 2198–2212.

McNulty, R. P., 1995. Severe and convective weather: A central region forecasting challenge. *Wea. Forec.*, **10**, 187–202.

Meitín, J. G. and J. B. Cunning, 1985. The Oklahoma–Kansas Preliminary Regional Experiment for STORM–Central (OK–PRESTORM), Volume 1, Daily Operations Summary. NOAA Tech. Memo. ERL ESG–20, Department of Commerce, Weather Research Program, Boulder, CO, 313 pp.

Messinger, F. and A. Arakawa, 1976. Numerical methods in atmospheric models. GARP Publication Series No. 17. World Meteorological Organization.

Mitchell, M. J., R. W. Arrit and K. Labas, 1995. A Climatology of the warm season great plains low-level jet using wind profiler observations. *Wea. Forec.*, **10**, 576–591.

Moller, A. R. and C. A. Doswell, 1988. A proposed advanced storm spotters' training program. *15th Conf. on Severe Local Storms*, Baltimore, MD, Amer. Meteor. Soc., 173–177.

Moller, A. R., C. A. Doswell M. P. Foster and G. R. Woodall, 1994. The operational recognition of supercell thunderstorm environments and storm structures. *Wea. Forec.*, **9**, 327–347.

Moller, A. R., C. A. Doswell and R. Pryzybilinski, 1990. High-precipitation supercells: A conceptual model and documentation. *16th. Conf. on Severe Local Storms*, Kanannaskis Park, Alberta, Canada, Amer. Meteor. Soc., 52–57.

Nachamkin, J. E. and W. R. Cotton, 1996. Numerical simulation of the growth of a high plains MCS. Proceedings, *7th Conference on Mesoscale Processes*, 9–13 September 1996, Reading, UK, American Meteorological Society.

Nair, U., M. Hjelmfelt and R. Pielke, 1995. Numerical simulation of the June 9–10, 1972 Black Hills storm using CSU RAMS. *7th Conference on Mountain Meteorology*, Breckenridge, CO, Amer. Meteor. Soc., 51–56.

Nicholls, M., R. A. Pielke and W. R. Cotton, 1991. Thermally forced gravity waves in an atmosphere at rest. *J. Atmos Sci.*, **48**, 1870–1884.

Olsson, P. Q., and W. R. Cotton, 1997a. Balanced and unbalanced circulations in a primitive equation simulation of a midlatitutde MCC. Part I: The numerical simulation. *J. Atmos. Sci.*, **54**, 457–478.

Olsson, P. Q., and W. R. Cotton, 1997b. Balanced and unbalanced circulations in a primitive equation simulation of a midlatitutde MCC. Part II: Analysis of balance. *J. Atmos. Sci.*, **54**, 479–497.

Pandya, R. E. and D. R. Durran, 1996. The influence of convectively generated thermal forcing on the mesoscale circulation around squall lines. *J. Atmos Sci.*, **53**, 2924–2951.

Pielke, R. A., W. R. Cotton, R. L. Walko, C. J. Tremback, W. E. Lyons, L. D. Grasso, M. E. Nicholls, M. D. Moran, D. A. Wesley, T. J. Lee and J. H. Copeland, 1992. A comprehensive meteorological modeling system - RAMS. *Meteor. and Atmos. Phys.*, **49**, 69–91.

Pitchford, L. and J. London, 1962. The low-level jet as related to nocturnal thunderstorms over midwest united states. *J. Appl. Meteor.*, **1**, 43–47.

Porter, J. L. Means, J. Hovde and W. Chappell, 1955. A synoptic study on the formation of squall lines in the north central united stated. *Bull. Amer. Meteor. Soc.*, **36**, 390–396.

Pothecary, J. W., 1954. Short-period variations in surface pressure and wind. *Quart. J. Royal Met. Soc.*, **80**, 395–401.

Proctor, F. H., 1989a. Numerical simulation of an isolated microburst. Part I: Dynamics and structure. *J. Atmos Sci.*, **45**, 3137–3160.

Proctor, F. H., 1989b. Numerical simulation of an isolated microburst. Part II: Sensitivity experiments. *J. Atmos Sci.*, **46**, 2143-2165.

Przybylinski, R. W., 1995. The bow echo: Observations, numerical Simulations and severe weather detection methods. *Wea. Forec.*, **10**, 203–218.

Przybylinski, R. W. and D. M. DeCaire, 1985. radar signatures associated with the derecho, a type of mesoscale convective system. *14th Conference on Severe Local Storms*, Indianapolis, IN, Amer. Meteor. Soc., 228–231.

Przybylinski, R. W., Y. Lin, C. Doswell, G. Schmocker, T. Shea, T. Funk, J. Kirkpatrick, K. Darmofal and M. Shields, 1996. Storm reflectivity and mesocyclone evolution associated with the 15 April 1994 derecho. Part I: Storm evolution over Missouri and Illinois. *18th Conference on Severe Local Storms*, San Francisco, CA, 509–515.

Raymond, D. J., 1983. Wave-CISK in mass-flux form. *J. Atmos Sci.*, **40**, 2561–2572.

Raymond, D. J., 1984. Wave-CISK model of squall lines. *J. Atmos Sci.*, **41**, 2561–2572.

Raymond, D. J., 1992. Nonlinear balance and potential vorticity thinking at large Rossby number. *Quart. J. Royal Met. Soc.*, **118**, 987–1015.

Raymond, D. J. and H. Jiang, 1990. A theory for long-lived mesoscale convective systems. *J. Atmos Sci.*, **47**, 3067–3077.

Rochette, S. M., J. T. Moore, P. S. Market, F. H. Glass and D. L. Ferry, 1995. Heavy rain events associated with elevated thunderstorms in the midwest. Postprints, 4th. National Winter Weather Workshop, NOAA Tech. Memo. NMW CR–112, 25-1-25-12.

Rottman, J. W., F. Einaudi, S. E. Koch and W. L. Clark, 1992. A case study of penetrative convection and gravity waves over the PROFS mesonetwork on 23 July 1983. *Meteor. Atmos. Phys.*, **47**, 205–227.

Rotunno, R. and J. Klemp, 1982. The influence of shear-induced pressure gradients on thunderstorm motion. *Mon. Wea. Rev.*, **110**, 136–151.

Rotunno, R. and J. Klemp, 1985. On the rotation and propagation of simulated supercell thunderstorms. *J. Atmos Sci.*, **42**, 271–292.

Schmidt, J. M., 1991. Numerical and Observational Investigation of Long–lived, MCS–induced, Severe Surface Wind Events: The Derecho. Atmospheric Science Paper No. 479, 196pp. [Available from Department of Atmospheric Science, Colorado State University, Fort Collins, CO 80523].

Schmidt, J. M. and W. R. Cotton, 1989. A High Plains squall line associated with severe surface winds. *J. Atmos. Sci.*, **46**, 281–302.

Schmidt, J. M. and W. R. Cotton, 1990. Interactions between upper and lower tropospheric gravity waves on squall line structure and maintenance. *J. Atmos. Sci.*, **47**, 1205–1222.

Schubert, W. H., S. R. Fulton and R. F. A. Hertenstein, 1989. Balanced atmospheric response to squall lines. *J. Atmos Sci.*, **46**, 2478–2483.

Scott, J. D. and S. A. Rutledge, 1995. Doppler radar observations of an asymmetric mesoscale convective system and associated vortex couplet. *Mon. Wea. Rev.*, **123**, 3437–3457.

Skamarock, W. C., M. L. Weisman and J. B. Klemp, 1994. Three-dimensional evolution of simulated long–lived squall lines. *J. Atmos Sci.*, **51**, 2563–2584.

Smagorinsky, J., 1963. General circulation experiments with the primitive equations. Part I: The basic experiment. *Mon. Wea. Rev.*, **91**, 99–164.

Smith, R. B., 1979. The influence of mountains in the atmosphere. Advances in Geophysics, Vol 26, Academic Press, 87–230.

Storm Data, 1985. National Oceanic Atmospheric Administration Environmental Data Series, **27**, Asheville, NC.

Tremback, C. J., 1990. Numerical simulations of a mesoscale convective complex: model development and numerical results. Atmospheric Science Paper No. 465, 247pp. [Available from Department of Atmospheric Science, Colorado State University, Fort Collins, CO 80523].

Tremback, C. J. and R. Kessler, 1985. A surface temperature and moisture parameterization for use in mesoscale numerical models. Preprints, 7th Conference on Numerical Weather Prediction, 17–20 June 1985, Montreal, Canada, AMS.

Trier, S. B. and D. B. Parson, 1993. Evolution of environmental conditions preceding the development of a nocturnal mesoscale convective complex. *Mon. Wea. Rev.*, **121**, 1078–1098.

Tripoli, G. J. and W. R. Cotton, 1989a. Numerical study of an observed orogenic mesoscale convective system. Part 1: Simulated genesis and comparison with observations. *Mon. Wea. Rev.*, **117**, 273–304.

Tripoli, G. J. and W. R. Cotton, 1989b. Numerical study of an observed orogenic mesoscale convective system. Part 2: Analysis of governing dynamics. *Mon. Wea. Rev.*, **117**, 305–328.

Uccellini, L. W. and S. E. Koch, 1987. The synoptic setting and possible energy sources for mesoscale wave disturbances. *Mon. Wea. Rev.*, **115**, 721–729.

Velasco, I. and J. M. Fritsh, 1987. Mesoscale convective complexes in the Americas. *J. Geophys. Res.*, **92**, 9591–9613.

Verlinde, J. and W. R. Cotton, 1990. Mesoscale vortex–couplet observed in the trailing anvil of a multi-cellular convective complex. *Mon. Wea. Rev.*, **118**, 993–1010.

Wakimoto, R. M., 1998. The life cycle of thunderstorm gust fronts as viewed with doppler radar and rawinsonde data. *Mon. Wea. Rev.*, **110**, 1060–1082.

Walko, R., W. Cotton, M. Meyers and J. Harrington, 1995a. New RAMS cloud microphysics parameterization. Part I: the single-moment scheme. *Atmos. Res.*, **38**, 29–62.

Walko, R. L., C. J. Tremback and R. F. A. Hertenstein, 1995b. RAMS—The regional atmospheric modeling system: Version 3b user's guide. Published by Aster Inc., P.O. Box 466, Fort Collins, Colorado, 117 pp.

Wallace, J. M., 1975. Diurnal variation in precipitation and thunderstorm frequency over the conterminous united states. *Mon. Wea. Rev.*, **103**, 406–419.

Weisman, M. L., 1992. The role of convectively generated rear-inflow jets in the evolution of long-lived convective systems. *J. Atmos Sci.*, **49**, 1826–1847.

Weisman, M. L., 1993. The genesis of severe, long–lived bow echoes. *J. Atmos. Sci*, **50**, 645–670.

Weisman, M. L., C. A. Davis, W. C. Skamarock and J. B. Klemp, 1996. The generation of mesoscale convective vortices within long-lived convective systems. *7th Conference on Mesoscale Processes*, Reading, UK, Amer. Meteor. Soc., 450–452.23

Weisman, M. L. and J. B. Klemp, 1984. The structure and classification of numerically simulated convective storms in directionally varying wind shears. *Mon. Wea. Rev.*, **112**, 2479–2497.

Xu, Q. and J. H. E. Clark, 1984. Wave-CISK and mesoscale convective systems. *J. Atmos Sci.*, **41**, 2089–2107.

Zhang, D.-L., K. Gao and D. B. Parsons, 1989. Numerical simulation of an intense squall line during 10–11 June 1985 PRE–STORM. Part I: Model Verification. *Mon. Wea. Rev.*, **117**, 960–994.

Zhong, S., J. Fast and X. Bian, 1996. A case study of the great plains low-level jet using wind profiler network data and a high resolution mesoscale model. *Mon. Wea. Rev.*, **124**, 785–806.